2013

Carbon Dioxide Enhanced Oil Recovery from the Citronelle Oil Field and Carbon Sequestration in the Donovan Sand, Southwest Alabama

Konstantinos A. Theodorou
University of Alabama at Birmingham

CARBON DIOXIDE ENHANCED OIL RECOVERY FROM THE CITRONELLE OIL FIELD AND CARBON SEQUESTRATION IN THE DONOVAN SAND, SOUTHWEST ALABAMA

by

KONSTANTINOS THEODOROU

PETER M. WALSH, COMMITTEE CHAIR
STAVROS A. BELBAS
IAN E. HOSCH
ROY P. KOOMULLIL
MELINDA M. LALOR

A DISSERTATION

Submitted to the Graduate Faculty of The University of Alabama at Birmingham,
in partial fulfillment of the requirements for the degree of
Doctor of Philosophy

BIRMINGHAM, ALABAMA

2013

CARBON DIOXIDE ENHANCED OIL RECOVERY FROM THE CITRONELLE OIL FIELD AND CARBON SEQUESTRATION IN THE DONOVAN SAND, SOUTHWEST ALABAMA

KONSTANTINOS THEODOROU

INTERDISCIPLINARY ENGINEERING

ABSTRACT

Capturing carbon dioxide (CO_2) from stationary sources and injecting it into deep underground geologic formations has been identified as a viable method for reducing carbon emissions to the atmosphere. Sedimentary rocks, such as sandstones overlain by shales or evaporites, are the preferred formations because their morphology and structure provide pore space, and containment for the long term storage of CO_2. Sandstone formations have also served as repositories to migrating hydrocarbons, and are the sites of many oil recovery operations. For many depleted oil reservoirs, secondary waterflooding recovery methods are no longer efficient or economically viable, hence the application of tertiary CO_2 enhanced oil recovery (CO_2-EOR) followed by CO_2 storage is an attractive and cost effective business plan.

Citronelle Oil Field, located in southwest Alabama, is the largest and longest producing sandstone oil reservoir in the state, having produced more than 170 million barrels of oil from its estimated 500 million barrels of original oil in place, since its discovery in 1955. The field is in the later stages of secondary recovery by waterflooding and daily oil production has declined considerably. The field is comprised of the Upper and Lower Donovan hydrocarbon bearing sandstones, which are separated by the saline-water-bearing sandstones of the Middle Donovan. The Ferry Lake Anhydrite, which overlies the three sections, serves as their caprock.

The present work is focused on an investigation of the feasibility of a CO_2-EOR project for the Citronelle Oil Field and the use of the Middle Donovan for long term CO_2 storage. A set of static calculations, based on estimation methods which were retrieved from publications in the field, was followed by computer simulations using MASTER 3.0, TOUGH2-ECO2N, and TOUGHREACT. Results using MASTER 3.0, for simulation of CO_2-EOR, indicated that nearly 50 million barrels of additional oil could be produced by tertiary recovery. Results using TOUGH2-ECO2N and TOUGHREACT, for the simulations of CO_2 storage, indicated that 159 million metric tons (175 short tons) of CO_2 could be stored in the Middle Donovan formation. An investigation into possible CO_2 leakage from the reservoirs indicated that the Ferry Lake Anhydrite serves as a very reliable long term storage seal.

The present work can serve as a template for preliminary assessment of tertiary oil recovery and CO_2 storage of similar oil reservoirs and saline-water formations.

DEDICATION

In memory of my parents.

ACKNOWLEDGEMENTS

I would like to extend my sincere gratitude to my committee, the Department of Mechanical Engineering staff, and to all that have assisted me along this learning journey. However, I would be remiss if I did not address individually:

Dr. P. M. Walsh, for his resolute support, uncompromised ethics and mentoring.

Dr. M. M. Lalor, for without her, I would not be in this program. She made it all happen.

Dr. S. A. Belbas, for waiting 25 years to witness this achievement.

Dr. I. E. Hosch and Dr. R. P. Koomullil, for their gracious last minute commitment to be members of my committee, and for their insightful comments and suggestions.

The material presented in this dissertation is based upon work supported by the U.S. Department of Energy, National Energy Technology Laboratory, under Award Number DE-FC26-06NT43029, entitled, "Carbon-Dioxide-Enhanced Oil Production from the Citronelle Oil Field in the Rodessa Formation, South Alabama," and upon work supported by the U. S. Department of Energy under American Recovery and Reinvestment Act Award Number DE-FE0002224, entitled, "Geologic Sequestration Training and Research."

TABLE OF CONTENTS

Page

ABSTRACT iii

DEDICATION v

ACKNOWLEDGEMENTS vi

LIST OF TABLES xii

LIST OF FIGURES xiv

LIST OF ABBREVIATIONS AND SYMBOLS xxi

CHAPTER

1 INTRODUCTION 1

1.1 Carbon Capture and Storage 1

1.2 Carbon Dioxide Sequestration 2

1.3 Depleted Hydrocarbon Reservoirs and Enhanced Oil Recovery 4

1.4 Saline-Water Formations 8

1.5 Mineralization 11

1.6 Research Objectives 13

2 THE ROLE OF CITRONELLE DOME IN CARBON STORAGE 15

2.1 Citronelle Dome 15

2.2 Citronelle Oil Field 17

2.3 Citronelle Oil Field Development 19

2.4 Qualitative CO_2 Sequestration Assessment of Citronelle Dome 20

2.4.1 Depleted Citronelle Oil Reservoirs 21

2.4.2 Citronelle Saline-Water Formations 23

TABLE OF CONTENTS (continued)

Page

3 UPPER BOUNDS ON STATIC CO_2 STORAGE CAPACITY ESTIMATES FOR THE DONOVAN SANDS 25

3.1 Introduction 25

3.2 Capacity Estimate Formulation 26
3.2.1 Static Estimates 26
3.2.2 Dynamic Estimates 27

3.3 Donovan Sandstones Capacity Estimate Categories 30

3.4 Upper and Lower Donovan Pore Volume Estimate 31

3.5 Middle Donovan Pore Volume Estimate 33

3.6 Upper Bound Capacity Estimate 36
3.6.1 Upper and Lower Donovan Upper Bound Estimate 38
3.6.2 Middle Donovan Upper Bound Estimate 38

3.7 Total Upper Bound Capacity Estimate 38

4 STATIC CO_2 STORAGE CAPACITY ESTIMATES FOR THE DONOVAN SANDS 40

4.1 Introduction 40

4.2 Depleted Oil Reservoirs 40
4.2.1 Estimate Based on the Formulation by Kovscek (2002) 41
4.2.2 Estimate Based on the Formulation by Shaw and Bachu (2002) 43
4.2.3 Estimate Based on the Formulation by the U.S. Department of Energy Carbon Sequestration Partnerships (2006) 45

4.3 Carbon Dioxide Storage Accompanying Enhanced Oil Recovery 47

4.4 Saline-water Formations 49
4.4.1 Estimate Based on the Formulation by Pruess et al. (2001) 49
4.4.2 Estimate Based on the Formulation by the U.S. Department of Energy Carbon Sequestration Partnerships (2006) 52

4.5 Mineralization 53

4.6 Static CO_2 Storage Capacity Estimates by Esposito et al. (2008) 53

5 SIMULATION OF CO_2-ENHANCED OIL RECOVERY FROM THE UPPER AND LOWER DONOVAN SANDS 55

5.1 Introduction 55

TABLE OF CONTENTS (continued)

Page

5.2 Carbon Dioxide-Enhanced Oil Recovery Pilot Test 57

5.3 Simulation of the CO_2-Enhanced Oil Recovery Pilot Test using MASTER 3.0 60
5.3.1 Simulation Summary and Model Specifications 61
5.3.2 Pre-Pilot Test Actual and Simulated Oil Production History 67
5.3.3 Pilot Test Simulation Results for Oil Production 67
5.3.4 Visualization Framework of Pilot Test Simulation Results 72
5.3.5 Visualization of Pilot Test Simulation Results for Phase Saturation Before CO_2 Injection 73
5.3.6 Visualization of Pilot Test Simulation Results for Phase Saturation at the End of the First CO_2 Injection 74
5.3.7 Visualization of Pilot Test Simulation Results for Phase Saturation at the End of the Interim Water Injection 76
5.3.8 Visualization of Pilot Test Simulation Results for Phase Saturation at the End of the Second CO_2 Injection 78

5.4 Pilot Test Simulation Results for Optimum Interim Water Injection Period 81

5.5 Simulation Results for 10-Year Water Alternating Gas Recovery Schemes 85

5.6 Simulation Results for 10-Year Water Alternating Gas Recovery Schemes Using Variable Injection Rates 89

5.7 Simulation Results for 10-Year Water Alternating Gas Recovery Based on Updated Field Data 93

5.8 Citronelle Pilot Test Field Operations 96
5.8.1 The CO_2 Storage Tanks, Pumps, and Tank Batteries 96
5.8.2 Carbon Dioxide Injection 97
5.8.3 Response to CO_2 Injection 98

6 SIMULATION OF CO_2 SEQUESTRATION IN THE MIDDLE DONOVAN SANDS 103

6.1 Introduction 103

6.2 Model Specifications 104

6.3 TOUGH2-ECO2N Simulation of CO_2 Injection into the Middle Donovan 105
6.3.1 TOUGH2-ECO2N Simulation Results of CO_2 Injection into the Middle Donovan 107

TABLE OF CONTENTS (continued)

Page

6.3.2 TOUGH2-ECO2N Simulation Results Using Variable CO_2 Injection Rates 117

6.4 TOUGH2-ECO2N Simulation of Permeability Reduction Due to Solid Salt Precipitation During CO_2 Injection into the Middle Donovan 121
6.4.1 Tubes-in-Series Model of Pore Channels Used in Permeability Reduction Simulation 122
6.4.2 Middle Donovan Porosity–Permeability Relationship 124
6.4.3 TOUGH2-ECO2N Simulation Results for Permeability Reduction 126

6.5 TOUGHREACT Simulation of CO_2 Injection into the Middle Donovan 140

6.6 TOUGHREACT Simulation Results of CO_2 Injection into the Middle Donovan 142

7 CARBON DIOXIDE LEAKAGE POTENTIAL FROM THE DONOVAN SANDS 155

7.1 Introduction 155

7.2 Leakage Potential from the Donovan Sands 156

7.3 Seal Formations Controlling Leakage from the Donovan Sands 158
7.3.1 Donovan Formation Shale 160
7.3.2 Mooringsport Shale and Ferry Lake Anhydrite 160

7.4 Analysis of CO_2 Leakage Potential from the Donovan Sands 161
7.4.1 Wettability and Capillary Pressure 161
7.4.2 Vertical Flow Equilibrium 164

7.5 Carbon Dioxide Vertical Migration Dynamics 166
7.5.1 Donovan Formation Parameter Estimates for Well Leakage Calculations 170
7.5.2 Calculation of Critical CO_2 Column Height in the Sandstone Reservoirs of the Upper, Middle, and Lower Donovan 173
7.5.3 Calculation of Critical CO_2 Column Height at the Sandstone–Shale Contact Horizon 175
7.5.4 Calculation of Critical CO_2 Column Height at the Shale–Anhydrite Contact Horizon 179

7.6 Vertical Leakage from Wells in the Citronelle Oil Field 180

7.7 A Rudimentary Estimate of Well Leakage Probability 182

TABLE OF CONTENTS (continued)

Page

7.8 Citronelle Oil Field Wells with Leakage Potential 184
7.9 A Reliability Fault Tree for Estimating Well Leakage Probability 187

8 SUMMARY AND CONCLUSIONS 192

8.1 Objective 192
8.2 Static CO_2 Storage Capacity Estimates for the Donovan Sand 192
8.3 Simulation of CO_2 Enhanced Oil Recovery in the Upper and Lower Donovan Sand 194
8.4 Simulation of CO_2 Sequestration in the Middle Donovan Sand 195
8.5 Carbon Dioxide Leakage Potential from the Donovan Sand 196

REFERENCES 198

LIST OF TABLES

Table *Page*

2.1 Citronelle Dome Cretaceous Upper and Lower Geologic Series 16

2.2 Timeline of major events in the Citronelle Oil Field development 20

3.1 Upper, Middle, and Lower Donovan CO_2 density estimates 37

5.1 Wells in the simulation of the CO_2-EOR pilot test 64

5.2 Primary reservoir parameters specified in the CO_2-EOR pilot test simulations 65

5.3 Well operation schedule for CO_2-EOR pilot test simulation 66

5.4 Summary of simulated cumulative incremental (above the waterflood base line) oil recovery during the CO_2-EOR pilot test from all of the production wells in the simulation grid 71

5.5 Events of interest and corresponding dates, regarding fluid saturations produced by MASTER 3.0 simulations for the pilot test grid 73

5.6 Maximum oil production rates and cumulative incremental oil recovery for all interim water injection scenarios 84

5.7 Oil production and CO_2 utilization for WAG scenarios using symmetric schemes, GROUP 1, and asymmetric schemes, GROUP 2 90

6.1 Primary input variables for the TOUGH2-ECO2N simulations of CO_2 injection into the Middle Donovan 105

6.2 Simulation Stages and Output Timetable for CO_2 Injection in the Middle Donovan 107

LIST OF TABLES

Table *Page*

6.3 Average initial volume fractions of primary mineral components identified in the sandstones of the Rodessa Formation at the Citronelle Oil Field 141

6.4 Possible secondary minerals that could form during TOUGHREACT simulation of CO_2 injection into the Middle Donovan, based on the primary minerals of the Rodessa Formation at the Citronelle Field 142

7.1 Input parameters used in Equations 7.2, 7.3, and 7.4 to estimate pore and pore-throat radii in the sandstone reservoirs 171

8.1 Summary of CO_2 static capacity estimates 193

8.2 Incremental oil recovery during 10-year CO_2-EOR, using the MASTER 3.0 reservoir simulator, for ten WAG scenarios 194

LIST OF FIGURES

Figure *Page*

2.1 Stratigraphic section with spontaneous potential (SP), resistivity well logs, and depth of the Mooringsport Formation, Ferry Lake Anhydrite, and Donovan Sand in the Citronelle Oil Field 17

5.1 Annual oil production at Citronelle Oil Field, (Alabama State Oil and Gas Board database, 2012) 56

5.2 Cumulative oil production at Citronelle Oil Field, (Alabama State Oil and Gas Board database, 2012) 56

5.3 Aerial photograph of the Citronelle Oil Field in the vicinity of the pilot test well pattern 58

5.4a Sand 14-1 thickness contours within and surrounding the inverted 5-spot well pattern 62

5.4b Sand 16-2 thickness contours within and surrounding the inverted 5-spot well pattern 62

5.5 Wells included in the CO_2-enhanced oil recovery simulation grid 63

5.6 Actual and simulated daily oil production rates from the 16 wells in the pilot test simulation grid, for the period from 1/1/1982 to 11/30/2009 68

5.7 Simulation of daily oil production for the CO_2-EOR pilot test (blue line) and continuous waterflood only (red line) 70

5.8 Simulation of cumulative oil production for the CO_2-EOR pilot test and comparison with waterflood only 71

5.9 Oil and water saturations in Sands 14-1(top) and 16-2 (bottom), just before CO_2 injection on 11/30/2009 75

5.10 CO_2, oil, and water saturations in Sands 14-1(top) and 16-2 (bottom), at the end of the first CO_2 injection on 8/20/2010 77

LIST OF FIGURES

Figure *Page*

5.11 CO_2, oil, and water saturations in Sands 14-1 (top) and 16-2 (bottom), at the end of the interim water injection on 4/27/2011 79

5.12 CO_2, oil, and water saturations in Sands 14-1 (top) and 16-2 (bottom), at the end of the second CO_2 injection on 11/1/2011 80

5.13 Simulated daily oil production for water injection intervals of varying duration, after the first 6804 t (7500 short tons) of CO_2 have been injected and before the second CO_2 injection begins 83

5.14 Simulated cumulative oil production for water injection intervals of varying duration, after the first 6804 t (7500 short tons) of CO_2 have been injected and before the second CO_2 injection begins 83

5.15 Simulated daily oil production rates for time-symmetric WAG schemes, in which the water and CO_2 injection intervals are of equal duration 86

5.16 Simulated daily oil production rates for time-asymmetric WAG schemes, in which the water injection interval is held constant at 6 months while the CO_2 injection interval is progressively increased 86

5.17 Simulated cumulative oil production for time-symmetric WAG schemes, in which the water and CO_2 injection intervals are of equal duration 87

5.18 Simulated cumulative oil production for time-asymmetric WAG schemes, in which the water injection interval is held constant at 6 months while the CO_2 injection interval is progressively increased 87

5.19 Incremental oil recovery at CO_2 injection rates of 18.1, 27.2, 31.8, 36.3, 40.8, 49.9, and 54.4 t/day (20, 30, 35, 40, 45, 55, and 60 short tons/day) 91

5.20 Daily oil production at CO_2 injection rates of 18.1, 27.2, 31.8, 36.3, 40.8, 49.9, and 54.4 t/day (20, 30, 35, 40, 45, 55, and 60 short tons/day) 92

LIST OF FIGURES

Figure *Page*

5.21 Cumulative oil production at CO_2 injection rates of 18.1, 27.2, 31.8, 36.3, 40.8, 49.9, and 54.4 t/day (20, 30, 35, 40, 45, 55, and 60 short tons/day) 92

5.22 Daily oil production during a 10-year WAG, with each cycle consisting of 12 months of CO_2 injection followed by 6 months of water injection 95

5.23 Cumulative oil production during a 10-year WAG, with each cycle consisting of 12 months of CO_2 injection followed by 6 months of water injection 95

6.1 TOUGH2-ECO2N simulation of CO_2 saturation, at 30 days, 1 year, 40 years, and 100 years, during and following CO_2 injection into the Citronelle Middle Donovan formation 108

6.2 TOUGH2-ECO2N simulation of pressure, at 30 days, 1 year, 40 years, and 100 years, during and following CO_2 injection into the Citronelle Middle Donovan formation 110

6.3 TOUGH2-ECO2N simulation of CO_2 mass fraction in the aqueous phase, at 30 days, 1 year, 40 years, and 100 years, during and following CO_2 injection into the Citronelle Middle Donovan formation 112

6.4 TOUGH2-ECO2N simulation of solid salt saturation, at 30 days,1 year, 40 years, and 100 years, during and following CO_2 injection into the Citronelle Middle Donovan formation 114

6.5 TOUGH2-ECO2N simulation of NaCl mass fraction in aqueous phase, at 30 days, 1 year, 40 years, and 100 years, during and following CO_2 injection into the Citronelle Middle Donovan formation 115

6.6 TOUGH2-ECO2N simulation of water mass fraction in gas phase, at 30 days, 1 year, 40 years, and 100 years, during and following CO_2 injection into the Citronelle Middle Donovan formation 115

6.7 TOUGH2-ECO2N simulation of gas phase density, at 30 days, 1 year, 40 years, and 100 years, during and following CO_2 injection into the Citronelle Middle Donovan formation 116

LIST OF FIGURES

Figure *Page*

6.8 TOUGH2-ECO2N simulation of aqueous phase density, at 30 days, 1 year, 40 years, and 100 years, during and following CO_2 injection into the Citronelle Middle Donovan formation 116

6.9 TOUGH2-ECO2N simulation of CO_2 saturation, at 40 years, for three CO_2 injection rates: 27.2 t/day (30 short tons/day), 36.3 t/day (40 short tons/day), and 45.4 t/day (50 short tons/day) 118

6.10 TOUGH2-ECO2N simulation of CO_2 saturation, at 100 years, for three CO_2 injection rates: 27.2 t/day (30 short tons/day), 36.3 t/day (40 short tons/day), and 45.4 t/day (50 short tons/day) 118

6.11 TOUGH2-ECO2N simulation of pressure, at 40 years, for three CO_2 injection rates: 27.2 t/day (30 short tons/day), 36.3 t/day (40 short tons/day), and 45.4 t/day (50 short tons/day) 120

6.12 TOUGH2-ECO2N simulation of pressure, at 100 years, for three CO_2 injection rates: 27.2 t/day (30 short tons/day), 36.3 t/day (40 short tons/day), and 45.4 t/day (50 short tons/day) 120

6.13 Model of pore channels as alternating segments of capillary tubes-in-series..... 123

6.14 Permeability reduction curves, for Middle Donovan Sands, as function of percent reduction in porosity, for initial porosities of 1%, 13%, and 14% 125

6.15 TOUGH2-ECO2N simulation of pressure, at 30 days and at 40 years 128

6.16 TOUGH2-ECO2N simulations with permeability reduction enabled. Permeability ratio, at 30 days, for three values of the van Genuchten parameter, *m*: 0.2, 0.5, and 0.9..... 129

6.17 TOUGH2-ECO2N simulations with permeability reduction enabled. Solid salt saturation, at 30 days, for three values of the van Genuchten parameter, *m*: 0.2, 0.5, and 0.9 129

6.18 TOUGH2-ECO2N simulations with permeability reduction enabled. Permeability ratio, at 40 years, for three values of the van Genuchten parameter, *m*: 0.2, 0.5, and 0.9..... 132

LIST OF FIGURES

Figure *Page*

6.19 TOUGH2-ECO2N simulations with permeability reduction enabled. Solid salt saturation, at 40 years, for three values of the van Genuchten parameter, *m*: 0.2, 0.5, and 0.9 132

6.20 TOUGH2-ECO2N simulations with permeability reduction enabled. Permeability ratio, at 100 years, for three values of the van Genuchten parameter, *m*: 0.2, 0.5, and 0.9 133

6.21 TOUGH2-ECO2N simulations with permeability reduction enabled. Solid salt saturation, at 100 years, for three values of the van Genuchten parameter, *m*: 0.2, 0.5, and 0.9 133

6.22 TOUGH2-ECO2N simulations with permeability reduction enabled. CO_2 saturation at 30 days, for three values of the van Genuchten parameter *m*: 0.2, 0.5, and 0.9 135

6.23 TOUGH2-ECO2N simulations with permeability reduction enabled. CO_2 saturation at 40 years, for three values of the van Genuchten parameter, *m*: 0.2, 0.5, and 0.9 135

6.24 TOUGH2-ECO2N simulations with permeability reduction enabled. Pressure at 30 days, for three values of the van Genuchten parameter, *m*: 0.2, 0.5, and 0.9 137

6.25 TOUGH2-ECO2N simulations with permeability reduction enabled. Pressure at 40 years, for three values of the van Genuchten parameter, *m*: 0.2, 0.5, and 0.9 137

6.26 TOUGH2-ECO2N simulations with permeability reduction enabled. Dissolved CO_2 in the aqueous phase at 30 days, for three values of the van Genuchten parameter, *m*: 0.2, 0.5, and 0.9 139

6.27 TOUGH2-ECO2N simulations with permeability reduction enabled. Dissolved CO_2in the aqueous phase at 40 years, for three values of the van Genuchten parameter, *m*: 0.2, 0.5, and 0.9 139

6.28 TOUGHREACT simulations with permeability reduction enabled. CO_2 saturation at 100, 1000, and 10,000 years 144

LIST OF FIGURES

Figure *Page*

6.29 TOUGHREACT simulations with permeability reduction enabled. Dissolved CO_2 at 100, 1,000, and 10,000 years 144

6.30 TOUGHREACT simulations with permeability reduction enabled. Dawsonite change in abundance at 100, 1000, and 10,000 years 146

6.31 TOUGHREACT simulations with permeability reduction enabled. Siderite change in abundance at 100, 1000, and 10,000 years 146

6.32 TOUGHREACT simulations with permeability reduction enabled. Ankerite change in abundance at 100, 1000, and 10,000 years 147

6.33 TOUGHREACT simulations with permeability reduction enabled. Calcite change in abundance at 100, 1000, and 10,000 years 147

6.34 TOUGHREACT simulations with permeability reduction enabled. Oligoclase change of abundance, at 100, 1000, and 10,000 years 148

6.35 TOUGHREACT simulations with permeability reduction enabled. Quartz change in abundance at 100, 1000, and 10,000 years 149

6.36 TOUGHREACT simulations with permeability reduction enabled. Kaolinite change in abundance, at 100, 1000, and 10,000 years..... 150

6.37 TOUGHREACT simulations with permeability reduction enabled. pH of aqueous phase at 100, 1000, and 10,000 years 150

6.38 TOUGHREACT simulations with permeability reduction enabled. Porosity at 100, 1000, and 10,000 years 152

6.39 TOUGHREACT simulations with permeability reduction enabled. Permeability at 100, 1000, and 10,000 years 152

6.40 TOUGHREACT simulations with permeability reduction enabled. Sequestration of CO_2 by carbonate precipitation at 100, 1000, and 10,000 years 153

7.1 Stratigraphic section with spontaneous potential (SP) and resistivity well logs of the Mooringsport Formation, Ferry Lake Anhydrite, and Donovan Sands in the Citronelle Oil Field..... 159

LIST OF FIGURES

Figure *Page*

7.2 Surface tension of a CO_2 globule immersed in brine and in contact with the rock surface 162

7.3 Diagram of a CO_2 globule migrating through rock grains, in a brine filled formation 167

7.4 Diagram of CO_2 migration in the pores of a sandstone (SS) rock matrix 174

7.5 Estimates of critical CO_2 column height using Equation 7.1, for the sandstone reservoirs of the Upper, Middle, and Lower Donovan 175

7.6 Diagram of CO_2 migration from a sandstone (SS) reservoir into overlying shale (SH) 176

7.7 Estimates of critical CO_2 column height using Equation 7.1, at sandstone–shale contact horizons in the Donovan formation 177

7.8 Diagram of CO_2 migration from shale (SH) into the overlying Ferry Lake Anhydrite (A) 180

7.9 Diagram of a vertical cross section of a well, showing the critical locations where CO_2 leakage could occur 182

7.10 Diagram of temporarily and permanently abandoned wells 186

7.11 Logic symbols used in Fault Tree Analysis 188

7.12 Fault tree of critical events for the temporarily and permanently abandoned wells at the Citronelle Oil Field 191

LIST OF ABBREVIATIONS AND SYMBOLS

Abbreviations

ASOGB	Alabama State Oil and Gas Board
BHP	bottom hole pressure of an injection or producing well
CCS	Carbon Capture and Storage
CO_2-EOR	Carbon Dioxide Enhanced Oil Recovery
EGU	Electric Generating Unit (or Utility)
EOR	Enhanced Oil Recovery
GHG	green house gases
IPCC	Intergovernmental Panel on Climate Change
MASTER	Miscible Applied Simulation Techniques for Energy Recovery (Ammer and Brummert, 1991; Ammer, Brummert, and Sams, 1991; Zeng, Grigg, and Chang, 2005)
MMP	minimum miscibility pressure
MW	megawatt, unit of power (1,000,000 watts)
NETL	National Energy Technology Laboratory
NIST	National Institute of Standards and Technology
OOIP	Original Oil in Place
pH	negative logarithm of hydrogen ion concentration
STB	Stock Tank Barrel

LIST OF ABBREVIATIONS AND SYMBOLS

UAB	University of Alabama at Birmingham, Birmingham, AL
USDW	underground sources of drinking water
VFE	Vertical Flow Equilibrium
VTK	Visualization Toolkit
WAG	water-alternating-gas method of enhanced oil recovery
USDOE	U.S. Department of Energy
USDOE-CSP	U.S. Department of Energy Carbon Sequestration Partnership
USEPA	U.S. Environmental Protection Agency

Symbols

B_o	formation volume factor, which expresses the change in oil volume between reservoir and standard conditions at surface, dimensionless
c_d	mass of CO_2 dissolved per unit volume of water, kg/m^3
c_f	capacity factor that considers the distribution of stored CO_2 among the three possible phases: gas, liquid, and solid, dimensionless
c_{fg}	capacity factor for the gas phase, dimensionless
c_{fl}	capacity factor for the liquid phase, dimensionless
c_{fs}	capacity factor for the solid phase, dimensionless
D	grain diameter, cm
D_e	effective grain diameter, based on permeability and porosity relationship, cm
E	efficiency factor ranging from 0.01 to 0.04, for CO_2 capacity estimates in saline water formations, dimensionless
e_f	efficiency factor for Middle Donovan, dimensionless

LIST OF ABBREVIATIONS AND SYMBOLS

g	acceleration due to gravity, 9.80665 m/s^2
h	formation thickness, m
h_c	critical height, which is the minimum height a liquid or gas column must attain, in order for vertical migration driven by buoyancy, to occur in the presence of an immiscible fluid, cm.
k	coefficient of permeability, m^2 or darcy
k_{air}	coefficient of air permeability, refers to permeability of a reservoir core sample measured in the laboratory using air as the fluid, m^2 or darcy
k_h	coefficient of mean horizontal permeability in a formation, m^2 or darcy
k_o	original permeability in the equation describing the permeability reduction due to precipitation of solids, m^2 or darcy
k_v	coefficient of mean vertical permeability in a formation, m^2 or darcy
l	lateral length of formation, m
L	total length of one section of pore and pore throat cylinders, in tubes-in-series model (Verma and Pruess, 1988), cm
L_l	length of pore cylinder in tubes-in-series model (Verma and Pruess, 1988), cm
m	van Genuchten (1980) parameter characterizing the spread of a pore size distribution, dimensionless
m_{all}	mass of CO_2 that could be stored in a reservoir volume if the entire pore volume were filled with pure CO_2, kg
m_{CO_2}	mass of stored CO_2, kg
$m_{CO_2}^g$	mass of CO_2 in the gas phase, kg
$m_{CO_2}^l$	mass of CO_2 in the liquid phase, kg
$m_{CO_2}^{g+l}$	mass of stored CO_2 in gas and liquid phases, kg

LIST OF ABBREVIATIONS AND SYMBOLS

n	number of independent basic events in a fault tree
p_i	the probability that a basic event *i* in a fault tree will occur
P_0	the probability that the top-event in a fault tree will occur
P_c	capillary pressure, dynes/cm^2 or N/m^2
p_p	capillary pressure in the pore, dynes/cm^2 or N/m^2
R	effective pore radius, equal to the radius of the largest sphere, constrained by the surrounding solid matrix, m
r_1	pore cylinder radius in tubes-in-series model (Verma and Pruess, 1988), cm
r_2	pore throat cylinder radius in tubes-in-series model (Verma and Pruess, 1988), cm
r_{bt}	fraction of original oil in place recovered at the time CO_2 breaks through at the production well during CO_2-EOR, dimensionless
R_l	parameter which determines the validity of Vertical Flow Equilibrium given by$(l/h)\sqrt{k_v/k_h}$, dimensionless
r_o	fraction of original oil in place recovered at time of interest, dimensionless
r_{oc}	cumulative primary and secondary oil recovery from the oil reservoirs in the Upper and Lower Donovan, m^3
r_{ou}	ultimate fraction of original oil in place recovered, dimensionless
r_p	pore radius in Berg's (1975) equation for critical height, cm
r_t	pore-throat radius in Berg's (1975) equation for critical height, cm
$\bar{S}_g$	average saturation of CO_2 in the gas phase, dimensionless
$\bar{S}_l$	average saturation of CO_2 in the liquid phase, dimensionless
$\bar{S}_s$	average saturation of CO_2 in the solid phase, dimensionless

LIST OF ABBREVIATIONS AND SYMBOLS

S_s critical solid salt saturation at which permeability becomes zero, dimensionless

S_{wihc} irreducible water saturation of hydrocarbon-bearing sandstones, dimensionless

S_{win} initial water saturation, dimensionless

S_{wis} irreducible water saturation of saline-water-bearing sandstones, dimensionless

S_{or} residual oil saturation of hydrocarbon-bearing sandstones, dimensionless

$\bar{v}_s$ average formation volume fraction occupied by CO_2 in solid carbonates, dimensionless

V_{bhcL} bulk volume of Lower Donovan hydrocarbon-bearing sandstones, m^3

V_{bhcU} bulk volume of Upper Donovan hydrocarbon-bearing sandstones, m^3

V_{bhcUL} total bulk volume of hydrocarbon-bearing sandstones, m^3

V_f total formation volume of the saline-water-bearing sandstones, m^3

V_{iw} volume of water injected into hydrocarbon-bearing sandstones, m^3

V_p available pore volume of formation, m^3

V_{phc} available pore volume in hydrocarbon-bearing sandstones, m^3

V_{ps} available pore volume in saline-water-bearing sandstones, m^3

V_{pw} volume of water produced from hydrocarbon-bearing sandstones, m^3

V_{rr} total reservoir rock volume of hydrocarbon-bearing sandstones, m^3

$\bar{X}_l^{CO_2}$ average mass fraction of CO_2 in the liquid phase, dimensionless

$\bar{X}_s^{CO_2}$ average mass fraction of CO_2 in the solid phase, dimensionless

γ	interfacial tension, dynes/cm or N/m
Γ	fractional length of pore cylinders in tubes-in-series model (Verma and Pruess, 1988), given by L_1/L
λ	component failure rate, number of failures/time
ρ_b	formation brine density under reservoir conditions, kg/m^3
ρ_{CO_2}	CO_2 density under reservoir conditions, kg/m^3
$\bar{\rho}_g$	average gas phase density, kg/m^3
$\bar{\rho}_l$	average liquid phase density, kg/m^3
ρ_L	average density of CO_2 at Lower Donovan conditions, kg/m^3
$\bar{\rho}_s$	average solid phase density, kg/m^3
ρ_U	average density of CO_2 at Upper Donovan conditions, kg/m^3
σ	parameter, depended on saturation of solids, in the equation describing the permeability reduction due to precipitation of solids, defined by Equation 6.2, dimensionless
φ	porosity, dimensionless
φ_{hc}	porosity of hydrocarbon-bearing sandstones, dimensionless
φ_{hcL}	porosity of Lower Donovan hydrocarbon-bearing sandstones, dimensionless
φ_{hcU}	porosity of Upper Donovan hydrocarbon-bearing sandstones, dimensionless
φ_o	original porosity in the equation describing the permeability reduction due to precipitation of solids, dimensionless
φ_r	fraction of original porosity at which permeability is reduced to zero given by φ/φ_0, dimensionless
φ_s	effective porosity of the saline-water formations, dimensionless

ω	parameter, depended on pore length, in the equation describing the permeability reduction due to precipitation of solids, defined by Equation 6.3, dimensionless

CHAPTER 1

INTRODUCTION

1.1 Carbon Capture and Storage

The debate concerning the effects of CO_2 (carbon dioxide) emissions from fossil-fuel-fired electric power generating facilities and other large-scale industrial sources such as oil refineries and fertilizer plants, will likely produce some form of legislation imposing CO_2 emission limits, and CO_2 reduction requirements. In March 2012, the U.S. Environmental Protection Agency (USEPA), proposed new source performance standards for emissions of CO_2 for new fossil-fuel-fired electric generating units (EGU). The agency is proposing these requirements because fossil-fuel-fired power plants are the largest stationary source emitters of green house gases (GHG) in the country. The proposed rules would require new fossil-fuel-fired EGU, with output capacity greater than 25 megawatt (MW), to meet an output-based standard of 1,000 pounds of CO_2 per megawatt-hour.

Notwithstanding regulatory proposals and future legislation outcomes, power generating companies have taken the initiative with a multitude of pilot and demonstration projects aimed at reducing CO_2 emissions. The set of options concerned with reducing CO_2 emissions is termed *Carbon Capture and Storage* (CCS), also referred to as *Carbon Capture and Sequestration*. Technical assessments conducted by the

Intergovernmental Panel on Climate Change (IPCC, 2005), suggest that CCS may be able to achieve up to 20% reduction in CO_2 emissions below present levels over the next 100 years, more than the expected reduction from deployment of renewable energy technologies and efficiency improvements. Among the most promising options is the capture and storage of CO_2 in subterranean formations, having as its ultimate goal the permanent or long-term (>1000 years) retention of CO_2 (IPCC, 2005).

Carbon Capture and Storage is the only set of options that allows the continued use of fossil fuels while reducing emissions. Because a complete transfer to noncarbon technology, for power generation and other CO_2 emitting industries, is expected to take a long time, dependence on fossil fuels and emissions of CO_2 will continue for the foreseeable future.

1.2 Geologic Carbon Dioxide Sequestration

The term *geologic carbon dioxide sequestration* refers to the process of removing CO_2 from anthropogenic sources and its subsequent long-term storage or permanent sequestration in suitable geologic reservoirs (Bachu, 2002). The storage space is comprised of the interstices of the rock matrix in the geologic formation, and is a function of the composition and geologic history of the formation. The sequestration process is enhanced by trapping mechanisms, dependent on the type of formation and its properties. The target formations serve as CO_2 *sinks* capable of geologic-scale retention times.

The preferred geologic formations for CO_2 sequestration are those found in sedimentary basins (Bachu, 2002; Hitchon et al., 1999). Typical sedimentary basins, by virtue of their morphology and diagenetic history, form subterranean structures having

properties identified as necessary for the success of CO_2 sequestration projects. There are three critical formation properties that are indispensable to geologic sequestration, regardless of location: (a) sufficient communicating interstitial space within the rock matrix, necessary for CO_2 storage (*effective porosity*); (b) sufficient network of passageways through the interstitial spaces necessary for mobility of CO_2 in the presence of other fluids (*relative permeability*); and (c) an impermeable overlying structure (*caprock*), to contain (*seal*) the CO_2 and prevent its vertical migration out of the target formation.

Sedimentary rock formations, such as sandstones, have served as repositories to migrating hydrocarbons by providing accumulation space, mobility, and containment through geologic time scales. The same attributes are basic requirements for the success of a geologic CO_2 sequestration project. Depleted hydrocarbon reservoirs residing in sedimentary basins are natural candidates for CO_2 sequestration. In comparison, geologic media associated with crystalline and metamorphic rocks are not well qualified for CO_2 storage. They contain many fractures and exhibit very low effective porosity, which renders them unsuitable as candidates for CO_2 sequestration. Similarly, orogenic belts and volcanic formations are considered unsuitable due to the high density of faults and fractures created during tectonic or volcanic activity.

Although limited in number, large-scale CO_2 sequestration projects are already well established in several locations around the world. The projects at Sleipner Vest gas field in Norway and Weyburn oil field in Canada are two examples demonstrating the viability of CO_2 sequestration to effectively mitigate CO_2 emissions (Petroleum Technology Research Center, 2011; Statoil, 2011). The successful design and operation

of these two projects serve as models and precursors for the wider application of geologic CO_2 sequestration. However, in order to evaluate the CO_2 sequestration potential of a candidate formation, a detailed evaluation of its properties should be carried out initially. Determining the physical properties of a sequestration target requires gathering a great deal of data and its careful assessment. Each target formation, even if in close proximity to similar candidates, should be examined individually. Pathways that might allow injected CO_2 to migrate upward from the storage reservoir and enter an underground source of drinking water or escape from the ground surface, are among the greatest concerns in geologic sequestration, and should be identified and assessed.

The sections that follow describe the most attractive variations of CO_2 sequestration, with regard to technical readiness and cost.

1.3 Depleted Hydrocarbon Reservoirs and Enhanced Oil Recovery

Many hydrocarbon reservoirs are found in sedimentary basins and a great number of them have been depleted or abandoned, as no longer economically viable. Depleted or abandoned hydrocarbon reservoirs are attractive candidates for examination as future repositories of sequestered CO_2 due to their inherent and demonstrated containment characteristics. The presence of a structural trap in a hydrocarbon-bearing formation that impeded migration of hydrocarbon fluids over geologic time is a principal attribute sought after in CO_2 sequestration candidate formations.

Depleted or abandoned hydrocarbon reservoirs have a historical record that illuminates the formation's expected response to CO_2 injection. Additionally, complete descriptions of the reservoir's physical properties are readily available. The advantages of

depleted hydrocarbon reservoirs as potential candidates and viable targets for CO_2 sequestration may be summarized by the following three critical attributes:

a) A considerable collection of *data* mapping the reservoir and its properties will be available. Information about the geology of the reservoir, its structure, and the characterization of the field should already be complete. Production records and well injection rates could provide valuable insight in planning and controlling the CO_2 injection process. An initial approximation of the potential volume of CO_2 to be stored could be obtained through material balance calculations using the hydrocarbon production history, estimates of original oil in place (OOIP), and the properties of the oil reservoir. Production, injection, and reservoir pressure records could provide data with which to predict the response of the reservoir during and after CO_2 injection.

b) Existing piping and well infrastructure may be converted and utilized for injection of CO_2, reducing the amount of capital investment necessary for the project. In cases where existing infrastructure requires repair and retrofitting, it is unlikely that their cost will equal the cost to drill new wells. Redundant infrastructure could be sold or leased for additional savings.

c) Oil and gas reservoirs have proven to be effective traps for liquids and gases, since hydrocarbons that migrated from other locations and accumulated in the reservoir were trapped there for millions of years. Assuming the integrity of the reservoir formation has not been

compromised by hydraulic fracturing, or water injection, during oil production, or CO_2 injection for enhanced oil recovery, it is reasonable to expect that the reservoir will also trap injected CO_2 for a long time. A thorough characterization of the reservoir formation prior to any CO_2 injection will be necessary to assure its integrity. Increased pressure in the reservoir during waterflooding may impose forces sufficient to create fractures and provide escape pathways for injected CO_2. Water or CO_2 injection rates should be controlled so they do not cause reservoir pressure to reach the caprock fracture threshold.

Many oil reservoirs are not thoroughly depleted but face declining production. Enhanced Oil Recovery (EOR) is a general term that refers to a set of chemical, thermal, or biological techniques utilized to increase oil production from a reservoir that can no longer produce economically under secondary recovery by waterflooding. Primary recovery is driven by the reservoir's own pressure, then by pumping. In secondary recovery, the declining reservoir pressure is supplemented through water injection. When secondary recovery becomes inefficient, production may enter an EOR stage if it is operationally and economically viable.

The most common EOR technique is gas injection, typically CO_2 or methane (CH_4). Depending on the reservoir properties, CO_2 flooding is classified as *miscible* or *immiscible*. Miscible flooding is applicable to reservoirs that can maintain the minimum miscibility pressure (MMP) necessary for the CO_2 to become miscible (single phase) with the oil, reducing the oil's viscosity and increasing its mobility. The injected gas enhances

the flow of oil by supplying additional pressure into the reservoir, by swelling the oil, and by reducing the oil viscosity, when the pressure is above MMP. Immiscible flooding provides gas pressure but does not reduce oil viscosity as much as miscible flooding. The petroleum industry has been operating CO_2-EOR projects successfully for many decades.

In order to reduce risk and increase profitability, it is necessary to assess initially whether or not a reservoir is a suitable candidate for CO_2-EOR. The management team will have to carefully examine the reservoir's current properties in light of its prior production history. An estimate of potential recovery during EOR would be necessary, and a viable CO_2 injection and flooding strategy would need to be implemented to achieve a profitable commercial project.

Reservoirs that have performed well under waterflooding typically perform well under CO_2 flooding. Reservoirs where waterflooding was inefficient will most likely not be good candidates for CO_2 enhanced recovery. In order to remediate sweep inefficiency issues, operators may employ various Water Alternating Gas (WAG) schemes. In a WAG scheme, periods of CO_2 injection alternate with periods of water injection, according to a specified schedule. Adjustments to the scheme may be made if the injection or production data show that performance could be improved. In a WAG project, the water injected following the gas creates a pressure front and a piston effect which drives CO_2 and oil through the reservoir more efficiently. In certain types of reservoirs, foams or other agents may be introduced to help control the mobility and sweep of CO_2.

Strategies for application of CO_2-EOR have been influenced by the availability and cost of CO_2. The focus in managing CO_2-EOR projects has traditionally been on

maximizing oil recovery while minimizing CO_2 costs. Optimization of performance with respect to these objectives has been the main impetus driving CO_2-EOR technology development. The emergence of CO_2 sequestration as a viable component of a strategy to simultaneously recover oil and store CO_2, has shifted the focus from the competing goals of maximizing oil recovery and minimizing CO_2 costs to co-optimization of the CO_2-EOR and CO_2 sequestration objectives.

1.4 Saline-Water Formations

Saline-water formations are subterranean porous and permeable formations that contain saline water, or brine in their pore space. They are generally found at depths greater than those of formations containing potable water. Due to their high salinity and great depth, the saline water cannot be economically exploited. Saline-water formations have been proposed as a viable CO_2 sequestration option that could serve as a major component of the CO_2 emissions reduction effort (Bachu et al., 1994; Cook et al., 2000; Gunter et al., 1993). The amount of CO_2 that could potentially be stored in saline-water formations, for a period of time long enough to consider the CO_2 permanently sequestered, is estimated to be very large (Parson and Keith, 1998). The caprock of the saline-water formations provides the structural trapping for the long-term security of CO_2 storage. The caprock, as in hydrocarbon reservoirs, is typically shale, or mudstone having no pathways that would allow CO_2 to migrate upward and escape into the overlying formations and ultimately to the surface.

Successful implementation of CO_2 sequestration in saline-water formations relies on the ability to predict the influence of the physical and chemical characteristics of the target formation on the short- and long-term migration and sequestration of the injected

CO_2. Migration of CO_2 in a saline-water formation occurs through the following three mechanisms: (a) volumetric displacement; (b) gravity segregation; and (c) viscous fingering (Johnson et al., 2004). Carbon dioxide is practically immiscible with water, hence, when injected into a saline-water formation will displace mobile water from the pore space as it propagates through the rock matrix. The lower density of CO_2 renders it buoyant in saline water, driving CO_2 vertically by gravity segregation. The vertical displacement is pronounced in the vicinity of the injection well, as the CO_2 plume is driven upward upon entering the formation. Over time the vertical profile will become more uniform as lateral velocities decrease.

Part of the CO_2 injected diffuses into the saline water, increasing its density and forming carbonic acid (H_2CO_3). As the diffusion process continues, and as the carbonic acid concentration increases, the denser solution slowly sinks, displacing the saline water below it, and establishing, over a long period of time, a convective process that increases the CO_2 uptake by dissolution in the saline water.

When one fluid displaces another in a porous medium, the displacement can be stable or unstable. Viscous fingering is flow instability due to difference in viscosity between phases or within a single phase containing a solute. In a saline-water formation, viscous fingering can occur in the horizontal direction if the saline-water–CO_2 interface is vertical, or it can occur in the vertical direction, driven by gravity, if the orientation of the interface is horizontal.

Injected CO_2 begins its migration as soon as it exits the injection well and enters the surrounding saline-water formation. Sequestration of the migrating CO_2 can take

place by four different mechanisms: (a) *solubility trapping* by dissolution of CO_2 in the saline water; (b) *mineral trapping* by reaction of CO_2 with solutes in the brine or with formation minerals to precipitate carbonates; (c) *structural* or *hydrodynamic trapping*, by constraining migration of CO_2; and (c) *capillary* (or *residual*) *trapping* by immobilizing residual CO_2. Understanding of the overall sequestration process requires sophisticated simulation software capable of modeling all of the competing processes.

As is the case with hydrocarbon reservoirs, there are many uncertainties associated with the ultimate fate of CO_2 injected into a saline-water formation. Whereas there is considerable empirical and technical experience with hydrocarbon reservoirs, the same is not the case with saline-water formations. There has never been much commercial demand for saline-water-formations water. As a result there has been less study of saline-water formations and their properties. The petroleum industry, where feasible, utilizes saline-water-formations water for waterflooding projects, but such activities do not require detailed analyses of the formations.

The ability of the saline-water-formations caprock to provide a seal against vertical migration and constrain the upward mobility of injected CO_2 is always a primary concern. Caprock integrity becomes a primary factor controlling containment, as gravity segregation over a long period of time drives CO_2 to the top of the saline-water formations. Equally important is any uncertainty associated with the areal extent of a saline-water formation and its lateral boundaries. The lateral boundaries of a formation may extend beyond its caprock, raising the possibility of spill from the perimeter of the caprock, followed by vertical migration. Hesse et al. (2006) derived approximate

theoretical expressions for the rate of propagation of the tip of a CO_2 plume along the caprock contour and the distance of the tip of the plume from the injection point vs. time.

1.5 Mineralization

CO_2 injected into subterranean formations may participate in chemical reactions with saline-water formations minerals. The reactions are influenced by formation conditions such as pressure and temperature and the composition of the minerals. The products of these reactions are precipitated solid carbonate compounds that render the CO_2 immobile, attenuating plume migration and alleviating long-term stability concerns. However, the fraction of CO_2 converted to immobile solid carbonates is estimated to be, on average, only 2 to 4% of the CO_2 injected (Det Norske Veritas, 2003). Furthermore, the reaction times are of geologic scale.

Efforts to increase CO_2 conversion to solids and accelerate the conversion rates have given rise to a sequestration option termed *mineralization*. The process, alternately referred to as *mineral* or *carbonate sequestration*, concerns the commercial, large-scale conversion of CO_2 into stable carbonate compounds, utilizing naturally-occurring minerals. These processes can be performed in the geologic formation (*in situ*) or at a facility removed from the sequestration site (*ex situ*). In the in situ method, CO_2 is transported via pipeline and injected into formations rich in minerals suitable for converting the CO_2 to solid carbonates. In the ex situ method, the CO_2 and minerals are transported to a dedicated facility where CO_2 is converted to carbonates.

The most common mineral carbonation reactions are those in which metal-oxide-bearing silicate minerals react with CO_2 to form solid carbonates. The greatest technical

challenge for large-scale application of mineralization is in accelerating the reaction rates between naturally-occurring minerals and CO_2, and adapting the process to accommodate the size and rate of CO_2 production by industry. Studies have been carried out and work continues, to identify the most efficient processes and methods for acceleration of mineral trapping reactions (Lackner et al.,1995; Gerdemann, 2007). A study by Herzog (2002), provided a comprehensive overview and assessment of CO_2 mineral sequestration processes. The overview describes the challenges faced in efforts to increase mineralization reaction kinetics and to develop a process that is commercially applicable and financially viable. As researchers overcome the technical barriers faced by both in situ and ex situ methods, large-scale commercial mineral sequestration may become an attractive option for carbon sequestration.

An example of in situ CO_2 sequestration is the CarbFix pilot project in Iceland (Matter et al., 2009). The project involves capturing CO_2 at the Hellisheidi Geothermal Power Plant and injecting it into basaltic rock for permanent storage. The injection depth ranges from 400 to 800 m (1312.3 to 2624.7 ft). The basaltic rocks consist primarily of calcium and magnesium silicate minerals that react with CO_2 to produce solid calcium and magnesium carbonates. Results of tracer tests indicate that there is a large reservoir volume available, having large surface area for reaction (Matter et al., 2009).

At the National Energy Technology Laboratory (NETL) Albany Research Center, research has focused on ex situ reactions of CO_2 with minerals containing high concentrations of the alkaline earth metals, calcium and magnesium. A pilot-scale mineral carbonation unit was constructed that, when scaled up could sequester 100% of the CO_2 emissions from a 1300 MW (electric) coal-fired power plant. This work

indicated that the full-scale carbonation process would require 49.9 x 10^3 t/day (55 x 10^3 short tons/day) of the mineral reactant, to mineralize 21.8 x 10^3 t/day (24 x 10^3 short tons/day) of CO_2. The power requirement for the carbonation unit was estimated to be 352 MW or 27% of the power plant's net output (Penner et al., 2003).

When all the technical issues have been managed, and when mineralization can be offered on commercial scale, it promises to be the most secure CO_2 sequestration option.

1.6 Research Objectives

The Citronelle Oil Field, located in Southwest Alabama, is the State's largest oil field and is comprised of the Upper and Lower Donovan formations that house more than 40 sandstone oil reservoirs. The two formations are separated by the brine-filled sandstone reservoirs of the Middle Donovan (Eaves, 1976). The geology of the Citronelle Oil Field is quite different from that of carbonate strata of the Permian Basin in Texas and New Mexico and the Williston Basin in North Dakota and Montana, well-known sites of commercially successful CO_2-EOR projects.

The objective of the present work is to investigate the oil recovery potential of a CO_2-EOR project in the Upper and Lower Donovan oil reservoirs of the Citronelle Oil Field and the feasibility of CO_2 injection into the Middle Donovan saline-water formation during interruptions in CO_2-EOR operations. To achieve the desired objectives, a set of static calculations, based on estimation methods which were retrieved from publications in the field was compiled, followed by computer simulations and results for CO_2-EOR using MASTER 3.0 (Ammer and Brummert, 1991; Ammer et al., 1991; Zeng et al., 2005), and CO_2 sequestration using TOUGH2-ECO2N (Pruess et al., 1999; Pruess, 2005)

and TOUGHREACT (Xu et al., 2004). An investigation into possible CO_2 leakage from the reservoirs completes the scope of the research.

The present work can serve as a template for preliminary assessment of tertiary oil recovery and CO_2 storage of similar oil reservoirs and saline-water formations.

CHAPTER 2

THE ROLE OF CITRONELLE DOME IN CARBON STORAGE

2.1 Citronelle Dome

Citronelle Dome is a broad, salt-cored ovate anticline in the eastern Mississippi Interior Salt Basin of southern Alabama. An anticline is an arch-shaped fold in rock in which the rock layers are upwardly convex with the oldest layers at the core. The expression of the deep salt intrusion extends to the surface and forms a four-way structural closure which dips away from the crest at 1–2° (Esposito et al., 2008). Several saline-water formations, capped by low permeability shale, make Citronelle Dome an attractive candidate for CO_2 sequestration. The most suitable formations for CO_2 sequestration are in the Upper and Lower Cretaceous series (Table 2.1), capped by a massive 396 m (1300 ft) thick chalk layer (*Selma Chalk*). The Selma Chalk forms a reliable seal between potential CO_2 sequestration targets in the Upper or Lower Cretaceous series, and underground sources of drinking water in the overlying Tertiary section.

Large-scale carbon emitting sources in the greater area of the Citronelle Dome provide opportunities for CO_2 sequestration projects. Advanced Resources International (2006) and Esposito et al. (2008, 2010), assessed the CO_2 sequestration suitability and produced capacity estimates for the saline-water formations in the Upper and Lower

Cretaceous series. The estimates were based exclusively on reservoir properties and geometry, and did not consider transient phenomena nor account for partitioning of CO_2 among phases. To incorporate complex chemical and physical processes when estimating CO_2 sequestration capacity, would require rigorous simulation software capable of modeling multicomponent transient phenomena and phase behavior during and after CO_2 sequestration.

Table 2.1. Citronelle Dome Cretaceous Upper and Lower Geologic Series.

Series	Stratigraphic Units And Subunits	Lithology	Type of Formation	Thickness, m (ft)
Upper	Navarro	Chalk	Seal	
	Taylor	Chalk	Seal	396 m (1300 ft)
	Selma	Chalk	Seal	
	Eutaw	Sandstone	Saline	30 m (100 ft)
	Tuscaloosa			
	Upper	Sandstone	Saline	152 m (500 ft)
	Middle	Shale	Seal	122 m (400 ft)
	Lower	Sandstone	Saline	122 m (400 ft)
Lower	Dantzler	Sandstone	Saline	
	Fredericksburg	Shale	Seal	1158 m (3800 ft)
	Paluxy	Sandstone	Saline	
	Mooringsport	Shale	Seal	
	Ferry Lake	Anhydrite	Seal	46 m (150 ft)
	Rodessa			
	Upper Donovan	Sandstone	Oil	108 m (400 ft)
	Middle Donovan	Sandstone	Saline	46 m (150 ft)
	Lower Donovan	Sandstone	Oil	52 m (171 ft)

2.2 Citronelle Oil Field

A very important feature of the Citronelle Dome is the group of hydrocarbon bearing sandstones in the Lower Cretaceous Donovan sand, as shown in Figure 2.1. Considered to be part of the Rodessa Formation (Eaves, 1976), the Donovan Sand houses the largest oil reservoir in Alabama (*Citronelle Oil Field*) with estimated Original Oil In Place (OOIP) of 537 x 10^6 bbl (Advanced Resources International, 2006). The Donovan Sand is capped first by 46 m (150 ft) of Ferry Lake Anhydrite, and then by 38 m (125 ft) of Mooringsport shale, both serving as long-term seals for the underlying oil reservoir.

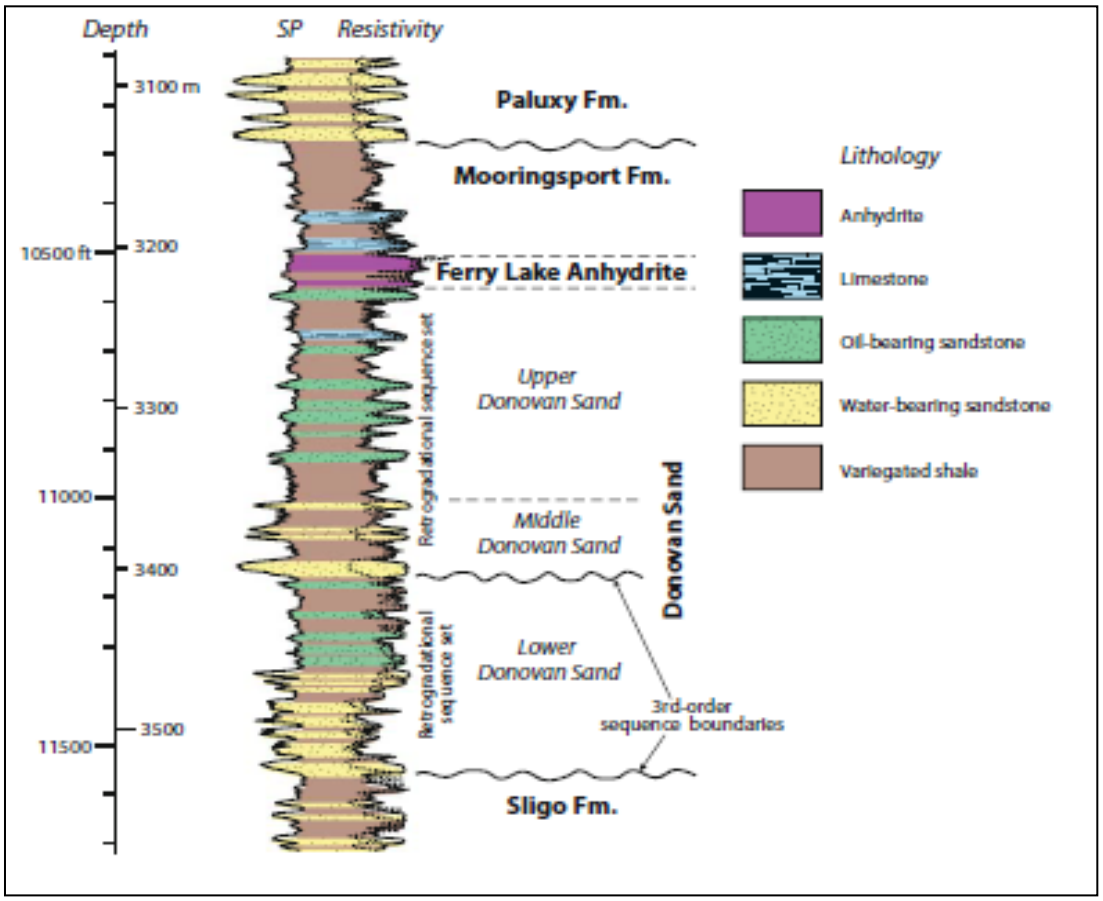

Figure 2.1. Stratigraphic section with spontaneous potential (SP), resistivity well logs, and depth of the Mooringsport Formation, Ferry Lake Anhydrite, and Donovan Sand in the Citronelle Oil Field. Figure reproduced, with permission, from R. A. Esposito, J. C. Pashin, D. J. Hills, P. M. Walsh, 2010.

Eaves (1976) subdivided the Donovan Sand into three stratigraphic sections based on rock properties and fluids present: (a) Upper Donovan, (b) Middle Donovan, and (c) Lower Donovan. The Upper and Lower Donovan contain hydrocarbon-bearing sandstone and shale. Together, these sections comprise 206 m (676 ft) of gross pay. The Middle Donovan contains saline-water-saturated sandstone and shale, and forms a 46 m (150 ft)-thick section separating the Upper from the Lower Donovan. Although the three sections share common geologic history, Eaves (1976) proposed that, due to the blanket-type deposition, fluid migration flushed the Middle Donovan sandstones of hydrocarbons, before salt movement trapped hydrocarbons in the Upper and Lower Donovan. The three sections appear to be interconnected downdip, since they registered the same bottom-hole pressure drop during primary production (Eaves, 1976).

The Citronelle Oil Field is comprised of a stacked series of 42 productive sandstone zones forming more than 330 separate reservoirs in the Upper and Lower Donovan (Esposito et al., 2008). None of the hydrocarbon-bearing sandstones spans the Citronelle Oil Field in any direction. Although the hydrocarbon-bearing sandstones exhibit irregular geometry, with alluvial meander channels crossing over each other and often commingling, the sandstones are almost parallel to the base of the Ferry Lake Anhydrite with 6 m (20 ft) maximum local departures (Wilson and Warne, 1964). Heterogeneity is very high in all three Donovan sections, with shale irregularly interbedded with siltstone, and mica. The volume of dispersed shale in the hydrocarbon-bearing sandstones was estimated at 40% of the rock matrix, based on visual observations of drill-core samples (Esposito et al., 2008). The Middle Donovan saline-water formations also shares a 60 to 40%, sandstone-to-shale ratio. Middle Donovan saline-

water-bearing sandstones exhibit slightly higher heterogeneity than the hydrocarbon-bearing sandstones of the Upper and Lower Donovan.

2.3 Citronelle Oil Field Development

Development of the Citronelle Oil Field began with a discovery well in 1955. Currently 414 wells are listed as active or temporarily abandoned (Esposito et al., 2008). All wells were developed on 40 acre (16 hectare) spacing. Cumulative oil production to date is 172,142,921 bbl (Alabama State Oil and Gas Board database, 2012). The oil reservoirs were *depletion drive* type, with no gas cap and no gas-oil contact. All of the gas in the reservoirs was dissolved in the liquid phase. In depletion drive type reservoirs when the reservoir pressure falls below the bubble point, the gas comes out of solution and forms gas bubbles, creating extra energy in the reservoir. Since the reservoirs in the Citronelle Oil Field were of depletion type, initial production resulted from the expansion of the undersaturated, single-phase oil, with negligible water influx from the saline-water sands. Initial oil reservoir pressure was 38 MPa (5500 psi) and the temperature was 98.8 °C (210 °F) (Esposito et al., 2008).

Reservoir production is currently in the latter part of a waterflood, referred to as the *mature waterflood stage*. The waterflood program was initiated in 1961 to increase reservoir pressure after its initial rapid decline. There was no particular waterflood pattern applied to the oil reservoir. Fowler et al. (1998) described the pattern utilized as a *random flood pattern*. Oil production rates under waterflooding peaked in 1963 at 22,521 barrels of oil per day (ASOGB database, 2012).

In the mid-1970s operators of the Citronelle Oil Field began to evaluate the feasibility of tertiary recovery. In 1981 a CO_2-EOR pilot program sponsored by the U. S. Department of Energy (USDOE) was initiated, but CO_2 injection operations were terminated for nontechnical reasons in 1983. Later changes in ownership at the Citronelle Oil Field, and consolidation of the various producing units under a single operator revived interest in CO_2-EOR. The interest resulted in a CO_2-EOR pilot test, begun in December 2009, to assess the efficacy of a field-wide CO_2-EOR project. Table 2.2 shows an up-to-date timeline summary of the major events in the Citronelle Oil Field.

Table 2.2. Timeline of major events in the Citronelle Oil Field development.

Time	Event
1955	Discovery of Citronelle Oil Field
1960	Permits granted for dual well completion
1961	Waterflood operations begin
1981–1983	First CO_2-EOR pilot test
2009–2013	Second CO_2-EOR pilot test

2.4 Qualitative CO_2 Sequestration Assessment of Citronelle Dome

Capacity for CO_2 storage and sequestration potential in Citronelle Dome depends on formation properties. The most basic capacity parameter is the available pore space. Factors that contribute to capacity variation include the accessible area and thickness of the formation, the fractions of fluids present in the pore space, and phase behavior of the fluids. The chemical and physical properties of the formation fluids determine their interaction with injected CO_2. Properties such as the salinity of *connate*—trapped in the

pores during formation of the rock—water, density differences, and solubility of CO_2 in the water, will be important in determining capacity.

2.4.1 Depleted Citronelle Oil Reservoirs

Upon depletion, the Citronelle Oil Field will be a prime candidate for injecting and sequestering CO_2. To maximize the sequestration potential of the oil reservoir it will be necessary to extract the maximum possible volume of hydrocarbons. In order to achieve maximum hydrocarbon extraction, production will have to continue for as long as economically possible. Current waterflood activities in the Citronelle Oil Field will continue until production reaches a critical limit which is a function of the financial return from oil production.

It was mentioned in Section 2.2.1 that the management team of the Citronelle Oil Field is evaluating the reintroduction of CO_2-EOR in the context of a field-wide tertiary recovery project. The decision to conduct CO_2-EOR is supported by the longevity and success of the waterflood, which is typically a strong predictor of the expected performance of CO_2-EOR. At the end of the commercial CO_2-EOR project, a fraction of the injected CO_2 will remain in the sandstone pore space (Jarrell et al., 2002, p. 17). Therefore, it is reasonable to consider CO_2-EOR as partial CO_2 sequestration. If CO_2-EOR is to be followed by CO_2 sequestration, the optimal strategy, during tertiary oil recovery, would be the dynamic co-optimization of oil extraction and CO_2 storage (Ghomian et al., 2007). As such, the CO_2-EOR phase would not be completely independent of the CO_2 sequestration phase. It is not necessary for the depletion state to be reached before CO_2 sequestration is begun; rather a simultaneous depletion–

sequestration coupling process could take place during CO_2-EOR. After the end of profitable CO_2-EOR, the sequestration project can continue injecting CO_2 until the reservoir reaches its CO_2 capacity limit.

Theoretically, CO_2 storage capacity in the depleted Citronelle reservoir will be commensurate with the net volume of fluids produced, since they will be replaced by an equivalent volume of CO_2. The sequestration capacity of the depleted reservoir will depend on the fraction of the original oil remaining in place at the end of CO_2-EOR. The hydrocarbon-bearing sandstones of the Citronelle oil reservoir are located within a depth interval ranging from 3231 m (10,600 ft) to 3450 m (11,319 ft) (Esposito et al., 2010). The hydrostatic pressure in the interval ranges from 34 MPa (4929 psi) to 36.3 MPa (5263 psi), assuming an average 10% by weight NaCl content of the water. The hydrostatic pressure range is considerably higher than the MMP requirement of 19.3 MPa (2800 psi) (Gilchrist, 1981), thus assuring that injected CO_2 forms a single phase with the hydrocarbons. The single hydrocarbon–CO_2 phase will reduce capillary effects and promote hydrocarbon mobility, resulting in a higher hydrocarbon recovery, and increased CO_2 sequestration capacity.

Given that the oil reservoir may undergo additional waterflooding by application of WAG recovery during CO_2-EOR, it is reasonable to expect that CO_2 sequestration capacity will be negatively affected by water remaining in the reservoir (*residual water saturation*) at the end of CO_2-EOR. The final distribution of fluid saturations during and after the end of CO_2-EOR will be influenced by the mobility of phases through the interstitial sandstone channels.

An equally important issue to the sequestration potential of the Citronelle oil reservoir is the long-term containment of the stored CO_2. The possible upward migration of stored CO_2 to underground sources of drinking water (USDW) and the atmosphere is a concern in any sequestration project. Low permeability shale formations listed in Table 2.1 and overlying the Citronelle Oil Field will provide barriers against upward migration of CO_2 (Esposito et al., 2008). Furthermore, the geometry of the Citronelle Dome provides a closure which ranges from about 76 m (250 ft) to 91 m (300 ft) in height, on the productive sandstones of the field (Fowler et al., 1998) that will prevent lateral migration of CO_2 from underneath the dome.

2.4.2 Citronelle Saline-Water Formations

As indicated in Table 2.1, there are a number of saline-water formations above the Citronelle oil reservoir that have potential for CO_2 storage. However, the absence of comprehensive geologic data pertaining to these saline-water formations presents significant challenges. Contrary to the hydrocarbon-bearing sandstone formations of the Upper and Lower Donovan, which are well documented, the saline-water formations in the Citronelle Dome have not received the same attention, since they have not been of economic interest. Their properties have not been thoroughly investigated, nor are there any comprehensive data bases available. Although the specific properties of the saline-water formations are not well documented, their depositional history and mineralogy have been described in detail (Aronow, 1974; Isphording and Lamb, 1971; Mancini et al., 1985).

A sequestration project targeting the saline-water formations of the Citronelle Dome would require coordination of the injection process in order to maximize the storage capacity of the many prospective targets, while pressures and lateral–vertical migration of CO_2 would need to be closely monitored. The extent of the saline-water formations and their fluid replenishment mechanisms would have to be identified, in order to establish the saline-water formations boundaries and natural migration routes to the surface. Closure and seal provisions of the saline-water formations would need to be identified, in order to assess possible CO_2 leakage routes and leakage potential.

CHAPTER 3

UPPER BOUNDS ON STATIC CO_2 STORAGE CAPACITY ESTIMATES FOR THE DONOVAN SANDSTONES

3.1 Introduction

There is no single formal definition for CO_2 sequestration *capacity*, however, in the present study the definition provided by Doughty et al. (2001, p. 2): "the volume fraction of the subsurface within a defined stratigraphic interval available for CO_2 sequestration" is adopted. Stratigraphic intervals can vary considerably in volumetric scale, spatial continuity, porosity, and permeability, thus it is useful to divide CO_2 capacity estimates into two spatial categories: (a) regional; and (b) local. In cases where a distinction between regional and local scales is not possible, alternate criteria (such as radial distance) could be introduced, but they should be applied consistently.

Regional capacity estimates are associated with large-scale CO_2 storage and sequestration. Capacity estimates for sedimentary basins or clusters of contiguous sedimentary basins are examples of regional estimates. They are defined approximately, and incorporate capacities of multiple formations as in the capacity estimates by Bachu (2002). Approximations in the calculation are magnified by the large spatial scale and are usually absorbed into a range bounded by estimates of upper and lower limits. Bachu (2002), Doughty et al. (2001), and Hitchson et al. (1999) have developed formulations

and methodologies aimed at regional CO_2 storage and sequestration capacity assessments.

Local capacity estimates are associated with small-scale CO_2 storage and sequestration, and are often formation-specific. Capacity estimates related to depleted oil reservoirs or specific saline-water formations, are examples of local estimates. In cases where it is applicable, local capacity estimates can be extended to include contiguous formations constrained by a common trapping mechanism or closure. Estimates in this category bear a higher degree of confidence than regional estimates, since approximations in the calculations are reduced due to the smaller spatial scale and often more complete knowledge of properties of the formation.

3.2 Capacity Estimate Formulation

The methods employed to produce regional or local CO_2 sequestration capacity estimates are based on volumetric concepts, formation properties, and mass balance principles. The complexity of the methods varies, depending on the level of analysis and spatial scale incorporated in the estimate. Successful development of CO_2 capacity estimate formulations relies on the appropriate selection of parameters, emulating as closely as possible the conditions of CO_2 injection and storage.

3.2.1 Static Estimates

Static CO_2 capacity estimates are invariant to time dependent parameters or processes since they do not consider any transient phenomena related to CO_2 sequestration. Static estimates are based on the presumption of fluid volume exchange

where the volume of injected CO_2 occupies all of the pore volume vacated by the original formation fluids. An implicit constraint to the presumption is that the sequestered volume cannot exceed the vacated pore volume.

Although static formulations are time independent their formulations consider parameters that are time dependent, such as residual oil or water saturation at the end of oil production. Hence, static estimates can be considered as the limiting cases of dynamic estimates.

Invariance to time does not invalidate the usefulness of static estimates since they can provide an initial assessment of CO_2 capacity. Notwithstanding the lack of consideration of transient behavior, obtaining a CO_2 static capacity estimate for a target formation is an important step, after establishing its suitability. If CO_2 capacity is shown by the static estimate to be too limited, plans for CO_2 sequestration may have to be abandoned, even if all other formation properties are found to be optimal. Static estimates provide approximate values for storage potential and a useful reference for estimates derived using time-dependent formulations.

Static capacity formulations for application to the Upper, Middle, and Lower Donovan were identified in the research literature and are presented in Chapter 4.

3.2.2 Dynamic Estimates

Dynamic CO_2 capacity estimates consider the influence of transient phenomena related to CO_2 sequestration processes. The classical approach to solving dynamic fluid and gas flow problems in porous reservoirs is common to many engineering areas. The

complexities of the problem and its properties are idealized and converted into mathematical equations which are then discretized and programmed into a computer algorithm to approximate their solution in time. Such dynamic estimates have been a staple of the petroleum industry for decades. The advent and increased sophistication of computers, algorithms and simulation software have provided petroleum engineers with valuable and increasingly accurate tools.

To investigate and understand the influence of transient phenomena associated with CO_2-EOR and CO_2 sequestration in the Donovan sandstones, three simulation software packages were selected:

1) Miscible Applied Simulation Techniques for Energy Recovery version 3.0 (MASTER 3.0) (Ammer and Brummert, 1991; Ammer et al., 1991; Zeng et al., 2005) was developed for the Department of Energy to support the Gas Miscible Displacement Enhanced Oil Recovery Program at the Morgantown Energy Technology Center. MASTER 3.0 is a multicomponent, pseudomiscible simulator that simultaneously tracks stock tank oil, natural gas, water, up to four solvent species, and a surfactant. For conventional oil–water–gas (*black-oil*) simulations, the miscible features can be easily bypassed, giving essentially a standard black-oil model. In this mode, MASTER 3.0 can be used to simulate most of the common recovery mechanisms such as solution gas drive, waterflood, and immiscible gas injection. With the miscible features engaged, MASTER 3.0 can be used to simulate a wide range of immiscible-to-miscible gas injection recovery processes, including CO_2 flooding. MASTER 3.0 uses a mixing-rule (pseudomiscible) approach to calculate effective fluid densities and viscosities.

MASTER 3.0 was utilized in the present body of work to simulate CO_2-EOR WAG in the Upper and Lower Donovan hydrocarbon-bearing sandstones. The application of the simulator and results obtained are presented in Chapter 5.

2) TOUGH2-ECO2N (Pruess, 2005) is a numerical simulation program for geologic sequestration of CO_2 in saline-water-bearing sandstones. ECO2N is a fluid property module for the TOUGH2 (Pruess et al., 1999) simulator, that reproduces fluid properties for the temperature, pressure and salinity conditions of interest. The module includes comprehensive description of thermodynamics and thermophysical properties of H_2O–NaCl–CO_2 mixtures. Flow processes can be modeled isothermally or non-isothermally, and phase conditions may include a single (aqueous or CO_2-rich) phase, or two phase mixtures. Fluid phases may appear or disappear in the course of the simulation, and solid salt may precipitate or dissolve. TOUGH2-ECO2N was utilized in the present body of work to simulate the sequestration process of CO_2 in the Middle Donovan saline-water-sandstones. The application of the simulator and results obtained are presented in Chapter 6.

3) TOUGHREACT (Xu et al., 2004) is a numerical simulation program for chemically reactive nonisothermal flows of multiphase fluids in porous and fractured media. The program was developed by introducing reactive chemistry into the multiphase flow code TOUGH2. Interactions between mineral assemblages and fluids can occur under local equilibrium conditions or at kinetic rates, and the gas phase can be chemically active. Precipitation and dissolution reactions can change formation porosity and permeability, and can also modify

the properties of the rock. TOUGHREACT was utilized in the present body of work to simulate the mineralization processes during CO_2 sequestration in the Middle Donovan saline-water-sandstones. The application of the simulator and results obtained are also presented in Chapter 6.

3.3 Donovan Sandstones Capacity Estimate Categories

Esposito et al. (2008) produced static capacity estimates for several stratigraphic intervals in Citronelle Dome, including the Donovan sandstones. The present body of work concentrates on the Donovan sandstones and utilizes the natural division in fluid content, between the hydrocarbon-bearing sandstones of the Upper and Lower Donovan and the saline-water-bearing sandstones of the Middle Donovan, to establish two areas of investigation: (a) application and effectiveness of CO_2-EOR in the hydrocarbon-bearing sandstones of the Upper and Lower Donovan, followed by CO_2 storage and sequestration in the depleted reservoirs; (b) CO_2 storage and sequestration in the saline-water-bearing sandstones of the Middle Donovan during interruptions in CO_2-EOR operations, in the Upper and Lower Donovan.

Based on storage method, formation type, or estimate formulation, CO_2 capacity estimates for Donovan sandstones can be classified according to the following five categories:

1) *Upper Bound*, for the maximum volume of CO_2 which could possibly be stored in the Upper, Middle, or Lower Donovan sandstones.
2) *Depleted Oil Reservoir*, for the volume of CO_2 that can be stored in the Upper and Lower Donovan hydrocarbon-bearing sandstones after the

maximum oil volume has been extracted. It is greatly influenced by the reservoir's long history of waterflooding and prospective CO_2-EOR.

3) *Enhanced Oil Recovery*, for the volume of CO_2 that can be stored in the Upper and Lower Donovan hydrocarbon-bearing sandstones during CO_2-EOR operations. If CO_2-EOR is implemented as WAG, the volume of CO_2 retained in the reservoir will decrease during each water injection cycle and increase during each CO_2 injection cycle. The final volume of CO_2 retained in the oil reservoir will depend on the number of WAG cycles and hysteretic effects of repeated CO_2 drainage and imbibition.
4) *Saline-water formations*, for the volume of CO_2 that can be stored in the Middle Donovan saline-water-bearing sandstones.
5) *Mineralization,* for the volume of CO_2 that can be stored in solid form when injected CO_2 reacts with rock minerals of the Middle Donovan saline-water-bearing sandstones and precipitates from solution. It is a function of formation mineralogy.

With the exception of *Upper Bound*, each capacity estimate category can be separated into a *static* and *dynamic* subcategory.

3.4 Upper and Lower Donovan Pore Volume Estimate

Available pore volume can be estimated by forming the product of reservoir rock volume, porosity and the fraction of pore volume not occupied by formation water held in

place by intergranular capillary forces (*irreducible water saturation*). The relationship is represented by Equation 3.1:

$$V_{phc} = V_{rr}(1 - S_{wihc})\varphi_{hc} \quad (3.1)$$

where

V_{phc} is available pore volume in hydrocarbon-bearing sandstones, m^3

V_{rr} is total reservoir rock volume of hydrocarbon-bearing sandstones, m^3

S_{wihc} is irreducible water saturation of hydrocarbon-bearing sandstones, dimensionless

φ_{hc} is porosity of hydrocarbon-bearing sandstones, dimensionless

The Unit Manager's Report (1999) estimated the reservoir rock volume of the Upper and Lower Donovan hydrocarbon-bearing sandstones, to be 1,043,721,760 m^3 (36,858,686,080 ft^3). The reservoir rock volume estimate represents the total volume of individually mapped sandstones in the Upper and Lower Donovan, as interpreted from well log data. Sandstones with less than 0.5 mdarcy air permeability were not mapped. Air permeability refers to the permeability of a reservoir core sample measured in the laboratory using air as the fluid. The average oil reservoir porosity was estimated to be 13.61% (Fowler, 1998).

Irreducible water saturation was calculated using Equation 3.2. The equation, cited by Fowler et al (1998), is based on laboratory analyses performed on reservoir cores obtained from Upper and Lower Donovan, relating irreducible water saturation to air permeability (k_{air}):

$$S_{wihc} = 0.4587 k_{air}^{-0.2518} \quad (3.2)$$

Using Equation 3.2 and air permeability values obtained from Fowler et al. (1998) for hydrocarbon-bearing sandstones in the Upper and Lower Donovan, an average irreducible water saturation of 0.323 was calculated.

Substituting values for reservoir rock volume, irreducible water saturation, and porosity in Equation 3.1 yields the following estimate for the maximum volume of hydrocarbon-bearing sandstones, available for CO_2 storage in the Upper and Lower Donovan:

V_{phc} = (1,043,721,760 m^3)(1 – 0.323)(0.1361)

= 96,168,210 m^3 (3,396,148,283 ft^3)

3.5 Middle Donovan Pore Volume Estimate

Unlike in the case of Upper and Lower Donovan, there is no reservoir rock volume estimate available for the Middle Donovan that can be used to calculate the pore volume of the saline-water-bearing sandstones. Well logging was focused on the hydrocarbon-bearing sandstones of the Upper and Lower Donovan hence there is no mapping of individual saline-water-bearing sandstones.

In order to obtain an estimate for the pore volume of the saline-water-bearing sandstones in Middle Donovan three assumptions were introduced: (a) the Middle Donovan volume is equal to the product of the areal extent of the formation and its thickness; (b) due to depositional conformity of the productive Donovan sandstones (Eaves, 1976), the areal extent of the Middle Donovan is equal to the plan areas of the

Upper and Lower Donovan, as mapped by the Citronelle Oil Field footprint; and (c) the fraction of volume that is not available for CO_2 storage in the Middle Donovan, is the same as that of the Upper and Lower Donovan, since the three formations share geologic history.

Assumptions (a) and (b) allowed the total volume of Middle Donovan to be estimated. Assumption (c) allowed an efficiency factor (e_f) to be estimated, to account for the fraction of the formation volume that is not available for CO_2 storage in the Middle Donovan.

The pore volume of the saline-water-bearing sandstones available to CO_2 storage, is expressed by Equation 3.3,

$$V_{ps} = V_f e_f (1 - S_{wis}) \varphi_s \tag{3.3}$$

where

V_{ps} is available pore volume in saline-water-bearing sandstones, m^3

V_f is total formation volume of the saline-water-bearing sandstones, m^3

e_f is the efficiency factor for Middle Donovan, dimensionless

S_{wis} is irreducible water saturation of the saline-water-bearing sandstones, dimensionless

φ_s is porosity of the saline-water-bearing sandstones, dimensionless

Eaves (1976), estimated the areal extent of the Citronelle Oil Field (i.e. Upper and Lower Donovan) at 16,400 acres (6637 hectares) or 6.637 x 10^7 m^2 (7.144 x 10^8 ft^2). It is reasonable to assume that the estimate of the areal extent of Middle Donovan would be

the same, since the three sections share depositional history. The average porosity of the Middle Donovan was estimated to be 12.7% (Fowler et al., 1998), and its thickness is 46 m (150 ft), (Table 2.1). There is no estimate available for efficiency factor or irreducible water saturation in the Middle Donovan. However, it is assumed that the Middle Donovan has the same efficiency factor and irreducible water saturation, as the Upper and Lower Donovan, since the three sections share depositional history.

To obtain an efficiency factor estimate for the Upper and Lower Donovan, Equation 3.3 was solved explicitly for the efficiency factor, e_f, and all the saline-water formation parameters were replaced by corresponding parameters from the Upper and Lower Donovan. Using 96,168,210 m^3 (3,396,148,283 ft^3), for the hydrocarbon-bearing sandstones pore volume, 6.637 x 10^7 m^2 (7.144 x 10^8 ft^2), for the areal extent of the Upper and Lower Donovan, 160 m (525 ft), for the combined thickness of the Upper and Lower Donovan, 13.61% for porosity (Fowler et al., 1998), and 0.323 (Fowler et al., 1998) for irreducible water saturation, an efficiency factor of 0.098 was obtained for the Upper and Lower Donovan.

Using the calculated value of 0.098 for efficiency factor, and the appropriate values for areal extent, formation thickness, irreducible water saturation, and porosity, Equation 3.3 yields the following estimate for the maximum volume of saline-water-bearing sandstones, available for CO_2 storage in the Middle Donovan:

V_{ps} = (6.637 x 10^7 m^2) (46 m) (0.098) (1-0.323) (0.127)

= 25,724,569 m^3 (908,454,596 ft^3)

3.6 Upper Bound Capacity Estimate

The upper bound for the mass of CO_2 that can be stored in a formation is the product of the available pore volume and the density of CO_2 at formation temperature and pressure, expressed by Equation 3.4:

$$m_{CO_2} = V_p \rho_{CO_2} \tag{3.4}$$

where

m_{CO_2} is mass of stored CO_2, kg

V_p is available pore volume of formation, m^3

ρ_{CO_2} is density of CO_2 at formation temperature and pressure, kg/m^3

Neglecting compressibility of the porous rock and chemical reactions, formation pore volume is a constant, but CO_2 density depends upon formation temperature and pressure. Temperature in the Donovan formation is expected to vary as a function of depth. Variations in average formation pressure are also expected, increasing during the CO_2 injection period and decreasing when injection ceases. Temperature and pressure variations affect density, and thus the capacity estimates. Therefore, what is most critical to capacity estimates is the ultimate condition of constant density, which is achieved after CO_2 injection has ceased and pressure in the formation returns to hydrostatic.

The mass of CO_2 stored in the formation does not change after the injection wells are shut in, even though formation pressure decreases tending toward hydrostatic. The decrease in pressure causes the actual volume of stored CO_2 to increase, reaching a maximum when all of the CO_2 is at the hydrostatic pressure.

Densities of CO_2 in the Upper, Middle, and Lower Donovan were obtained using the hydrostatic pressure and temperature at the depth of each section. Hydrostatic pressures were estimated using the depth from ground surface to the vertical center of each section (Esposito et al.,2010) and a hydrostatic gradient of 0.465 psi/ft for brines containing 10% NaCl by weight (Schlumberger, 2011).

A temperature gradient of 27.33°C/1000 m (15°F/1000 ft) (Schlumberger, 2011) was used to estimate the temperature in each section. Surface temperature was assumed at 18.3 °C (65 °F). Table 3.1, formed using the National Institute of Standards and Technology (NIST) reference database (Lemmon et al., 2002), summarizes the densities under the conditions estimated at the center of each section.

Table 3.1. Upper, Middle, and Lower Donovan CO_2 density estimates.

Formation	Depth from surface to vertical center of section, m (ft)	Pressure at vertical center of section, MPa (psi)	Temperature at vertical center of section, °C (°F)	Density[a], kg/m^3 (lb/ft^3)
Upper Donovan	3276.6 (10,750)	34.47 (4998.75)	125.7 (258.3)	622.62 (38.85)
Middle Donovan	3360.4 (11,025)	35.35 (5126.63)	128.0 (262.4)	624.91 (38.99)
Lower Donovan	3419.8 (11,220)	35.97 (5217.30)	129.6 (265.3)	626.56 (39.09)

[a]Lemmon et al., 2002

3.6.1 Upper and Lower Donovan Upper Bound Estimate

The pore space estimate of the hydrocarbon-bearing sandstones is allocated according to the relative thicknesses of the Upper and Lower Donovan, as 68% and 32% respectively (Esposito et al., 2010). Substituting the appropriate values in Equation 3.4, the following estimate for the mass of CO_2 that can be stored in the hydrocarbon-bearing sandstones of the Upper and Lower Donovan, was obtained:

$$m_{CO_2} = (96{,}168{,}210\ m^3)\ [(0.68)(622.62\ kg/m^3) + (0.32)(626.56\ kg/m^3)]$$

$$= 60 \times 10^9\ kg \qquad (66{,}135{,}844 \text{ short tons})$$

3.6.2 Middle Donovan Upper Bound Estimate

Substituting the data for Middle Donovan in Equation 3.4, the following estimate for the mass of CO_2 that can be stored in the saline-water-bearing sandstones of the Middle Donovan was obtained:

$$m_{CO_2} = (25{,}724{,}569\ m^3)(624.91\ kg/m^3)$$

$$= 16.1 \times 10^9\ kg \qquad (17{,}720{,}229 \text{ short tons})$$

3.7 Total Upper Bound Capacity Estimate

Results obtained in Sections 3.6.1 and 3.6.2 represent the upper bounds for CO_2 storage in the Upper, Middle, and Lower Donovan sandstones. Combining the estimate for the Upper and Lower Donovan with the estimate for the Middle Donovan, yields the following upper bound for total CO_2 storage in the three Donovan sections:

$$m_{CO_2} = 76.1 \times 10^9\ kg \qquad (83{,}856{,}073 \text{ short tons})$$

An upper bound on the capacity estimate can be used as an initial reference for more realistic estimates obtained by incorporating additional features and constraints that are formation specific.

CHAPTER 4

STATIC CO_2 STORAGE CAPACITY ESTIMATES FOR THE DONOVAN SANDS

4.1 Introduction

In Section 3.3 Donovan Sandstones CO_2 storage capacities were classified into five categories, and in Section 3.7 a total capacity estimate for the Upper Bound category was obtained. In the present chapter estimates for the static capacity of Depleted Oil Reservoir, Enhanced Oil Recovery, Saline-water formations, and Mineralization categories are presented based on methods developed by other research groups (Kovscek, 2002; Pruess et al., 2001; Shaw and Bachu, 2002; USDOE Carbon Sequestration Partnerships, 2006). All of the estimates are based on CO_2 densities calculated at local hydrostatic equilibrium pressures, and temperatures calculated using the geothermal gradient. Parameter values and reservoir properties were identified, where possible, from existing and available reports and publications. Wherever values for parameters and properties could not be formed, they were based on plausible expert knowledge or inference.

4.2 Depleted Oil Reservoirs

Following profitable CO_2-EOR from the Citronelle Oil Field, injection of CO_2 may be continued, utilizing the depleted oil reservoir as a sequestration site. Conditions

in the reservoir at the end of CO_2-EOR, and the fluids present, will determine the fraction of reservoir pore volume available for CO_2 storage. At the end of the CO_2-EOR, the reservoir pore volume will be taken up by oil, referred to as the *residual oil saturation*, water (formation saline water and injected fresh water), and CO_2, usually in supercritical condition.

Residual oil is comprised of two fractions: (a) oil which may still be mobile and recoverable at the end of CO_2-EOR, but at a rate insufficient for economic exploitation; (b) oil which is not recoverable, referred to as the *irreducible oil* saturation. Water is also comprised of two fractions: (a) water which is mobile and displaceable by the injected CO_2; (b) water which is immobile, held in place by capillary forces, (i.e. irreducible water saturation).

4.2.1 Estimate Based on the Formulation by Kovscek (2002)

The formulation by Kovscek (2002) is comprised of two parts, each considering separate fractions of reservoir volume available for CO_2 storage. The first part of the formulation considers the volume that becomes available for storage due to removal of displaceable fluids during oil production. The second part of the formulation considers the additional volume that can be gained by dissolution of CO_2 in the residual water phase. No volumetric adjustment is made for the case where CO_2 dissolves in the residual oil phase.

The reservoir is considered to be depleted and the oil and water saturations are assumed to be at the residual and irreducible fractions, respectively. The formulation is given by (Kovscek, 2002):

$$m_{CO_2} = (V_{bhcU}\,\varphi_{hcU}\rho_U + V_{bhcL}\,\varphi_{hcL}\rho_L)(1 - S_{or} - S_{wihc}) + V_{bhcUL}c_d S_{wihc} \qquad (4.1)$$

where

m_{CO_2} is mass of stored CO_2, kg

V_{bhcU} is bulk volume of Upper Donovan hydrocarbon-bearing sandstones, m^3

V_{bhcL} is bulk volume of Lower Donovan hydrocarbon-bearing sandstones, m^3

V_{bhcUL} is total bulk volume of hydrocarbon-bearing sandstones, m^3

ρ_U is average density of CO_2 at Upper Donovan conditions, kg/m^3

ρ_L is average density of CO_2 at Lower Donovan conditions, kg/m^3

S_{or} is residual oil saturation of hydrocarbon-bearing sandstones, dimensionless

S_{wihc} is irreducible water saturation of hydrocarbon-bearing sandstones, dimensionless

φ_{hcU} is porosity of Upper Donovan hydrocarbon-bearing sandstones, dimensionless

φ_{hcL} is porosity of Lower Donovan hydrocarbon-bearing sandstones, dimensionless

c_d is mass of CO_2 dissolved per unit volume of water, kg/m^3

The upper bound on the CO_2 mass for the Upper and Lower Donovan was estimated in Section 3.6.1 to be 60 x 10^9 kg, and the residual oil saturation was estimated by Fowler et al. (1998) to be 0.2074. A value of 55 kg/m^3 was used for the dissolution of CO_2 in water (Kovscek, 2002). Substituting these values in Equation 4.1 produced an estimate of m_{CO_2} = 44.2 x 10^9 kg, (48.7 x 10^6 short tons) for the storage capacity of the depleted oil reservoirs. This estimate is 73.7% of the upper bound capacity estimate

obtained in Section 3.6.1 for the Upper and Lower Donovan hydrocarbon-bearing sandstones.

4.2.2 *Estimate based on the Formulation by Shaw and Bachu (2002)*

Waterflooded oil reservoirs undergo massive fresh or saline water injections to increase reservoir pressure and drive additional oil to production. A fraction of the injected water is recovered with oil at the production wells. However, a considerable amount of water remains in place within the interstitial space of the hydrocarbon-bearing sandstones at the end of oil production. Injected water remaining in place increases the residual water saturation and reduces the pore volume available for CO_2 storage.

The formulation of Bachu and Shaw (2002) considers the volume of water injected and produced during waterflooding and the effect of the corresponding increase in residual water. The formulation is comprised of two parts: (a) the volume of oil recovered, which is expected to be replaced by an equivalent volume of injected CO_2; and (b) the reduction in available storage capacity due to the increase in water volume resulting from the water injection, assuming that the additional water is not displaced during the CO_2 injection.

The formulation, applied separately to the Upper and Lower Donovan, because of the difference in CO_2 density in the two reservoirs, is given by (Bachu and Shaw, 2002):

$$m_{CO_2} = \rho_{CO_2}\left[V_{phc}(1 - S_{win})r_{ou} - V_{iw} + V_{pw}\right] \tag{4.2}$$

where

m_{CO_2} is mass of stored CO_2, kg

ρ_{CO_2} is density of CO_2 as a function of formation pressure and temperature, kg/m^3

V_{phc} is pore volume of hydrocarbon-bearing sandstones, m^3

S_{win} is initial water saturation, dimensionless

r_{ou} is ultimate fraction of original oil in place recovered, dimensionless

V_{iw} is volume of water injected into hydrocarbon-bearing sandstones, m^3

V_{pw} is volume of water produced from hydrocarbon-bearing sandstones, m^3

Citronelle Oil Field has been subjected to waterflooding since 1961. To estimate the volume of water injected into the Citronelle Oil Field to date, the volume of water injected during the period from 1961 to 1998, cited by Fowler et al. (1998) as 300,000,000 bbl, was extrapolated to the present time. The extrapolation produced an estimate of 384,320,000 bbl (61,100,159 m^3), for the volume of water injected to date, assuming 20% reduction in injection rate due to temporary closure or abandonment of injection wells, during the period from 1998 to date. The 20% reduction factor was estimated using Citronelle Oil Field well data for the period 1961 to 1998, obtained from the ASOGB database (2012).

Oil and water production data obtained from the ASOGB database (2012) for the Citronelle Oil Field, also indicate that the volume of produced water, to date, is 135,381,451 bbl (21,523,967 m^3), and oil production, to date, is 172,142,921 bbl. A value

of 559,554,368 bbl for OOIP was obtained, using 1,043,721,760 m^3 for the reservoir rock volume of the hydrocarbon-bearing sandstones (Unit Manager's Report, 1999), porosity of 0.1361, and initial water saturation of 0.3737 (Unit Manager's Report, 1999). The oil production estimate of 172,142,921 bbl, is 30.8% of OOIP. Assuming a CO_2-EOR recovery factor of approximately 15% of OOIP for Gulf Coast sandstone oil reservoirs (Holtz et al., 2005) the ultimate recovery factor is estimated to be 45.8%.

Substituting appropriate values in Equation 4.2, yields a CO_2 storage capacity for the Upper Donovan of 1.89 x 10^9 kg (2.08 x 10^6 short tons), and for the Lower Donovan, 0.89 x 10^9 kg (0.99 x 10^6 short tons). The total CO_2 storage capacity is then estimated to be 2.78 x 10^9 kg (3.06 x 10^6 short tons), which is 4.7% of the upper bound estimate. The low capacity underscores the impact of injected water on the estimate of the volume available for CO_2 storage, under the assumption that the additional water is not displaced by the CO_2.

4.2.3 *Estimate Based on the Formulation by the U.S. Department of Energy Carbon Sequestration Partnerships (2006)*

This formulation was developed by the Capacity and Fairways Subgroup of the Geologic Working Group of the Department of Energy Carbon Sequestration Regional Partnerships, for the 2006 National Capacity Assessment white paper and was updated in 2008 (Hovorka, 2006). The formulation is based on replacing cumulative primary and secondary oil production, with an equivalent volume of CO_2, as an effective means of estimating CO_2 storage in oil reservoirs. Miscibility of CO_2 into oil, dissolution of CO_2 into residual water, hysteretic effects associated with hydrocarbon production, CO_2 injection, and waterflooding are not considered in the analysis.

The estimate can be obtained using the following expression for the available CO_2 storage in the oil reservoirs of the Upper and Lower Donovan:

$$m_{CO_2} = \rho_{CO_2} r_{oc} B_o \tag{4.3}$$

where

m_{CO_2} is mass of stored CO_2, kg

ρ_{CO_2} is density of CO_2 as a function of formation pressure and temperature, kg/m^3

r_{oc} is cumulative primary and secondary oil recovery in the Upper and Lower Donovan, m^3

B_o is formation volume factor, dimensionless

Formation volume factor, B_o, is a dimensionless ratio of the volume of oil under reservoir conditions to the volume at standard conditions of 20 °C (68 °F) and 101.325 kPa (14.696 psi) at the surface. Eaves (1976), cites an average value of 1.119 for the formation volume factor of the Citronelle Oil Field. Primary and secondary oil recovery is 172,142,921 bbl, and average oil reservoir density is 624.7 kg/m^3 (38.97 lb/ft^3) (Table 3.1). Substituting these values in Equation 4.3 yields a combined CO_2 storage estimate for the Upper and Lower Donovan hydrocarbon-bearing sandstones of 19.1 x 10^9 kg (21.1 x 10^6 short tons). The estimate is 31.8% of the upper bound for the Upper and Lower Donovan.

4.3 Carbon Dioxide Storage Accompanying Enhanced Oil Recovery

Enhanced oil recovery using CO_2 results in a fraction of the injected CO_2 being retained in the hydrocarbon-bearing sandstones at the conclusion of the tertiary recovery operations. Shaw and Bachu (2002) proposed a method by which to estimate the volume of CO_2 stored in an oil reservoir during EOR. The formulation relates the volume of CO_2 retained to the volume of oil produced, distinguishing two stages in CO_2-EOR operations: (a) the injection period prior to CO_2 breakthrough, during which the volume of CO_2 retained is equal to the volume of oil produced, both measured under reservoir conditions; and (b) the injection period following breakthrough, during which the volume of CO_2 retained is a fixed fraction of the volume of oil recovered. The formulations are given by (Shaw and Bachu, 2002):

a) at CO_2 breakthrough,

$$m_{CO_2} = \rho_{CO_2} r_{bt} V_o B_o \tag{4.4}$$

b) at any arbitrary stage of oil production following CO_2 breakthrough,

$$m_{CO_2} = \rho_{CO_2} V_o B_o [r_{bt} + 0.6(r_o - r_{bt})] \tag{4.5}$$

where

m_{CO_2} is mass of stored CO_2, kg

ρ_{CO_2} is density of CO_2 as a function of formation pressure and temperature, kg/m^3

r_{bt} is fraction of original oil in place recovered at breakthrough, dimensionless

V_o is volume of original oil in place at reservoir conditions, m^3

B_o is formation volume factor, dimensionless

r_o is fraction of original oil in place recovered at time of interest, dimensionless

Data from U.S. CO_2-EOR projects (Hadlow, 1992), indicate that 40% of the injected CO_2 is recovered at the producer wells, suggesting that 60% of the CO_2 is retained following CO_2 breakthrough, if separation and reinjection are not considered. It is estimated that oil recovery is 45.8% of OOIP (Section 4.2.2) at the end of tertiary production from the Upper and Lower Donovan oil reservoirs, and 35% of OOIP at CO_2 breakthrough.

Substituting these values in Equations 4.4 and 4.5 yields the following CO_2 storage estimates during CO_2-EOR from the Upper and Lower Donovan:

a) at breakthrough, CO_2 storage, m_{CO_2}= 19.4 x 10^9 kg (21.4 x 10^6 short tons) or 32.3% of the upper bound estimate.

b) at the end of tertiary oil production, CO_2 storage, $m_{CO_2} = 23.0$ x 10^9 kg (25.4 x 10^6 short tons), or 38.4% of upper bound estimate, with ultimate oil recovery estimated at 256,275,900 bbl.

4.4 Saline-water Formations

Two formulations are considered for the estimation of CO_2 storage capacity in the Middle Donovan saline-water-bearing sandstones: (a) the model of Pruess et al. (2001); (b) and the procedure of the U.S. Department of Energy Carbon Sequestration Partnerships (2006). The calculations were performed under the assumption, introduced in Section 3.5, that the Middle Donovan shares geologic history and areal extent with the hydrocarbon-bearing sandstones of the Upper and Lower Donovan.

4.4.1 *Estimate Based on the Formulation by Pruess et al. (2001)*

The formulation is based on a capacity factor, c_f, that considers the distribution of stored CO_2 among the three possible phases: gas, liquid, and solid. Each phase is weighed by a factor, c_{fi} $(i = gas, liquid, or\ solid)$, that determines the fraction of stored CO_2 residing in that phase. The capacity factor is defined by comparing the mass of CO_2 in the gas, liquid, and solid phases with the mass of CO_2 that could be stored in the same reservoir volume if the entire pore volume were filled with pure CO_2 at the same temperature and pressure. The capacity factor is then given by (Pruess et al., 2001):

$$c_f = \frac{m_{CO_2}}{m_{all}} = c_{fg} + c_{fl} + c_{fs} \tag{4.6}$$

The contribution from each phase is given by its respective phase saturation fraction, assuming that CO_2 is the only material present in the pore space. For the gas phase, the fraction is equal to the gas saturation. The contributions are given by (Pruess et al., 2001):

$$c_{fg} = \bar{S}_g \tag{4.7}$$

$$c_{fl} = \frac{\bar{S}_l \bar{\rho}_l \bar{X}_l^{CO_2}}{\bar{\rho}_{\mathrm{g}}} \tag{4.8}$$

$$c_{fs} = \frac{\bar{v}_s \bar{\rho}_s \bar{X}_s^{CO_2}}{\varphi_s \bar{\rho}_{\mathrm{g}}} \tag{4.9}$$

where

c_{fg} is capacity factor for the gas phase, dimensionless

c_{fl} is capacity factor for the liquid phase, dimensionless

c_{fs} is capacity factor for the solid phase, dimensionless

$\bar{S}_g$ is average gas phase saturation, dimensionless

$\bar{S}_l$ is average liquid phase saturation, dimensionless

$\bar{S}_s$ is average solid phase saturation, dimensionless

$\bar{\rho}_g$ is average gas phase density, kg/m^3

$\bar{\rho}_l$ is average liquid phase density, kg/m^3

$\bar{\rho}_s$ is average solid phase density, kg/m^3

$\bar{X}_l^{CO_2}$ is average mass fraction of CO_2 in the liquid phase, dimensionless

$\bar{X}_s^{CO_2}$ is average mass fraction of CO_2 in the solid phase, dimensionless

$\bar{v}_s$ is average formation volume fraction occupied by CO_2 in solid carbonates, dimensionless

φ_s is effective porosity of the saline-water formations, dimensionless

To calculate the mass of CO_2 in each phase, the pore volume is multiplied by the density of the phase and the corresponding phase capacity factor. However, the solid phase capacity factor, which is the mineral trapping component of CO_2 storage, is considered separately in the *Mineralization* capacity estimate category. Neglecting the contribution from the capacity factor for the solid phase, the expression for the CO_2 storage of the Middle Donovan is given by (Pruess et al., 2001):

$$m_{CO_2}^{g+l} = m_{CO_2}^{g} + m_{CO_2}^{l} \tag{4.10}$$

where

$m_{CO_2}^{g+l}$ is mass of stored CO_2 in gas and liquid phases, kg

$m_{CO_2}^{g}$ is mass of CO_2 in the gas phase, kg

$m_{CO_2}^{l}$ is mass of CO_2 in the liquid phase, kg

Pruess et al. (2001) provide some values for gas and liquid phase capacity factors according to formation type. Choosing *sandy clay* for the Middle Donovan, the value of the gas phase factor is given as 0.159, and the value for the liquid phase factor as 0.047. The porosity of the Middle Donovan is 0.127 (Eaves, 1976), and from Table 3.2, the density of CO_2 is 624.91 kg/m^3 (38.99 lb/ft^3). Substituting these values in Equations 4.7, 4.8, and 4.10, a value of 6.9 x 10^9 kg (7.6 x 10^6 short tons) is obtained for CO_2 storage in gas and liquid phases in the Middle Donovan. This estimate is 43.1% of the upper bound estimate for the Middle Donovan.

4.4.2 *Estimate Based on the Formulation by the U.S. Department of Energy Carbon Sequestration Partnerships (2006)*

This is an estimate utilizing the efficiency factors proposed by the DOE Carbon Sequestration Regional Partnerships (2006). The formulation is based on the volumetric capacity of the saline-water formations discounted by an efficiency factor that is attributed to the variations and uncertainties in the values of the parameters involved. The range of efficiency factors suggested by the partnerships is 0.01 to 0.04. The formulation of the estimate is given by Equation 4.11:

$$m_{CO_2} = V_{ps}\rho_{CO_2}E \tag{4.11}$$

where

m_{CO_2} is mass of stored CO_2, kg

V_{ps} is saline-water formations pore volume, m^3

ρ_{CO_2} is density of CO_2 as a function of formation pressure and temperature, kg/m^3

E is efficiency factor, dimensionless

Substituting appropriate values for the parameters into Equation 4.11 yield values for CO_2 storage of: (a) for 0.01 efficiency, 0.16 x 10^9 kg (0.18 x 10^6 short tons) ; and (b) for 0.04 efficiency, 0.64 x 10^9 kg (0.71 x 10^6 short tons). The estimates are 1% and 4% respectively of the upper bound estimate for the Middle Donovan. The low values arise from the low efficiency factors employed in the estimates.

4.5 Mineralization

To calculate a capacity based on mineralization of CO_2 stored in the Middle Donovan saline-water formations the capacity factor for the solid phase given by Equations 4–9 is utilized. Values tabulated by Pruess et al. (2001) indicate that the CO_2 mass converted to solid phase, per unit volume of mineral, is 1169.5 kg/m^3 (73 lb/ft^3) for amphibole-type mineral groups similar to those in the Middle Donovan sandstones. As a representative case (Pruess et al., 2001), it is assumed that 1% of the volume of the formation reacts with CO_2 to form solid carbonates.

Using the above values yields a CO_2 capacity estimate for mineralization in the Middle Donovan saline-water-bearing sandstones of 0.524 x 10^9 kg (0.577 x 10^6 short tons). This represents 7.6% of the Middle Donovan estimate obtained using the model of Pruess et al. (2001) in Section 4.4.1 for CO_2 stored in the gas and liquid phases.

4.6 Static CO_2 Storage Capacity Estimates by Esposito et al. (2008)

In a study concerning the CO_2 storage capacity of the Citronelle Dome, Esposito et al. (2008) have reported static CO_2 storage estimates for the oil reservoirs in the Upper and Lower Donovan, and the saline-water-bearing sandstones in the Middle Donovan. The CO_2 storage estimates cited by these authors, for the oil reservoirs in the Upper and Lower Donovan, range from a low of 115 x 10^9 kg (126.8 x 10^6 short tons), to a high of 460 x 10^9 kg (507 x 10^6 short tons). These estimates were based on the assumption that after oil recovery is complete, CO_2 injection will continue until the reservoirs are returned to a pressure of 34.5 MPa (5000 psi).

The CO_2 storage estimates for the saline-water-bearing sandstones in the Middle Donovan range from a low of 24 x 10^9 kg (26.5 x 10^6 short tons), to a high of 100 x 10^9 kg (110.2 x 10^6 short tons). These estimates were based on volumetric calculations using the formation area, thickness, porosity, temperature, pressure, and CO_2 density. Efficiency factors were introduced to account for residual water saturation and shale dispersion. Carbon dioxide was assumed to have the density of the supercritical fluid under reservoir conditions. Dissolution of CO_2 in brine and mineralization were assumed to be negligible.

CHAPTER 5

SIMULATION OF CO_2-ENHANCED OIL RECOVERY FROM THE UPPER AND LOWER DONOVAN SANDS

5.1 Introduction

Annual oil production at the Citronelle Oil Field began in 1955, but development was erratic (Eaves, 1976). Oil production rates increased in the first few years of the field's production, as the number of drilling permits and wells increased. However, five years into production in 1960, unit operators at Citronelle Oil Field were experiencing declining oil production rates. To increase production they began secondary recovery in 1961 (Esposito et al., 2008), using waterflood, which continues to this day. Peak oil rate was reached in 1963 with annual production of 8,220,364 bbl, but has declined to 570,282 bbl/year in 2012, as shown in Figure 5.1, (ASOGB database, 2012).

Cumulative oil production from the Citronelle Oil Field is shown in Figure 5.2. The slope of the curve reflects the changes in oil production rate. Initially, the slope of the cumulative oil curve is increasing, indicating a period of rising production rates. The slope is approximately constant from the mid-nineteen sixties to the mid-nineteen seventies indicating constant oil production rates. The slope of the cumulative oil curve decreases from 1975 to this day, indicating gradual decline in the waterflood's effectiveness. To increase oil production rates and extend the productive life of the field, the reservoir management team is considering the application of tertiary recovery.

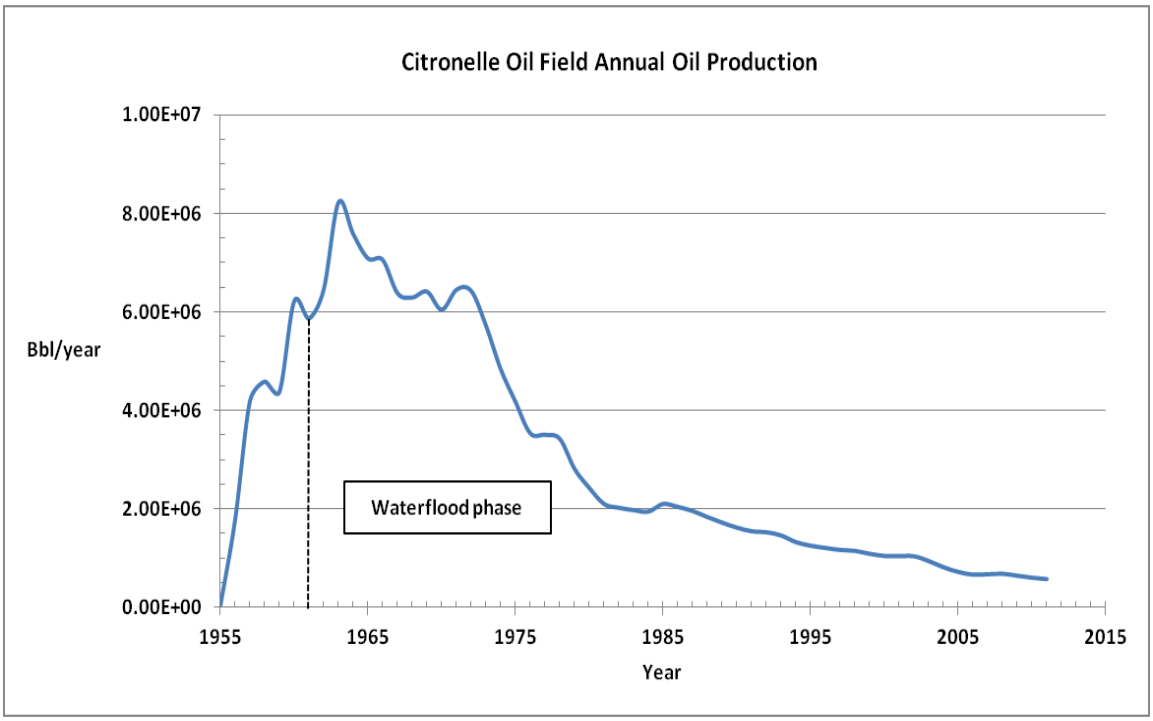

Figure 5.1. Annual oil production at Citronelle Oil Field, (ASOGB database, 2012).

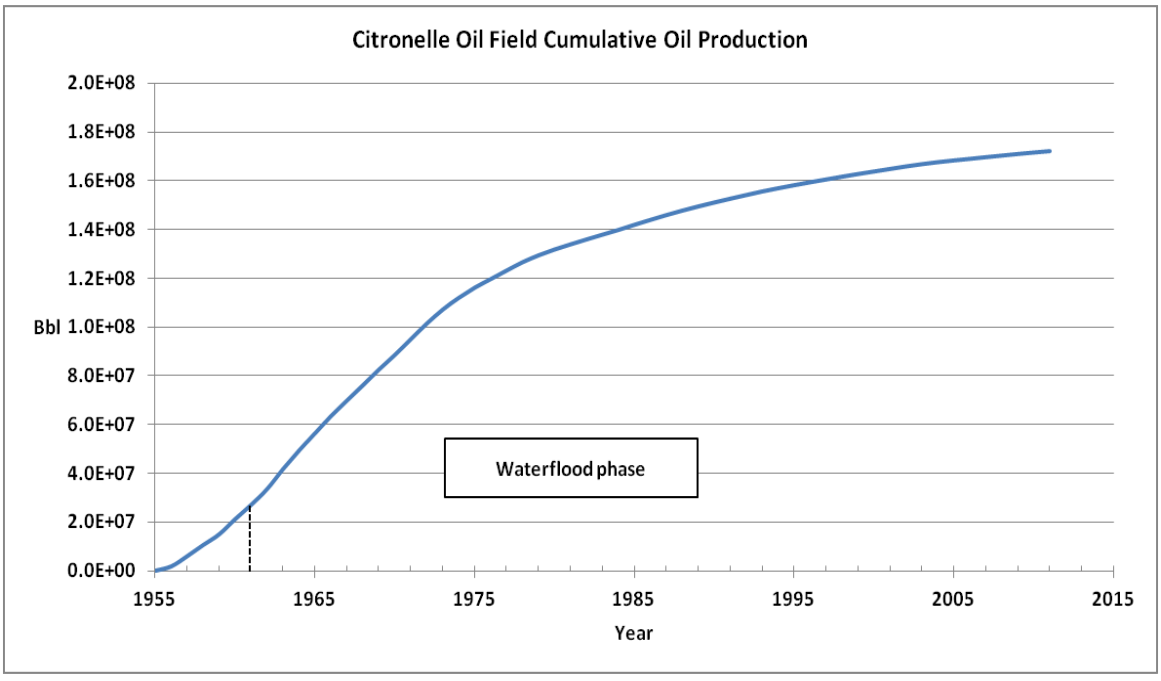

Figure 5.2. Cumulative oil production at Citronelle Oil Field, (ASOGB database, 2012).

A consortium formed by investigators from Alabama Agricultural and Mechanical University, Denbury Resources, Inc. (the current operator of Citronelle Oil Field), Geological Survey of Alabama, Southern Company Services, Inc., University of Alabama, University of Alabama at Birmingham, and University of North Carolina at Charlotte, is engaged in a Cooperative Agreement with the U.S. Department of Energy, National Energy Technology Laboratory, to evaluate the potential for carbon-dioxide-enhanced oil recovery and carbon-dioxide sequestration in the Citronelle Oil Field. A major component of the project was the development and operation of a pilot test, to investigate the CO_2-EOR potential to increase production in a field-wide CO_2 flood.

5.2 Carbon Dioxide-Enhanced Oil Recovery Pilot Test

After an extensive investigation the team decided on a cluster of five wells, in Sector B-19 of the North-Eastern section of the Citronelle Oil Field, as a good candidate for an *inverted five-spot* pattern in which to conduct the CO_2-EOR pilot test. Well B-19-10#2 (Permit No. 3232) was designated as the injection well for the pattern. The well was originally permitted as a gas injector, but had been operated as a producer. The producers selected to be monitored most closely were B-19-7 (Permit No. 1215), B-19-8 (Permit No. 1235), B-19-9 (Permit No. 1205), and B-19-11 (Permit No. 1209). An aerial photograph of the oil field in the vicinity of the test pattern, with the wells identified by number, is shown in Figure 5.3. Well B-19-10 (Permit No. 1206) had originally been included in the pattern but had been plugged and abandoned. Efforts to bring it back to production were not successful. Well B-19-11, which was the next closest production

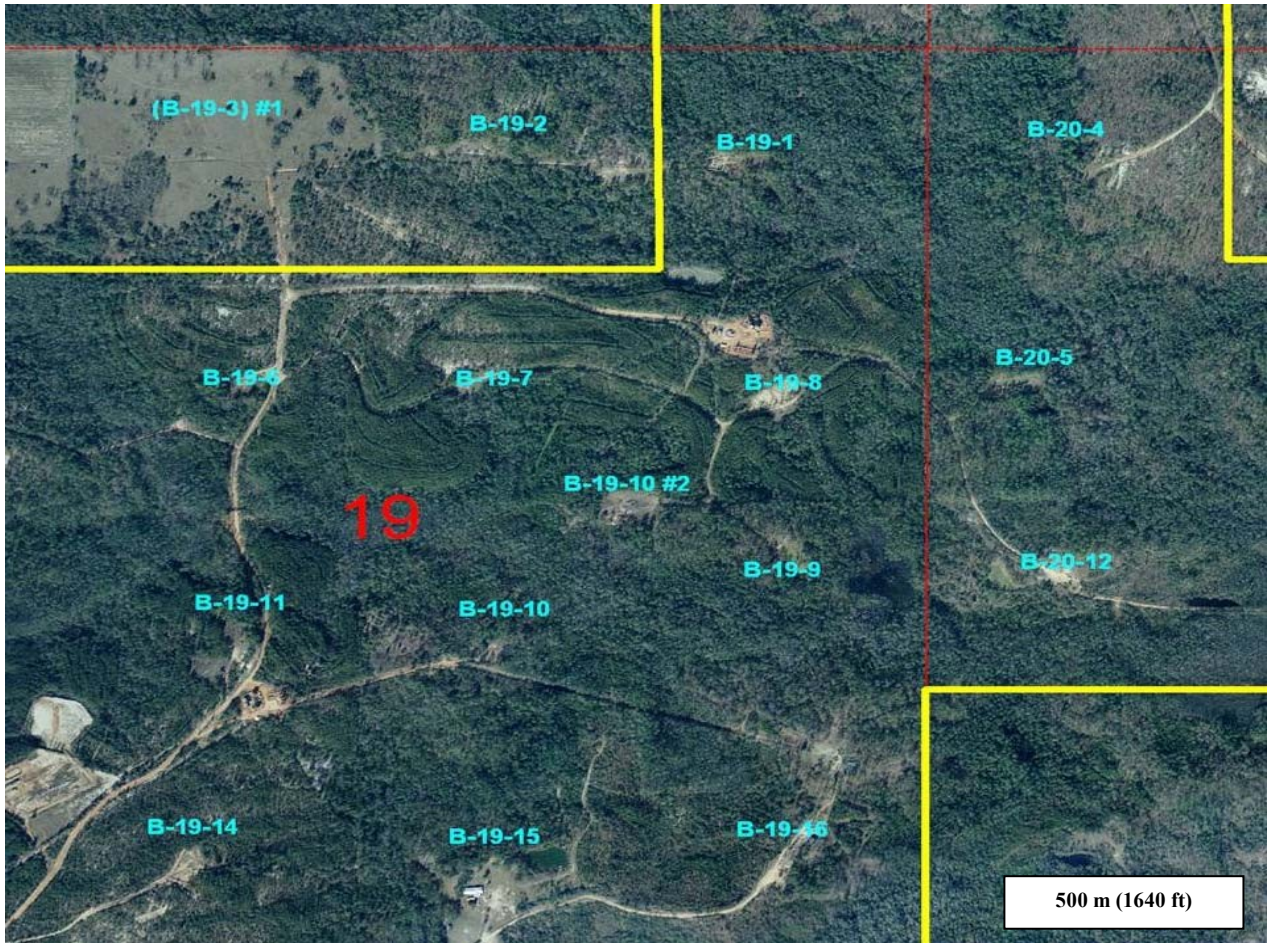

Figure 5.3. Aerial photograph of the Citronelle Oil Field in the vicinity of the pilot test well pattern. The test pattern consists of injector, Well B-19-10 #2, and producers, Well B-19-7, Well B-19-8, Well B-19-9, and Well B-19-11. The top edge of the photograph faces North. Tank Battery B-19-8 is visible just to the Northwest of Well B-19-8. Tank Battery B-19-11 is to the South of Well B-19-11, between the roads. Image courtesy of Denbury Resources.

well, was chosen to replace Well B-19-10, to complete the inverted five-spot pattern. Substitution of Well B-19-11 for Well B-19-10 changed what was originally intended to be a more symmetric inverted five-spot pattern in to a skewed arrangement.

Production casing in Well B-19-10#2 is perforated in three zones, two of which are in the Upper Donovan sands, and the third in the Lower Donovan sands. The perforation in the Lower Donovan has been plugged since 1992. The Upper Donovan perforations are open to Sands 14-1 and 16-2. Based on well-log cross sections, the two sands were considered to be good candidates for the CO_2-EOR pilot test.

The CO_2 injection plan was comprised of two CO_2 injection phases separated by an interim water injection phase. In the first injection phase 6804 t (7500 short tons) of CO_2 were to be injected into Sands 14-1 and 16-2. In the interim water phase, Well B-19-10#2 would be converted to a water injector for a period of approximately 250 days at the end of the first CO_2 injection phase of the pilot test. The second injection phase would begin at the end of the interim water phase. In the second injection phase, Well B-19-10#2 would be converted to an injector, and a second slug of 6804 t (7500 short tons) of CO_2 would be injected. Preliminary simulations indicated that the volume of CO_2 chosen for injection would be sufficient to mobilize incremental oil to the production wells (Theodorou and Walsh unpublished work, 2007).

Prior to initiating the CO_2-EOR pilot test, water was injected into Well B-19-10 #2, to establish a baseline for oil production. Water injection began on March 25, 2008, and stabilized at a steady injection rate of 170 bbl/day. During this period, Wells B-19-7

and B-19-9 each produced 4 to 5 bbl/day of oil and Wells B-19-8 and B-19-11 each produced 8 to 9 bbl/day of oil.

After a period of preparation and technical adjustments, CO_2 injection for the first phase of the pilot test began on December 1, 2009 and ended on September 25, 2010. The total CO_2 volume injected exceeded the planned amount, due to surplus CO_2 deliveries, with 7290 t (8036 short tons) injected into hydrocarbon-bearing Sands 14-1 and 16-2. Following the first CO_2 injection phase, Well B-19-10#2 was converted back to a water injector. To date no time frame has been set for the second CO_2 injection phase.

Rates of CO_2 injection varied during the first phase, with an average rate of 28.1 t/day (31 short tons/day). Tracer tests indicated that the CO_2 volumes injected into Sands 14-1 and 16-2 were 57% and 43% respectively. During the initial water injection, the distribution of water flow into Sands 14-1 and 16-2 was 82% and 18%, respectively.

5.3 Simulation of the CO_2-Enhanced Oil Recovery Pilot Test using MASTER 3.0

A software package capable of simulating CO_2-EOR in an oil reservoir was utilized to evaluate the performance of the Citronelle CO_2-EOR pilot test and investigate the potential of various long-term CO_2-enhanced recovery scenarios. The software chosen was the US DOE/NETL reservoir simulator, MASTER 3.0 (Ammer and Brummert, 1991; Ammer et al., 1991; Zeng et al., 2005), described in Section 3.3.2. The simulator was used with all its miscible gas injection features enabled, and CO_2 as the injected gas.

5.3.1 Simulation Summary and Model Specifications

The simulations were based on a single layer, 40- by 32-block grid. Each block in the grid measured 53.65 m by 53.65 m (176 ft by 176 ft). The thickness of each block in the simulation grid varied according to the sand thickness contours. Figure 5.4a, and Figure 5.4b show the thickness contours of Sands 14-1 and 16-2 in the area of the simulation grid, respectively. The thicknesses were estimated from computer-generated net pay contours (Esposito et al., 2010).

The simulation grid was extended beyond the five-spot pattern, to include the influence of peripheral oil production and water injection wells on the behavior of the wells in the five-spot pattern. Sixteen wells were considered in the simulation, and their arrangement within the simulation grid is shown in Figure 5.5. Table 5.1 lists the well number, permit number and type (producer or injector) for each well included in the simulation.

The primary reservoir parameters specified in the simulations of the CO_2-EOR pilot test are listed in Table 5.2. The average reservoir pressure in the simulation grid was estimated to be 31.0 MPa (4500 psi). The value is based on fluid head and bottom hole pressure (BHP), recorded in a reservoir pressure field log dated October, 1992, that was retrieved (September 9, 2008) from the Citronelle Oil Field archives, at the Alabama State Oil and Gas Board. Pressure in the simulation grid is considerably higher than the average reservoir pressure of the Citronelle Oil Field, estimated at 20.7 MPa (3000 psi), (Esposito et al., 2010). Low permeabilities in the simulation grid have caused reservoir pressure to increase locally during the waterflood to establish the baseline for oil production.

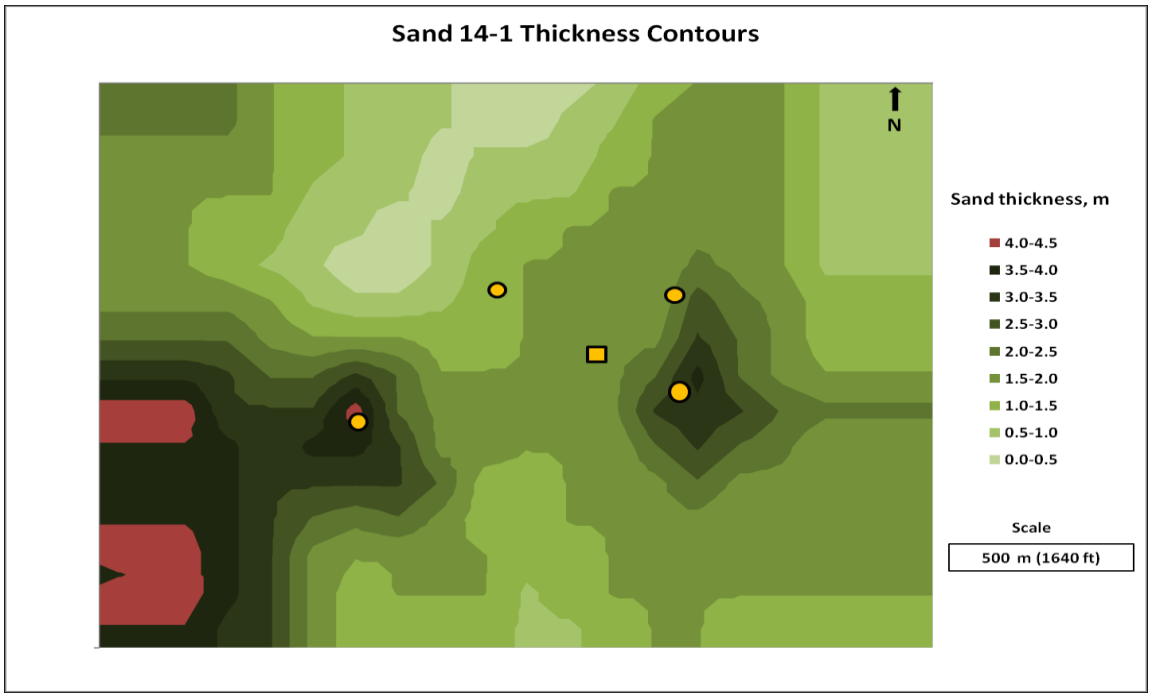

Figure 5.4a. Sand 14-1 thickness contours within and surrounding the inverted 5-spot well pattern. The contour interval is 0.5 m (1.64 ft). The injector, Well B-19-10#2, is indicated by the rectangular marker (after Esposito et al., 2010).

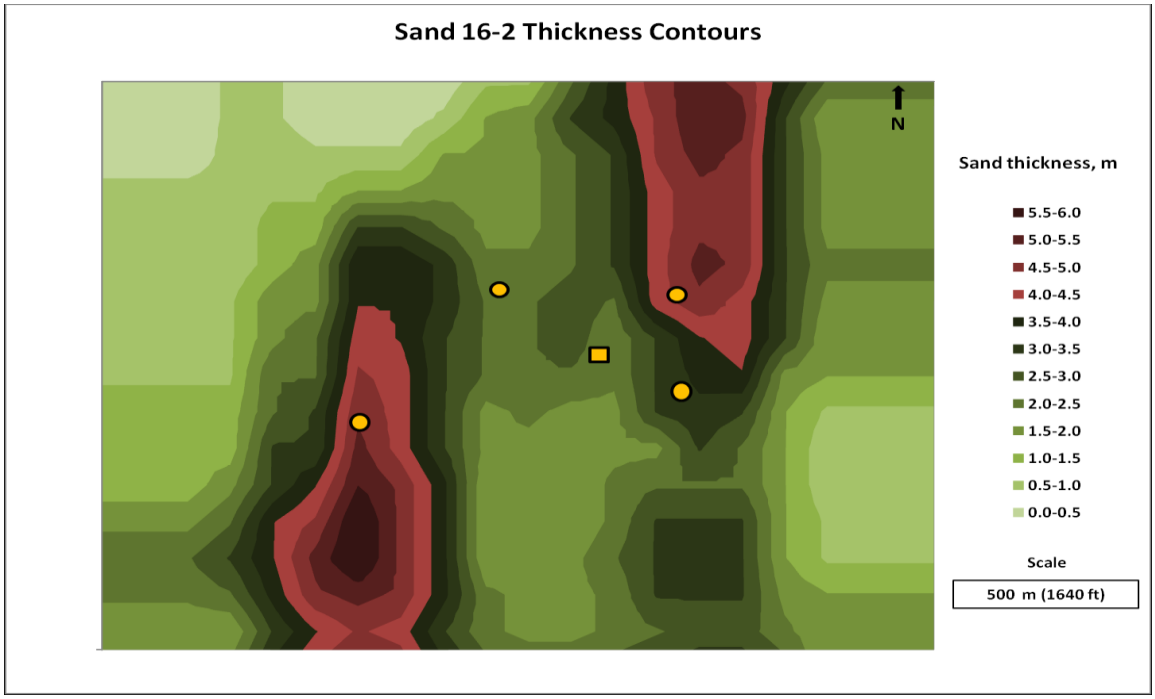

Figure 5.4b. Sand 16-2 thickness contours within and surrounding the inverted 5-spot well pattern. The contour interval is 0.5 m (1.64 ft). The injector, Well B-19-10#2, is indicated by the rectangular marker (after Esposito et al., 2010).

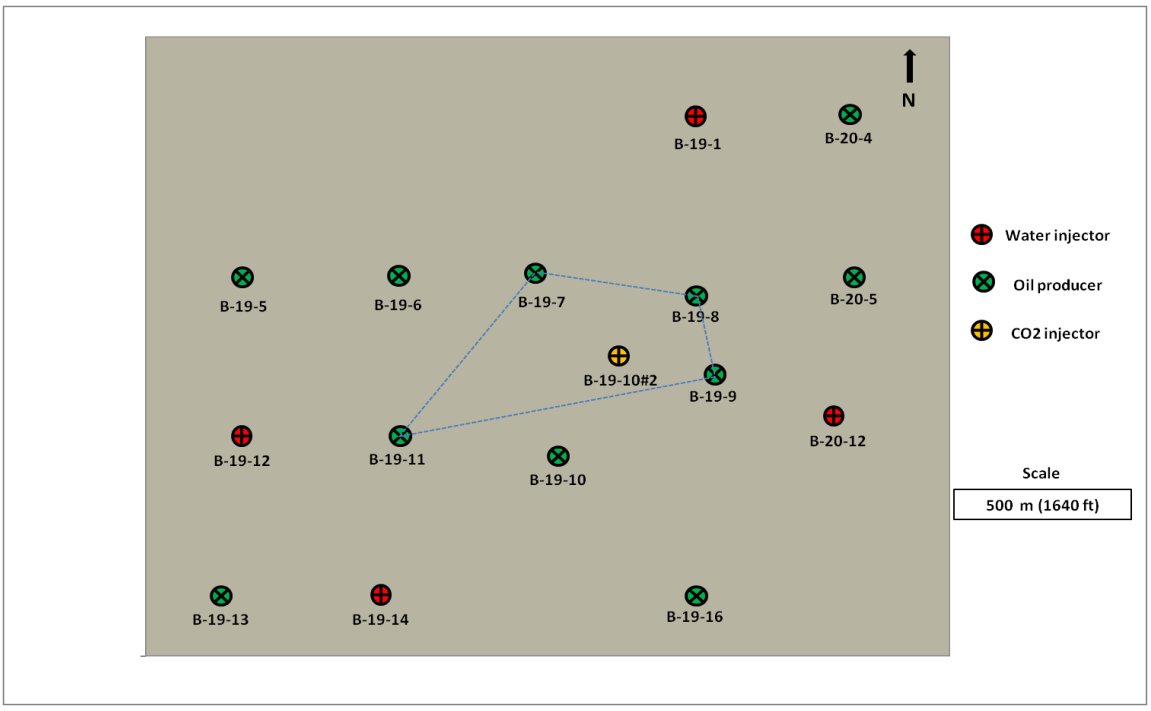

Figure 5.5. Wells included in the CO_2-enhanced oil recovery simulation grid. The dashed line indicates the inverted five-spot well pattern (after Merit Energy Company, Citronelle Field, Posted Well Data, 2004).

The ASOGB database contains information for each well in the Citronelle Oil Field, including its production history. Using the production records, an operational time-line for all the wells in the simulation grid was created, as shown in Table 5.3.

The record begins on January 1, 1982, coinciding with the start of the early CO_2-EOR pilot, and extends to the present time, providing the history of oil production and water injection for the wells included in the simulation. The well records shown in Table 5.3 were incorporated in all the simulations of the pilot test, and in the simulated long-term forecasts.

Table 5.1. Wells in the simulation of the CO_2-EOR pilot test.

Well Number	Permit Number	Type
B-19-5	1232	Oil producer
B-19-6	1214	Oil producer
B-19-7	1215	Oil producer
B-19-8	1235	Oil producer
B-19-9	1205	Oil producer
B-19-10	1206	Oil producer
B-19-10#2	3232	Water/CO_2 injector
B-19-11	1209	Oil producer
B-19-13	787	Oil producer
B-19-16	1208	Oil producer
B-20-4	1256	Oil producer
B-20-5	1230	Oil producer
B-19-1	1254	Water injector
B-19-12	1197	Water injector
B-19-14	898	Water injector
B-20-12	1225	Water injector

Days 1 (1/1/1982) through 9504 (1/9/2008), shown in Table 5.3, constitute the pre-pilot test period in the simulation. Activities that follow day 9504 (1/9/2008), fall in the pilot-test or post-pilot-test period. Monthly oil production records, for the period from 1/1/1982 through 1/9/2008, were obtained for each well in the simulation grid from the ASOGB database (2012). Using the monthly rates, a record of average daily oil production was constructed for each well over the pre-pilot test period.

Table 5.2. Primary reservoir parameters specified in the CO_2-EOR pilot test simulations.

Parameter	Value	Source
Average oil reservoir pressure	31.0 MPa (4500 psi)	Field pressure log, 1992
Reservoir oil saturation	0.55 fraction	Unit Manager's Report, 1999
Reservoir water saturation	0.45 fraction	Unit Manager's Report, 1999
CO_2-oil miscibility pressure	19.3 MPa (2800 psi)	Gilchrist, 1981
Average porosity	0.1361 fraction	Fowler et al., 1998
Average permeability	10 mdarcy	Fowler et al., 1998

A simulation was performed to produce a record of daily oil production for the pre-pilot test period and compare it to the field record. The simulation was performed using the pressure-controlled option available in MASTER 3.0, for all of the wells in the simulation grid. Under the pressure-control option, the bottom-hole pressure for each well is set, and water injection and oil production rates are calculated based on total fluid mobility within the grid block containing each well.

Figure 5.6 shows the record of daily oil production and that predicted by the simulation for the pre-pilot test period. Simulations for Sand 14-1 were performed separately from Sand 16-2 and the results were combined to determine the total daily oil production.

Table 5.3. Well operation schedule for CO_2-EOR pilot test simulation.

Well number	Status	Date	Net days[a]	Cumulative days
B-19-1	On	1/1/1982	0	0
B-19-4	On	1/1/1982	0	0
B-19-5	Off	1/1/1982	0	0
B-19-6	On	1/1/1982	0	0
B-19-8	On	1/1/1982	0	0
B-19-9	On	1/1/1982	0	0
B-19-10	On	1/1/1982	0	0
B-19-11	On	1/1/1982	0	0
B-19-13	On	1/1/1982	0	0
B-19-14	On	1/1/1982	0	0
B-19-16	On	1/1/1982	0	0
B-19-9	Off	3/1/1983	424	424
B-20-12	On	10/16/1987	1690	2114
B-19-9	On	3/1/1988	137	2251
B-19-12	On	6/1/1989	457	2708
B-19-10	Off	7/1/1990	395	3103
B-19-5	On	3/1/1991	243	3346
B-19-16	Off	5/1/1991	61	3407
B-19-10	On	1/1/1992	245	3652
B-19-10	Off	3/1/1992	60	3712
B-19-10#2	On	5/1/1992	61	3773
B-19-6	Off	7/15/1992	75	3848
B-19-8	Off	1/1/1993	170	4018
B-19-5	Off	12/22/1993	355	4373
B-19-5	On	5/25/1994	154	4527
B-19-8	On	2/1/1995	252	4779
B-19-5	Off	7/26/1996	541	5320
B-19-8	Off	8/1/1996	6	5326
B-19-8	On	9/1/1996	31	5357
B-19-5	On	10/31/1996	60	5417
B-19-10#2	Off	1/1/1997	62	5479
B-19-9	Off	2/1/1999	761	6240
B-19-5	Off	5/7/1999	95	6335
B-19-10#2	On	2/1/2004	1731	8066
B-19-10#2	Off	3/1/2004	29	8095
B-19-13	Off	5/3/2004	63	8158
B-19-13	On	7/3/2004	61	8219
B-19-13	Off	9/1/2005	425	8644
B-19-13	On	11/1/2006	426	9070
B-19-10#2	On	3/1/2007	120	9190
B-19-10#2	Off	1/9/2008	314	9504

[a]Net days are counted starting on January 1, 1982, which is day one in the simulations.

5.3.2 Pre-Pilot Test Actual and Simulated Oil Production History

The simulated daily oil production curve, shown in Figure 5.6, follows the trend of the actual oil production curve, although in some time intervals there is considerable separation between the two curves. The separation is greater in the earlier part of the simulation than in the later part, with an interim period of good agreement during the time interval from 1992 to 1999. The discrepancy in the earlier part of the simulation is partly attributed to differences between the controlled rate imposed on production wells during field operations, and the maximum possible oil production rate calculated by the simulator, based on mobility. Production rate constraints for the Citronelle Oil Field were imposed by regulatory and contractual restrictions, because in the history of the field, multiple unit operators sharing economic interest were jointly involved in its management. Abrupt changes in the simulation curve are caused by the response of the simulator to the changes in the operational well schedule shown in Table 5.3.

5.3.3 Carbon-Dioxide Pilot Test Simulation Results for Oil Production

Field observations during and after the CO_2-EOR pilot test provide valuable information regarding the effectiveness of the CO_2 injection and its ability to mobilize a significant volume of oil. The parameter of greater importance, when assessing the effectiveness of CO_2-EOR, is the daily oil production rate, which can be measured and compared to past oil production records. However, oil production rates during CO_2 or water injection, can be influenced directly by sweep efficiency (vertical and horizontal), gravity override, fingering, and variations in water and oil saturations. Obtaining field

information regarding these parameters is a difficult task. Most often, one has to rely on simulations.

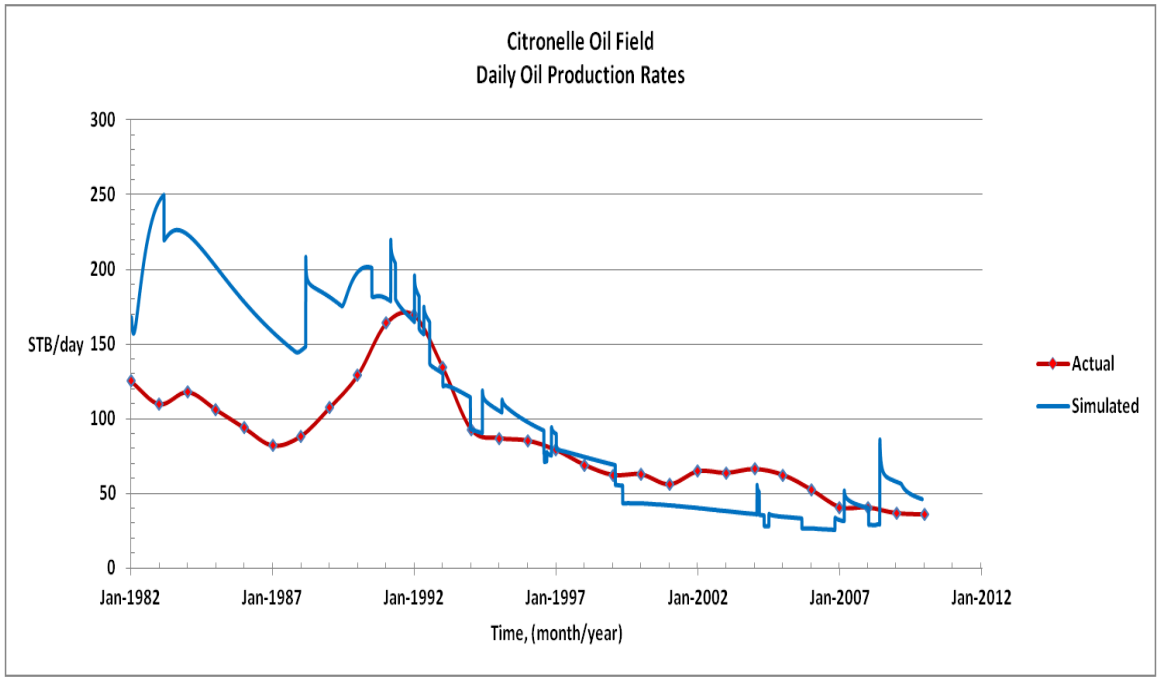

Figure 5.6. Actual and simulated daily oil production rates from the 16 wells in the pilot test simulation grid, for the period from 1/1/1982 to 11/30/2009.

A simulation, using the model specifications and primary parameter values cited in Section 5.3.1, was performed for the time period of the CO_2-EOR pilot test. The primary objective of the simulation was to generate a daily oil production record for the duration of the pilot test and to determine CO_2, oil, and water saturations at the end of each of the three phases of the test.

During the simulation, CO_2 injection Well B-19-10#2 was under rate-control and its injection schedule emulated the actual CO_2 injection rates and schedule of field operations, up to the time the simulations were performed. This information was obtained from the schedule of CO_2 delivery and injection rates which was recorded daily by the

operators, and forwarded to the investigators at regular intervals. All other wells in the simulation grid were under pressure-control, with output values for injection and production rates based on mobility. Bottom-hole pressure for the injection wells was 60.3 MPa (8740 psi), and 26.5 MPa (3850 psi) for the producing wells. During the interim water injection phase, the injection rate was 170 bbl/day.

In the simulation time-line, December 1, 2009 marks the beginning, and August 20, 2010 marks the end of the first CO_2 injection in the pilot test. Water injection begins on August 21, 2010 and ends on April 27, 2011. The second CO_2 injection in the pilot test begins on April 28, 2011 and ends on November 1, 2011.

Figure 5.7 shows the daily oil production during the three phases of the CO_2-EOR pilot test, compared to daily oil production for the same time period if waterflooding had continued, without any CO_2 injection. During the first CO_2 injection phase, oil production increases only marginally, increasing by approximately 5 STB/day. Mobilization of oil takes place in the region of the injected CO_2, but is hindered by the higher water pressure ahead of the CO_2 front.

During the water injection phase, the miscible oil-CO_2 bank is driven toward the production wells, resulting in a significant increase in oil production, increasing by approximately 40 STB/day. At the end of the water injection phase, a single WAG cycle has been completed and oil production appears to taper off.

During the second CO_2 injection phase, oil production begins to increase again, as more residual oil is mobilized by the CO_2. Using the same data as those used for input in the simulations, the hydrocarbon pore volume for Sands 14-1, and 16-2, within the

inverted five-spot area, was estimated at 34,820 m^3 (1,229,700 ft^3). The total CO_2 mass injected during the pilot test simulation was 13,608 t (15,000 short tons). The injected mass corresponds to a CO_2 volume of 21,856 m^3 (771,840 ft^3), injected into the Upper Donovan, using 622.62 kg/m^3 for the CO_2 density (Table 3.1). Based on the mass and density figures, the volume of injected CO_2 during the pilot test represents 0.63 of the hydrocarbon pore volume of Sands 14-1 and 16-2, within the inverted five-spot pattern.

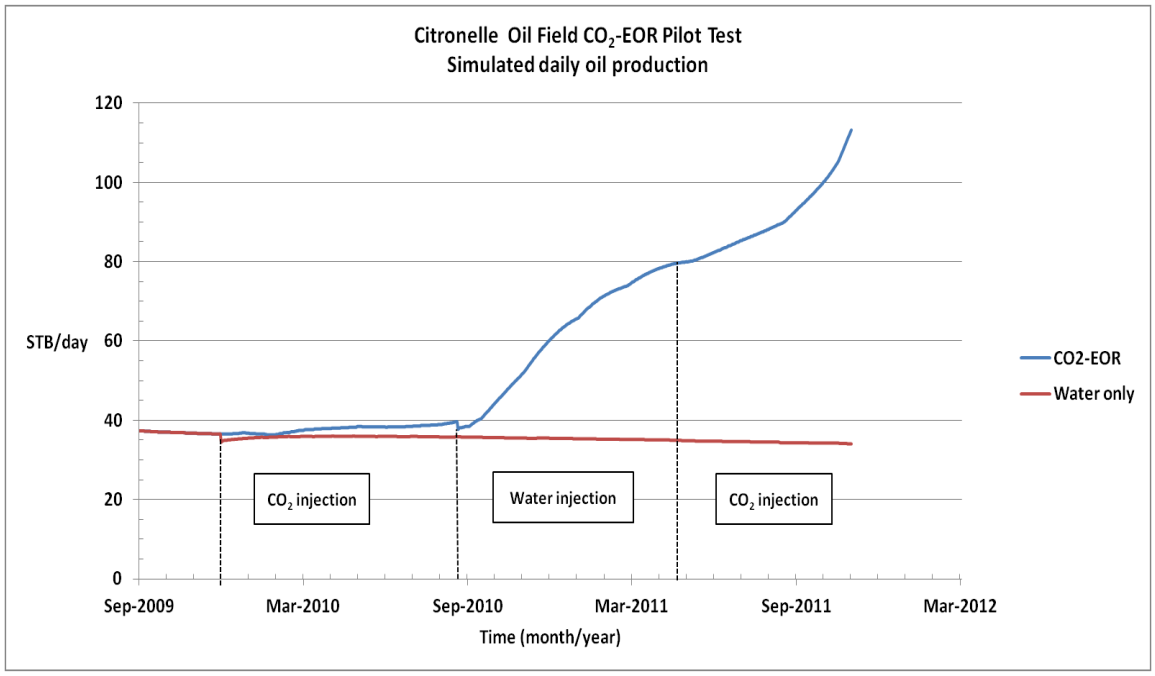

Figure 5.7. Simulation of daily oil production for the CO_2-EOR pilot test (blue line) and continuous waterflood only (red line). During each CO_2 injection cycle, 6804 t (7500 short tons) of CO_2 were injected. The interim water injection period is 250 days, and water injection rate is 170 bbl/day.

The results of the simulation indicate that the oil reservoir's production response to the CO_2 injection volume, as fraction of the reservoir hydrocarbon pore volume, was promising. Cumulative oil for CO_2-EOR, during the pilot test, and comparison with waterflood only, are shown in Figure 5.8. Table 5.4 summarizes the cumulative

incremental volumes of oil recovered and the percent increase, at the end of each injection phase of the CO_2-EOR pilot test, compared to the volume of oil that would have been recovered if waterflood had continued, without any CO_2 injection.

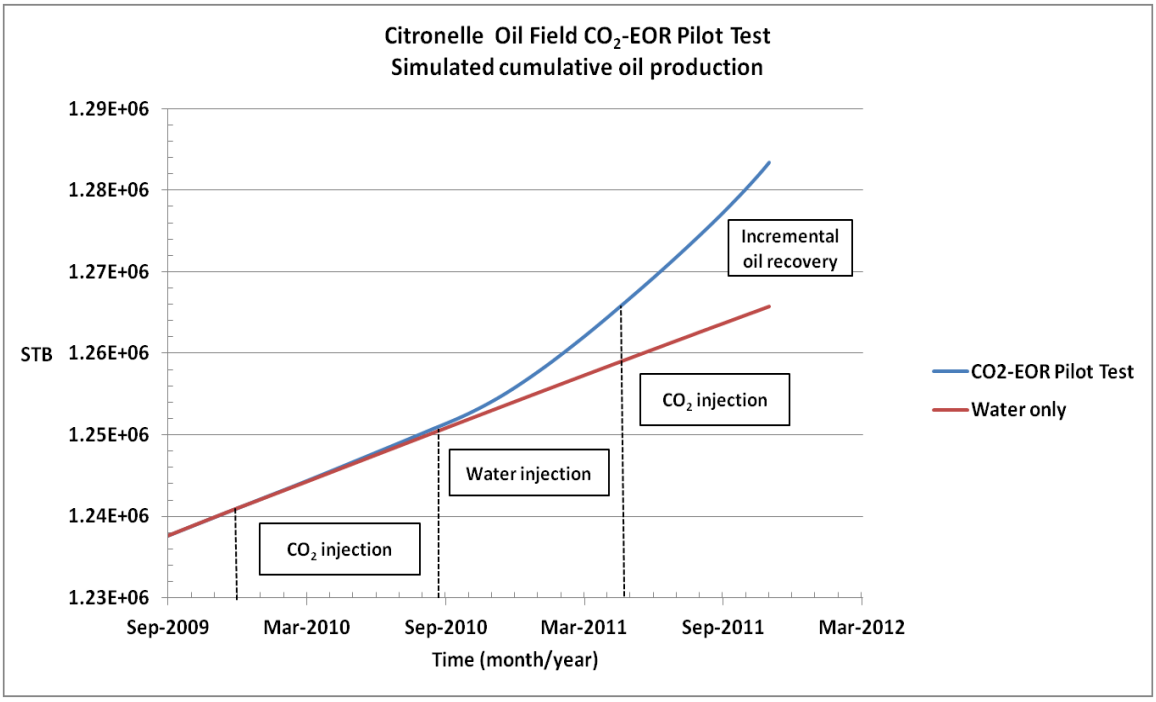

Figure 5.8. Simulation of cumulative oil production for the CO_2-EOR pilot test and comparison with waterflood only. During each CO_2 injection cycle, 6804 t (7500 short tons) of CO_2 were injected. The interim water injection period is 250 days.

Table 5.4. Summary of simulated cumulative incremental (above the waterflood base line) oil recovery during the CO_2-EOR pilot test from all of the production wells in the simulation grid.

CO_2-EOR pilot test phase	Incremental oil recovery (STB)	% increase over waterflood only
End of first CO_2 injection	522	5.5
End of interim water injection	6629	73.3
End of second CO_2 injection	10,528	162.1

5.3.4 Visualization Framework of Pilot Test Simulation Results

Corey Shum, from the Enabling Technology Laboratory at the University of Alabama at Birmingham (UAB), created animations of the evolution of fluid saturations in Sands 14-1 and 16-2 during the pilot test. The raw output from the reservoir simulation was parsed with a custom application to extract the CO_2, oil, and water saturation results for each point in space and time.

The parsed data was exported to the open source 3-D data visualization software, Visualization Toolkit (VTK), (Schroeder et al., 1993), which together with other custom visualization applications, was used to create animations of the time-dependent data. Still images were extracted from the animations for events and times of interest, as listed in Table 5.5. These still images are shown in Figures 5.9, 5.10, 5.11, and 5.12.

The still images contain a cutout of satellite photographic imagery showing the inverted five-spot test pattern in the Citronelle Oil Field. Lines from the well locations at ground surface are extruded down the image, to identify the corresponding locations in the CO_2, oil, and water saturation graphs.

The levels of saturation are represented both by the height at each location, on each graph, and also by its color intensity, according to the color legend in the upper-left corner of the image. As the simulation progresses, the day and the injection activity are displayed in the lower-right corner of the image.

Table 5.5. Events of interest and corresponding dates, regarding fluid saturations produced by MASTER 3.0 simulations for the pilot test grid.

Event of interest	Date	Simulation time step (days)[a]
Day before first CO_2 injection	11/30/2009	10196
End of first 6804 t (7500 short tons) CO_2 injection	8/20/2010	10459
End of 250 day interim water injection	4/27/2011	10709
End of second 6804 t (7500 short tons) CO_2 injection	11/1/2011	10897

[a] Simulation time step one is 1/1/1982.

5.3.5 Visualization of Pilot Test Simulation Results for Phase Saturation Before CO_2 Injection

There was no CO_2 saturation distribution on 11/30/2009 (day 10196), because CO_2 injection had not begun, as shown in Figure 5.9. The oil and water saturation distributions are shown for both Sands 14-1 and 16-2. Oil and water saturations have been influenced by the water injection that was underway, to establish the baseline oil production. Low oil saturations are present in the Southwestern quadrant of the simulation grid, as oil was driven away by the water injected into Wells B-19-12 and B-19-14. The oil saturations are higher, due to the pressure drawdown, in the direction of the production wells B-19-13 and B-19-11. Large areas of low oil saturation dominate on either side of the high oil saturation conduit that has formed diagonally across the Southwestern quadrant, indicating significant oil drainage.

A large area of high oil saturation dominates the Northwestern quadrant of the simulation grid where Well B-19-5 has been shut-in since 1999, and where Well B-19-6 has been plugged and abandoned since 1992.

In the Northeastern quadrant, oil has been driven by the water injected into Well B-19-1 in the direction of production wells B-20-4 and B-20-5. Production wells B-19-7 and B-19-8, located in the lower part of the quadrant, also draw oil in their direction. The quadrant is dominated by low oil saturation, under the influence of these wells.

In the Southeastern quadrant, oil is driven in the direction of production wells B-19-16 and B-19-9, under the influence of the water injected into Well B-20-12.

Oil saturations are low near the CO_2 injection well, B-19-10#2, where oil has been mobilized by water, after the well was converted to a water injector on 3/25/2008, to establish the baseline of oil production for the CO_2-EOR pilot test.

Water and oil saturations, in the absence of CO_2, are complementary, so water saturations simply reflect the opposite of the oil saturation trends in the simulation grid, with low water saturations in the Northwestern and lower right corner of the Southeastern quadrants.

5.3.6 Visualization of Pilot Test Simulation Results for Phase Saturation at the End of the First CO_2 Injection

August 20, 2010 (day 10459) marks the end of the first 6804 t (7500 short tons) of CO_2 injection. The saturation distributions at this point are shown in Figure 5.10. The low oil saturation areas have decreased further and expanded in the Southwestern and

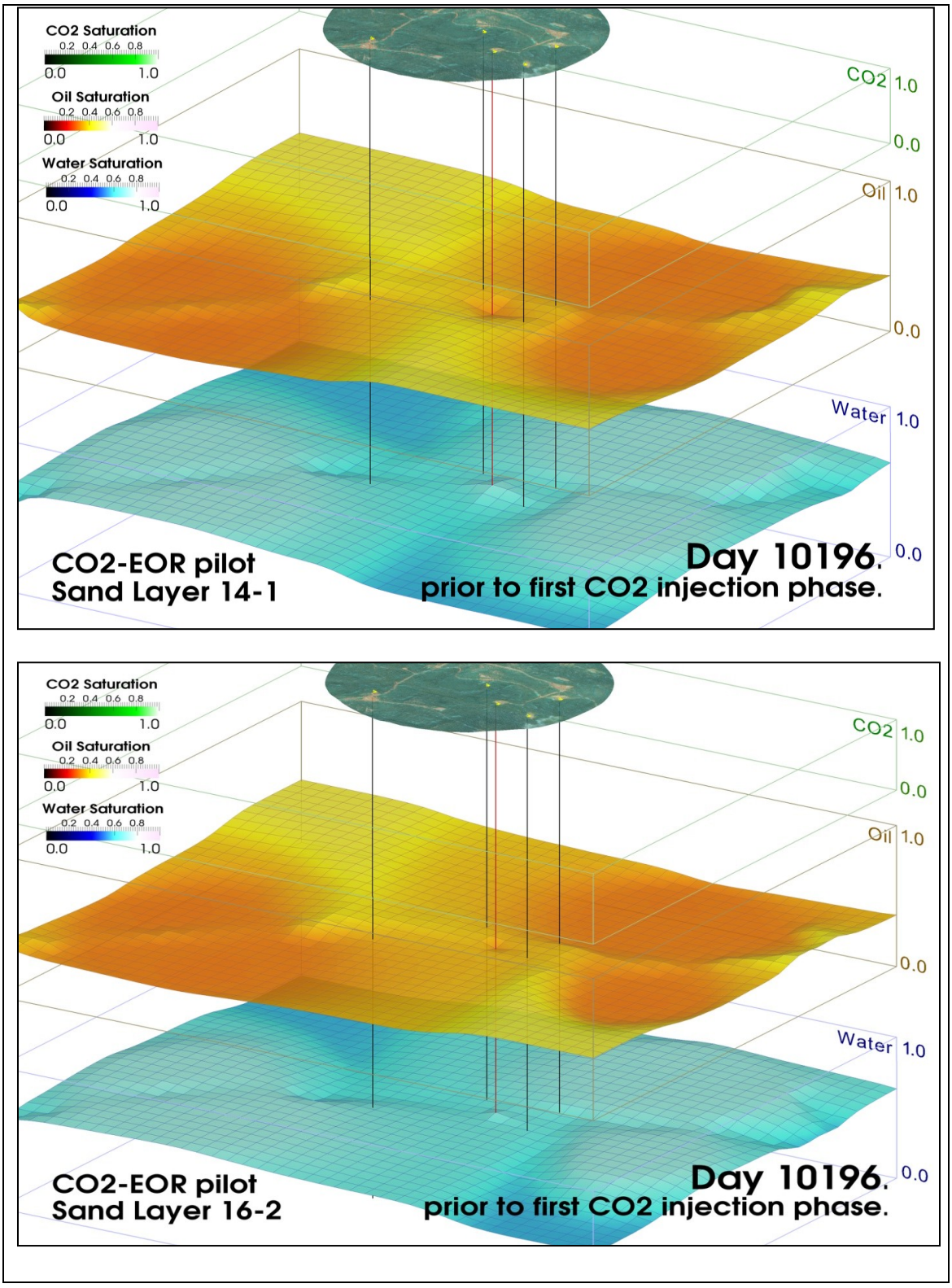

Figure 5.9. Oil and water saturations in Sands 14-1(top) and 16-2 (bottom), just before CO_2 injection on 11/30/2009. Upper right edges of the grids face North. Visualization by P. Corey Shum, UAB.

Northeastern quadrants. In these same quadrants, the high oil saturations along the pressure drawdown conduits from the water injection wells to the oil production wells are still evident.

The low and high oil saturation areas in the Northeastern quadrant have remained the same, except for an increase in oil saturation that has occurred near the oil production wells, B-20-4 and B-20-5, in Sand 16-2. Oil in the vicinity of the CO_2 injection well has been mobilized and has formed a high oil saturation front that appears as a circular ridge having a low oil saturation at its center, driven by the CO_2 injection into Well B-19-10#2.

Saturations of CO_2 have reached almost 100% in the vicinity of the injection well, and CO_2 breakthrough has occurred at Wells B-19-8 and B-19-9. The simulated breakthrough times (in August 2010) were near those observed in the field at both wells.

Water saturations decrease significantly as CO_2 displaces oil which, in turn, displaces water as the high oil saturation front is formed.

5.3.7 Visualization of Pilot Test Simulation Results for Phase Saturation at the End of the Interim Water Injection

April 27, 2011 (day 10709) marks the end of the interim water injection phase, which lasted 250 days. The distribution of CO_2, oil, and water saturations in Sands 14-1 and 16-2 at this stage are shown in Figure 5.11. The CO_2 front, driven by the injected water, has increased in size since the end of the CO_2 injection phase.

The high oil saturation front has also expanded in size, indicating continued mobilization of residual oil in the CO_2 sweep area, as the miscible oil-CO_2 phase is driven in the direction of the production wells by the injected water.

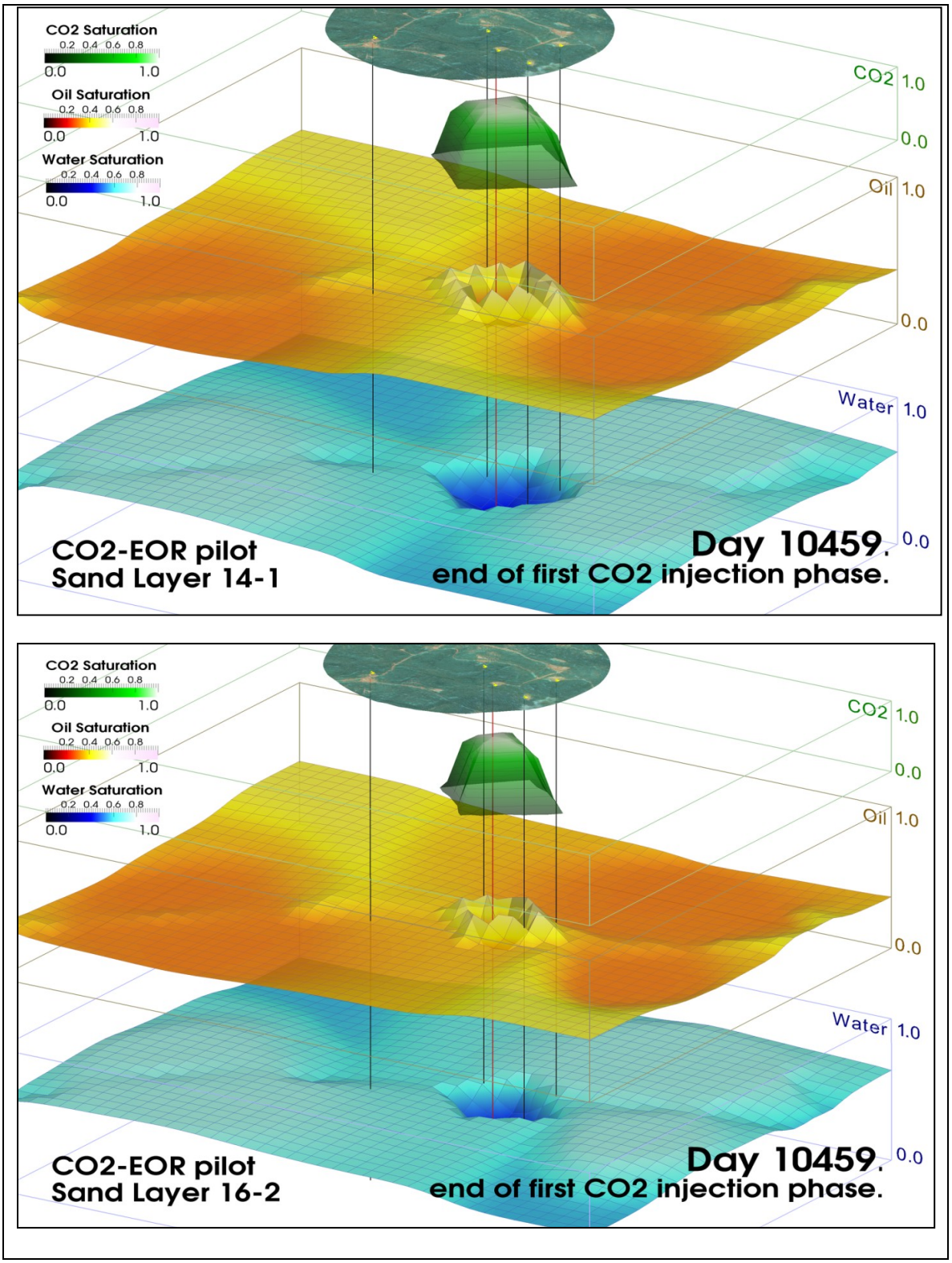

Figure 5.10. CO_2, oil, and water saturations in Sands 14-1(top) and 16-2 (bottom), at the end of the first CO_2 injection on 8/20/2010. Upper right edges of the grids face North. Visualization by P. Corey Shum, UAB.

Water has returned in the vicinity of the CO_2 injection well, filling the pore space left by the oil and the CO_2, with water saturations adjacent to the well reaching 100% in Sand 14-1.

5.3.8 Visualization of Pilot Test Simulation Results for Phase Saturation at the End of the Second CO_2 Injection

November 1, 2011 (day 10897) marks the end of the second CO_2 injection phase. The distribution of CO_2, oil, and water saturations in Sands 14-1 and 16-2 at this stage, are shown in Figure 5.12. The CO_2 front has further increased in size, while CO_2 saturations have increased near the injection well as newly injected CO_2 displaces water in the vicinity of the injector. However, water saturations in Sand 14-1 are higher at this stage than at the end of the first CO_2 injection phase (Figure 5.9), when water was first driven from the vicinity of the CO_2 injection well.

It appears that the second CO_2 injection has not been able to drive away the same volume of water as during the first CO_2 injection. This is not the case in Sand 16-2, where the second CO_2 injection drives the same volume of water away from the vicinity of the injection well as during the first CO_2 injection.

As shown in Figure 5.11, the very high fraction of water (82%) injected into Sand 14-1 during the interim water injection period displaces most of the CO_2 in the vicinity of the injection well. As a result, when CO_2 is injected, following the interim water injection, water saturations in the vicinity of the five-spot pattern, in Sand 14-1, do not decrease to the same level as at the end of the first CO_2 injection.

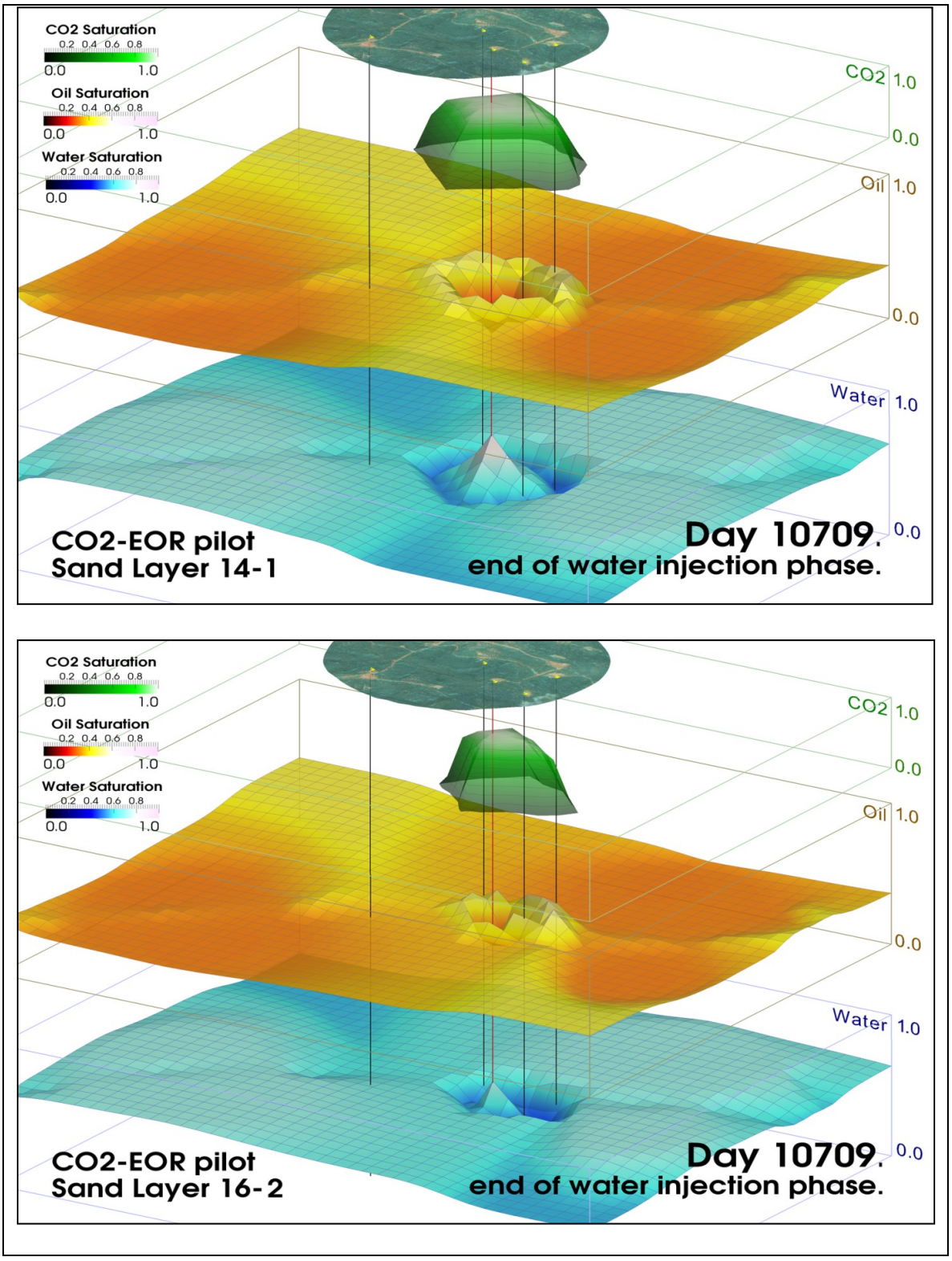

Figure 5.11. CO_2, oil, and water saturations in Sands 14-1 (top) and 16-2 (bottom), at the end of the interim water injection on 4/27/2011. Upper right edges of the grids face North. Visualization by P. Corey Shum, UAB.

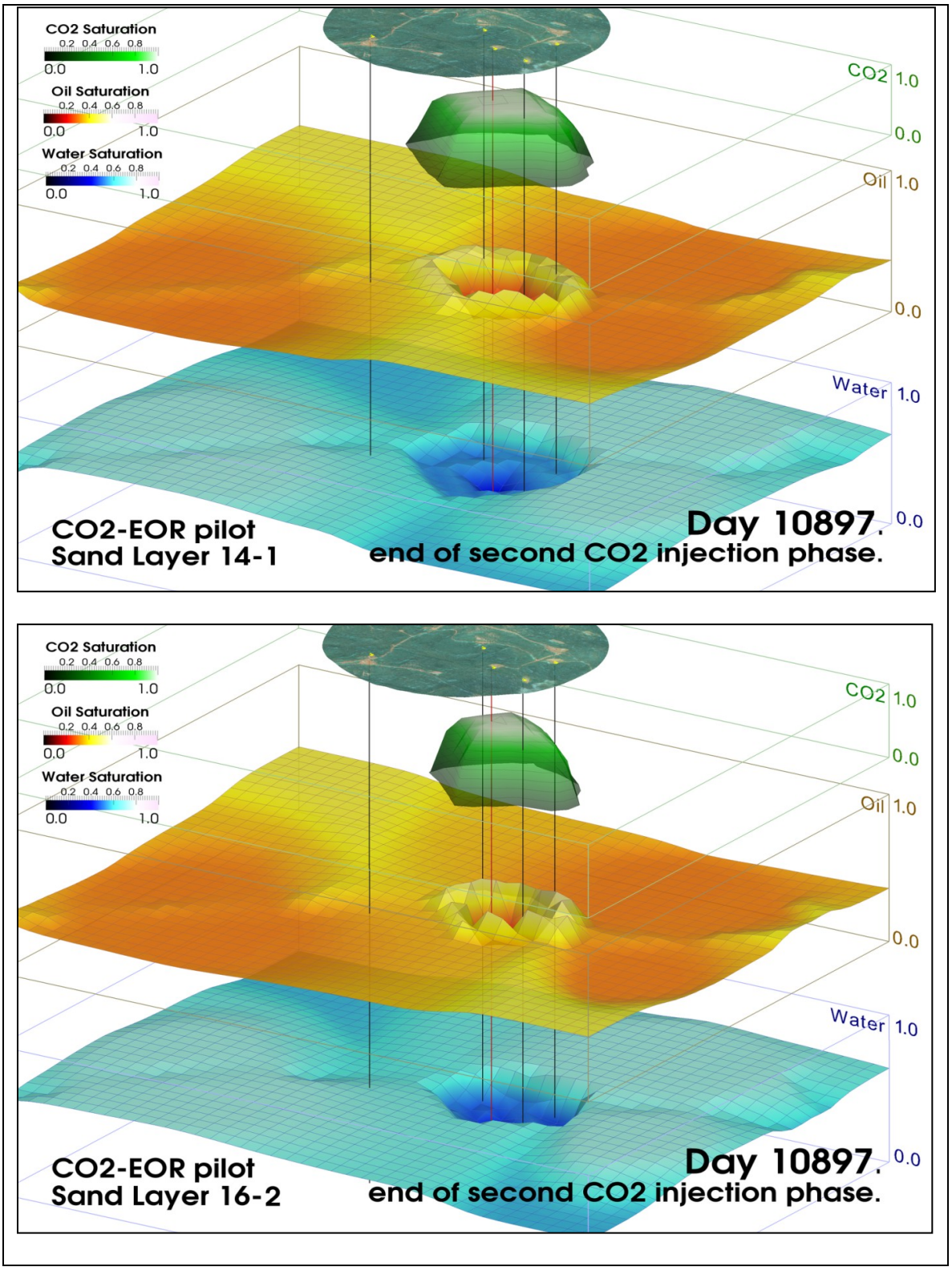

Figure 5.12. CO_2, oil, and water saturations in Sands 14-1 (top) and 16-2 (bottom), at the end of the second CO_2 injection on 11/1/2011. Upper right edges of the grids face North. Visualization by P. Corey Shum, UAB.

Very close to the injection well CO_2 has displaced nearly all of the water. The oil saturation peak has grown in size but the saturations themselves have decreased slightly, due to the expansion.

When considering all eight images of the simulation grid, shown in Figures 5.9, 5.10, 5.11, and 5.12, a distinct high oil saturation ridge is seen to run from the Southwest quadrant to Northeast quadrant intersecting the high oil saturation ridge in the vicinity of the injection well. The pattern is evident in both sands.

Prediction of the formation of a distinct high saturation oil bank, during the pilot test, is encouraging and suggests that a full scale CO_2-EOR project would mobilize significant incremental oil.

5.4 Pilot Test Simulation Results for Optimum Interim Water Injection Period

In the simulation time-line the first 6804 t (7500 short tons) of CO_2 injection into the hydrocarbon bearing Sands 14-1 and 16-2 was completed on 8/20/2010. Well B-19-10#2 was then converted from CO_2 to water injector. A set of simulations using MASTER 3.0 was conducted to identify the optimal interim water injection period, before the start of the second CO_2 injection.

The simulations utilized the 40- by 32-block grid and included the same cluster of wells used in the model for the CO_2-EOR pilot test. Simulations for Sand 14-1 were conducted separately from Sand 16-2. The allocation of injected CO_2 volume was 57% to Sand 14-1 and 43% to Sand 16-2, while the water allocations, were 82% and 18%, respectively. Reservoir porosity was 13.61% and permeability was 10 mdarcy.

Simulated CO_2 injection rates, during the first CO_2 injection phase, were matched with up-to-date field reported injection rates. In this simulation's time-line, the initial injection period of 6804 t (7500 short tons) of CO_2 was followed by a water injection period of varying length, in order to test its influence on oil production. The time intervals tested were 2, 4, 6, 8, 10, 12, and 18 months. Additionally, water-only and CO_2-only runs were included in the set for comparison. The water-only injection simulation provided the base-line that was needed to calculate incremental oil recoveries.

Water injection rates were set at 170 barrels per day, total for both sands, for all water injection time intervals tested. The rate was estimated from field measurements before CO_2 injection and was specified only for the rate-controlled injection well, B-19-10#2. All other wells were specified as pressure-controlled, and for water injectors the injection rates were calculated by the simulator, based on total fluid mobility within the grid block containing the well.

Results for daily oil production rates and cumulative oil recoveries under nine different water injection scenarios, are shown in Figures 5.13 and 5.14, respectively. The maximum oil production rate, and cumulative incremental oil recovery for each interim water injection scenario are summarized in Table 5.6.

When considering all three phases of the test, the curves for oil production rates, shown in Figure 5.13, indicate that production rates decrease as the water injection time interval increases. The curves, except for CO_2 and water-only, separate at the time when the second phase of 6804 t (7500 short tons) of CO_2 injection begins.

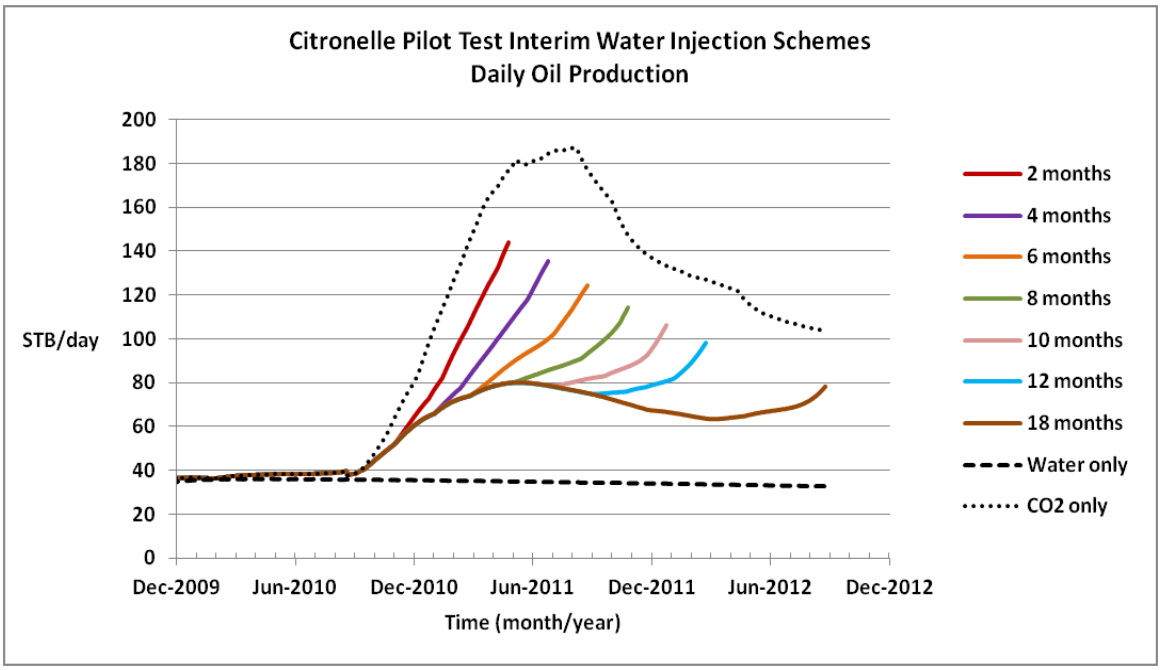

Figure-5.13. Simulated daily oil production for water injection intervals of varying duration, after the first 6804 t (7500 short tons) of CO_2 have been injected and before the second CO_2 injection begins. Water-only, and CO_2-only scenarios are also included.

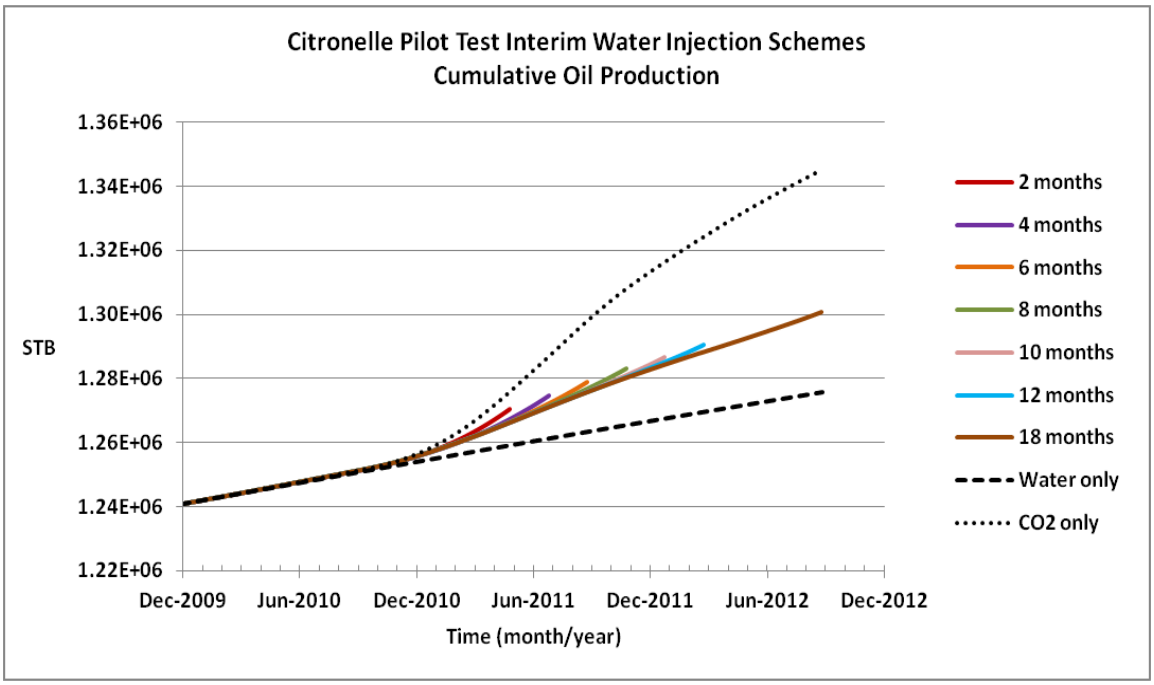

Figure 5.14. Simulated cumulative oil production for water injection intervals of varying duration, after the first 6804 t (7500 short tons) of CO_2 have been injected and before the second CO_2 injection begins. Water-only, and CO_2-only scenarios are also included.

When considering only the second phase of CO_2 injection, oil production rates increase in all cases, but at progressively slower rates, as the water injection time interval increases. When considering only the water injection phase, oil production rates increase for the 2, 4, 6, and 8-month water injection intervals, but decrease for the 10, 12, and 18-month water injection intervals. The highest oil production rate occurs at the end of the 8-month water injection interval (Table 5.6).

Table 5.6. Maximum oil production rates and cumulative incremental oil recovery for all interim water injection scenarios.

Interim water injection duration (months)	Maximum oil production rate during interim water injection period (STB/day)	Cumulative incremental oil recovery at the end of second CO_2 injection (STB)
0		4582
2	49.1	4319
4	63.8	3752
6	73.3	3190
8	79.6	2751
10	79.1	2499
12	75.7	2261
18	63.9	1536

Cumulative incremental oil, at the end of the second CO_2 injection, decreases as the water injection interval increases. When considering the second CO_2 injection, the largest increase in cumulative incremental oil occurs when the water injection interval is 2 months. The only scenario performing better is the continuous CO_2 injection with water

injection interval zero. As the water injection interval increases the cumulative incremental oil recovery decreases.

5.5 Simulation Results for 10-Year Water Alternating Gas Recovery Schemes

A series of simulations was conducted to investigate the performance of the oil field when CO_2 is injected under various WAG schemes for enhanced oil recovery. The simulations utilized the 40- by 32-block grid and the same wells in the extended pattern of previous simulations. As before, the fraction of CO_2 volume into Sand 14-1 was 57% while the fraction into Sand 16-2 was 43%. The fraction of injected water volume into Sand 14-1 was 82% and the fraction into Sand 16-2 was 18%. Sand porosity was 13.61% and permeability was 10 mdarcy.

All WAG schemes in the simulations followed immediately after the pilot test, and utilized the input parameters shown in Table 5.2. The CO_2 injection rate, into Well B-19-10#2, was set at 28.1 t/day (31 short tons/day) but follows the field reported daily injection rates during the pilot test period. The WAG simulations were run for 10 years.

Results for the oil production rate are shown in Figure 5.15, for *time-symmetric* WAG schemes, in which the water injection interval has the same duration as the CO_2 injection interval. Figure 5.16 shows *time-asymmetric* WAG schemes, in which the water injection interval is held constant at a period of 6 months, while the CO_2 injection interval ranges from a low value of 2 months to a high value of 24 months. Figures 5.17 and 5.18 show the cumulative oil production for the time-symetric and time-asymetric WAG schemes, respectively. Incremental oil recoveries for the various WAG schemes and volumes of CO_2 injected are summarized in Table 5.7.

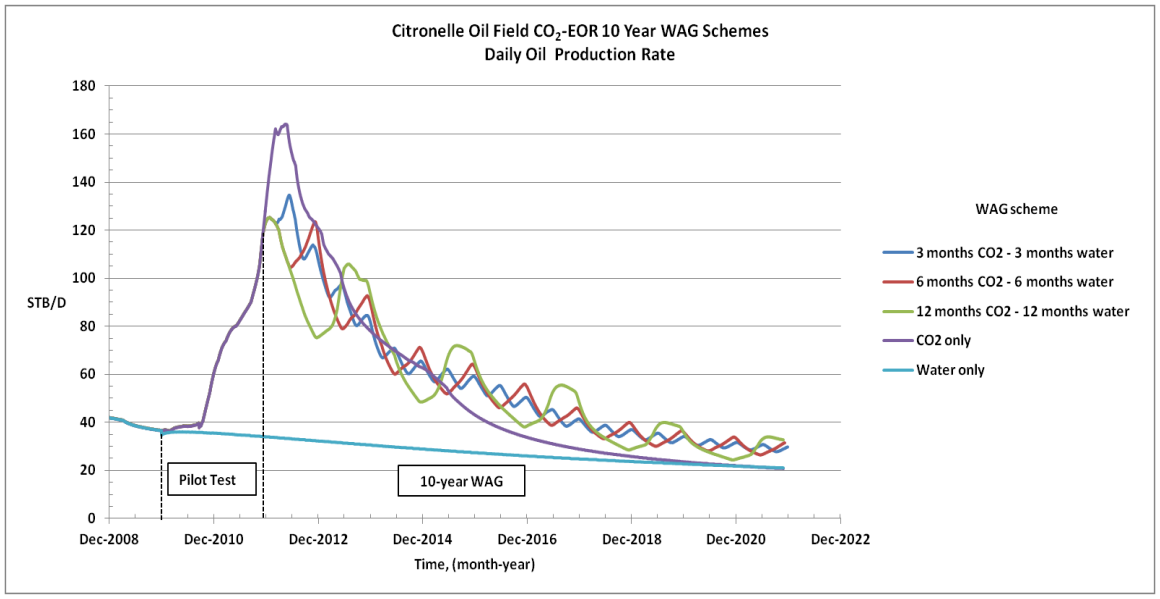

Figure 5.15. Simulated daily oil production rates for time-symmetric WAG schemes, in which the water and CO_2 injection intervals are of equal duration. Water-only and CO_2-only injection schemes are also included. WAG recovery follows immediately after the pilot test period. The CO_2 injection rate was 28.1 t/day (31 short tons/ day).

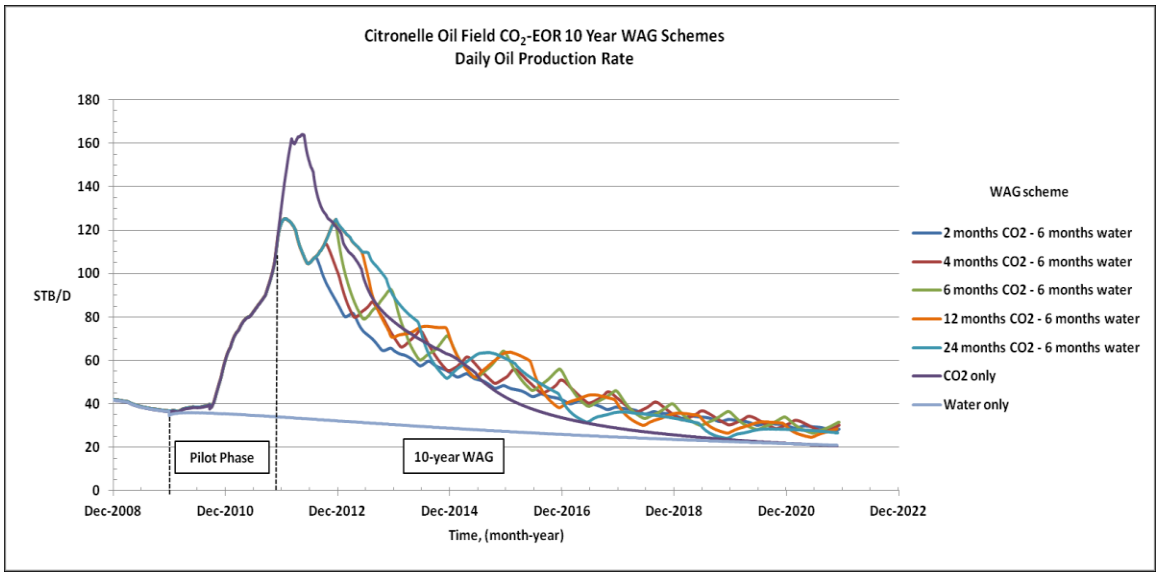

Figure 5.16. Simulated daily oil production rates for time-asymmetric WAG schemes, in which the water injection interval is held constant at 6 months while the CO_2 injection interval is progressively increased. Water-only and CO_2-only injection schemes are also included. WAG recovery follows immediately after the pilot test period. The CO_2 injection rate was 28.1 t/day (31 short tons/day).

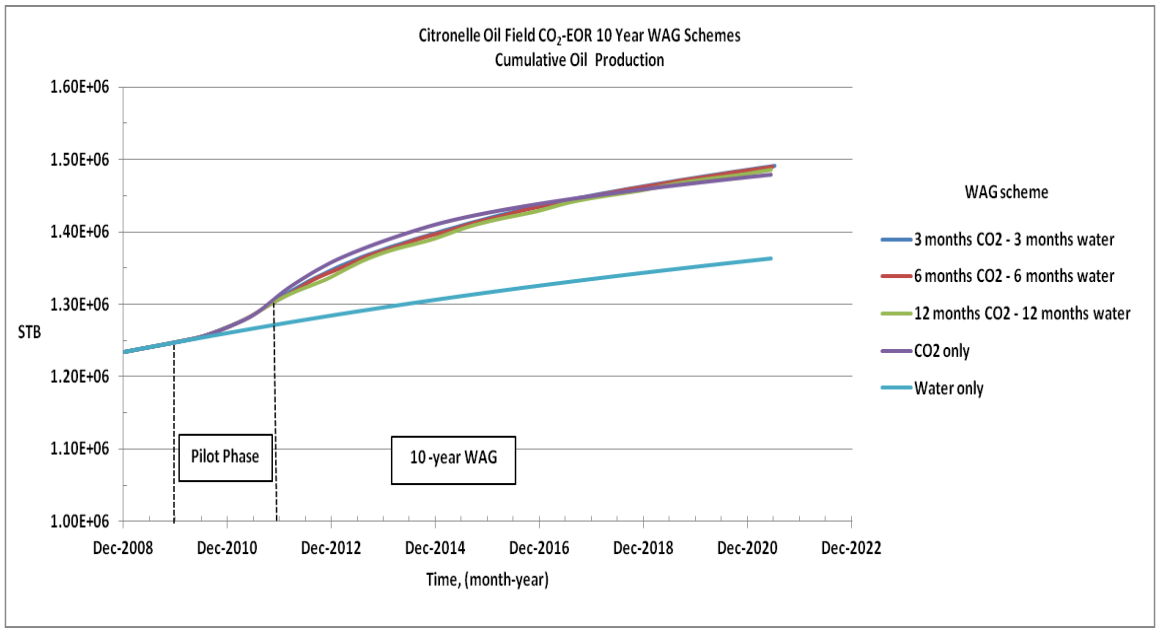

Figure 5.17. Simulated cumulative oil production for time-symmetric WAG schemes, in which the water and CO_2 injection intervals are of equal duration. Water-only and CO_2-only injection schemes are also included. WAG recovery follows immediately after the pilot test period. The CO_2 injection rate was 28.1 t/day (31 short tons/ day).

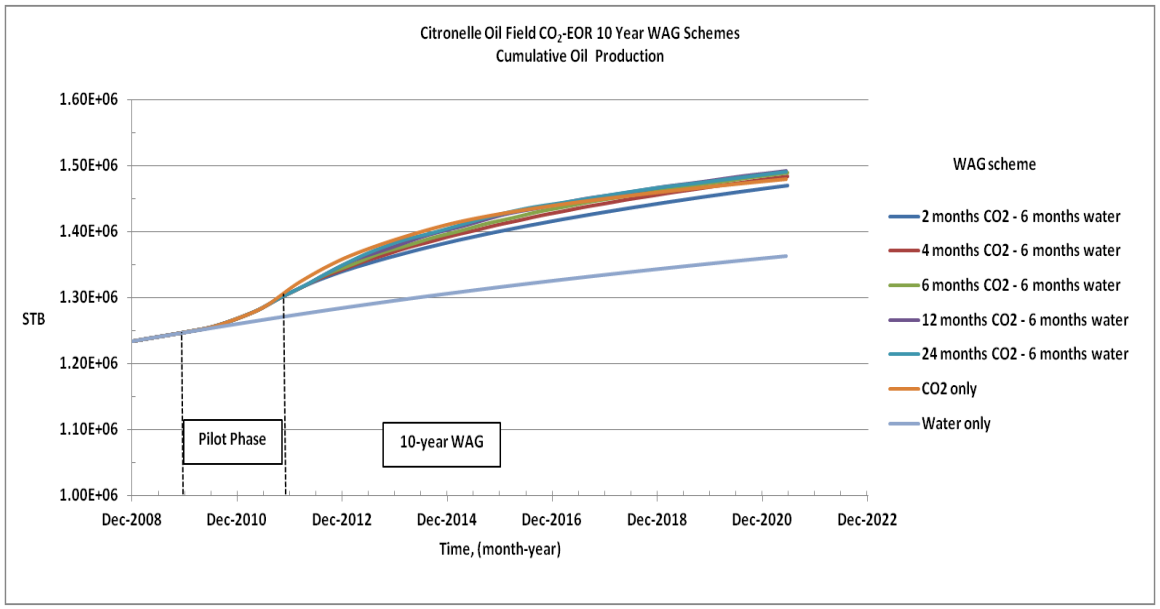

Figure 5.18. Simulated cumulative oil production for time-asymmetric WAG schemes, in which the water injection interval is held constant at 6 months while the CO_2 injection interval is progressively increased. Water-only and CO_2-only injection schemes are also included. WAG recovery follows immediately after the pilot test period. The CO_2 injection rate was 28.1 t/day (31 short tons/day).

Symmetric WAG schemes are better performing alternatives to continuous CO_2 injection particularly, after 5 to 6 years of injection time, as shown in Figure 5.15. For asymmetric WAG schemes oil recovery increases as the length of the CO_2 injection interval increases, as shown in Figure 5.16. However, this pattern reaches a point of maximum return and begins to decline when the CO_2 injection interval reaches 24 months. Continuous CO_2-only injection yields the best production rates at short times, but it declines more rapidly and begins lagging all other WAG schemes after about 5 or 6 years, as shown in both figures.

The WAG scheme demonstrating the best incremental oil recovery over the 10-year period, considering both symmetric and asymmetric schemes, is the asymmetric scheme of 12 months of CO_2 followed by 6 months of water, as shown in table 5.7. That scheme produced an incremental oil recovery of 128,735 Stock Tank Barrels (STB), over 10 years. Three other WAG schedules (3 months CO_2–3 months water, 6 months CO_2–6 months water, and 24 months CO_2–6 months water) exhibit similar performance. The optimal time-symmetric WAG scheme is 3 months of CO_2 injection followed by 3 months of water injection. Continuous CO_2 injection underperforms all WAG schemes except 2 months of CO_2 followed by 6 months of water.

Figures 5.17 and 5.18 indicate that cumulative oil production does not vary significantly under the WAG schemes investigated. For example, the difference in incremental oil recovery between the highest yielding (128,735 STB) and next highest (127,675 STB) WAG schemes, is only 1060 STB over 10 years. However, the incremental recoveries reported are for a single well producing from only two sands, and this difference would be magnified in a field-wide CO_2-EOR application. Assuming, for

example, that the field-wide CO_2-EOR incorporates 150 producer wells and 25 sands, a difference of 1060 STB could result in an additional 3,975,000 STB of oil recovered under the highest yielding WAG scheme.

5.6 Simulation Results for 10-Year Water Alternating Gas Recovery Schemes Using Variable Injection Rates

Carbon dioxide injection rates during the first phase of the CO_2-EOR pilot test varied from 27.21 t/day (30 short tons/day) to 40.82 t/day (45 short tons/day), eventually stabilizing near 31.75 t/day (35 short tons/day). A set of simulations was performed to assess the effect of daily variation in CO_2 injection rate on incremental oil recovery.

The simulations were based on the following scenario: A total volume of 74,503 t (82,125 short tons) of CO_2, equivalent to an average rate of 40.82 t/day (45 short tons/day) for five years, was injected into Sands 14-1 and 16-2. The CO_2 was injected at rates 18.1, 27.2, 31.8, 36.3, 40.8, 49.9, and 54.4 t/day (20, 30, 35, 40, 45, 55, and 60 short tons/day) and the incremental oil recovery was recorded for each injection rate.

The allocation of injected CO_2 was 57% to Sand 14-1 and 43% to Sand 16-2. The allocation of water injection was 82% to Sand 14-1 and 18% to Sand 16-2. A 6 month CO_2–6 month water WAG scheme was implemented at all injection rates, with adjustment of the number of gas-water cycles to accommodate the planned volume of CO_2. The 40- by 32-block simulation grid included the same cluster of producer and injector wells as in previous CO_2-EOR pilot test simulations. Permeability was 10 mdarcy, and porosity 13.61%. The response of incremental oil recovery to changes in CO_2 injection rate, is shown in Figure 5.19.

Table 5.7. Oil production and CO_2 utilization for WAG scenarios using symmetric schemes, GROUP 1, and asymmetric schemes, GROUP 2.

WAG Scenario	Results				
		GROUP 1	**Symmetric (water interval = CO_2 interval)**		
WAG injection scenario (total time is 10 years)	**EOR oil, STB**	**EOR incremental oil, STB**	**CO_2 injected, 1000 scf**	**CO_2 recovered, 1000 scf**	**Net CO_2 in place, 1000 scf**
3 months CO_2 - 3 months water	249,806	127,675	1,466,125	909,727	556,398
6 months CO_2 - 6 months water	248,394	126,263	1,466,125	900,141	565,984
12 months CO_2 - 12 months water	244,668	122,537	1,466,125	887,508	578,617
		GROUP 2	**Asymmetric (water interval ≠ CO_2 interval)**		
WAG injection scenario (total time is 10 years)	**EOR oil, STB**	**EOR incremental oil, STB**	**CO_2 injected, 1000 scf**	**CO_2 recovered, 1000 scf**	**Net CO_2 in place, 1000 scf**
2 months CO_2 - 6 months water	228,837	106,706	858,250	426,804	431,446
4 months CO_2 - 6 months water	243,275	121,144	1,223,015	701,774	521,241
6 months CO_2 - 6 months water	248,394	126,263	1,466,125	900,141	565,984
12 months CO_2–6 months water	250,866	128,735	1,830,826	1,253,621	577,205
24 months CO_2–6 months water	249,133	127,002	2,195,565	1,578,381	815,506
CO_2 - only	238,607	116,476	2,681,905	2,114,059	567,846
Water - only	122,131	0	0	0	0

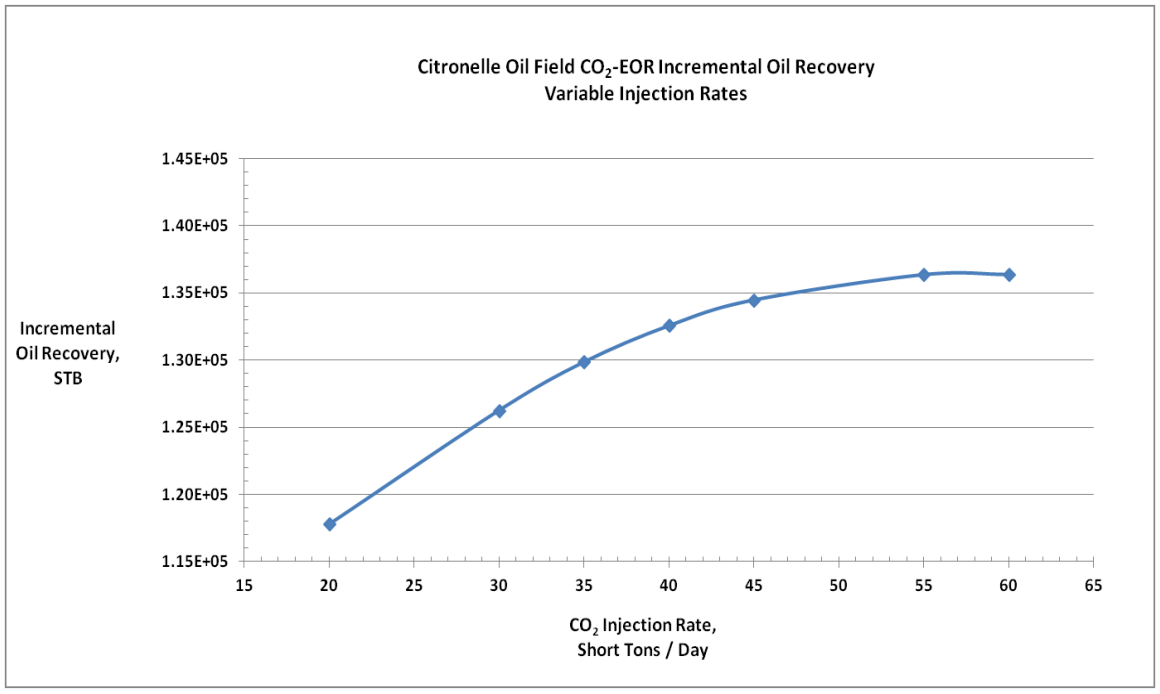

Figure 5.19. Incremental oil recovery at CO_2 injection rates of 18.14, 27.21, 31.75, 36.29, 40.82, 49.90, and 54.43 t/day (20, 30, 35, 40, 45, 55, and 60 short tons/day). A total of 74,503 t (82,125 short tons) of CO_2 was injected in all cases, under a symmetric WAG scheme of 6 months of CO_2 followed by 6 months of water, immediately following the pilot test period.

Incremental oil recovery increases more rapidly at low injection rates, between 18.1 and 31.8 t/day (20 and 35 short tons/day), and begins to taper off above 49.9 t/day (55 short tons/day). The maximum incremental oil recovery occurs at 49.9 t/day (55 short tons/day). The range of operation from 27.2 to 40.8 t/day (30 to 45 short tons/day) represents a difference of approximately 8000 STB of oil recovered for the same volume of injected CO_2.

Daily oil production curves are shown in Figure 5.20 and cumulative oil production curves are shown in Figure 5.21. Incremental oil recovery is based on the

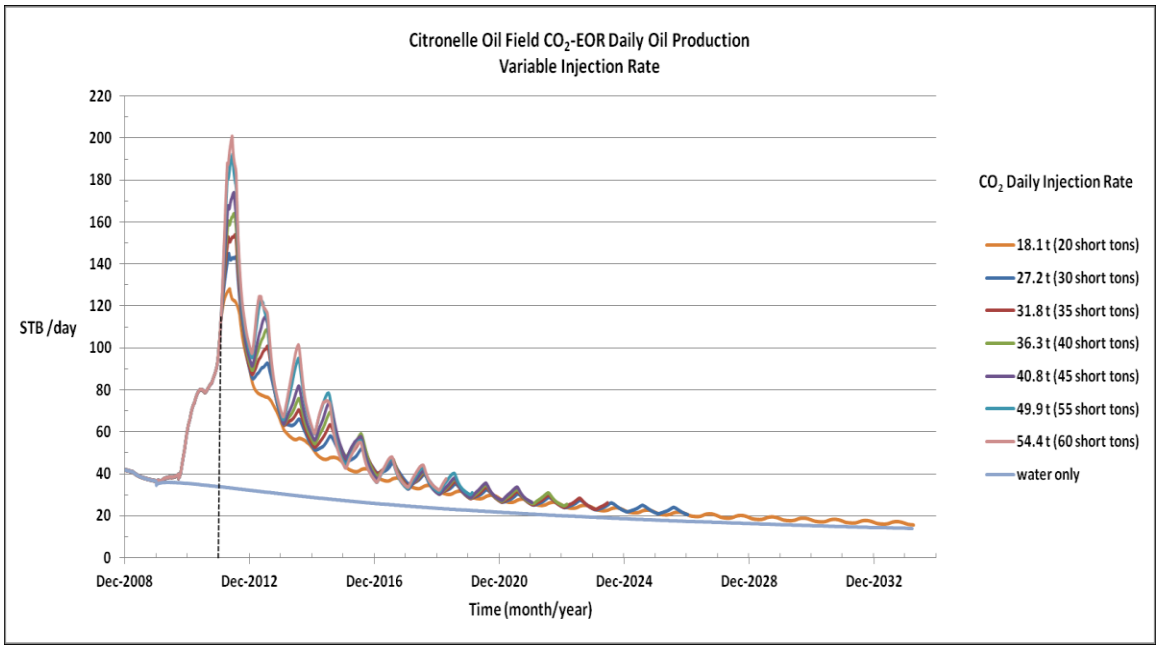

Figure 5.20. Daily oil production at CO_2 injection rates of 18.1, 27.2, 31.8, 36.3, 40.8, 49.9, and 54.4 t/day (20, 30, 35, 40, 45, 55, and 60 short tons/day). A total of 74,503 t (82,125 short tons) of CO_2 was injected in all cases, under a symmetric WAG scheme of 6 months of CO_2 followed by 6 months of water, immediately following the pilot test period, indicated by the vertical dashed line in the figure.

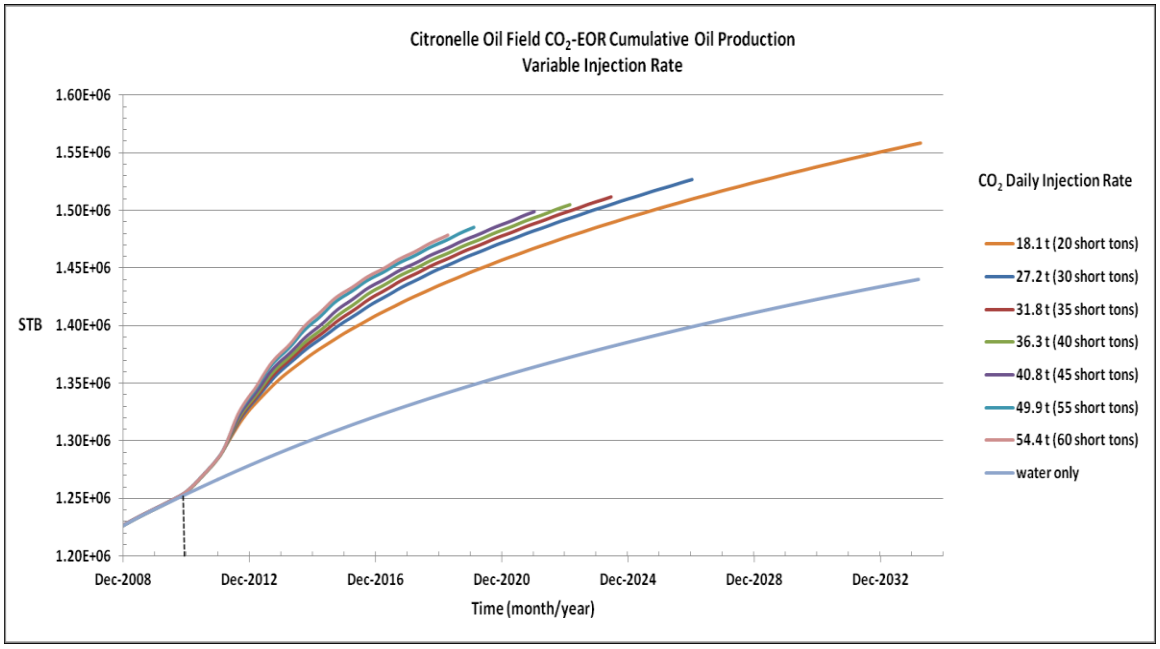

Figure 5.21. Cumulative oil production at CO_2 injection rates of 18.1, 27.2, 31.8, 36.3, 40.8, 49.9, and 54.4 t/day (20, 30, 35, 40, 45, 55, and 60 short tons/day). A total of 74,503 t (82,125 short tons) of CO_2 was injected in all cases, under a symmetric WAG scheme of 6 months of CO_2 followed by 6 months of water, immediately following the pilot test period, indicated by the vertical dashed line in the figure.

difference between cumulative oil recovery under a given scenario and the cumulative recovery under continuous water injection.

The daily oil production curves of Figure 5.20 indicate that, as the CO_2 injection rate increases, the daily oil production increases during the first five WAG cycles (5 years). After the fifth WAG cycle, the production curves have equal amplitudes, with the exception of the 18.1 t/day (20 short tons/day) curve which has the smallest amplitude. Cumulative oil production increases as the CO_2 injection rate decreases, as shown in Figure 5.21, suggesting that smaller CO_2 injection rates yield higher cumulative recovery.

5.7 Simulation Results for 10-Year Water Alternating Gas Recovery Based on Updated Field Data

The simulations presented in the previous sections were based on empirical and estimated input parameters, gathered from a variety of sources, old and recent. The various teams participating in the consortium described in Section 5.1 have been periodically reporting results of their work and revising and updating their measurements and conclusions as the project moves forward.

As part of their research effort, Peter Clark and his group at the University of Alabama obtained and reported an oil–CO_2 MMP in the range, 2340 ± 250 psig (Peter E. Clark, personal communication, 2011). The results were obtained using a rolling ball viscometer designed and built by the group, on samples of oil collected from the Citronelle field. In the simulations conducted in the previous sections, the MMP was set to 2800 psi (Gilchrist, 1981).

An injection profile test, run on injection Well B-19-10#2 in January 2012, established that 35% of the flow of water is to Sand 14-1, and 65% is to Sand 16-2. In the simulations described in the previous sections, the allocation of water was 82% to Sand 14-1 and 18% to Sand 16-2, based on a test performed before the CO_2 injection.

In order to investigate the influence of the updated water flow allocation and MMP on oil production, a set of simulations was performed using the optimal WAG scenario of 12 months of CO_2 followed by 6 months of water injection, discussed in Section 5.5. All other input parameters were kept the same.

Results of the simulations are shown in Figure 5.22 for the oil production rate, and in Figure 5.23 for cumulative oil production. Daily oil production is lower for the 35%–65% split of water flow, in the earlier part of the pilot test, but the trend reverses at longer times. There is no significant net oil production gain from chosing one water flow distribution over the other, as shown in Figure 5.23.

The maximum difference in daily oil production between the two curves in Figure 5.22 is approximately 10 STB/day. However, the reversal in the positions of the curves several times during the 10-year WAG nulifies any gain of one water distribution over the other. The zero net gain is best illustrated by comparison of the two curves for cumulative oil, shown in Figure 5.23. There is almost no distinction between the two cumulative oil curves, suggesting minimal influence on the results of the simulations

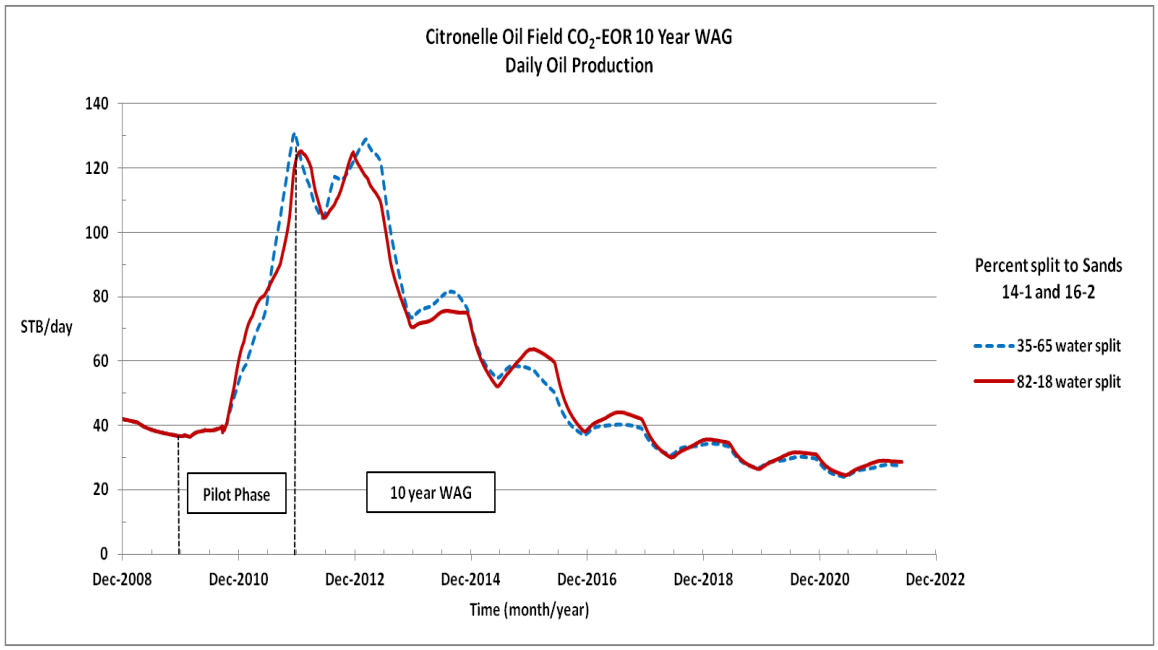

Figure 5.22. Daily oil production during a 10-year WAG, with each cycle consisting of 12 months of CO_2 injection followed by 6 months of water injection. The dashed curve represents a water flow split of 35% to Sand 14-1 and 65% to Sand 16-2. The solid curve represents a water flow split of 82% to Sand 14-1 and 18% to Sand 16-2.

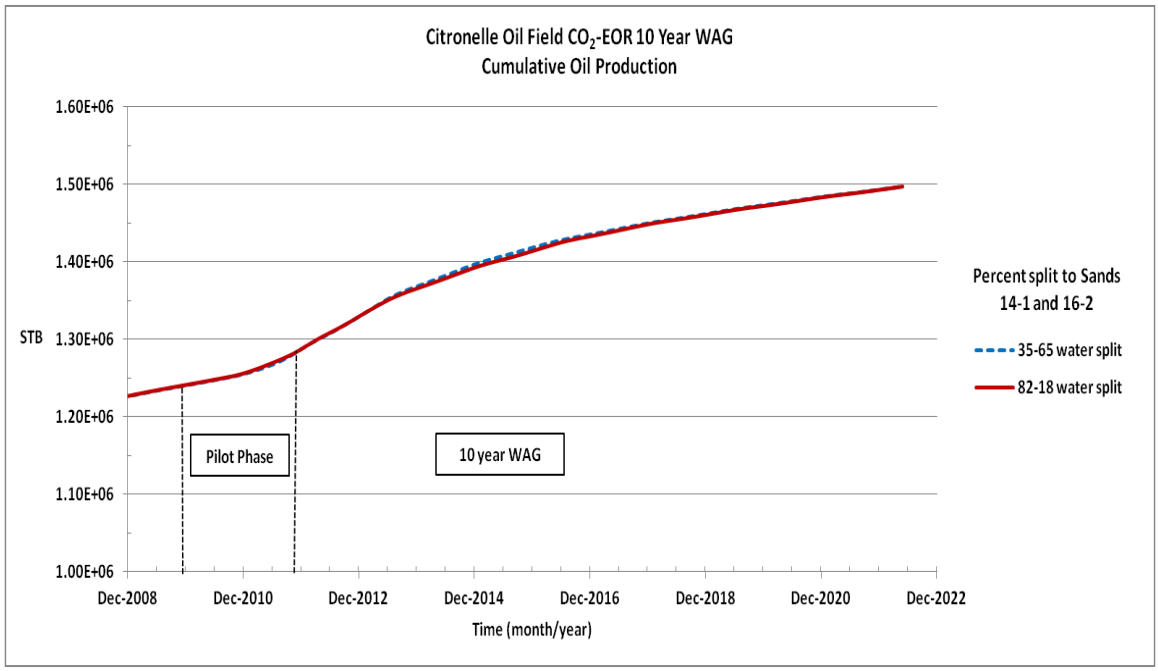

Figure 5.23. Cumulative oil production during a 10-year WAG, with each cycle consisting of 12 months of CO_2 injection followed by 6 months of water injection. The dashed curve represents a water flow split of 35% to Sand 14-1 and 65% to Sand 16-2. The solid curve represents a water flow split of 82% to Sand 14-1 and 18% to Sand 16-2.

using the updated distribution of water. This in turn increases confidence in the results produced by the simulations in the previous sections.

5.8 Citronelle Pilot Test Field Operations

The following subsections describe field conditions, events, and results during and after the CO_2-EOR pilot test at Citronelle.

5.8.1 The CO_2 Storage Tank, Pumps, and Tank Batteries

A 50-ton liquid CO_2 storage tank, charge pump, and triplex plunger positive displacement pump are located at the B-19-8 Tank Battery (Figure 5.3). Oil produced from three wells in the test pattern (B-19-7, B-19-8, and B-19-9) is gathered, along with production from five other wells to the north and east, at Tank Battery B-19-8. Produced oil from well B-19-11 in the test pattern goes to Tank Battery B-19-11, along with production from three other wells to the west and south (Figure 5.3).

Both tank batteries are equipped with gas-liquid cylindrical cyclone separators, to separate produced oil and water from gas. Oil and water are collected, but the gas, which is primarily CO_2, because of the unusually low gas yield from Citronelle oil, is vented.

The flow meters installed to measure power oil and produced fluid flow rates going to and from the production wells were found not to have sufficient resolution to distinguish the power oil and produced fluid flow rates (4–9 bbl/day of produced oil versus 450–500 bbl/day of power oil per well).

5.8.2 Carbon Dioxide Injection

After the first delivery of CO_2 on March 2, 2009, a number of problems were encountered during attempts to begin CO_2 injection. In spite of several rounds of improvements to the pumping system during this early period, steady, continuous CO_2 injection could not be maintained for more than a short time. The problem was traced to vapor-lock in the positive displacement pump, due to dead space around the plunger and between the inlet and outlet valves. The dead space was allowing the CO_2 to compress, which created a temperature spiral until eventually the CO_2 vaporized between the valves and would stop pumping. This problem was solved by fabricating and installing Teflon sleeves to fill the dead space. After also implementing a low-flow shut-down system to protect the triplex pump, should vapor-lock reoccur, CO_2 injection began around-the-clock at the test site on December 22, 2009. The injection rate settled at 42.2 t/day (46.5 short tons CO_2/day).

However, after a short period of trouble-free operation at the injection rate of 42.2 t/day (46.5 short tons CO_2/day), problems with the triplex pump surfaced again, due to damage of the Teflon sleeves, which had been installed to minimize dead volume in the pump, to prevent vapor-lock. In spite of these problems, injection continued, with constant attention and maintenance to the pump, for about 11 hours per day. Approximately 18 t (20 short tons) of CO_2 were typically injected each day; equal to slightly more than half of the anticipated minimum rate of 31.8 t/day (35 tons/day). After improving the design of the Teflon sleeves and repairing a tubing leak during January 2010, continuous injection of CO_2 was maintained, at an average rate of 28.1 t/day (31 short tons/day), including down time for maintenance, to the end of September 2010. The total amount of CO_2 injected was 7290 t (8036 short tons).

5.8.3 Response to CO_2 Injection

From March to December 2009 B-19-8 Tank Battery had been experiencing an average decline in oil production of 20 bbl/day/year. Beginning in January 2010, coinciding with the start of continuous CO_2 injection, the decline in production was reversed, and, from January to September 2010, when the CO_2 injection was complete, oil production increased at the average rate of 18 bbl/day/year.

However, in October 2010, following the return to water injection, oil production began to decline. The decline accelerated in subsequent months, dropping, by March 2011, to only 36% of the rate at the September 2010 peak and to less than half of the rate just before the start of CO_2 injection. One reason for the decline was the frequency with which the power oil pumps in wells whose fluids are gathered at B-19-8 Tank Battery had to be pulled because of excessive wear due to contamination of the power oil with particles mobilized by CO_2. The frequency of pump pulls had begun to increase in August 2010, just before the end of the CO_2 injection, and increased by approximately a factor of ten from July 2010 to January and February 2011, when oil production approached its lowest point. As they were pulled, the pumps were replaced by new ones having longer stroke and parts made from harder material, so the frequency of pump maintenance began to decline in February 2011 and there was a corresponding increase in oil production over the next 12 months, to 44 bbl oil/day in March 2012.

The recent average rate (March 2013) of 38 bbl oil/day is lower than the peak rate of 59 bbl oil/day recorded in September 2010 and slightly less than the rate of 45 bbl oil/day just before the start of CO_2 injection in December 2009, but it is significantly

higher than the decline curve established during the 10 months from March to December 2009, prior to CO_2 injection.

The response to CO_2 injection at B-19-11 Tank Battery was quite different from that observed at B-19-8 Tank Battery. In contrast to the immediate increase in oil production observed at B-19-8 Tank Battery, production at B-19-11 Tank Battery continued for four months on the trajectory that it had been following for the previous 10 months. Then, coinciding with breakthrough of CO_2 at Well B-19-11, production at the battery abruptly declined, by approximately the typical production from Well B-19-11 (8 to 9 bbl/day), then continued a steady decline, with no significant response to the termination of CO_2 injection and return to water injection in September 2010.

The estimate of incremental oil production at Tank Battery B-19-8, to March 31, 2013 is 17,664 bbl and the estimate of the incremental deficit in oil production at Tank Battery B-19-11 is -16,664 bbl, giving a net positive cumulative incremental production, of 1000 bbl.

A second reason for the decline in oil production, beginning at the end of the CO_2 injection and return to water injection in September 2010, is that the water injection rate, which had been 170 bbl water/day before CO_2 injection, decreased to approximately 60 bbl water/day and remained, except for occasional spikes, at this low level. An injection profile test run on the injector in January 2012 established that 35% of the water flow is to Sand 14-1 and 65% is to Sand 16-2, so neither injection zone is completely blocked.

On May 25, 2010, five months after continuous CO_2 injection began, high pressure was detected in the vertical oil/water separator at B-19-11 Tank Battery, where

produced fluids from Well B-19-11 are collected. Well B-19-11 is the producer in the southwest corner of the test pattern, farthest from the injector. Close agreement of the Delta carbon-13 isotope ratio in CO_2 ($\delta^{13}CO_2$) in a sample of produced gas with the isotope ratio in injected CO_2, showed that the CO_2 in produced gas at B-19-11 was breakthrough from CO_2 injection at Well B-19-10 #2. Rapid breakthrough of CO_2 was unexpected, because no evidence of natural fractures had ever been observed in drill core from Citronelle Sands by Jack C. Pashin and his coworkers at the Geological Survey of Alabama (personal communication, 2010). Records also indicate that Well B-19-10 #2 had never been intentionally hydraulically fractured.

Produced gas samples were collected again on August 4, 2010 for comparison of the composition of produced gas from all four producers in the test pattern with the analysis of injected CO_2, from the storage tank. It was found that the gas from one well, B-19-7, had approximately the same CO_2 content as gas from all of the wells before CO_2 injection began, and its low value (large negative number) for $\delta^{13}CO_2$ is characteristic of Citronelle solution gas. The CO_2 and $\delta^{13}CO_2$ analyses for the other wells show that the order of CO_2 breakthrough at the producers was B-19-11, B-19-9, then B-19-8.

Produced gas from wells both inside and outside the test pattern was then monitored for increased CO_2. Breakthrough was detected at Well A-25-10, far to the southwest of the injector, providing evidence for distant travel of CO_2 across depositional trends.

Testing to determine the cause of low injectivity to water, following the CO_2 injection, began with a pressure-transient injection and fall-off test, from November 28 to

December 12, 2011. The results from that test were analyzed by Eric Carlson and indicated that there is a substantial hydraulic fracture originating at the injector, having a total length of 183 to 305 m (600 to 1000 ft) (Eric S. Carlson, personal communication, 2012). The pressure-transient test does not provide any information about the direction of the fracture, but the most likely direction is that of maximum horizontal compressive stress in the Southeastern U.S., typically N70E to N80E (Jack C. Pashin, personal communication, 2012). Two of the wells at which early breakthrough of CO_2 was detected lie on the line at N69E relative to the injector. The other two wells at which early breakthrough was detected lie on the line at N44E relative to the injector.

The following are likely conclusions: (a) a hydraulic fracture along the direction of maximum horizontal compressive stress was opened by water or CO_2 injection into Well B-19-10 #2; and (b) the fracture provided a preferential pathway for CO_2, compromising the sweep efficiency of CO_2 in the pilot test.

Surfactant was added to the water at the injector, Well B-19-10 #2, to determine if the low injectivity to water, following the CO_2 injection, is due to capillary effects. The water injection rate responded almost immediately to the surfactant, increasing from 50 bbl water/day on July 23–25, 2012 to 80–120 bbl water/day from August 8 to 14, 2012. The water injection rate from September 26 to October 12, 2012 reached 100 to 150 bbl water/day, with an average of 120 bbl water/day, so the injection rate had then recovered approximately 55% of its initial loss following CO_2 injection. The ability of the surfactant to increase injectivity indicates that capillary pressure at the interfaces between water or brine and CO_2 trapped in pores is the likely cause of at least part of the loss in injectivity.

Understanding of these observations has significant bearing on the design and management of a commercial CO_2 flood at Citronelle.

CHAPTER 6

SIMULATION OF CO_2 SEQUESTRATION IN THE MIDDLE DONOVAN SANDS

6.1 Introduction

Sequestration of CO_2 in Middle Donovan, is an auxiliary component of the CO_2-EOR operations in the Upper and Lower Donovan. Interruptions during CO_2-EOR operations in Upper and Lower Donovan may require interim injection of CO_2 into the Middle Donovan Sands to avoid venting CO_2 from a separation plant. If interim CO_2 injection is to be considered as an option, it is necessary to assess the potential of the Middle Donovan Sands as CO_2 sinks. The present chapter, however, investigates the feasibility of a broader CO_2 injection scenario into the Middle Donovan Sands. The broader scenario considers continuous CO_2 injection into the Middle Donovan Sands during the 10-year CO_2-EOR in the Upper and Lower Donovan, followed by an additional 30 years of continuous CO_2 injection.

The broader scenario allows for a more comprehensive investigation of the Middle Donovan Sands' potential, to accommodate 40 years of continuous CO_2 injection and long-term sequestration. Implicit in the investigation of this broader scenario, is the feasibility of using the Middle Donovan as a sink, during CO_2-EOR operations in the Upper and Lower Donovan.

Investigating the feasibility of the broader scenario for CO_2 injection and sequestration in the Middle Donovan Sands, required the use of the simulators TOUGH2-ECO2N, and TOUGHREACT, already described in Section 3.3.2. A set of simulations was performed using the simulator TOUGH2-ECO2N, to assess the near-term (100 years) effects and fate of the injected CO_2. A separate set of simulations was performed using the simulator TOUGHREACT, to assess the long-term (10,000 years) effects, as well as to investigate possible chemical-mineralogical reactions induced by the presence of CO_2 in the formation.

6.2 Model Specifications

All simulations of CO_2 injection into the Middle Donovan Sands were performed employing a two-dimensional symmetric radial grid with a single CO_2 injection well at the center. The radius of the grid extended to a large distance of 100,000 m (328,084 ft) from the injection well, to assure that the simulated system could maintain constant pressure at the boundary (acting as an infinite reservoir). The radius of the well was 0.07 m (0.23 ft), and the grid block length was increased progressively, with increasing distance from the wellbore, according to a logarithmic rule calculated by the simulator internally. The progressive increase in grid block length provided sufficient resolution of the injection process near the high pressure well-bore region, while maintaining constant pressure at the boundary.

Table 6.1 summarizes the primary input variables, corresponding values, and the sources utilized in all of the simulations of CO_2 injection into the Middle Donovan Sands.

The simulations were performed under isothermal conditions, and assumed the formation was homogeneous and isotropic. Gravity and inertial effects were neglected.

Table 6.1 indicates a Middle Donovan formation temperature of 98.9 °C (210 °F), and pressure of 34 MPa (4931.3 psi), suggesting that CO_2 in the formation will remain in the supercritical state, well above the critical temperature of 31.1 °C (87.98 °F) and pressure of 7.39 MPa (1071.8 psi).

Table 6.1. Primary input variables for the TOUGH2-ECO2N simulations of CO_2 injection into the Middle Donovan.

Primary Variable	Value	Source
Effective formation thickness	27.6 m (90.5 ft)	Esposito et al., 2008
Porosity	13%	Esposito et al., 2008
Permeability	13 mdarcy	Esposito et al., 2008
Formation pressure	34 MPa (4931.3 psi)	Calculated hydrostatic
Formation temperature	98.9 °C (210 °F)	Esposito et al., 2008
NaCl fraction in brine	10 wt%	Personal communication with Dr. J. C. Pashin, 2009

6.3 TOUGH2-ECO2N Simulation of CO_2 Injection into the Middle Donovan

A set of simulations, using TOUGH2-ECO2N, was performed to investigate the two-phase flow of CO_2 and brine in the Middle Donovan Sands for a period of 100 years. Field records, obtained during the CO_2-EOR pilot test in the Upper Donovan, indicated that CO_2 injection rates ranged, approximately, from 27.2 to 45.4 t/day (30 to 50 short tons/day). The CO_2 will be injected into the Middle Donovan through the existing pipeline infrastructure.

The CO_2 injection rates are assumed to be in the same range as those encountered during the pilot test. This assumption is based on the notion that injection rate is a function of permeability, which in the Middle Donovan is 13 mdarcy (Table 6.1), a value close to the 10 mdarcy in Sands 14-1 and 16-2 of the pilot test.

The simulations were performed using a CO_2 injection rate of 36.3 t/day (40 short tons/day), representing the average value of the lowest and highest injection rates recorded in the field during the CO_2-EOR pilot test. The simulations were separated into two chronological stages. The first stage comprised the CO_2 injection period, whose duration was set to 40 years. The second stage comprised the *shut-in* period, following immediately after the CO_2 injection period. Termination of the second stage was set to an arbitrary value of 100 years. The final conditions of the 40-year CO_2 injection period simulations, were used as initial conditions for the shut-in period simulations.

Simulation output was obtained at four different time intervals. The simulation output variables produced by TOUGH2-ECO2N are: CO_2 saturation, formation pressure, solid salt saturation, salt mass fraction in the aqueous phase, CO_2 mass fraction in the aqueous phase, water mass fraction in the gas phase, density of CO_2, and density of brine.

The simulation output variables were plotted using a logarithmic scale on the horizontal axis, to compress the size of the radial grid. Table 6.2 lists the stages, output times, and significance of output at the prescribed times.

Table 6.2. Simulation Stages and Output Timetable for CO_2 Injection in the Middle Donovan.

Stage	Output Time	Significance
CO_2 injection	30 days	Conditions at very early stage of CO_2 injection
CO_2 injection	1 year	Arbitrary benchmark to assess short-term injection conditions
CO_2 injection	40 years	Conditions at end of injection period
Shut-in	100 years	Arbitrary benchmark to assess long-term shut-in conditions

6.3.1 TOUGH2-ECO2N Simulation Results of CO_2 Injection into the Middle Donovan

Among the output variables produced by TOUGH2-ECO2N, CO_2 saturation and pressure are of particular interest and significance, because they heavily influence the feasibility of CO_2 sequestration. For example, if pressure exceeds reservoir rock fracture pressure, fractures may occur in the rock matrix allowing upward mobility of CO_2, or CO_2 saturation levels may indicate that the CO_2 plume has migrated beyond the closure of the formation. In either case, CO_2 injection operations may have to be significantly modified or terminated.

The development and migration of the CO_2 plume is traced by the CO_2 saturation values along the radial grid profile. The simulated CO_2 saturation profiles, for CO_2 injection into the Middle Donovan, are shown in Figure 6.1, and reveal the development of three distinct regions during the 40-year CO_2 injection period.

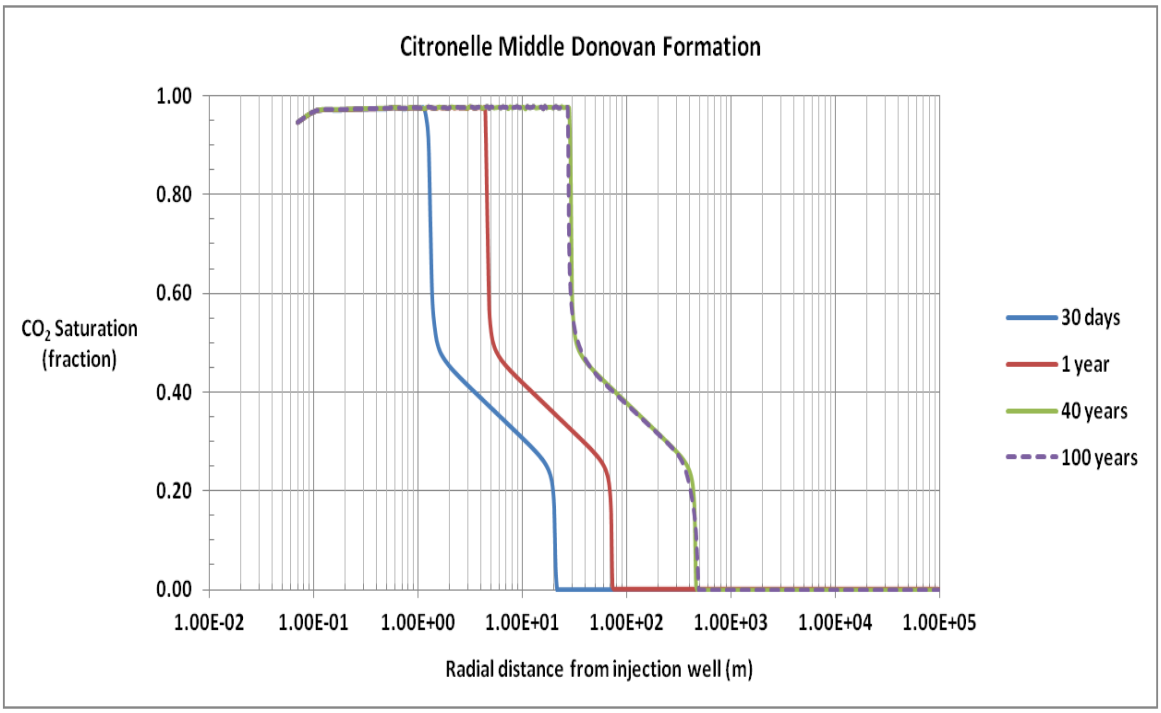

Figure 6.1. TOUGH2-ECO2N simulation of CO_2 saturation, at 30 days, 1 year, 40 years, and 100 years, during and following CO_2 injection into the Citronelle Middle Donovan formation. The CO_2 injection period is 40 years at a constant injection rate of 36.3 t/day (40.0 short tons/day). The injection period is followed by a shut-in period to 100 years. The radius of the injection well is 0.07 m (0.23 ft).

The first region, (*dried-out*), corresponds to a zone where complete dry-out of the aqueous phase has occurred, leaving solid salt (NaCl) behind. Gas saturation in this region is slightly less than 100% due to the presence of the solid salt. The dried-out region extends from the injection well to 27 m (88.6 ft) at the end of the 40-year CO_2 injection period. During the shut-in period the dried-out region extends to 30 m (98.4 ft), an increase of only 3 m (9.8 ft), indicating that the development, and advancement of the dried-out region is a function of the pressure gradient and flow during the CO_2 injection period.

The second region, (*transition*), corresponds to a transition zone in which supercritical CO_2 and liquid aqueous phases coexist, as partitioning and mixing between the two phases takes place continuously. This intermediate region extends from 27 m (88.6 ft) to 500 m (1640.4 ft), at the end of the 40-year CO_2 injection period. The transition from the first to the second region occurs rapidly, with significant reduction in the CO_2 saturation. During the transition between the first and second regions, the CO_2 saturation decreases by approximately 40% from its high value, in the dried-out zone, of 97.7%.

In the transition region, the slope of the CO_2 saturation curve decreases non-monotonically with time. The slope indicates a rate of decrease in CO_2 saturation of 1% per meter at 30 days, 0.25% per meter at 1 year, and 0.05% per meter at 40 and 100 years. At the outer boundary of the transition region the CO_2 saturation fraction decreases rapidly to zero.

The radial extent of the transition region increases from 20 m (65.6 ft) at 30 days, to approximately 400 m (1312.3 ft) at the end of the 40-year CO_2 injection period. During the shut-in period the extent of the transition region increases by only 30 m (98.4 ft), as advancement of the CO_2 front slows down in the absence of the pressure from CO_2 injection.

The third region, (*aqueous*), corresponds to an outer zone of single-phase aqueous solution (brine), extending to the boundary of the system at 100,000 m (328,084 ft). The conditions in this region are unaffected by the CO_2 injection.

Figure 6.2 shows the development of the pressure profile for the simulation period. The average initial hydrostatic pressure in the Middle Donovan was calculated to be 34 MPa (4931.3 psi). Pressure near the injection well, at a radial distance less than 2 m (6.56 ft), is 34.74 MPa (5038.6 psi) at 30 days, or 0.74 MPa (107.3 psi) higher than the average formation pressure of 34 MPa (4931.3 psi). Pressure reaches a maximum of 34.82 MPa (5050.2 psi) at the end of the 40-year injection period, but decreases to near the average formation pressure during the shut-in period.

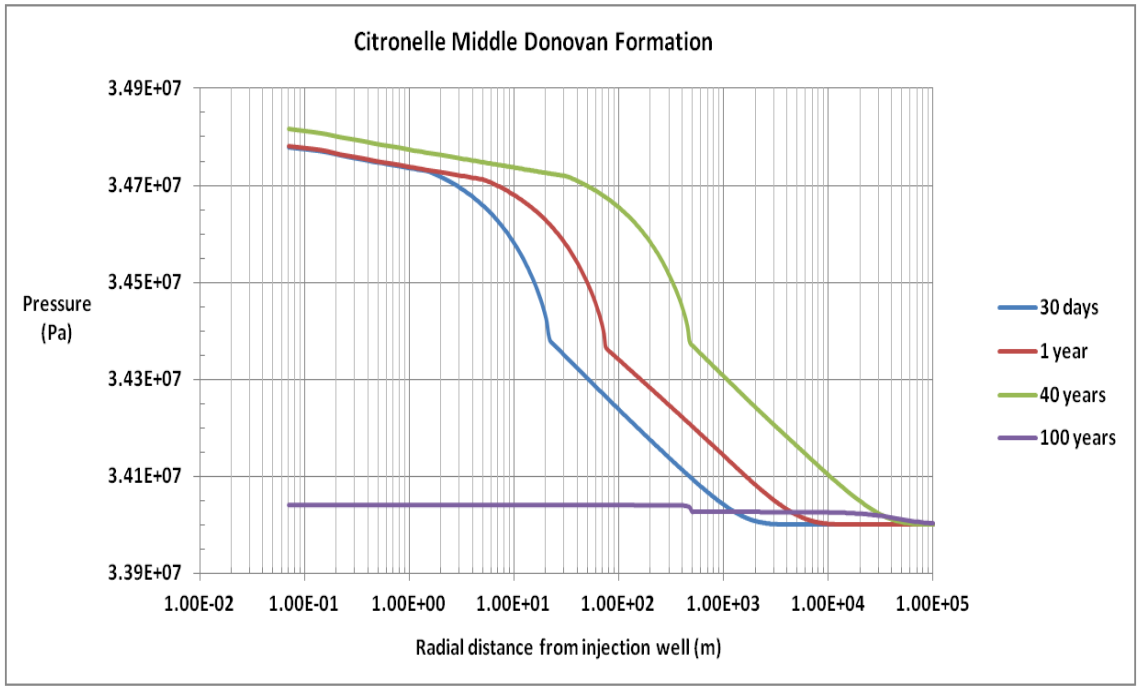

Figure 6.2. TOUGH2-ECO2N simulation of pressure, at 30 days, 1 year, 40 years, and 100 years, during and following CO_2 injection into the Citronelle Middle Donovan formation. The CO_2 injection period is 40 years at a constant injection rate of 36.3 t/day (40.0 short tons/day). The injection period is followed by a shut-in period to 100 years. The radius of the injection well is 0.07 m (0.23 ft).

Figure 6.2, also shows that in the time period between 30 days and 1 year, and within a radial distance of 1.5 m (4.9 ft) from the injection well, pressure appears to increase only marginally. The marginal increase suggests that the maximum change in pressure occurs early in the CO_2 injection period, and inside the dried-out region, where gas is the only phase present. Pressure begins to decline at a faster rate entering the two phase transition region, while at the same location the CO_2 saturation starts to decrease. The inflection point appearing in the pressure profiles, shown in Figure 6.2, coincides with the end of the transition region in the CO_2 saturation profiles as shown in Figure 6.1.

The initial average pressure of the Citronelle oil reservoir, considering both the Upper and Lower Donovan sands, was estimated at 38 MPa (5511.4 psi) (Esposito, 2008), suggesting that the reservoir rock fracturing pressure must be at least above this value. The maximum pressure predicted by the simulation is 34.82 MPa (5050.2 psi), which is below the initial pressure of the oil reservoir. It is assumed that the pressure gradient during CO_2 injection will not increase sufficiently to cause the formation to exceed its fracturing pressure.

In Section 6.2 it was stated that extending the simulation grid to a radial distance of 100,000 m (328,084 ft), was considered necessary in order to impose a constant pressure boundary condition. Figure 6.2 indicates that the constant pressure condition was maintained at the boundary, since the maximum reach of the leading edge of the pressure increase was less than 80,000 m (262,467 ft) from the injection well, and pressure at the boundary remained at 34 MPa (4931.3 psi).

In addition to CO_2 saturation and formation pressure, the mass fraction of CO_2 dissolved in the aqueous phase is also a parameter of interest. In Section 1.4, it was stated that dissolution of gas phase CO_2 in the aqueous phase is an important trapping mechanism, reducing the likelihood that CO_2 will return to the atmosphere.

Figure 6.3 shows the mass fraction of CO_2 dissolved in the aqueous phase. Dissolution begins to take place as soon as gas phase CO_2 contacts the aqueous phase. The dissolved CO_2 mass fraction rises to a high value of 3.68 wt%, at the interface between the gas and aqueous phases, and remains at this value inside the transition region. At the end of the transition region, the dissolved CO_2 mass fraction drops to zero and remains at this value in the aqueous region.

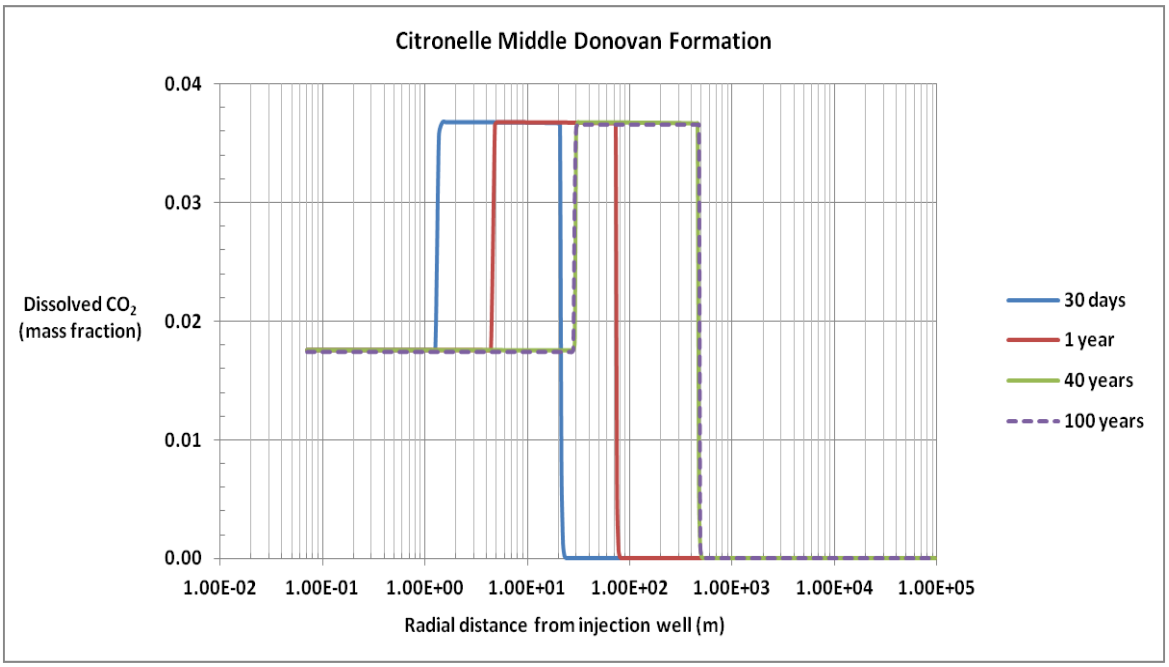

Figure 6.3. TOUGH2-ECO2N simulation of CO_2 mass fraction in the aqueous phase, at 30 days, 1 year, 40 years, and 100 years, during and following CO_2 injection into the Citronelle Middle Donovan formation. The CO_2 injection period is 40 years at a constant injection rate of 36.3 t/day (40.0 short tons/day). The injection period is followed by a shut-in period to 100 years. The radius of the injection well is 0.07 m (0.23 ft).

Following the end of the CO_2 injection, the dried-out region gradually retracts, as the aqueous phase slowly reimbibes into the pore space that it occupied before it was forced out by the advancing CO_2.

The process can also be identified, in Figure 6.4, by the contraction of the solid salt saturation region, which takes place during the shut-in period, and in Figure 6.5, by the retraction of the NaCl mass fraction in the aqueous phase, during the shut-in period. In the aqueous region the NaCl mass fraction remains at the initial value of 0.10 in native brine.

The small decrease in NaCl mass fraction in the transition region is due to the increase in volume of the aqueous phase upon CO_2 dissolution. The sharp peak in NaCl concentration, occurring at the inner boundary (start) of the transition region, indicates that conditions are nearing dry-out at that location. As partitioning and mixing take place in the transition region, water from the aqueous phase enters the gas phase, in the form of water vapor. The water vapor-in-gas phase mass fraction is shown in Figure 6.6, and is indicated by the slight rise in NaCl concentration at the outer boundary of the transition region, in Figure 6.5.

The fraction by mass of the aqueous phase entering the gas phase is shown, in Figure 6.6, to be less than 1%. In the aqueous region the gas phase is reduced to zero. There is only a 15 m (49.2 ft) increase in the extent of the transition region, as result of its expansion, during the shut-in period.

Gas density is shown in Figure 6.7. At 30 days gas density reaches a high value of 717.4 kg/m^3 (44.8 lb/ft^3) in the injection well grid block, decreasing slightly, to 713.8

kg/m^3 (44.6 lb/ft^3), at the end of the transition region. Water vapor affects the density of the gas phase. There is no gas in the aqueous region. During the 40-year CO_2 injection period, gas density varies by only a small amount. During the shut-in period, gas density decreases slightly to a constant value of 710.4 kg/m^3 (44.3 lb/ft^3).

Liquid density is shown in Figure 6.8. There is no aqueous phase in the dried-out region. Dissolution of CO_2 into the aqueous phase and the concentration of NaCl affect the density of the liquid phase where both liquid and CO_2 are present. The liquid density reaches a high value of 1184.6 kg/m^3 (73.9 lb/ft^3) at the start of the transition region, decreasing to 1049.2 kg/m^3 (65.5 lb/ft^3) at the end of the transition region. Density is 1043.7 kg/m^3 (65.2 lb/ft^3) in the undisturbed aqueous region.

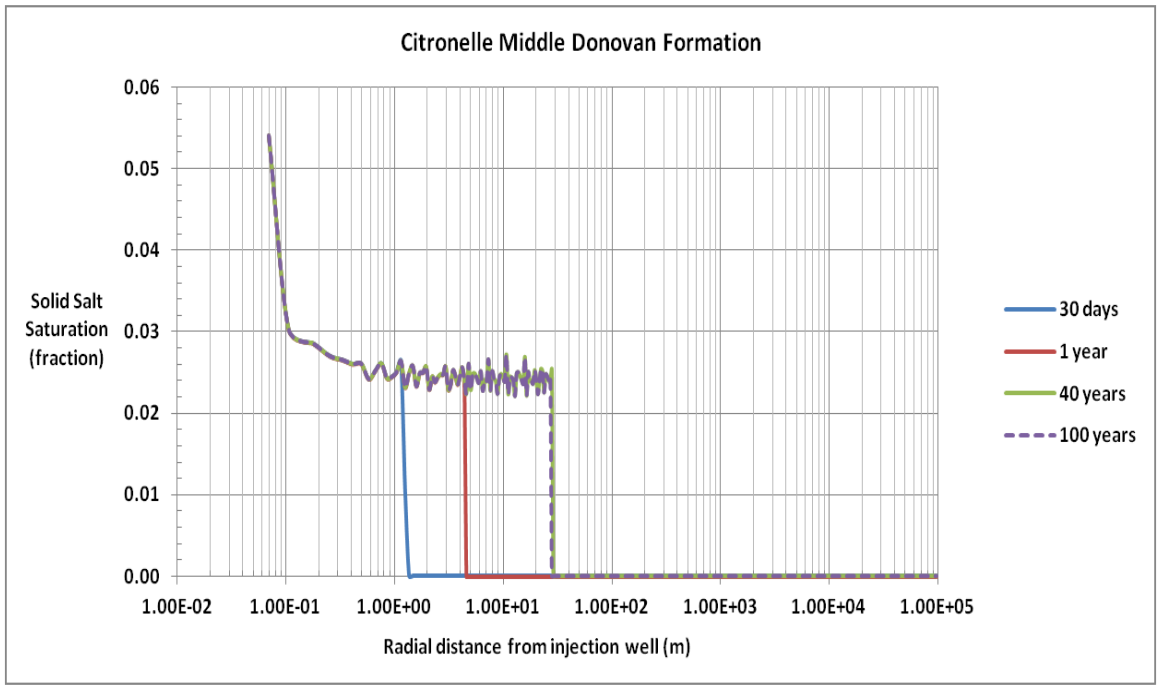

Figure 6.4. TOUGH2-ECO2N simulation of solid salt saturation, at 30 days, 1 year, 40 years, and 100 years, during and following CO_2 injection into the Citronelle Middle Donovan formation. The CO_2 injection period is 40 years at a constant injection rate of 36.3 t/day (40.0 short tons/day). The injection period is followed by a shut-in period to 100 years. The radius of the injection well is 0.07 m (0.23 ft).

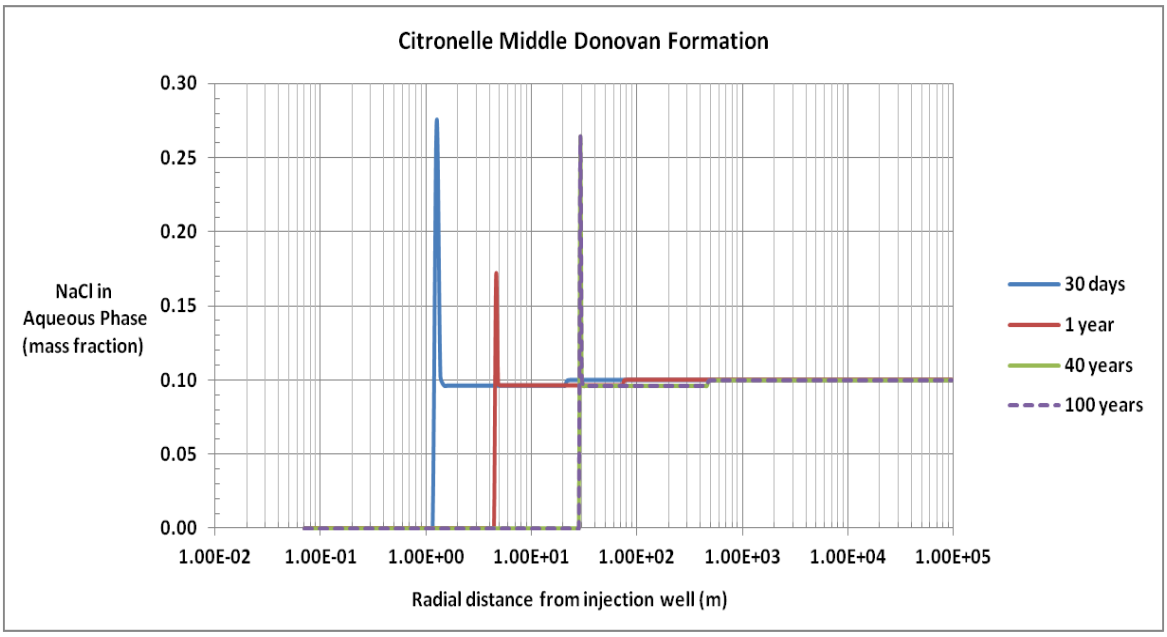

Figure 6.5. TOUGH2-ECO2N simulation of NaCl mass fraction in aqueous phase, at 30 days, 1 year, 40 years, and 100 years, during and following CO_2 injection into the Citronelle Middle Donovan formation. The CO_2 injection period is 40 years at a constant injection rate of 36.3 t/day (40.0 short tons/day). The injection period is followed by a shut-in period to 100 years. The radius of the injection well is 0.07 m (0.23 ft).

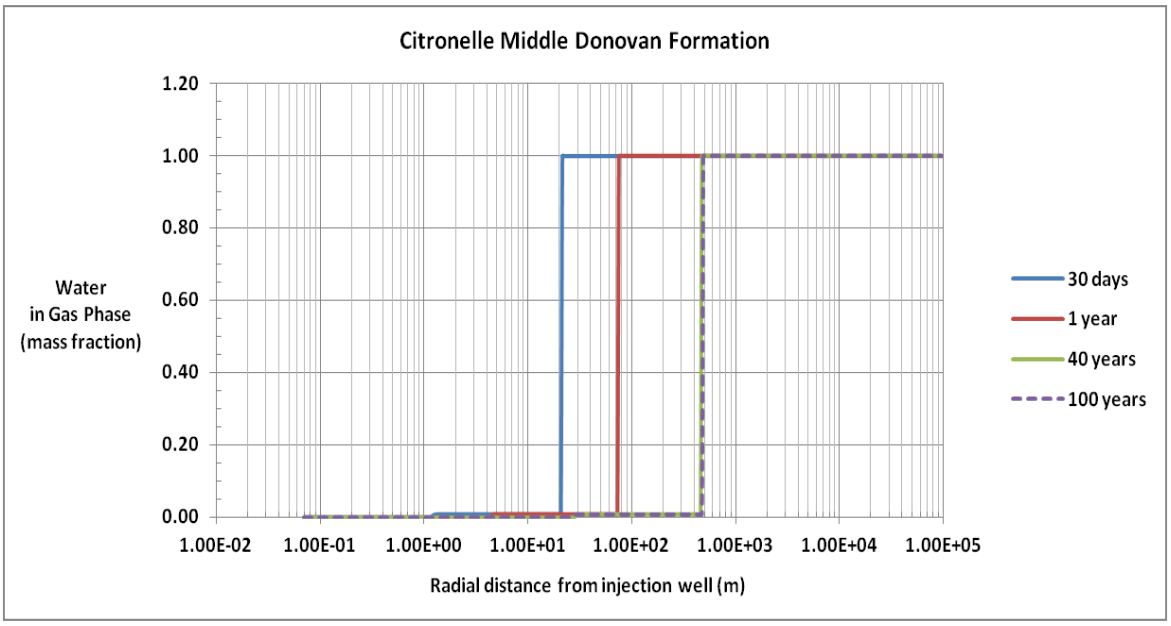

Figure 6.6. TOUGH2-ECO2N simulation of water mass fraction in gas phase, at 30 days, 1 year, 40 years, and 100 years, during and following CO_2 injection into the Citronelle Middle Donovan formation. The CO_2 injection period is 40 years at a constant injection rate of 36.3 t/day (40.0 short tons/day). The injection period is followed by a shut-in period to 100 years. The radius of the injection well is 0.07 m (0.23 ft).

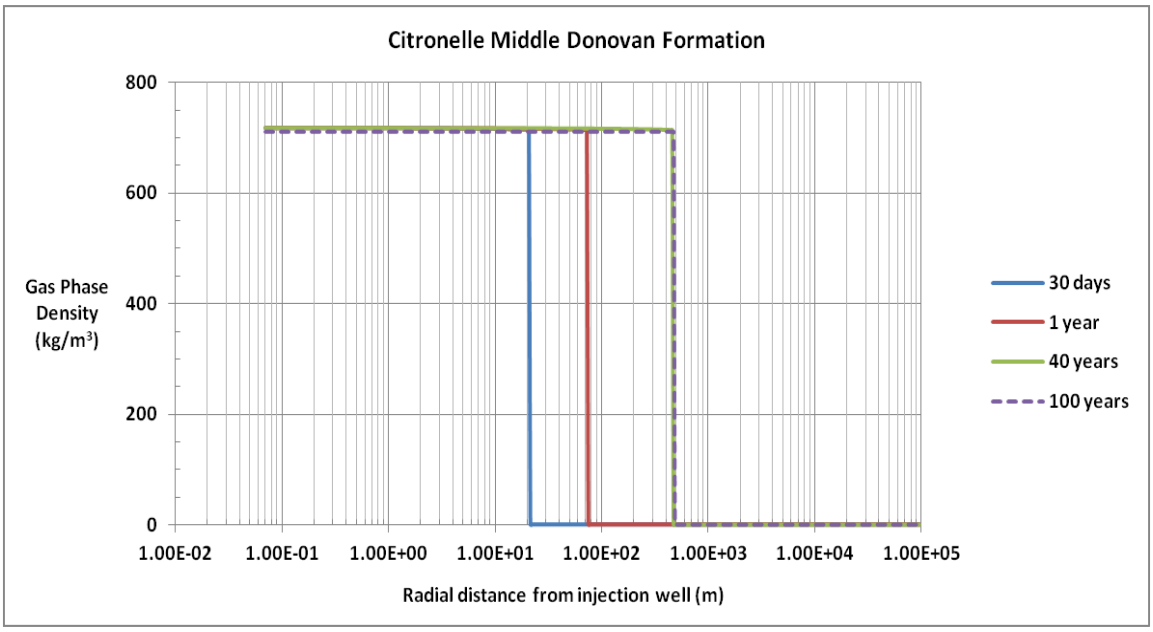

Figure 6.7. TOUGH2-ECO2N simulation of gas phase density, at 30 days, 1 year, 40 years, and 100 years, during and following CO_2 injection into the Citronelle Middle Donovan formation. The CO_2 injection period is 40 years at a constant injection rate of 36.3 t/day (40.0 short tons/day). The injection period is followed by a shut-in period to 100 years. The radius of the injection well is 0.07 m (0.23 ft).

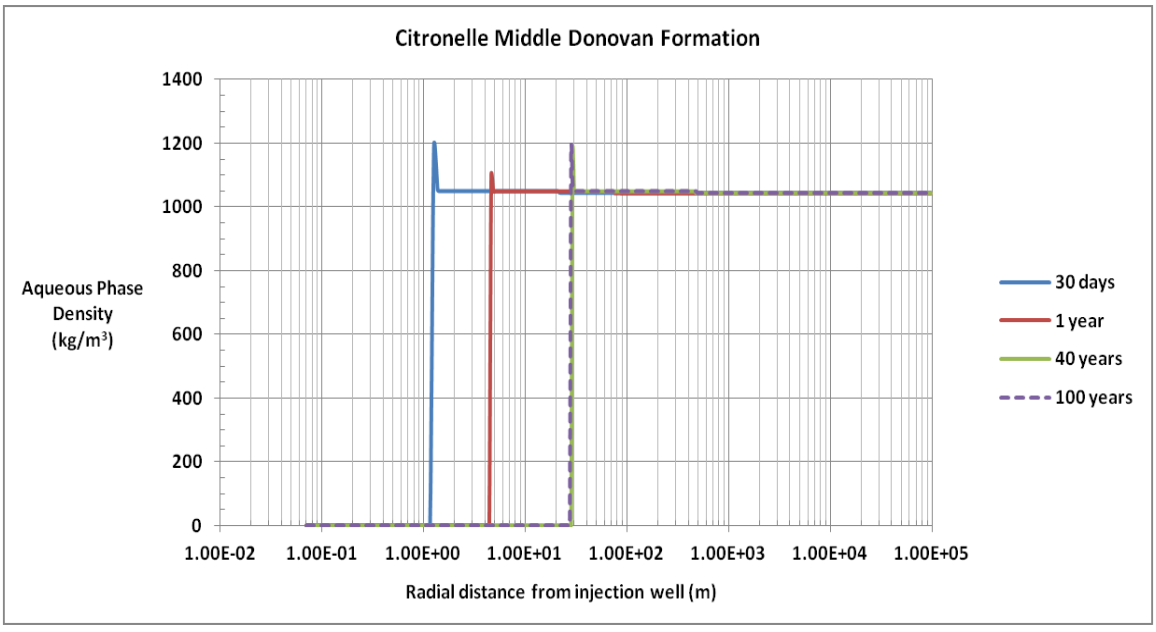

Figure 6.8. TOUGH2-ECO2N simulation of aqueous phase density, at 30 days, 1 year, 40 years, and 100 years, during and following CO_2 injection into the Citronelle Middle Donovan formation. The CO_2 injection period is 40 years at a constant injection rate of 36.3 t/day (40.0 short tons/day). The injection period is followed by a shut-in period to 100 years. The radius of the injection well is 0.07 m (0.23 ft).

6.3.2 TOUGH2-ECO2N Simulation Results Using Variable CO_2 Injection Rates

Simulation results obtained in Section 6.3.1 were based on an average CO_2 injection rate of 36.0 t/day (40 short tons/day). The CO_2 injection rates reported in the field during the CO_2-EOR pilot test, ranged approximately from 27.2 to 45.4 t/day (30 to 50 short tons/day).

A set of simulations was conducted using TOUGH2-ECO2N, with inputs identical to those used in the simulations of Section 6.3.1, except for the CO_2 injection rate. Two separate simulations were performed; one using a *low-end* CO_2 injection rate of 27.2 t/day (30 short tons/day), and the other, a *high-end* CO_2 injection rate of 45.4 t/day (50 short tons/day).

The objective of these simulations was to investigate the effect of CO_2 injection rate on output parameters, especially CO_2 saturation and formation pressure. Results obtained for both the low and high injection rates were combined, for comparison, with results obtained in Section 6.3.1, using the average CO_2 injection rate of 36.3 t/day (40 short tons/day). The results are presented by simulation output time at 40 and 100 years.

Figures 6.9, and 6.10, show the CO_2 saturation in the Middle Donovan at 40 years and 100 years, respectively. Each figure displays the CO_2 saturation at three CO_2 injection rates: 27.2 t/day (30 short tons/day), 36.3 t/day (40 short tons/day), and 45.4 t/day (50 short tons/day).

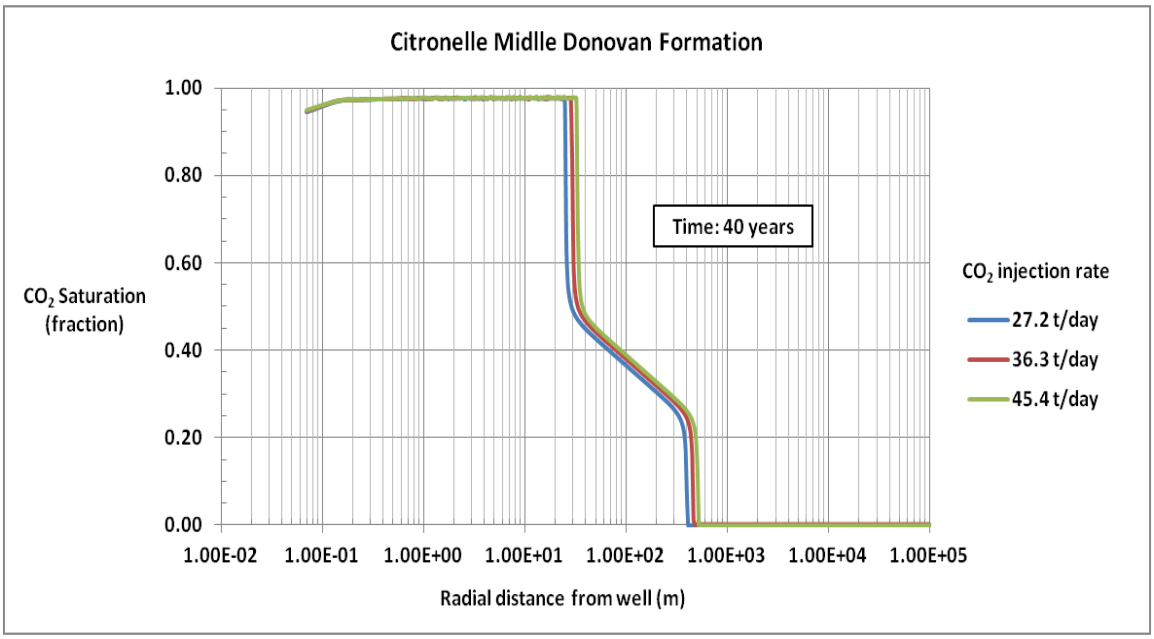

Figure 6.9. TOUGH2-ECO2N simulation of CO_2 saturation, at 40 years, for three CO_2 injection rates: 27.2 t/day (30 short tons/day), 36.3 t/day (40 short tons/day), and 45.4 t/day (50 short tons/day). The CO_2 injection period is 40 years. The injection period is followed by a shut-in period to 100 years. The radius of the injection well is 0.07 m (0.23 ft).

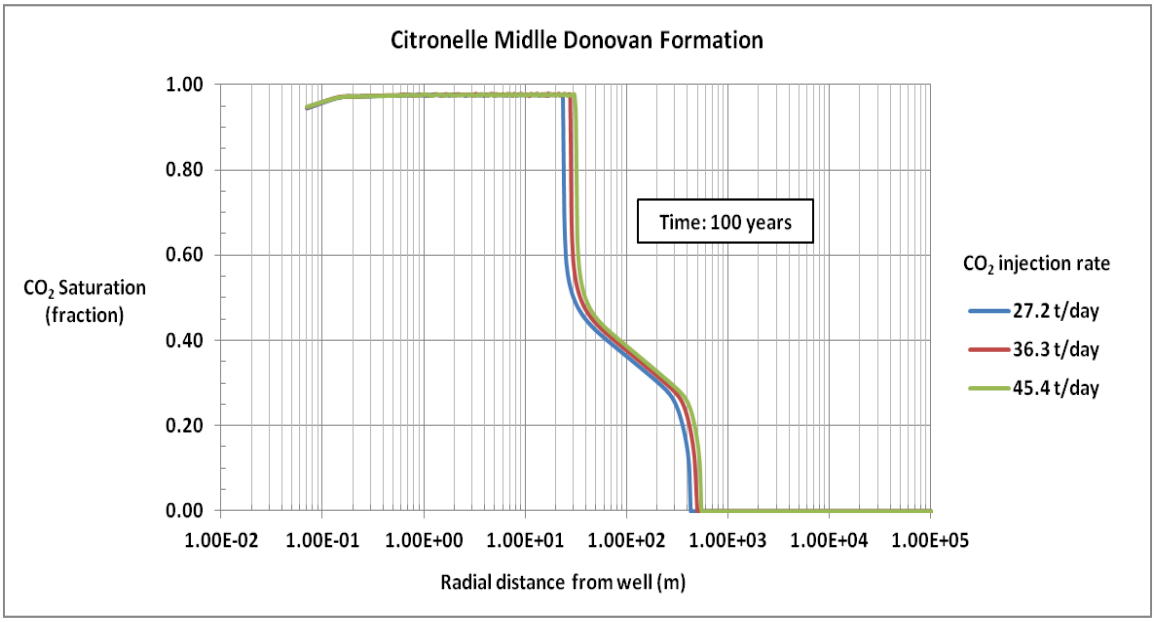

Figure 6.10. TOUGH2-ECO2N simulation of CO_2 saturation, at 100 years, for three CO_2 injection rates: 27.2 t/day (30 short tons/day), 36.3 t/day (40 short tons/day), and 45.4 t/day (50 short tons/day). The CO_2 injection period is 40 years. The injection period is followed by a shut-in period to 100 years. The radius of the injection well is 0.07 m (0.23 ft).

The results, shown in Figures 6.9, and 6.10, indicate that there is no effect on the absolute magnitudes of the CO_2 saturation fraction when varying the CO_2 injection rate. There is, however, some effect on the position of the CO_2 pressure profile. Using the leading edge of the transition region as reference, the variation in radial distance among the CO_2 saturation profiles, when comparing either the low or high CO_2 injection rate to the average rate, is within ± 15%.

Figures 6.11, and 6.12, show the Middle Donovan pressure profiles at 40 years and 100 years, respectively. Each figure displays the CO_2 saturation at the three CO_2 injection rates: 27.2 t/day (30 short tons/day), 36.3 t/day (40 short tons/day), and 45.4 t/day (50 short tons/day).

The results at 40 years, shown in Figure 6.11, indicate that the changes in CO_2 injection rate caused only small changes in the absolute magnitude of pressure and in the radial position of the pressure profile. The highest pressure at the well bore is 34.6 MPa (5018.3 psi), at the low CO_2 injection rate of 27.2 t/day (30short tons/day), and 35 MPa (5076.3 psi), at the high rate of 45.4 t/day (50 short tons/day). These values are within ±0.6% of the value of 34.8 MPa (5047.3 psi), at the CO_2 injection rate of 36.3 t/day (40 short tons/day). The highest pressure observed, among the three CO_2 injection rates, was 35 MPa (5076.3 psi), which is well below the average initial reservoir pressure of 38 MPa (5511.4 psi) (Esposito, 2008). At 100 years, shown in Figure 6.12, pressure in the transition region declines to within 0.05 MPa (7 psi) of the average initial reservoir pressure, in all three cases.

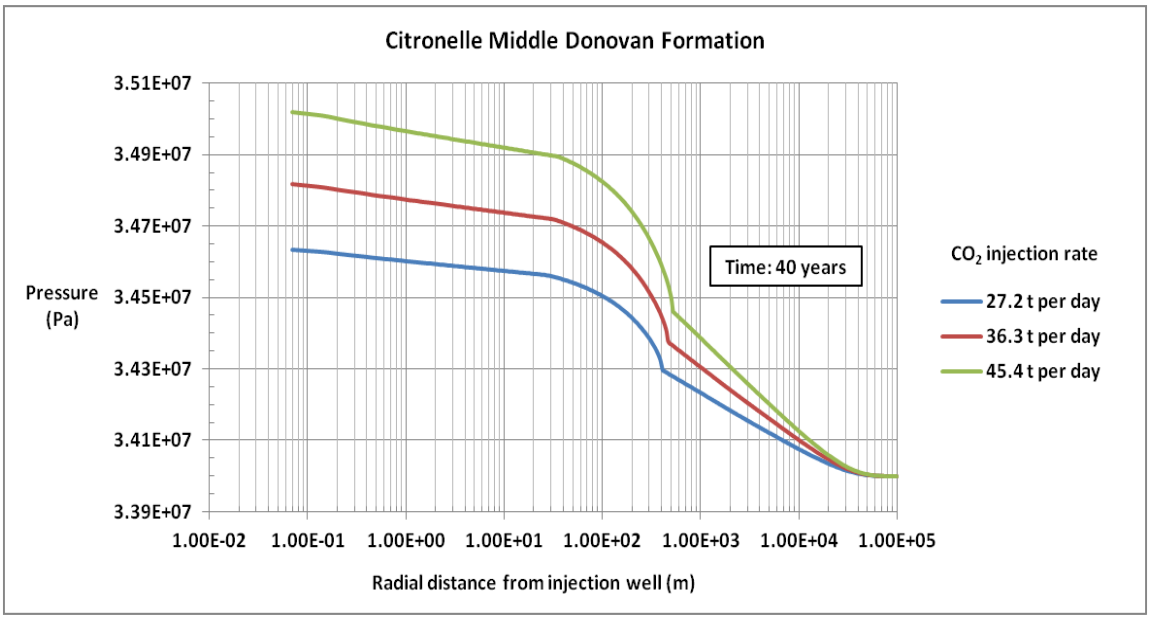

Figure 6.11. TOUGH2-ECO2N simulation of pressure, at 40 years, for three CO_2 injection rates: 27.2 t/day (30 short tons/day), 36.3 t/day (40 short tons/day), and 45.4 t/day (50 short tons/day). The CO_2 injection period is 40 years. The injection period is followed by a shut-in period to 100 years. The radius of the injection well is 0.07 m (0.23 ft).

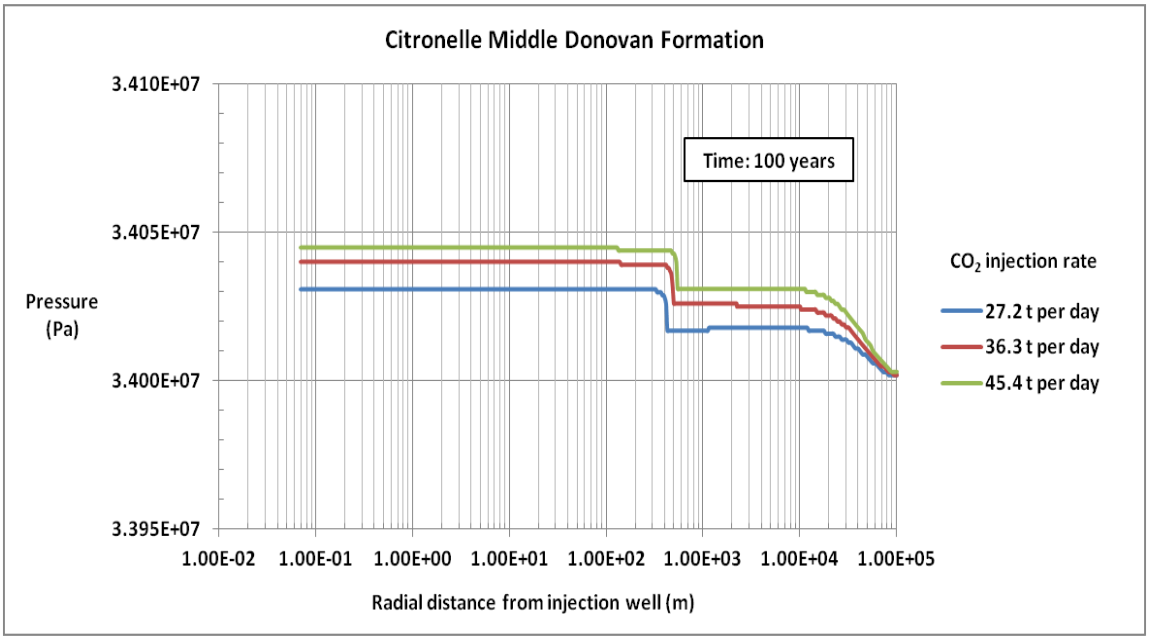

Figure 6.12. TOUGH2-ECO2N simulation of pressure, at 100 years, for three CO_2 injection rates: 27.2 t/day (30 short tons/day), 36.3 t/day (40 short tons/day), and 45.4 t/day (50 short tons/day). The CO_2 injection period is 40 years. The injection period is followed by a shut-in period to 100 years. The radius of the injection well is 0.07 m (0.23 ft).

6.4 TOUGH2-ECO2N Simulation of Permeability Reduction Due to Solid Salt Precipitation During CO_2 Injection into the Middle Donovan

The simulation results presented in Section 6.3.1 revealed the development of a dried-out region near the wellbore, where the injected CO_2 plume completely displaced and dried-out the aqueous phase. The drying process leads to a local increase in salt concentration, which eventually reaches the solubility limit, and begins to precipitate as solid salt.

Precipitation of solids reduces formation pore volume and can adversely affect the flow of fluids through the interconnected channels. The simulations discussed in Section 6.3.1 were conducted without consideration of any dependence of permeability on changes in porosity. However, a number of studies, (Pape et al., 1999; Verma and Pruess, 1988; Xu et al., 2004), have shown that even modest reductions in porosity can potentially lead to considerable reductions in permeability. Permeability reduction could adversely affect CO_2 injection rates and create increased skin effects around the injection well bore.

The TOUGH2-ECO2N simulator incorporates a subroutine that can be enabled or disabled, depending on whether it is desirable to engage or disengage the permeability reduction option during the simulations. The results presented in Section 6.3.1 were produced with the permeability reduction parameter disabled. A separate set of simulations was performed, with the permeability reduction parameter enabled. The inputs were identical in all other respects to those discussed in Section 6.3.1.

The objective of the new set of simulations was to investigate possible effects of solid salt precipitation on porosity and permeability, during and after CO_2 injection into

the Middle Donovan Sands. The simulations considered solid salt precipitation induced only by drying, without consideration of chemical interaction of CO_2 with dissolved species or with formation minerals. To simulate permeability reduction, TOUGH2-ECO2N uses a *tubes-in-series* model, that captures the converging-diverging nature of natural pore channels.

6.4.1 Tubes-in-Series Model of Pore Channels Used in Permeability Reduction Simulation

When the permeability reduction option is enabled, the equation of state module ECO2N offers several choices which can be used to model the functional dependence of the relative change in permeability on the relative change in active flow porosity.

The simplest conceptual models of permeability in porous media are those described by capillary tubes in various arrangements and sizes (Scheidegger, 1954, 1960). In models that use straight capillary tubes, permeability remains finite for as long as porosity is non-zero. To capture the converging-diverging nature of natural pore channels, ECO2N employs the Verma and Pruess (1988) model of alternating segments of capillary tubes having larger and smaller radii, as shown in Figure 6.13.

The *tubes-in-series* model describes permeability reduction due to precipitation of solids, as a function of initial porosity, and has only two independent parameters that need to be specified: (a) the fraction of original porosity at which permeability is reduced to zero, φ_r; and (b) the fractional length of the larger pore bodies, L_1/L.

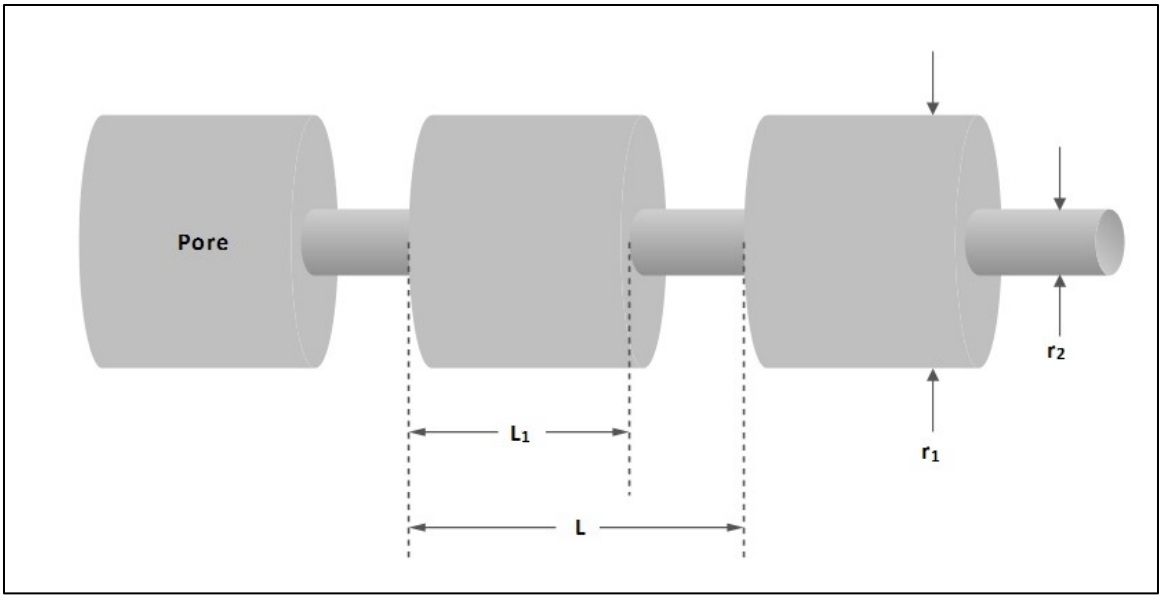

Figure 6.13. Model of pore channels as alternating segments of capillary *tubes-in-series*. Fractional length of the larger pore radii is determined by L_1/L (after Verma and Pruess, 1988).

The fraction of original porosity at which permeability is reduced to zero is given by $\varphi_r = \varphi/\varphi_0 = 1 - S_s$, where φ is the porosity at zero permeability, φ_0 is the original porosity, and S_s is the critical solid salt saturation at which permeability becomes zero. Using the tube-in-series model, shown in Figure 6.13, the following relationship can be derived (Verma and Pruess, 1988):

$$\frac{k}{k_o} = \sigma^2 \frac{1 - \Gamma + \Gamma/\omega^2}{1 - \Gamma + \Gamma[\sigma/(\sigma + \omega - 1)]^2} \tag{6.1}$$

where,

$$\sigma = \frac{1 - S_s - \varphi_r}{1 - \varphi_r} \tag{6.2}$$

$$\omega = 1 + \frac{1/\Gamma}{1/\phi_r - 1} \tag{6.3}$$

Parameter σ, depends on the fraction $1 - S_s$ of original pore space that remains available to fluids, and on the parameter φ_r, which denotes the fraction of original porosity at which permeability is reduced to zero. Parameter Γ, is the fractional length L_1/L.

6.4.2 Middle Donovan Porosity–Permeability Relationship

The empirical relationships that have been formulated for correlating porosity and permeability in the Upper and Middle Donovan are assumed to be valid for the Middle Donovan Sands as well. Data from field reports and laboratory analyses were engaged to establish sand parameters such as permeability, porosity, saturations, and injectivity-productivity indices for the Upper and Lower Donovan (Fowler et al., 1998). An empirical relationship, for the Citronelle Oil Field, was developed by Fowler et al. (1998), that expresses porosity as a function of permeability. Porosity (fraction) is calculated using mean air permeability values k (mdarcy), derived from productivity index analyses, by the following equation:

$$\varphi = \frac{log_{10}(k_{air}) + 3.556}{33.133} \tag{6.4}$$

Rearranging the equation and solving for permeability as a function of porosity yields the following modified equation:

$$log_{10}(k_{air}) = 33.133\varphi - 3.556 \tag{6.5}$$

Equation 6.5 was used to generate the plot shown in Figure 6.14, displaying permeability as a function of initial porosity, using 12%, 13% and 14% for the initial porosity values, where 13% is the estimated initial porosity of Middle Donovan Sands (Esposito et al., 2008). The curves shown in Figure 6.14 indicate that significant decrease in permeability is possible with only moderate decreases in porosity. For example, using an initial porosity value of 0.14, a 10% decrease in porosity would result in reduction of permeability from 12 to 4 mdarcy, corresponding to a decrease in permeability of 66.7%. A 66.7% reduction in permeability could have significant impact on the flow of fluids through the formation, and on injection rates, since the precipitation of solids is more pronounced in the vicinity of the CO_2 injection wellbore.

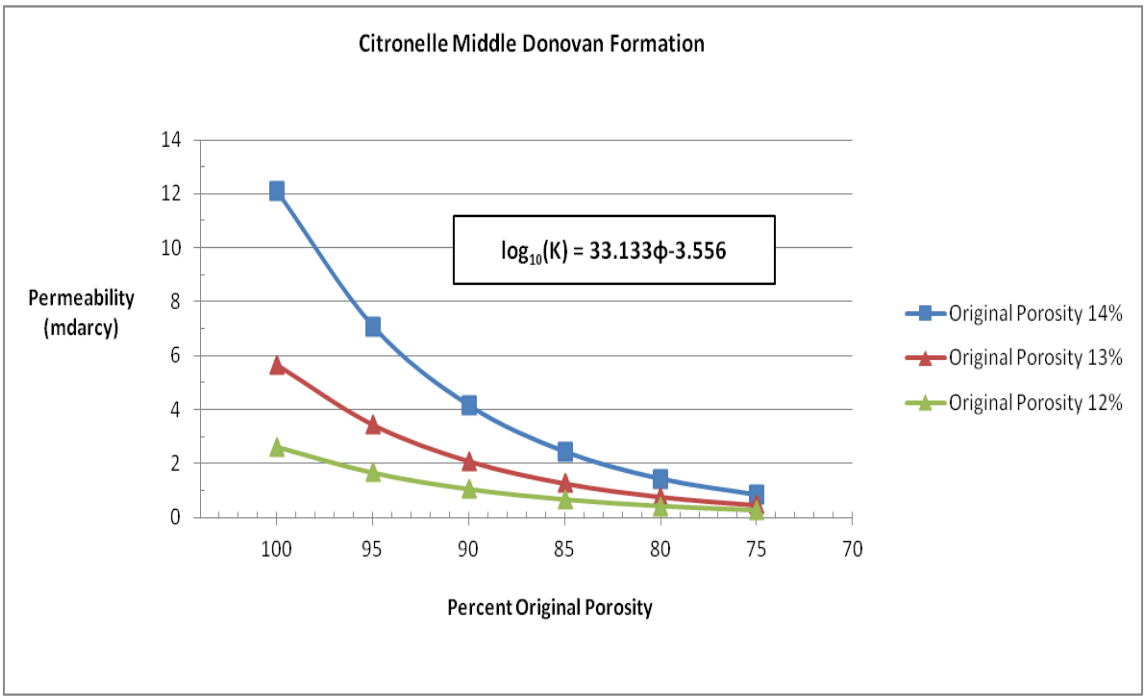

Figure 6.14. Permeability reduction curves, for Middle Donovan Sands, as function of percent reduction in porosity, for initial porosities of 12%, 13%, and 14%. The initial porosity of Middle Donovan Sands is 13%. Based on the works of Fowler et al. (1998).

The TOUGH2-ECO2N simulator offers a number of models for the relative permeability function. The model chosen was that of van Genuchten (1980), in conjunction with the model of Corey (1954), for gas relative permeability. These models were used in the simulations discussed in Section 6.3.1, and also in the new set of simulations, in which the permeability reduction function was enabled.

The van Genuchten-Corey relative permeability and capillary pressure models, are governed by an exponential parameter, *m*. The value of the parameter, *m*, which can range from zero to one, is typically derived from empirical data and is a function of the spread of the rock matrix pore size distribution. Scott and Barker (2006), using mercury injection capillary pressure measurements for a set of sandstone samples, obtained values for the parameter, *m*, ranging from 0.42 to 0.88. Bloomfield et al. (2001), also using mercury injection capillary pressure measurements for a set of sandstones, obtained values for *m* ranging from 0.03 to 0.92. The TOUGH2-ECO2N results presented in Section 6.3.1, were obtained with the permeability reduction parameter disabled, using a value for *m* of 0.5. In the new set of simulations, with the permeability reduction parameter enabled, three different values for the van Genuchten parameter, *m*, were chosen and tested: a low value of 0.2, a medium value of 0.5, and a high value of 0.9.

6.4.3 TOUGH2-ECO2N Simulation Results for Permeability Reduction

The results of the permeability reduction simulations were combined with results presented in Section 6.3.1, and organized into three groups. The first group assesses the sensitivity of simulations to the permeability reduction option. The second group assesses

the effects on permeability reduction from changes in the value of the van Genuchten parameter, *m*. The third group assesses the influence of the van Genuchten parameter, *m*, on the following simulation output parameters: CO_2 saturation, pressure, CO_2 dissolution, and solid salt saturation.

In the first assessment group, results of simulations performed with the permeability reduction parameter disabled are compared to those performed with the parameter enabled. In both sets of simulations the CO_2 injection rate was 36.3 t/day (40 short tons/day), and all other input parameter values were identical to those established in Sections 6.2, and 6.3.

Figure 6.15 shows pressure, at 30 days and 40 years, for the simulations with permeability reduction enabled and disabled. The maximum formation pressure, during the simulation with permeability reduction enabled, increased by 0.017 MPa (2.47 psi) at 30 days, and by 0.028 MPa (4.06 psi) at 40 years, compared to the maximum pressure encountered in the simulation with permeability reduction disabled. The increases in pressure are very small and have no effect in the likelihood of fracture in the Middle Donovan formation. Pressures, for both options, are practically identical beyond 0.3 m (0.98 ft) from the CO_2 injection well at 30 days, and beyond 2 m (6.6 ft) at 40 years.

Pressure was the only parameter that displayed discernible difference when comparing results of the simulations with the permeability reduction disabled to those with the permeability reduction enabled. All other simulation output parameters were identical over the entire radial profile, including simulations performed using values of 0.2 and 0.9 for the van Genuchten parameter, *m*.

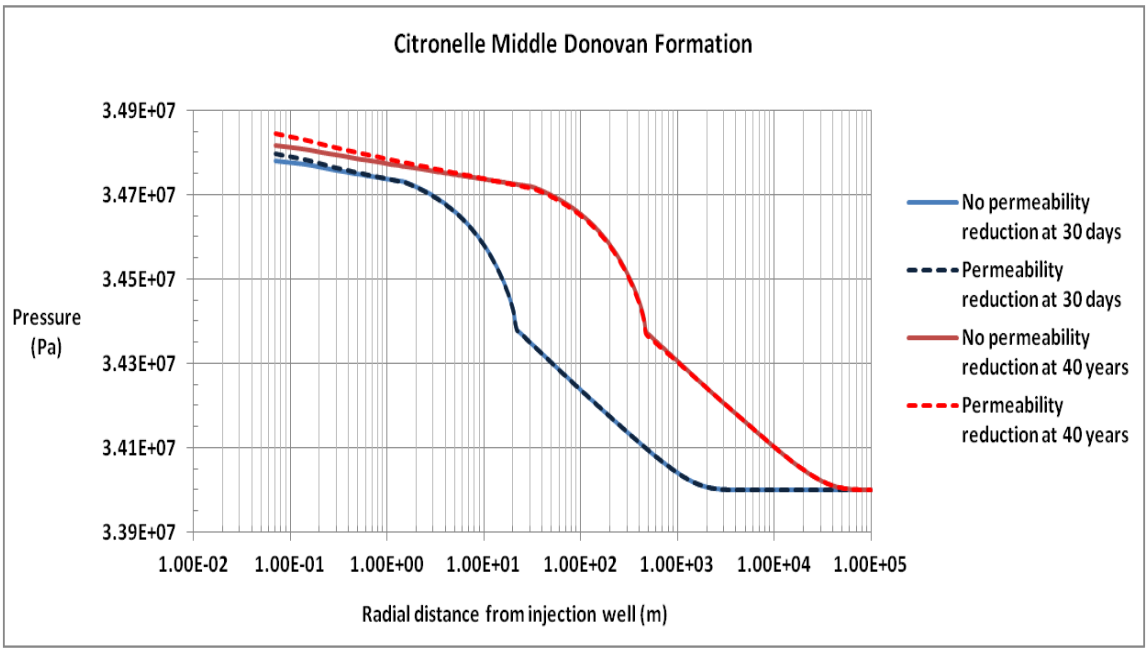

Figure 6.15. TOUGH2-ECO2N simulation of pressure, at 30 days and at 40 years. Solid lines represent simulations performed with permeability reduction disabled, and dashed lines represent simulations performed with permeability reduction enabled. The van Genuchten parameter, *m*, is 0.5 in both cases. The CO_2 injection rate is 36.3 t/day (40.0 short tons/day).

The second group of results assesses the sensitivity of the simulations performed with the permeability reduction parameter enabled, to changes in the van Genuchten parameter, *m*. Simulations considered in this group used a CO_2 injection rate of 36.3 t/day (40 short tons/day). Since permeability reduction is caused by solid salt precipitation in the dried-out region, the results for permeability reduction and solid salt saturation are presented together. Results are presented for each of the three values of the van Genuchten parameter, *m*, used in the simulations. The results, at 30 days, for the permeability reduction fraction and solid salt saturation, are shown in Figures 6.16, and 6.17 respectively. The results at 40 years are shown in Figures 6.18, and 6.19, and at 100 years in Figures 6.20, and 6.21. A permeability reduction fraction equal to unity indicates that the original permeability was unaffected.

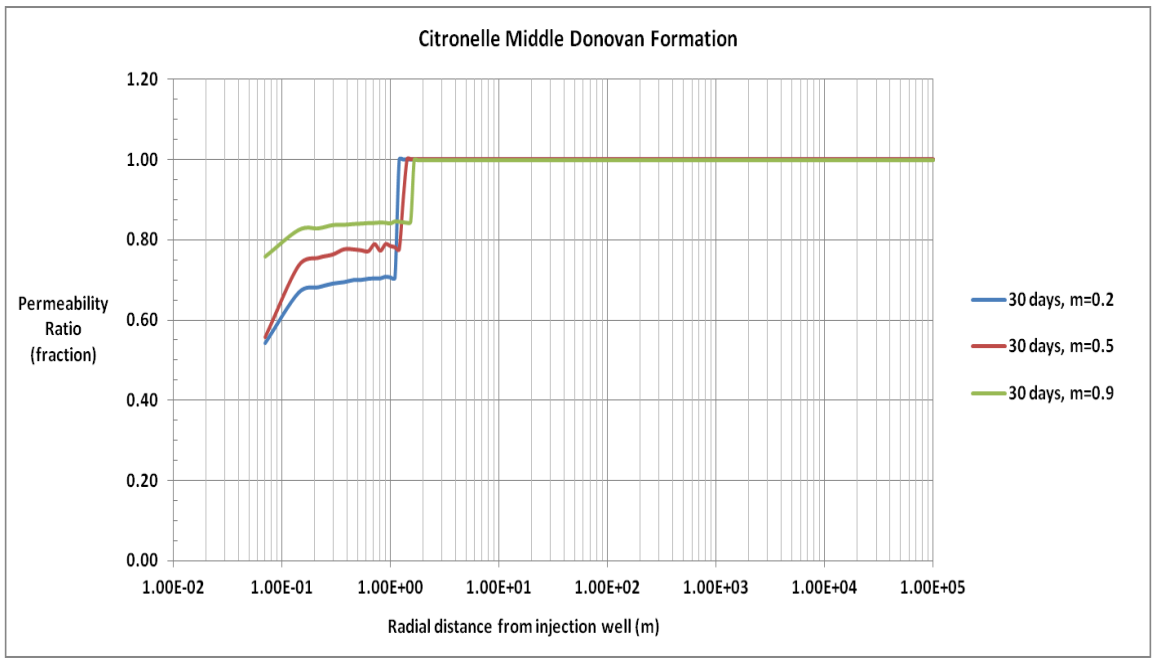

Figure 6.16. TOUGH2-ECO2N simulations with permeability reduction enabled. Permeability ratio, at 30 days, for three values of the van Genuchten parameter, *m*: 0.2, 0.5, and 0.9. The CO_2 injection rate is 36.3 t/day (40.0 short tons/day).

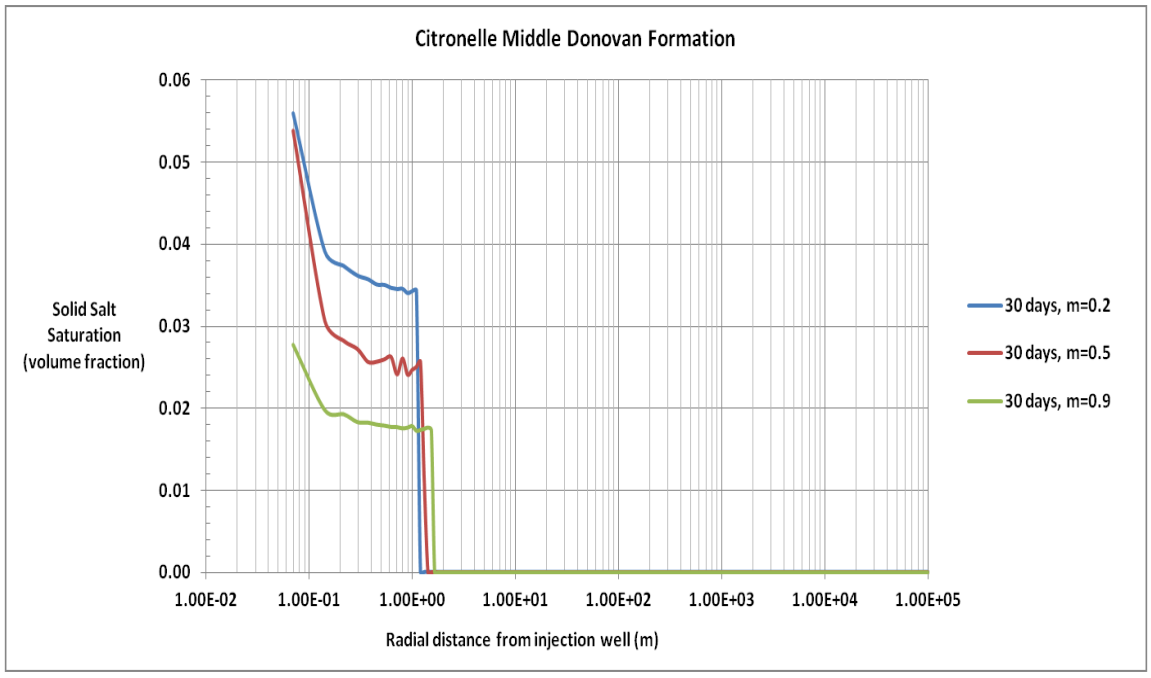

Figure 6.17. TOUGH2-ECO2N simulations with permeability reduction enabled. Solid salt saturation, at 30 days, for three values of the van Genuchten parameter, *m*: 0.2, 0.5, and 0.9. The CO_2 injection rate is 36.3 t/day (40.0 short tons/day).

Figure 6.16 indicates that 30 days into the CO_2 injection period, permeability reduction in the well grid block reaches a maximum of 54.2% of the original permeability, when the value of the van Genuchten parameter, *m*, is 0.2. Permeability reduction in the well grid block reaches a maximum of 55.7% of the original permeability when *m* is 0.5, and reaches 75.8% when *m* is 0.9. This trend indicates that the onset of permeability reduction is not a linear function of the van Genuchten parameter, *m*, though it is monotonic.

A region, measuring 0.1 m (0.33 ft) thick, has formed adjacent to the injection well, in which the permeability reduction increases at a rapid rate. The rate of increase is invariant to time, but dependent on the value of the van Genuchten parameter, measuring 0.14 % per centimeter (0.36% per inch) when *m* is 0.2, 0.19% per centimeter (0.48% per inch) when *m* is 0.5, and 0.07% per centimeter (0.18% per inch) when *m* is 0.9.

The rapid increase in permeability tapers off between 0.17 m (0.56 ft) and the outer boundary of the dried-out region. Permeability stabilizes at around 72% of the original permeability when *m* is 0.2, 79% when *m* is 0.5, and 85% when *m* is 0.9. Beyond the dried-out region the permeability reduction fraction is zero and permeability is at its original pre-CO_2 injection value of 13 mdarcy.

The variations in the absolute measures of the permeability reduction fractions, between those obtained at 30 days and those obtained at 40, and 100 years, are marginal, as shown by Figures 6.16, 6.18, and 6.20. Only the radial extent of the affected region increases with CO_2 injected and time.

Solid salt saturation displays similar but complementary traits to those identified in the permeability reduction fraction. The maximum solid salt saturation occurs in the well grid block, and reaches a value of 5.61% at 30 days, when *m* is 0.2, as shown in Figure 6.17. When *m* is 0.5, the maximum solid salt saturation at 30 days is 5.39%, and when *m* is 0.9 the maximum saturation is 2.78%.

As in the case of the permeability reduction fraction, a region measuring 0.1 m (0.33 ft) thick, has formed adjacent to the injection well, in which the solid salt saturation decreases at a rapid rate, as shown in Figure 6.17. In this region, solid salt saturation displays a negative gradient of 2.2% per centimeter (5.6% per inch), 2.8% per centimeter (7.1% per inch), and 1.1% per centimeter (2.8% per inch), for values of the parameter, *m*, of 0.2, 0.5, and 0.9, respectively. The rate of decrease, as in the case of the permeability reduction fraction, is invariant to time, as shown in Figures 6.19 and 6.21. The rapid decrease of the solid salt saturation tapers off between 0.17 m (0.56 ft) and the outer boundary of the dried-out region.

At 40 years solid salt saturation stabilizes at 3.4% for *m* set equal to 0.2, at 24% for *m* equal to 0.5, and at 1.7% for *m* equal to 0.9. These saturation values remain at this level to end of the simulation. Beyond the dried-out region the solid salt saturation is zero. The maximum values of the solid salt saturation observed in Figures 6.17, 6.19, and 6.21 remain at the same levels regardless of output time or value of the parameter, *m*.

The variations in the absolute measures of the solid salt saturation, between those obtained at 30 days and those obtained at 40, and 100 years, are marginal, as shown by Figures 6.17, 6.19, and 6.21. Only the radial extent of the affected region increases with

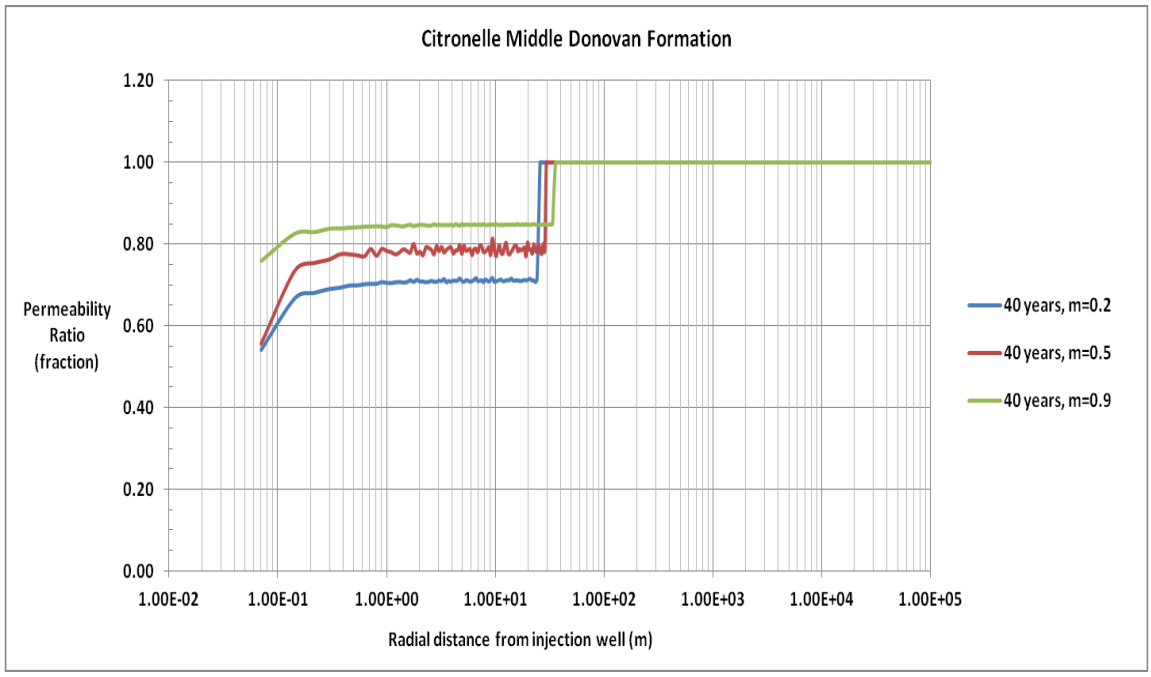

Figure 6.18. TOUGH2-ECO2N simulations with permeability reduction enabled. Permeability ratio, at 40 years, for three values of the van Genuchten parameter, *m*: 0.2, 0.5, and 0.9. The CO_2 injection rate is 36.3 t/day (40.0 short tons/day).

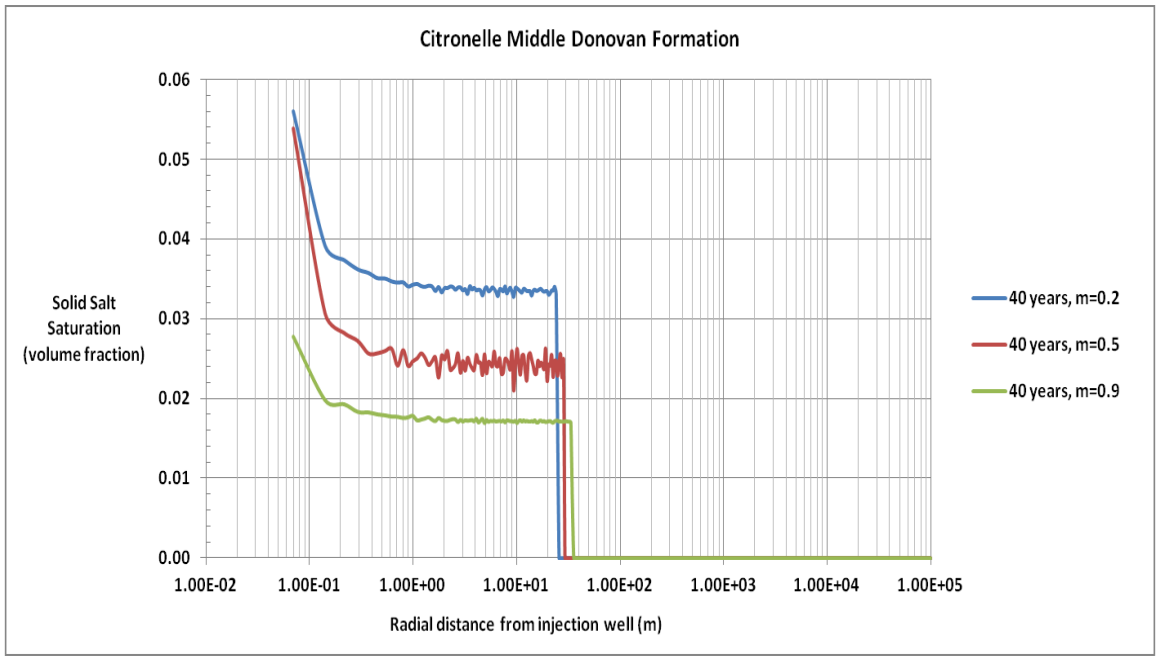

Figure 6.19. TOUGH2-ECO2N simulations with permeability reduction enabled. Solid salt saturation, at 40 years, for three values of the van Genuchten parameter, *m*: 0.2, 0.5, and 0.9. The CO_2 injection rate is 36.3 t/day (40.0 short tons/day).

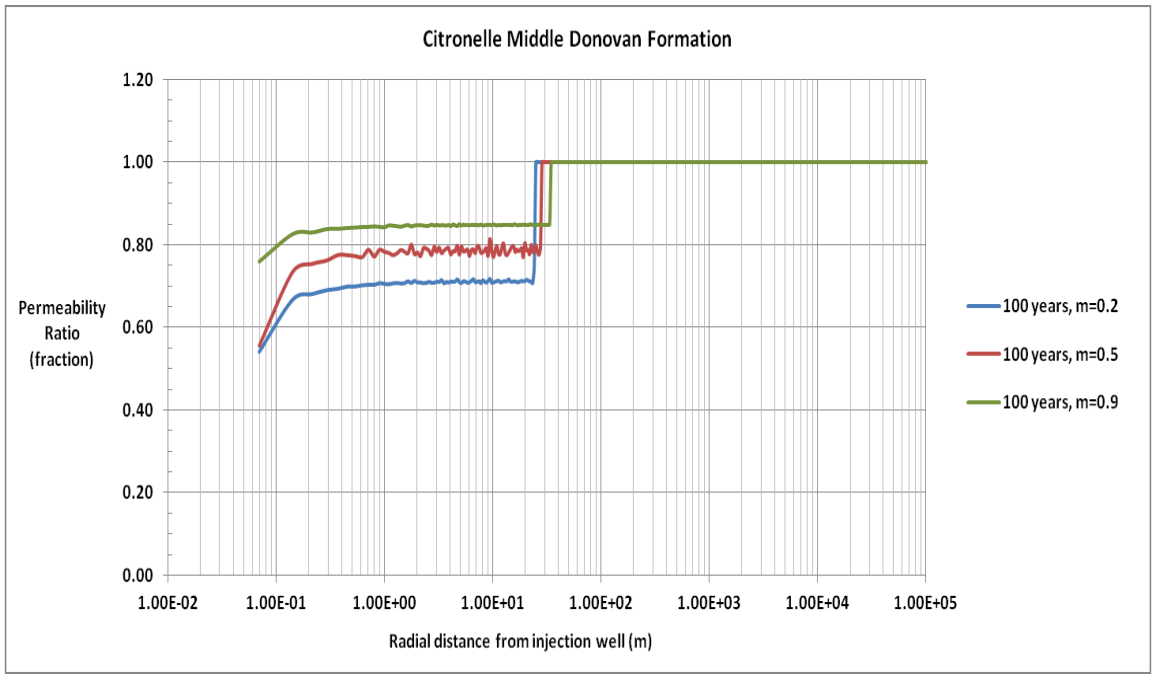

Figure 6.20. TOUGH2-ECO2N simulations with permeability reduction enabled. Permeability ratio, at 100 years, for three values of the van Genuchten parameter, *m*: 0.2, 0.5, and 0.9. The CO_2 injection rate is 36.3 t/day (40.0 short tons/day).

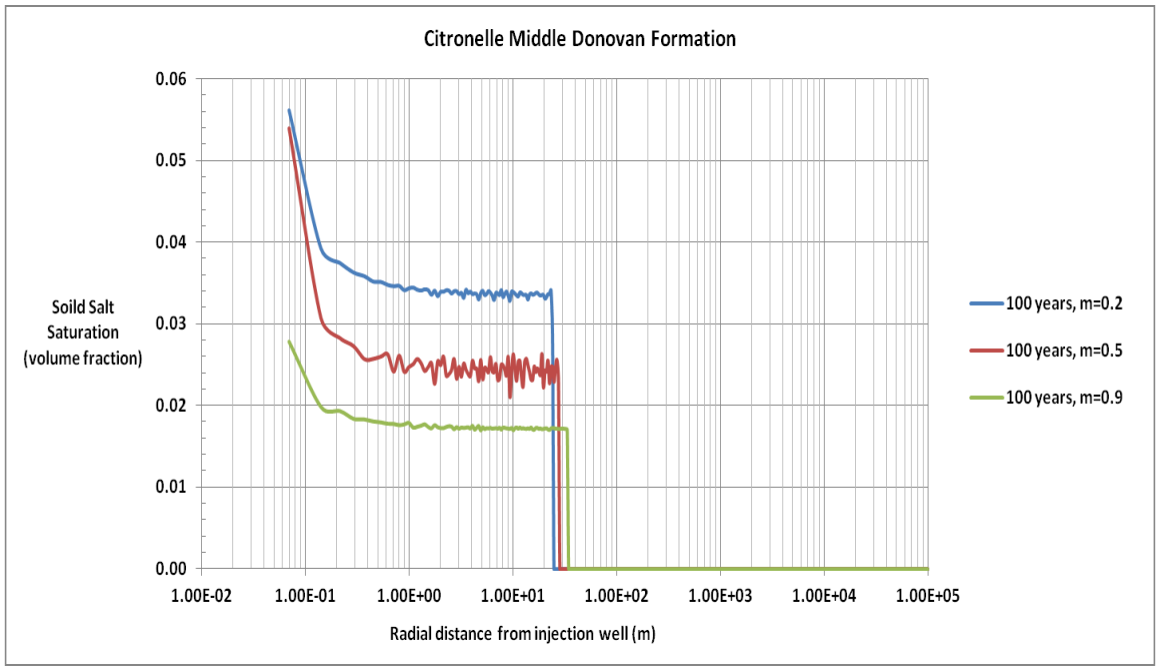

Figure 6.21. TOUGH2-ECO2N simulations with permeability reduction enabled. Solid salt saturation, at 100 years, for three values of the van Genuchten parameter, *m*: 0.2, 0.5, and 0.9. The CO_2 injection rate is 36.3 t/day (40.0 short tons/day).

CO_2 injected and time. The figures also indicate that increasing the value of the van Genuchten parameter, promotes expansion of the dried-out region, in concordance with the response of dissolved CO_2 and CO_2 saturation to similar changes in the value of the parameter.

Figure 6.19, shows that at 40 years, the leading edge of the dried-out region is at 25 m (82 ft) when *m* is 0.2, at 28.5 m (93.5 ft) when *m* is 0.5, and at 34.7 m (113.8 ft) when *m* is 0.9. The figure also indicates that in the dried-out region, solid salt saturation stabilizes at 3.5% when *m* is 0.2, at 2.6% when *m* is 0.5, and at 1.7% when *m* is 0.9.

The third group of results assesses the influence of the van Genuchten parameter on simulation output parameters. All of the simulations considered in this group were performed with the permeability reduction parameter enabled, CO_2 injection rate of 36.3 t/day (40 short tons/day), and were repeated for van Genuchten parameter values, *m*, equal to 0.2, 0.5, and 0.9. The output parameters discussed are: CO_2 saturation, formation pressure, CO_2 dissolution in aqueous phase, and solid salt saturation. Output times are at 30 days and 40 years.

Figures 6.22, and 6.23, show the CO_2 saturation response to changes in the van Genuchten parameter, *m*, at 30 days, and 40 years respectively. The development of the dried-out region is affected by changes in the van Genuchten parameter, as shown in Figure 6.22, indicating that higher values of the parameter, promote evaporation and expansion of the dried-out region. At 30 days the leading edge of the dried-out region is at 1.5 m (4.9 ft), when *m* is 0.9, at 1.3 m (4.3 ft) when *m* is 0.5, and at 1.1 m (3.6 ft) when *m* is 0.2, as shown in Figure 6.22.

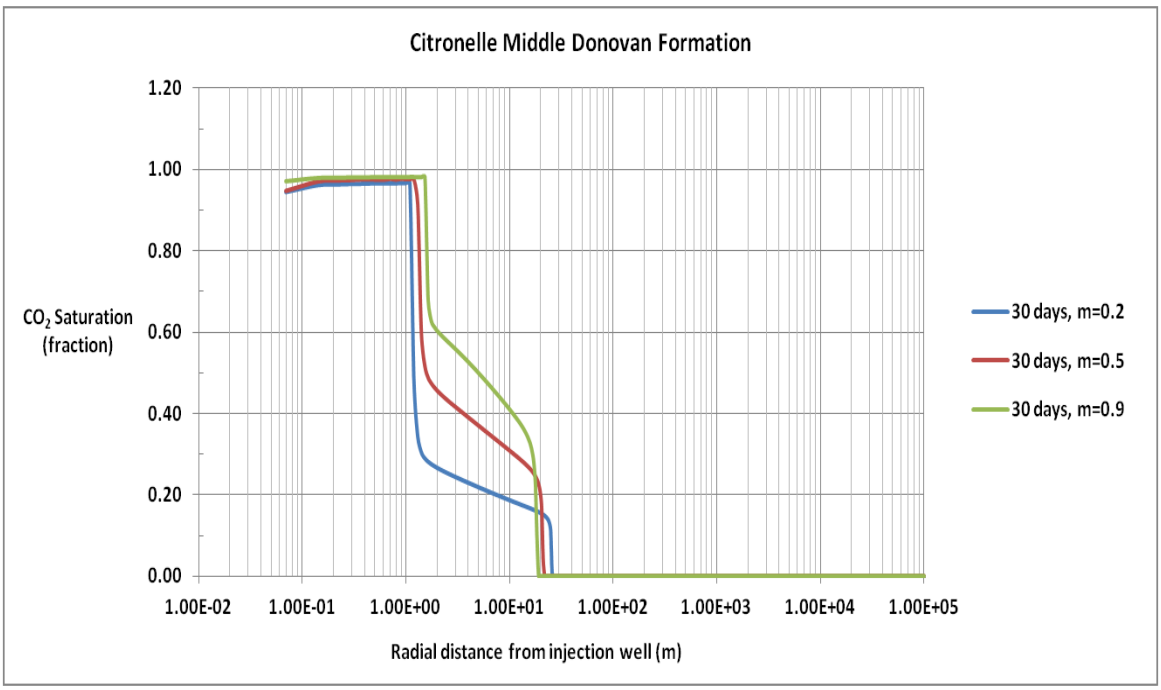

Figure 6.22. TOUGH2-ECO2N simulations with permeability reduction enabled. CO_2 saturation at 30 days, for three values of the van Genuchten parameter *m*: 0.2, 0.5, and 0.9. The CO_2 injection rate is 36.3 t/day (40.0 short tons/day).

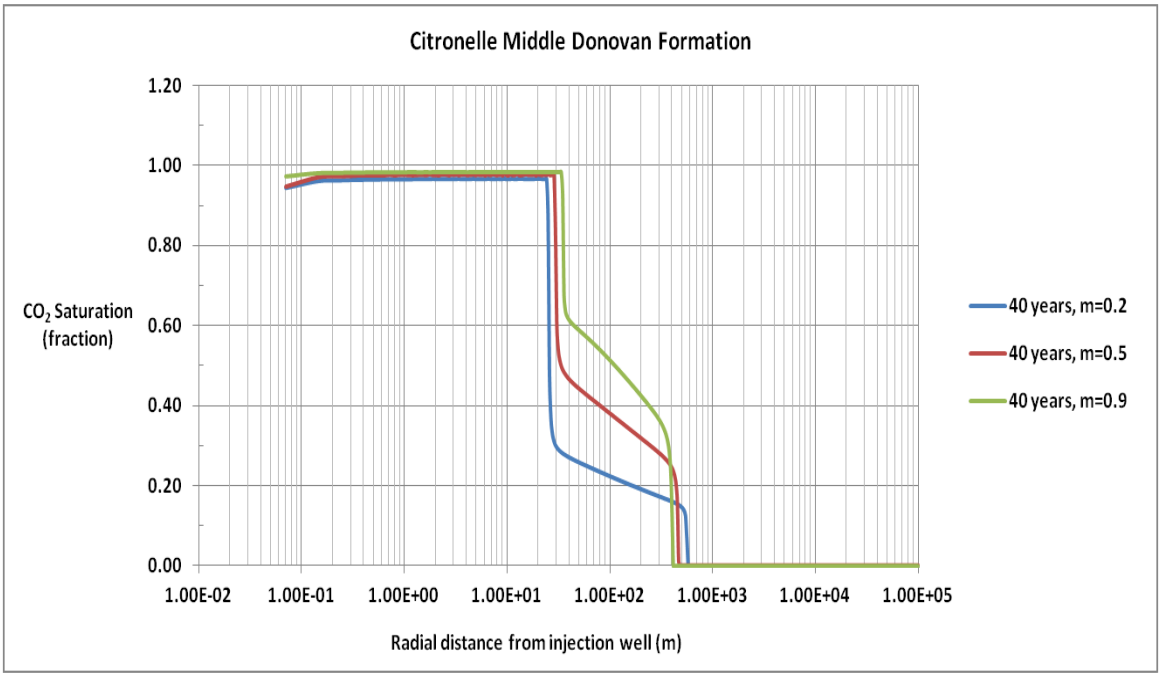

Figure 6.23. TOUGH2-ECO2N simulations with permeability reduction enabled. CO_2 saturation at 40 years, for three values of the van Genuchten parameter, *m*: 0.2, 0.5, and 0.9. The CO_2 injection rate is 36.3 t/day (40.0 short tons/day).

Significant changes in the saturation fraction also take place inside the transition region with changes in the van Genuchten parameter. Figure 6.22, shows that when the value of the parameter, *m*, is 0.2, the CO_2 saturation fraction ranges from a high of 30% at the trailing edge of the transition region, to a low of 17% at its leading edge. This range changes from a high of 47% to a low of 22% when *m* is 0.5, and changes from a high of 63% to a low of 33%, when *m* is 0.9.

Figure 6.23 shows that at 40 years, the CO_2 saturation fraction high and low values, inside the transition region, change by only a small amount compared to the ranges identified at 30 days. At 40 years, the leading edge of the dried-out region is at 25.8 m (84.6 ft), when *m* is 0.9, at 30.4 m (99.7 ft) when *m* is 0.5, and at 35.8 m (117.5 ft) when *m* is 0.2. Figures 6.22, and 6.23, indicate that changes in the value of the van Genuchten parameter cause changes in the CO_2 saturation fraction. Changes in CO_2 saturation, in turn, affect development of the CO_2 plume, with the greatest influence observed in the transition region.

Effects of the van Genuchten on pressure, are shown in Figures 6.24 and 6.25. Figure 6.24 shows the pressure response to changes in the van Genuchten parameter at 30 days. Pressure in the dried-out region reaches a maximum value of 37 MPa (5366.4 psi), when the value of the parameter, *m*, is 0.2, which is 1 MPa (145 psi) below the maximum reservoir pressure of 38 MPa (5511.4 psi). Pressure decreases rapidly inside the transition region, reaching 34.4 MPa (4989.3 psi) at its leading edge. The maximum pressure is 34.8 MPa (5047.3 psi) when *m* is 0.5, and 34.6 MPa (5018.3 psi) when *m* is 0.9. The pressure drops to reservoir pressure for all three values of the van Genuchten parameter, at a radial distance of 2,000 m (6561.7 ft) from the injection well.

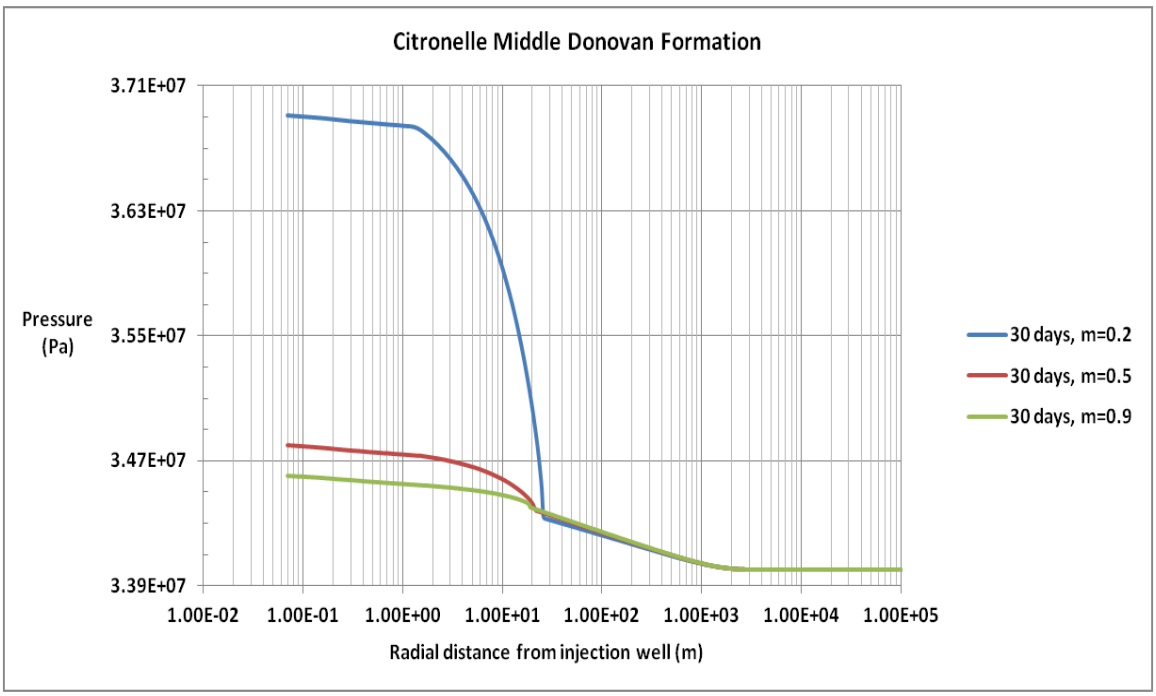

Figure 6.24. TOUGH2-ECO2N simulations with permeability reduction enabled. Pressure at 30 days, for three values of the van Genuchten parameter, *m*: 0.2, 0.5, and 0.9. The CO_2 injection rate is 36.3 t/day (40.0 short tons/day).

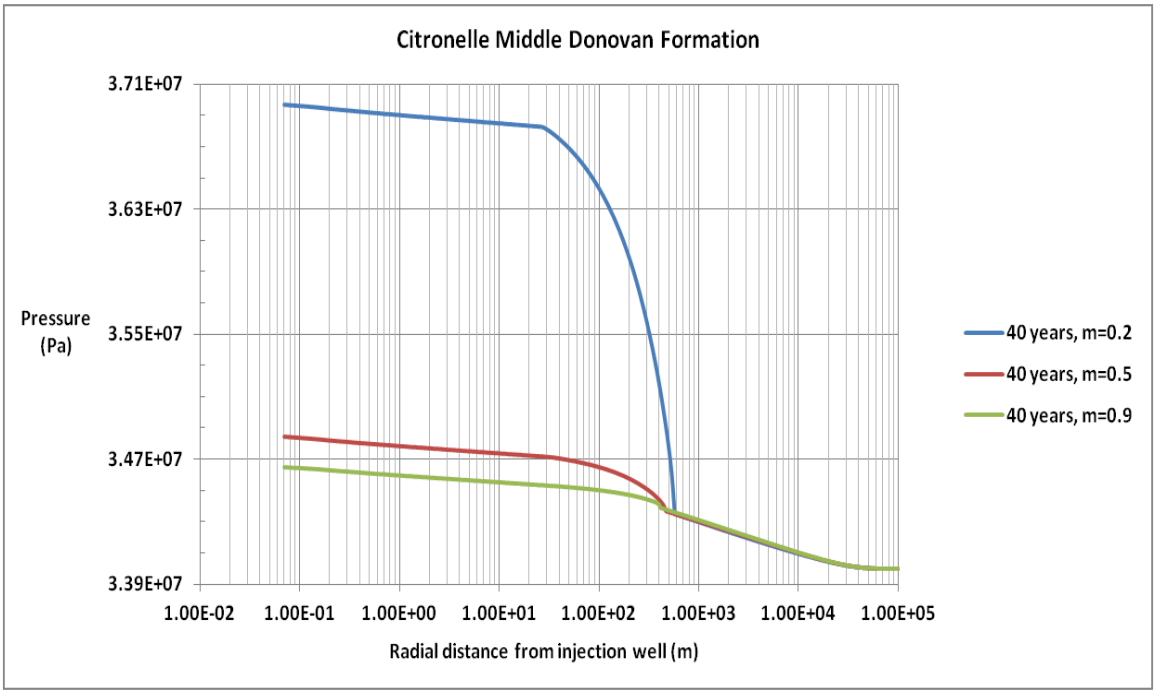

Figure 6.25. TOUGH2-ECO2N simulations with permeability reduction enabled. Pressure at 40 years, for three values of the van Genuchten parameter, *m*: 0.2, 0.5, and 0.9. The CO_2 injection rate is 36.3 t/day (40.0 short tons/day).

Figure 6.25 shows the pressure response to changes in the van Genuchten parameter at 40 years. The maximum pressure in the dried-out region increases by 0.058 Mpa (8.4 psi) when the value of the parameter, *m*, is 0.2. Pressure again decreases rapidly inside the transition region, reaching 34.4 MPa (4989.3 psi) at the leading edge of the region. The maximum pressure increases by 0.048 MPa (7 psi) when *m* is 0.5, and by 0.043 MPa (6.2 psi) when *m* is 0.9. In all cases, pressure decreases to the initial reservoir pressure at a radial distance of 80 km (49.7 miles) from the injection well. Results indicate that changes in the van Genuchten parameter can produce significant changes in formation pressure. The pressure response is exponential, with pressure increasing as the value of the van Genuchten parameter decreases.

Figures 6.26 and 6.27, show the response of CO_2 dissolved in the aqueous phase, to changes in the van Genuchten parameter at 30 days and 40 years, respectively. Figure 6.26, shows that increase in the value of the parameter, *m*, promotes contraction of the transition region. There is a contraction of 8 m (26.3 ft), in the location of the leading edge of the transition region, when changing the value of *m* from 0.2 to 0.9. The contraction increases to 147 m (482.3 ft) at 40 years, as shown in Figure 6.27.

These results indicate that increasing the value of the van Genuchten parameter causes the transition region to contract. The response of dissolved CO_2 to changes in the van Genuchten parameter is the underlying cause for the corresponding changes in CO_2 saturation fraction.

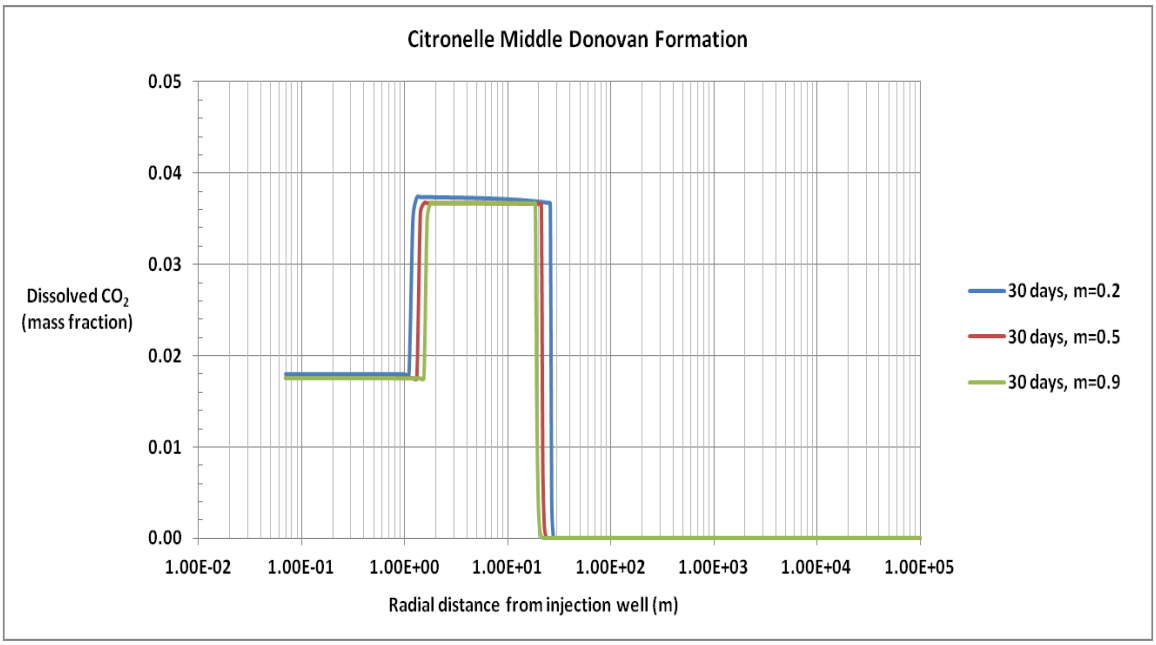

Figure 6.26. TOUGH2-ECO2N simulations with permeability reduction enabled. Dissolved CO_2 in the aqueous phase at 30 days, for three values of the van Genuchten parameter, *m*: 0.2, 0.5, and 0.9. The CO_2 injection rate is 36.3 t/day (40.0 short tons/day).

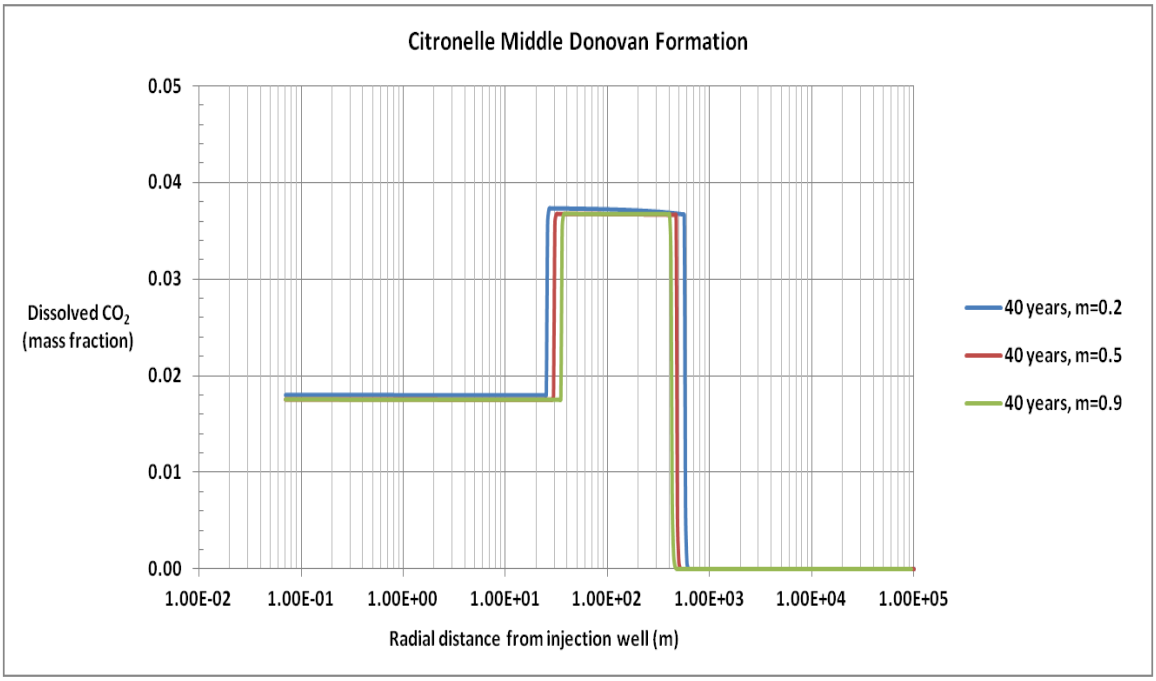

Figure 6.27. TOUGH2-ECO2N simulations with permeability reduction enabled. Dissolved CO_2 in the aqueous phase at 40 years, for three values of the van Genuchten parameter, *m*: 0.2, 0.5, and 0.9. The CO_2 injection rate is 36.3 t/day (40.0 short tons/day).

6.5 TOUGHREACT Simulation of CO_2 Injection into the Middle Donovan

Permeability reduction due to precipitation of solid salt is a consequence of the drying out process. Permeability reduction, however, can also occur from precipitation of minerals as products of chemical reactions among CO_2, brine, and mineral species in the rock matrix. Section 1.4 briefly described some of the processes that may take place when CO_2 is injected into saline-water-bearing formations. Subsection 1.4.1 described the process of mineralization, in which the products of reactions are precipitated carbonate compounds that render the original CO_2 immobile, alleviating long-term stability concerns. The reactions require considerable time to complete and are functions of the formation pressure and temperature.

TOUGH2-ECO2N, used for the simulations discussed in Sections 6.3 and 6.4, does not consider chemical reactions between fluids and formation minerals. As described in Section 3.3.2, TOUGHREACT is a numerical simulator and an extension of the TOUGH code having the ability to simulate chemical processes that may occur during and after CO_2 injection into saline-water formations. A set of simulations using TOUGHREACT, and using the model specifications cited in Section 6.2, was performed to investigate the long-term sequestration of CO_2. The simulation begins with a 40-year CO_2 injection period, followed by a shut-in period that ends at 10,000 years. The simulations were performed using a CO_2 injection rate of 36.3 t/day (40 short tons/day), with the permeability reduction option enabled, and the van Genuchten parameter, *m,* equal to 0.5.

To simulate chemical processes, TOUGHREACT requires as inputs the initial volume fractions of the formation's primary mineral components, and their

corresponding kinetic properties. Table 6.3 summarizes the primary mineral components of the sandstones in the Rodessa Formation at the Citronelle Oil Field, and their average volumetric abundance, established by Hills et al. (2010). The kinetic rate law parameters and reactive surface areas used in the simulations for the components listed in Table 6.3 were obtained from the TOUGHREACT manual (Xu et al., 2004).

Minerals that precipitate during and after CO_2 injection are classified as secondary by TOUGHREACT, and their formation depends on the primary minerals considered. Primary minerals can also dissolve and precipitate due to changing conditions and the chemical reactions induced by the injection of CO_2 into the medium. Based on the list of primary minerals in Table 6.3, the possible secondary minerals that could form during and after CO_2 injection into the Middle Donovan are listed in Table 6.4. These minerals are the products of chemical reactions that take place as result of the CO_2 injection.

Table 6.3. Average initial volume fractions of primary mineral components identified in the sandstones of the Rodessa Formation at the Citronelle Oil Field.

Sandstone Primary Mineral Component	Chemical Formula	Average Volume Fraction in Sandstone
Quartz	SiO_2	0.44
Clay	$Al_2(Si_2O_5)(OH)_4$ $(K,H_3O)(Al,Mg,Fe)_2(Si,Al)_4O_{10}[(OH)_2,(H_2O)]$	0.22
Feldspar	$(K, Na, Ca)AlSi_3O_8$	0.14
Calcite	$CaCO_3$	0.09
Mica	$H_2KAl_3(SiO_4)_3$ $K(Mg, Fe^{2+})_3(Al, Fe^{3+})\ Si_3O_{10}(OH, F)_2$	0.04

Table 6.4. Possible secondary minerals that could form during TOUGHREACT simulation of CO_2 injection into the Middle Donovan, based on the primary minerals of the Rodessa Formation at the Citronelle Field.

Secondary Mineral	Chemical Formula
Magnesite	$MgCO_3$
Dolomite	$CaMg(CO_3)_2$
Siderite	$FeCO_3$
Dawsonite	$NaAlCO_3(OH)_2$
Ankerite	$CaMg_{0.3}Fe_{0.7}(CO_3)_2$
Albite	$NaAlSi_3O_8$
Ca-smectite	$Ca_{0.145}Mg_{0.26}Al_{1.77}Si_{3.97}O_{10}(OH)$
Pyrite	FeS_2

6.6 TOUGHREACT Simulation Results of CO_2 Injection into the Middle Donovan

Output from the simulations was obtained at 100 years, 1000 years, and 10,000 years. The parameters and points of interest are: CO_2 saturation, dissolved CO_2 in the aqueous phase, secondary minerals produced by chemical reactions due to the presence of CO_2, porosity and permeability changes due to the chemical reactions taking place in the formation, and sequestration yield of CO_2 in the solid phase due to mineralization.

Figure 6.28 shows the CO_2 saturation at 100, 1000, and 10,000 years. The results show that at 100 years, the dried-out region is still dominant within 10 m (32.8 ft) from the injection well. At 1000 years, the dried-out region has been reinvaded by the aqueous phase and CO_2 saturation in that region has decreased to 32.4%. The transition region has expanded, and taken over the dried-out region. Although the notion of transition from the dried-out to the mixed phases is no longer pertinent, the location of the transition is

retained as reference through the remainder of this chapter. At 10,000 years, the CO_2 saturation has declined to 12.7%, and the leading edge of the transition region is 680 m (2231 ft) from the injection well.

Figure 6.29, shows dissolved CO_2 in the aqueous phase at 100, 1000, and 10,000 years. The results indicate that the maximum dissolved CO_2 mass fraction is 5% in the transition region, for all three values of the van Genuchten parameter, *m*. At 100 years, the trailing edge of the transition region is at 10 m (32.8 ft), but retracts to 3 m (9.8 ft) at 10,000 years, due to reinvasion of the aqueous phase into the dried-out region. The leading edge of the transition region is 767 m (2516 ft), from the injection well at 10,000 years, which is 87 m (285.4 ft) farther than the leading edge of the CO_2 saturation curve at the same time, shown in Figure 6.28. Expansion of the transition region at 1000 and 10,000 years, shown in Figure 6.29, implies that more CO_2 dissolves into the aqueous phase, leading to more chemical reactions taking place within the transition region.

As CO_2 dissolves into the aqueous phase, it dissociates into H^+ and HCO_3^-. These ions, in turn, react with the minerals in place, and depending on the mineralogy of the formation, the reactions may induce precipitation of carbonate minerals such as ankerite, dawsonite, calcite, dolomite, and siderite. The process effectively converts CO_2 into minerals.

The first five minerals listed in Table 6.4 are carbonate minerals in which CO_2 can be mineralized, during and after CO_2 injection. During the simulation, not all of the

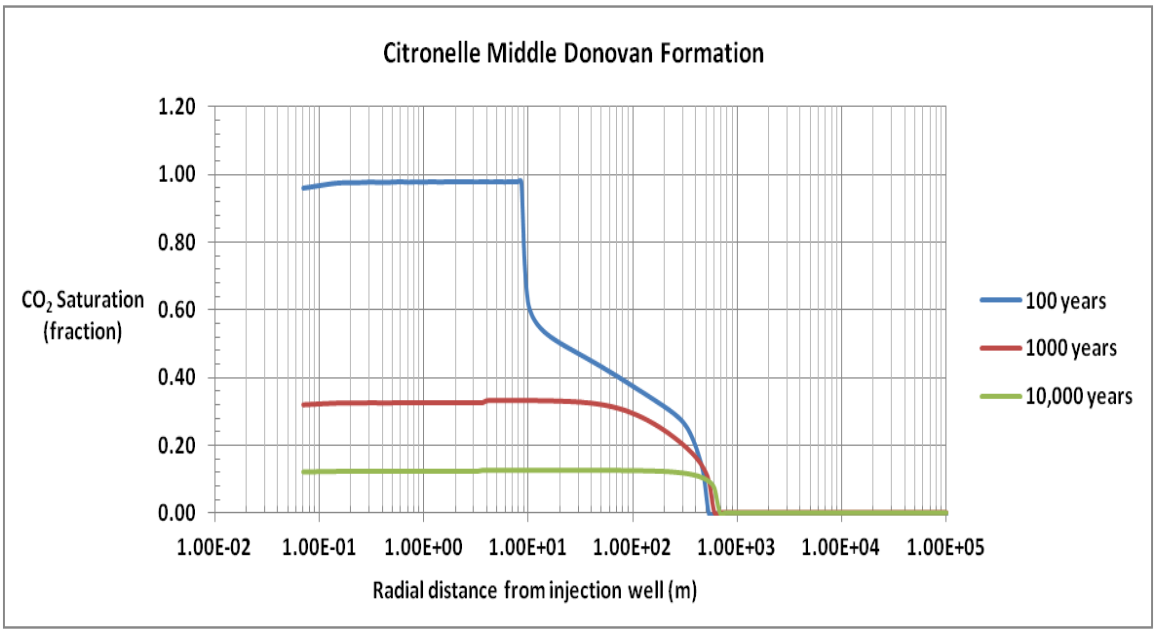

Figure 6.28. TOUGHREACT simulations with permeability reduction enabled. CO_2 saturation at 100, 1000, and 10,000 years. The CO_2 injection rate is 36.3 t/day (40.0 short tons/day). The value of the van Genuchten parameter, *m*, is 0.5.

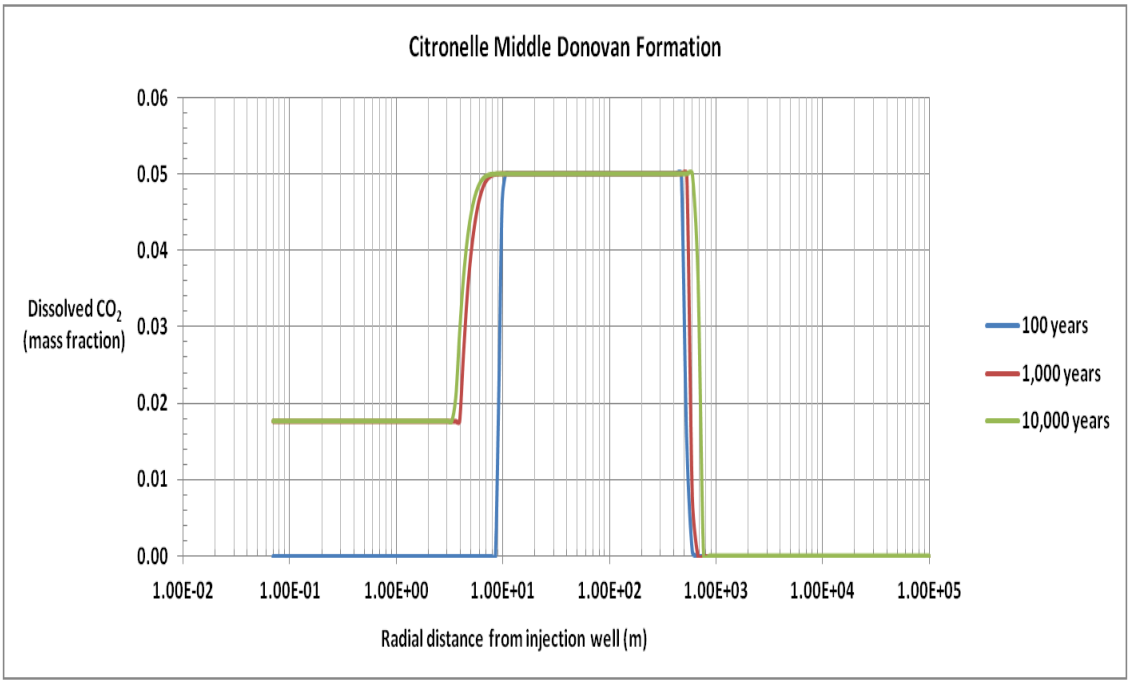

Figure 6.29. TOUGHREACT simulations with permeability reduction enabled. Dissolved CO_2 at 100, 1,000, and 10,000 years. The CO_2 injection rate is 36.3 t/day (40.0 short tons/day). The value of the van Genuchten parameter, *m*, is 0.5.

primary and possible secondary minerals listed in Tables 6.3 and 6.4, were present in the system at a given time. For example, magnesite and dolomite were included in the list of possible secondary mineral phases for the simulations, but did not form, and consequently did not contribute to CO_2 mineralization.

The minerals that formed during the simulation were siderite, dawsonite, and ankerite, each contributing to mineralization of CO_2. The abundances of dawsonite, siderite, and ankerite are shown in Figures 6.30, 6.31, and 6.32, respectively.

Significant dawsonite precipitates due to CO_2 injection and dissolution of alumino-silicate minerals as shown in Figure 6.30. Minor siderite and ankerite precipitations take place, as shown in Figures 6.31 and 6.32, respectively. Ankerite shows an increase in precipitation at 1000 years but then decreases to minimal levels at 10,000 years, because of competition with siderite, for iron.

Another mineral that contributed to mineralization of CO_2 is the primary carbonate mineral calcite ($CaCO_3$), shown in Figure 6.33, which, after minor dissolution near the injection well at 100 years, increases in abundance. Calcite precipitation requires a source of calcium cations which were provided by the dissolution of oligoclase. Figure 6.34 shows that dissolution of oligoclase, in the first 100 years, strongly correlates to the formation of calcite during the same time period, as shown in Figure 6.33.

Other primary and secondary minerals that formed or dissolved during the simulation include quartz (SiO_2), clay in the form of kaolinite ($Al_2Si_2O_5(OH)_4$), mica in the form of illite ($K_{0.6}Mg_{0.25}Al_{1.8}(Al_{0.5}Si_{3.5}O_{10})(OH)_2$), and feldspar in the form of oligoclase ($CaNa_4A_{l6}Si_{14}O_{40}$).

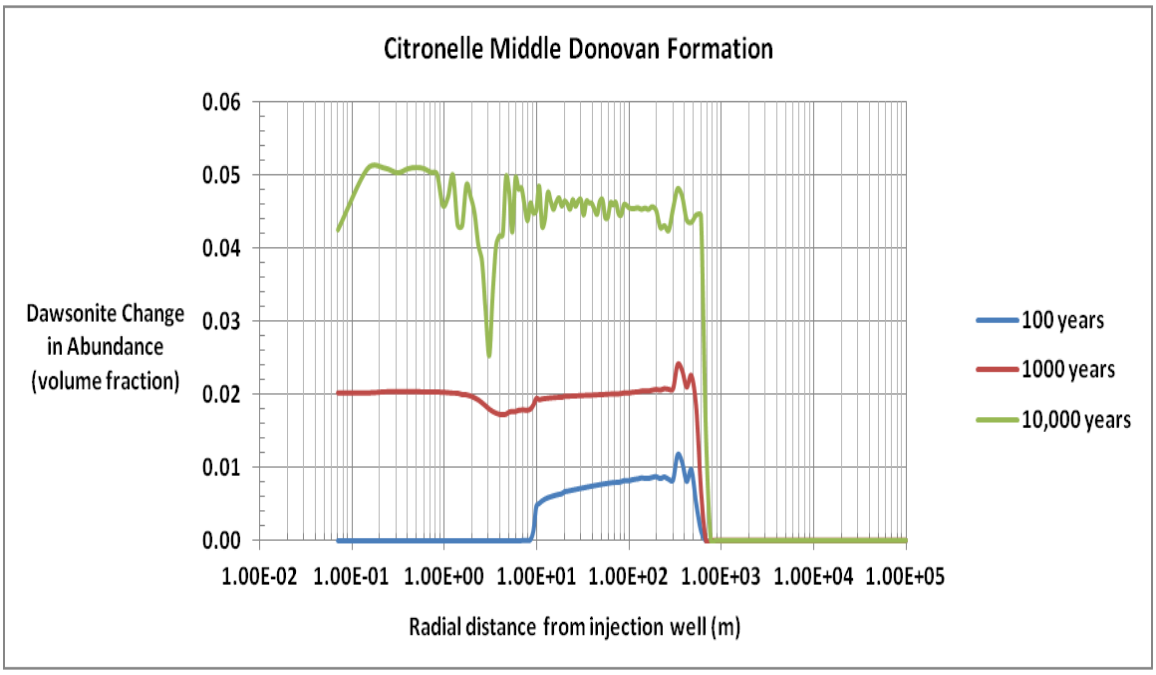

Figure 6.30. TOUGHREACT simulations with permeability reduction enabled. Dawsonite change in abundance at 100, 1000, and 10,000 years. The CO_2 injection rate is 36.3 t/day (40.0 short tons/day). The value of the van Genuchten parameter, *m*, is 0.5.

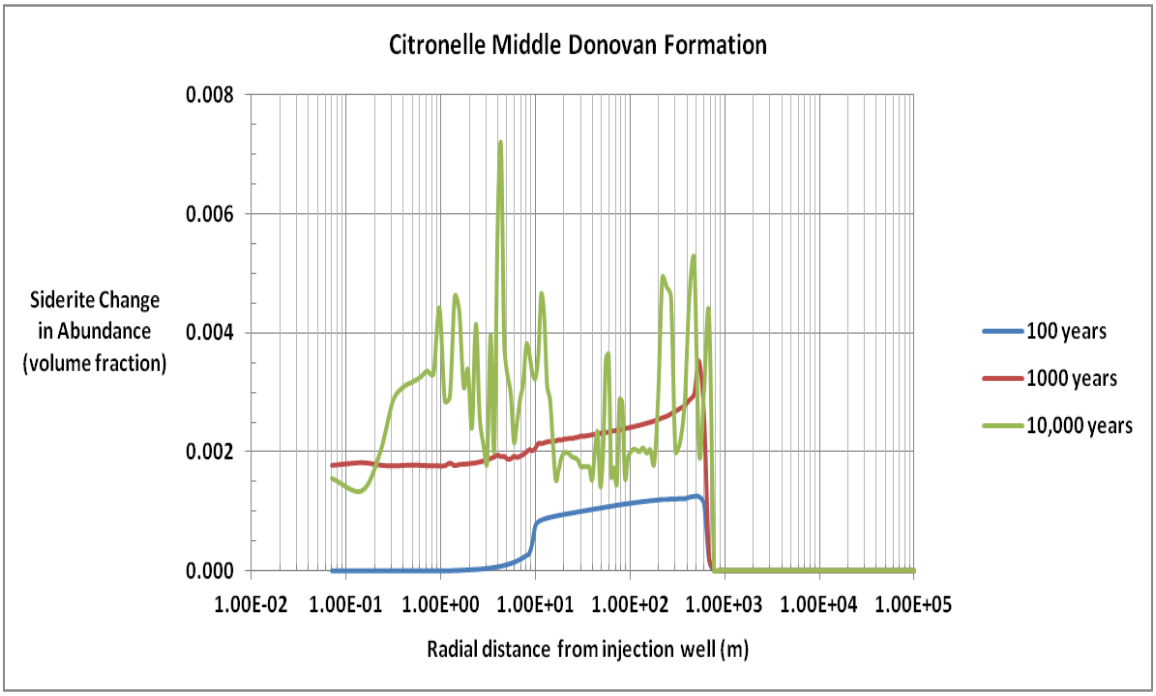

Figure 6.31. TOUGHREACT simulations with permeability reduction enabled. Siderite change in abundance at 100, 1000, and 10,000 years. The CO_2 injection rate is 36.3 t/day (40.0 short tons/day). The value of the van Genuchten parameter, *m*, is 0.5.

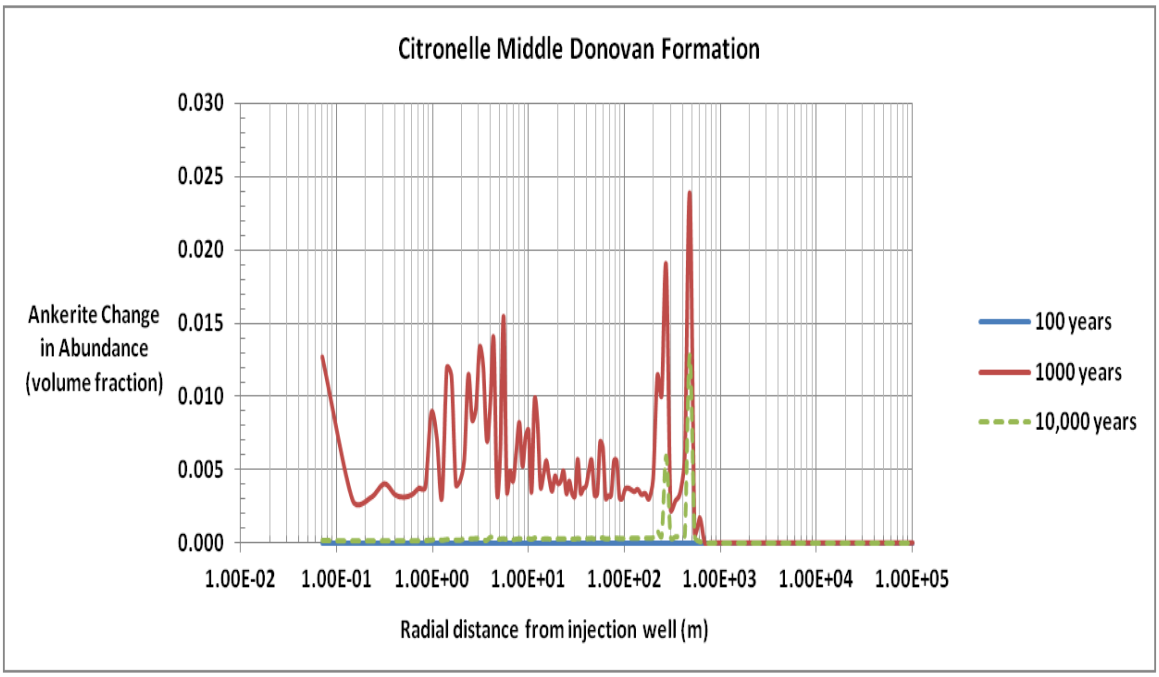

Figure 6.32. TOUGHREACT simulations with permeability reduction enabled. Ankerite change in abundance at 100, 1000, and 10,000 years. The CO_2 injection rate is 36.3 t/day (40.0 short tons/day). The value of the van Genuchten parameter, *m*, is 0.5.

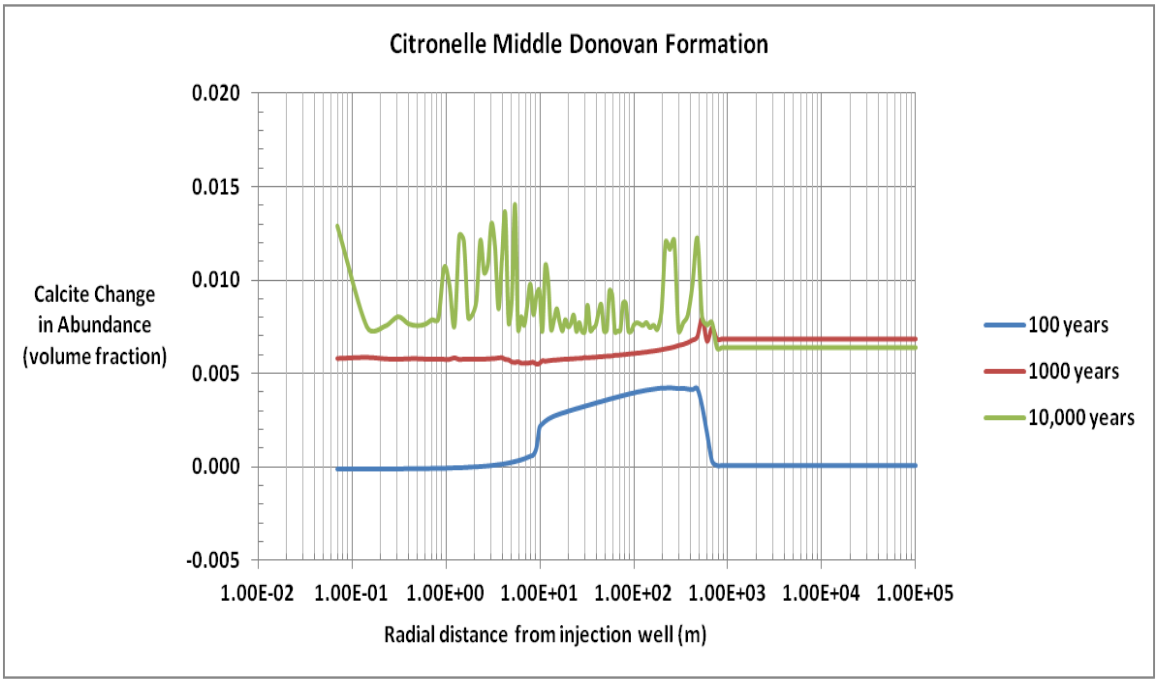

Figure 6.33. TOUGHREACT simulations with permeability reduction enabled. Calcite change in abundance at 100, 1000, and 10,000 years. The CO_2 injection rate is 36.3 t/day (40.0 short tons/day). The value of the van Genuchten parameter, *m*, is 0.5. Positive values denote precipitation, and negative values dissolution.

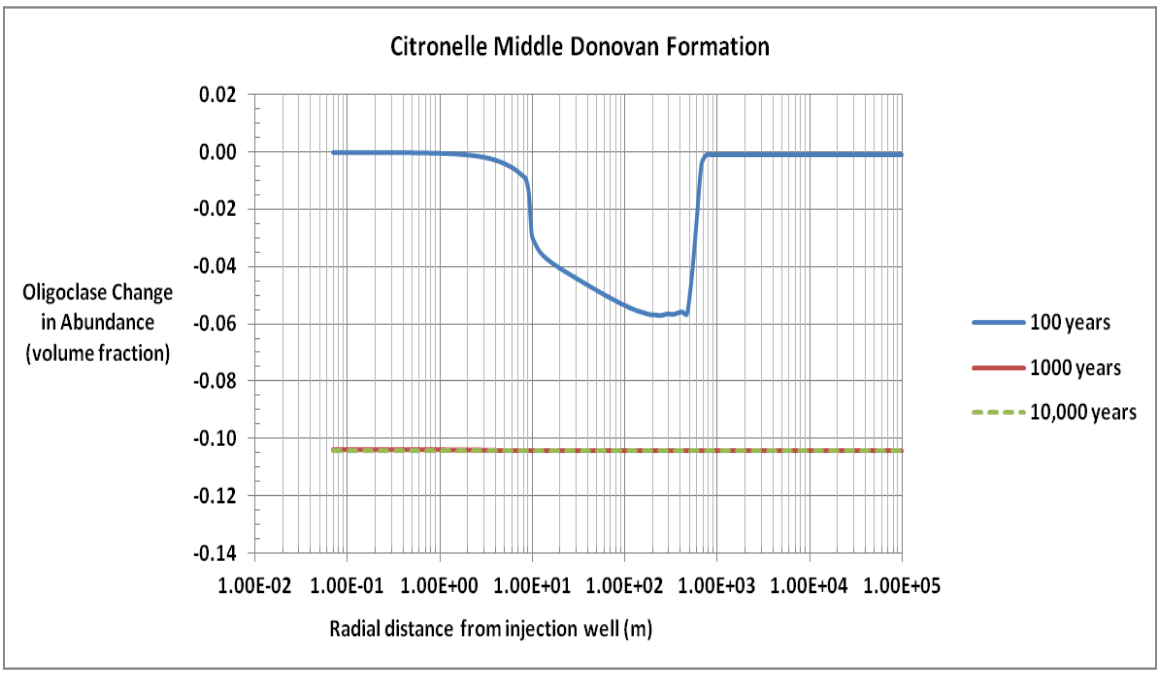

Figure 6.34. TOUGHREACT simulations with permeability reduction enabled. Oligoclase change of abundance, at 100, 1000, and 10,000 years. The CO_2 injection rate is 36.3 t/day (40.0 short tons/day). The value of the van Genuchten parameter, *m*, is 0.5. Positive values denote precipitation, and negative values dissolution.

Quartz and clays comprised 66 vol% of the minerals in the sandstones of the Middle Donovan, as listed in Table 6.3. These minerals, although not contributing to CO_2 mineralization, are important because they also precipitate and dissolve, changing formation porosity and permeability, thus modifying fluid flow. Changes in the abundance of quartz and kaolinite are shown in Figures 6.35 and 6.36 respectively. Figure 6.35, shows that quartz precipitation increases with time, due to the dissolution of kaolinite observed in Figure 6.36.

Dissolution and precipitation of minerals is also affected by changes in pH. Figure 6.37 shows the levels of pH at 100, 1000, and 10,000 years. At 100 and 1000 years, pH, at distances less than 1 m (3.28 ft) from the injection well, has decreased to 4.8, under the influence of the injected CO_2. At 10,000 years, and within the same range, pH has

increased to 6.1 as CO_2 saturations decreased. Figure 6.37 also shows that the pH decreases and stabilizes at 5.9 in the transition region at 100 and 1000 years, as the formation of carbonate minerals releases H^+, and as the dissolution of kaolinite and illite consumes OH^-. Precipitation and dissolution continue, and pH is suppressed to 5.7 at 10,000 years. In the aqueous region, pH increases to 9 at 100 years, as kaolinite and oligoclase dissolve. The levels of pH stabilize to 6.7, in the aqueous region, at 10,000 years. The low pH values in the vicinity of the injection well, indicate possible acidification in that region, which may lead to deterioration of cement and casing. Close monitoring of the integrity of the wells will be necessary, and procedures to buffer the pH may have to be implemented.

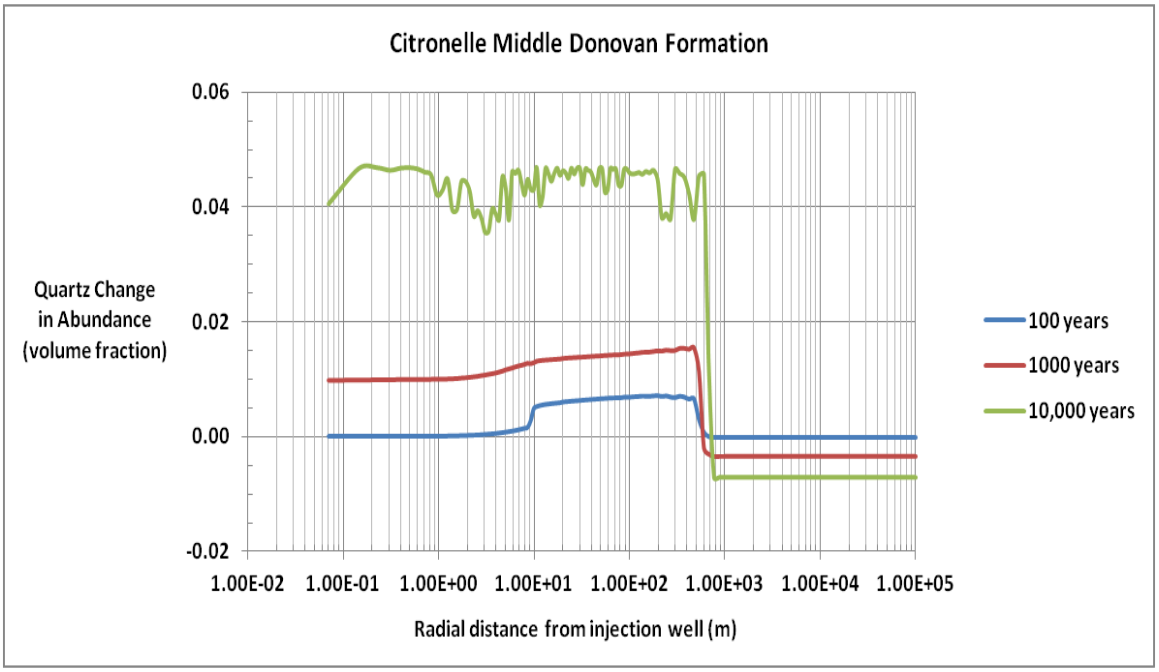

Figure 6.35. TOUGHREACT simulations with permeability reduction enabled. Quartz change in abundance at 100, 1000, and 10,000 years. The CO_2 injection rate is 36.3 t/day (40.0 short tons/day). The value of the van Genuchten parameter, *m*, is 0.5. Positive values denote precipitation, and negative values dissolution.

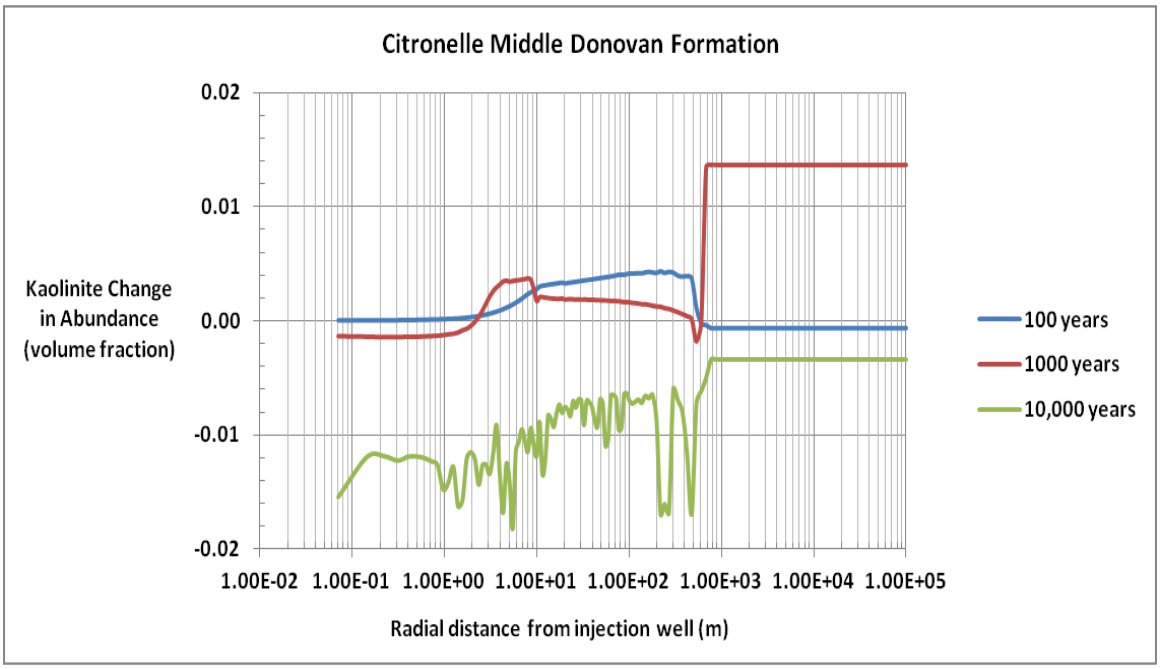

Figure 6.36. TOUGHREACT simulations with permeability reduction enabled. Kaolinite change in abundance, at 100, 1000, and 10,000 years. The CO_2 injection rate is 36.3 t/day (40.0 short tons/day). The value of the van Genuchten parameter, *m*, is 0.5. Positive values denote precipitation, and negative values dissolution.

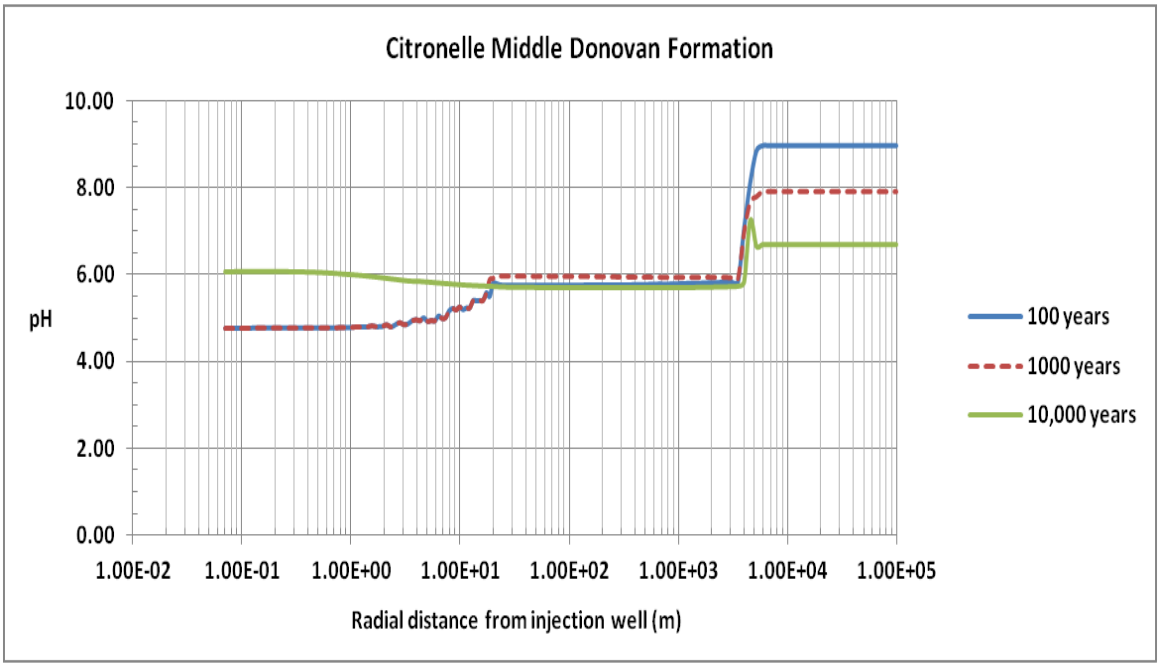

Figure 6.37. TOUGHREACT simulations with permeability reduction enabled. pH of aqueous phase at 100, 1000, and 10,000 years. The CO_2 injection rate is 36.3 t/day (40.0 short tons/day). The value of the van Genuchten parameter, *m*, is 0.5.

Precipitation and dissolution of minerals affect porosity and permeability of the formation. The precipitation and dissolution of the minerals cited in this section, during and after CO_2 injection into the Middle Donovan, produced the changes in porosity and permeability illustrated in Figures 6.38 and 6.39, respectively.

Porosity, as shown in Figure 6.38, is unaffected near the injection well at 100 years, but decreases from its initial value of 13% to almost 12% near the leading edge of the transition region. At 1000 years, porosity decreases to 10.5% in the injection well grid block, due to precipitation of solid salt and carbonate minerals. Moving outward from the well porosity quickly rises to 11.5%, then undergoes another significant decrease to 9.5%, near the leading edge of the transition region. At 10,000 years porosity has decreased to an average of 10.5% in the transition region, and 12.8% in the aqueous region.

Permeability, as shown in Figure 6.39, follows similar trends to the porosity. It is unaffected near the injection well at 100 years, from its initial value of 13 mdarcy, but decreases to a low of 10.5 mdarcy near the leading edge of the transition region. In the injection well grid block it decreases to 7.1 and 6.7 mdarcy at 1000 and 10,000 years, respectively. At 10,000 years, permeability averages 7 mdarcy in the transition region and 12.6 mdarcy in the aqueous region.

Siderite, ankerite, dawsonite, and calcite are the minerals in which CO_2 is converted to a solid, during and after CO_2 injection into the Middle Donovan. The cumulative sequestration of CO_2 by carbonate formation is shown in Figure 6.40.

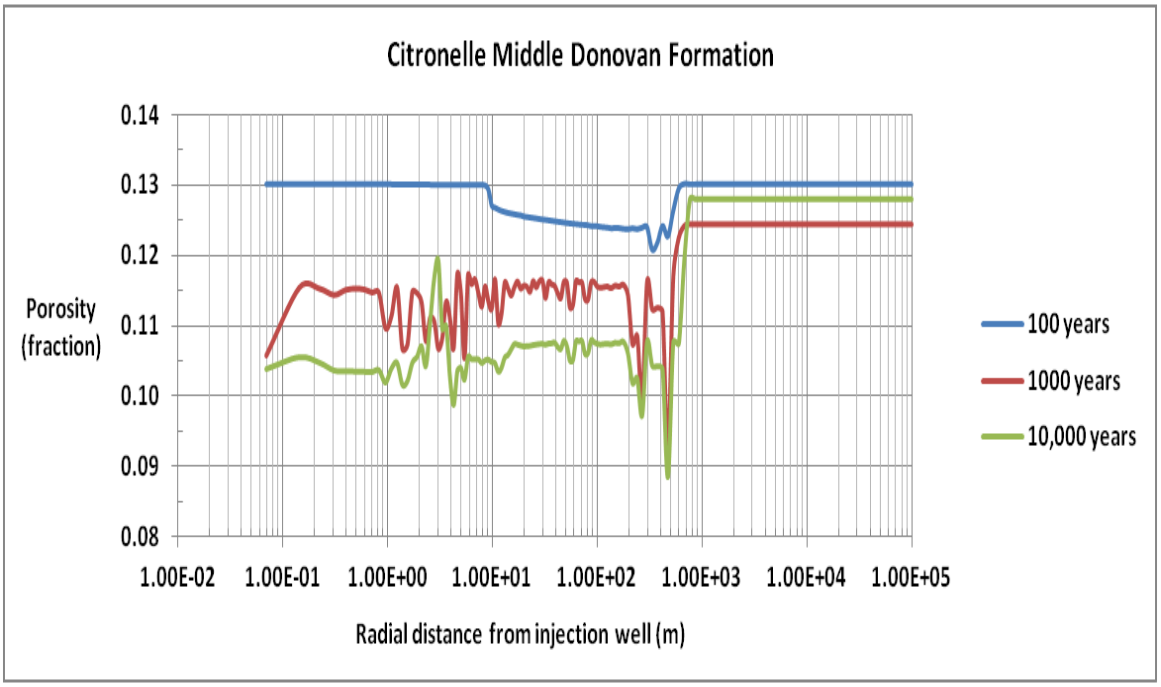

Figure 6.38. TOUGHREACT simulations with permeability reduction enabled. Porosity at 100, 1000, and 10,000 years. The CO_2 injection rate is 36.3 t/day (40.0 short tons/day). The value of the van Genuchten parameter, *m*, is 0.5.

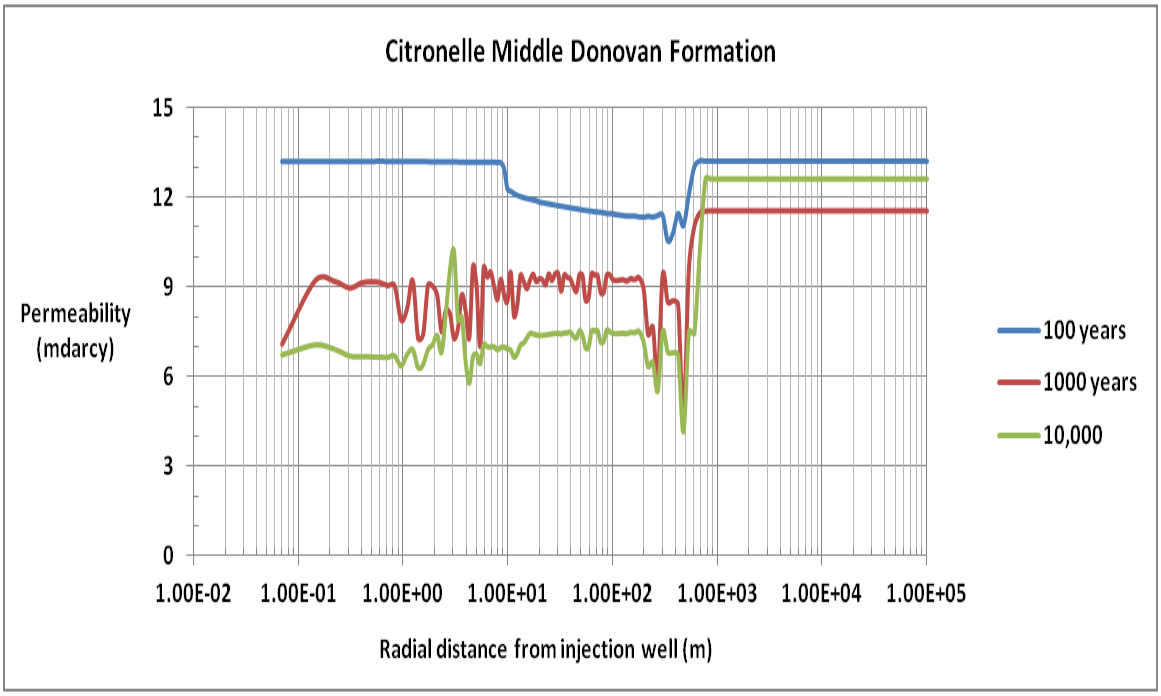

Figure 6.39. TOUGHREACT simulations with permeability reduction enabled. Permeability at 100, 1000, and 10,000 years. The CO_2 injection rate is 36.3 t/day (40.0 short tons/day). The value of the van Genuchten parameter, *m*, is 0.5.

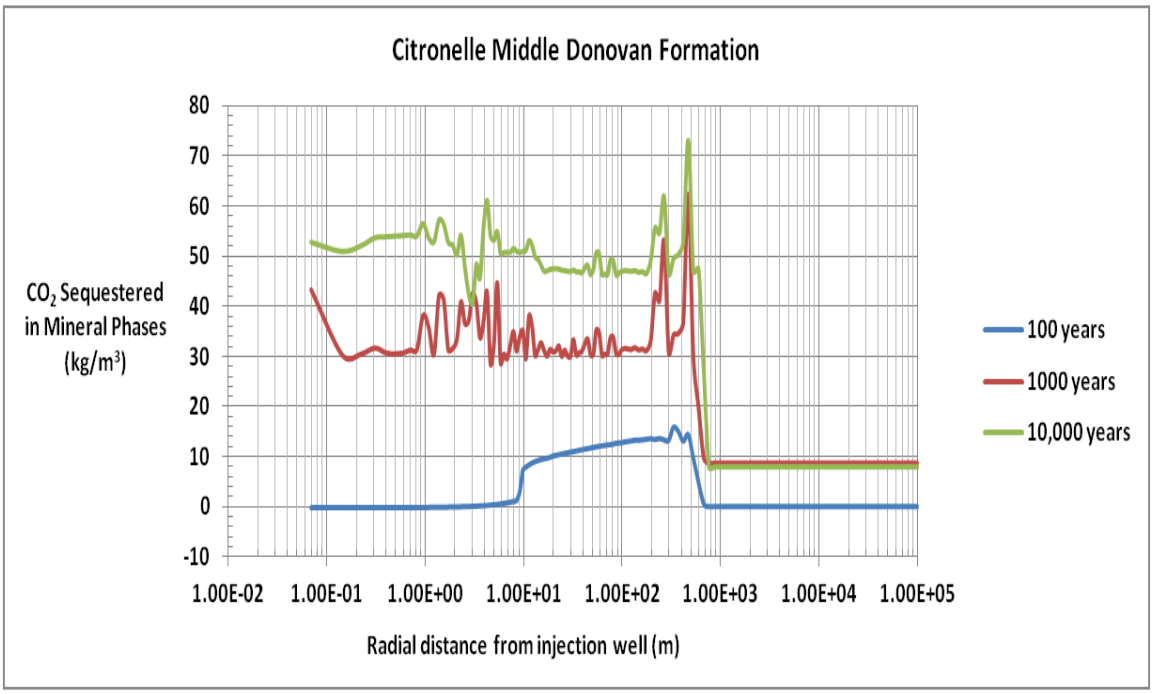

Figure 6.40. TOUGHREACT simulations with permeability reduction enabled. Sequestration of CO_2 by carbonate precipitation at 100, 1,000, and 10,000 years. The CO_2 injection rate is 36.3 t/day (40.0 short tons/day). The value of the van Genuchten parameter, *m*, is 0.5. Carbonate minerals were, in order of abundance: dawsonite, siderite, and ankerite. Positive values denote precipitation, and negative values dissolution.

The maximum mineralization of CO_2 in carbonates reaches 73 kg/m^3 (4.56 lb/ft^3) of formation, near the leading edge of the transition region. The average value over the entire CO_2 plume is 50 kg/m^3 (3.12 lb/ft^3) of formation.

The total amount of CO_2 injected at the end of the 40-year injection period is 530,000 t (584,224 short tons). A 1000 MWe coal-fired power plant, operating at 35% efficiency, emits approximately 7.9 x 10^6 t (8.7 x 10^6 short tons) of CO_2 per year. This rate of CO_2 production would require 597 wells, each injecting at a rate of 36.3 t/day (40 short tons/day) into the Middle Donovan formation, to store 100% of the CO_2.

The impetus for the simulations performed and presented in this chapter was the benefit from having a site for interim injection of CO_2 into the Middle Donovan Sands during upset conditions, or maintenance of equipment associated with enhanced oil recovery. It is also possible that the Middle Donovan may become, along with the Upper and Lower Donovan formations, an attractive carbon storage reservoir when oil recovery from the Citronelle field is no longer profitable. It is implicit in the results obtained and discussed, that any interim CO_2 injection schedule would be feasible as long as its parameters resemble those of the simulations presented in this chapter.

CHAPTER 7

CARBON DIOXIDE LEAKAGE POTENTIAL FROM THE DONOVAN SANDS

7.1 Introduction

As discussed in Section 1.1, the objective of geologic sequestration is the long-term storage of CO_2 that would otherwise have been released to the atmosphere. Therefore, success of geologic sequestration is critically dependent on the effectiveness of the trapping mechanisms introduced in Section 1.4, to confine the injected CO_2 within the bounds of the intended storage reservoir for thousands of years. Migration of injected CO_2 away from the intended storage reservoir is undesirable, and is considered as *leakage*. However, the term leakage does not refer only to migration resulting in net loss of CO_2 to the atmosphere but also to any vertical or lateral migration of CO_2, beyond the confines of the intended plume height and plan area. This stricter characterization is introduced because the confines of the plume constitute a containing system, rendering any migration of CO_2 beyond those boundaries as leakage.

It is important to assess the potential for CO_2 leakage prior to implementing geologic sequestration. Leakage mechanisms and pathways that may exist or have the likelihood to develop within the storage formation must be identified, and the site should be actively monitored to detect CO_2 leakage that may occur during and after the injection period. In the event that leakage is detected, corrective measures must be implemented.

The most likely types of leakage mechanisms and pathways, by which mobile CO_2 could migrate, include loss of cap rock seal integrity due to natural or mechanically induced faults and fractures, loss of seal integrity in well bores or casing, and seismic activity. The nature of these leakage mechanisms and pathways introduces a high degree of uncertainty associated with the ultimate fate of migrating CO_2. However, uncertainty can be significantly reduced with knowledge of the properties of the storage reservoir, overlying caprock formations, and mechanisms influencing CO_2 migration.

7.2 Leakage Potential from the Donovan Sands

The formations into which CO_2 will be injected can be separated by operational objective into the following two categories: (a) the hydrocarbon-bearing sandstones of the Upper and Lower Donovan for EOR; and (b) the saline-water-bearing sandstones of the Middle Donovan for interim injection during interruptions in the CO_2-EOR operations in the Upper and Lower Donovan. However, in the investigation of leakage potential from the Donovan Sands, the scope of these objectives is expanded to include respectively: (a) the possibility of large-scale CO_2 injection, for the purpose of long-term storage, into the depleted oil reservoirs of the Upper and Lower Donovan, following the end of CO_2-EOR; and (b) the possibility of 40-year continuous CO_2 injection into the saline-water-bearing sandstones of the Middle Donovan, as discussed in Section 6.1. Results obtained for the expanded scope of the CO_2 injection, will also be applicable to leakage potential under any other injection scenario of narrower scope.

In assessing CO_2 leakage from the Donovan Sands, only the fraction of injected CO_2 that is mobile and able to migrate is considered. Migration of CO_2 that has been

rendered immobile by various mechanisms is not considered. For example, as discussed in Section 2.3.1, CO_2 injected into the Upper and Lower Donovan reservoirs during EOR will form a single miscible phase with residual hydrocarbons because the depth of the reservoirs is sufficient to assure that their pressure remains above the MMP. When CO_2-EOR operations are terminated and production wells are shut-in, the CO_2 remaining in place will be in a miscible state with the residual oil. It is unlikely that CO_2, miscible in oil, will migrate away from the sandstones of the Upper and Lower Donovan, since the oil will be confined by the same trapping mechanisms that kept it in place for many millennia. However, during EOR, contact of CO_2 with oil will be hindered by reservoir heterogeneities which can cause a fraction of the injected CO_2 follow preferential paths having high mobility ratios, bypassing the oil. Water blocking, due to high water saturations after waterflooding, may also shield some portions of oil from coming into contact with CO_2.

The volume fraction of CO_2 that does not come into contact with oil, and is not recovered at the production wells during EOR, will be free to migrate vertically or laterally. It is assumed that during the injection period laterally migrating CO_2 will be driven by pressure drawdown toward the production wells where it will be recovered. Following the injection period it is assumed that hydrostatic conditions will control migration. Furthermore, due to the absence of any natural water drive in the oil reservoirs it is assumed that transverse migration of CO_2 under the influence of formation water drive is not significant and therefore it is not considered.

There are no reports of seismic activity in the region, and there are no major fractures or faults identified within the Donovan formation. Hence, leakage potential

associated with these features is not considered in the present work. Moreover, fractures induced by salt expansion due to salt formation and precipitation during and after CO_2 injection, are also not considered.

Considering the assessments and assumptions presented in this section, CO_2 leakage potential from the Donovan Sands is classified into the following two categories: (a) vertical leakage through pores in seal layers; and (b) vertical leakage through well bores or casings penetrating the Donovan formation, among the active or abandoned wells associated with oil recovery operations, whose integrity has been compromised.

7.3 Seal Formations Controlling Leakage from the Donovan Sands

The ability of a rock formation to serve as a seal is referred to as the *sealing capacity* of the rock, and it is a function of the rock's permeability and *capillary entry pressure*, which is the minimum pressure required to displace connate water from the pores of the seal rock. Nelson et al. (2005) classified seals into *membrane* and *hydraulic*. A rock formation is called a membrane seal if leakage is through pre-existing pores and described as an hydraulic seal if leakage is through fractures opened by reservoir pressure. Song and Zhang (2013), reported that argillaceous rocks, like shale, are very good seals because they exhibit low permeability and high capillary entry pressure. Those authors also reported that evaporites are excellent seals because they exhibit even lower permeability and higher capillary entry pressure than shales.

The potential leakage categories listed in Section 7.2, concern vertical migration of CO_2 from the Upper, Middle, and Lower Donovan sandstone reservoirs. Therefore, the

formations of greatest importance are those that can serve as seals against vertical migration of CO_2 from the sandstone reservoirs. Candidate seal formations are: (a) the shale in the Donovan Formation; and (b) the Mooringsport Shale and Ferry Lake Anhydrite caprocks overlying the Donovan Formation. The stratigraphic position of the Donovan Sands in relation to the Mooringsport Formation and Ferry Lake Anhydrite is shown in Figure 7.1.

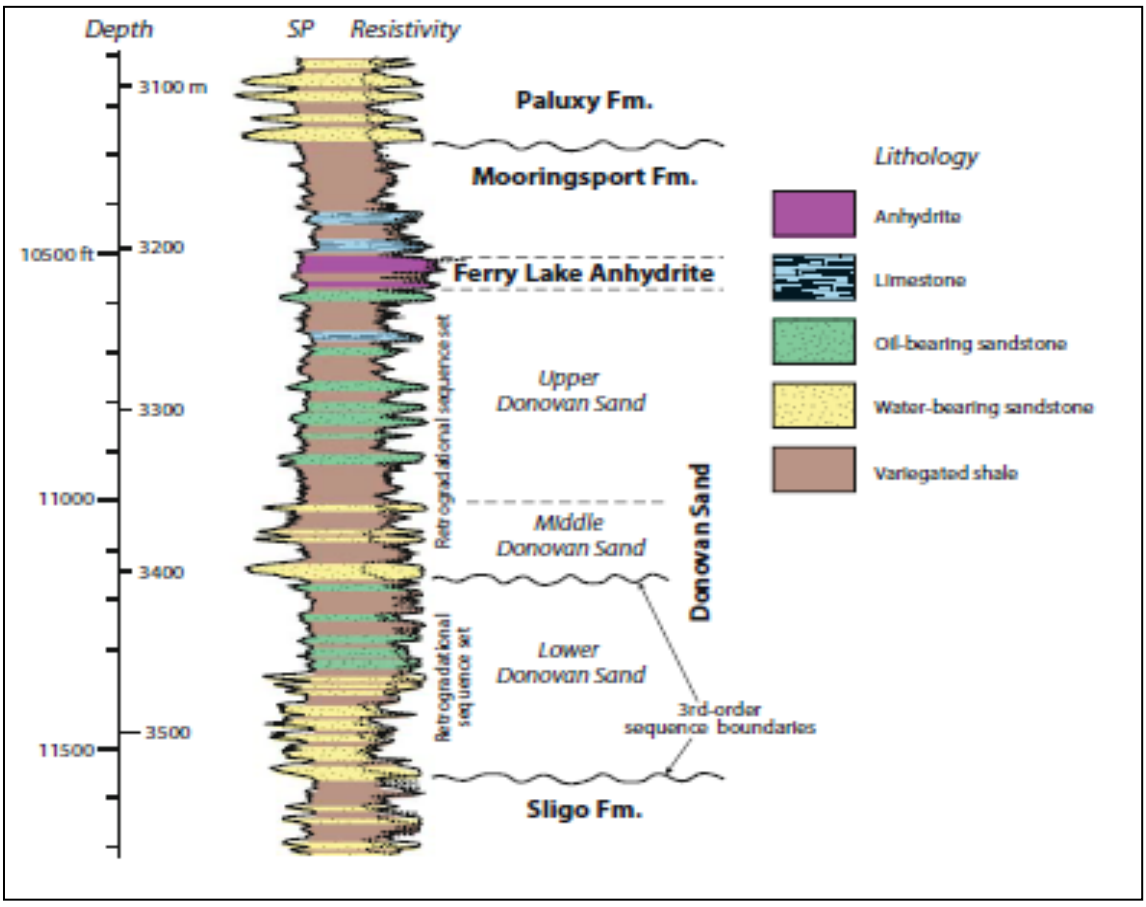

Figure 7.1. Stratigraphic section with spontaneous potential (SP) and resistivity well logs of the Mooringsport Formation, Ferry Lake Anhydrite, and Donovan Sands in the Citronelle Oil Field. Figure reproduced, with permission, from R. A. Esposito, J. C. Pashin, D. J. Hills, P. M. Walsh, 2010.

7.3.1 Donovan Formation Shale

All sandstone reservoirs in the Upper, Middle, and Lower Donovan are imbedded in shale which comprises the rock matrix of the Donovan formation. The shale, indicated as *variegated* (i.e., red and gray) shale in the legend of Figure 7.1, consists of poorly sorted *siliciclastic* sediments, with small amounts of gray to brown broken shale irregularly interbedded with siltstone, asphaltene, and a high fraction of mica (Eaves, 1976).

7.3.2 Mooringsport Shale and Ferry Lake Anhydrite

The Mooringsport Formation is the interval between the top of the Ferry Lake Anhydrite and the base of the Paluxy Formation. It consists of red, dark red, or maroon shale interbedded with very-fine- to fine-grained sandstones. (Mancini et al., 1999). The Ferry Lake Anhydrite, appearing just below the Mooringsport formation, is a series of anhydrites interbedded with shale and limestone (Raymond, 1995).

Although both formations can serve as long-term seals against upward CO_2 migration from the underlying reservoirs of the Donovan Sands, the Ferry Lake Anhydrite is of greater significance due to its contact horizon with the shale overlying the uppermost oil reservoirs in the Upper Donovan. Furthermore, because the permeability of the Ferry Lake Anhydrite is lower than the permeability of the Mooringsport Shale, it is unlikely that in instances whenCO_2 migration is not contained by the Ferry Lake Anhydrite, it would be contained by the Mooringsport Formation.

7.4 Analysis of CO_2 Leakage Potential from the Donovan Sands

The analytical methods used to investigate CO_2 migration and the sealing efficiency of low permeability rocks are based on principles and concepts developed in the study of oil and ground-water reservoirs. These principles describe displacement processes in oil reservoirs or water aquifers, and the properties of the formations in which these reservoirs are found. Modifying the principles to describe CO_2 behavior has been the basis of CO_2-EOR studies for decades, and more recently of CO_2 sequestration. The subsections that follow present the fundamental principles, concepts, and assumptions applied in assessing leakage potential from the Donovan Sands.

7.4.1 Wettability and Capillary Pressure

Wettability refers to the interaction between fluids (including gases) and a solid surface. It is used to describe the tendency of a fluid to preferentially adhere to a solid surface in the presence of a second, immiscible fluid. In the case of CO_2 sequestration, wettability refers to the degree to which CO_2 adheres to the rock surface in the presence of brine. The degree of preference is measured by the contact angle that an elemental volume (*globule*) of CO_2 makes with the rock surface, while resting on it, surrounded by brine, as shown in Figure 7.2. If the contact angle between the CO_2 globule and the rock surface is approximately zero then the rock is considered *water-wet*. In this case the brine is called the *wetting phase* and CO_2 the *nonwetting* phase. As the contact angle increases the wettability changes from mostly water-wet to mostly CO_2-wet. When the contact angle approaches 180° the rock is considered CO_2-wet. In this case CO_2 is the wetting phase and brine the nonwetting phase.

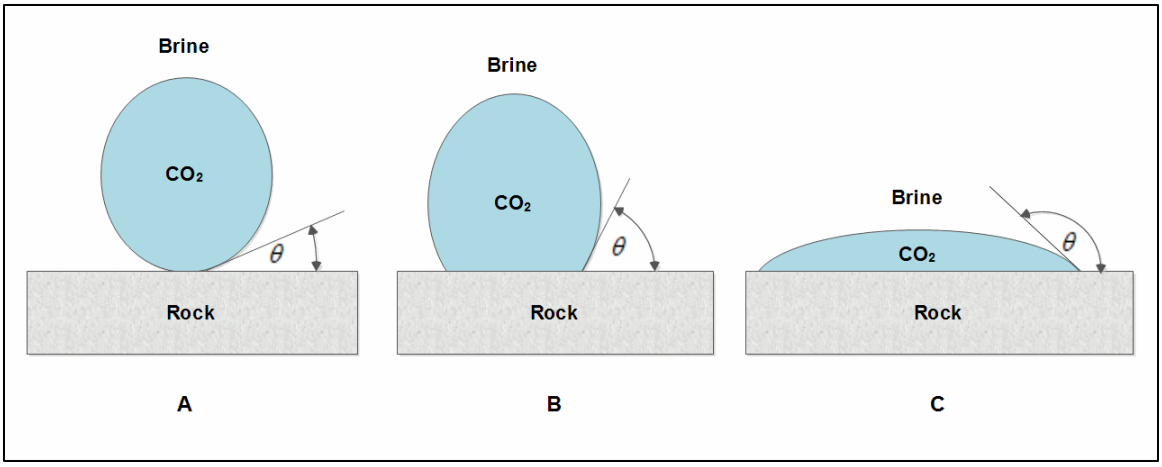

Figure 7.2. Surface tension of a CO_2 globule immersed in brine and in contact with the rock surface. In a water-wet rock the CO_2 globule shape is such that its surface boundary, at the contact point with the rock, creates a low acute contact angle (θ) with the rock surface (part A). On an intermediate-wet rock surface the globule forms a bead but with a higher acute contact angle resulting from the balance of the interfacial tension forces (part B). On a CO_2-wet rock surface the globule spreads producing an obtuse contact angle (part C) (after Chalbaud et al., 2009).

It is assumed that the sandstone reservoirs in the Upper, Middle, and Lower Donovan are *water-wet*. The assumption is based on the prevailing theory that reservoirs were completely saturated with formation water prior to hydrocarbon migration from the source rock. Moreover, the Upper and Lower Donovan reservoirs have been subjected to over 50 years of water injection for secondary oil recovery, which continues to date. The Middle Donovan, which was flushed of its hydrocarbons by formation water (Eaves, 1976), is also assumed to be water-wet.

Measuring contact angles in a formation to determine wettability is not practical. However, wettability influences the capillary-pressure–saturation relationship, which control fluid distribution in the formation. When two or more immiscible fluids contact each other—for example, while flowing through the narrow pathways in a formation—a

distinct interface develops between the contacting phases due to interfacial tension effects. Pressure on the concave side of the curved surface exceeds that on the convex side (*Laplace pressure*), and the resulting net pressure is defined as the capillary pressure. The fluid on the concave side is the nonwetting fluid while that on the convex side is the wetting fluid.

Capillary pressure for CO_2 stored in a saline-water-bearing formation can be expressed by the standard Young-Laplace equation (Chalbaud et al., 2009):

$$P_c = P_{CO_2} - P_{brine} = \frac{2\gamma cos\theta}{R} \quad 7.1$$

where, γ (N/m) is the interfacial tension on the boundary between the brine and the CO_2 phases, θ (rad) is the wetting angle (contact angle of CO_2 through the brine phase), and R (m) is the effective pore radius, which is considered to be equal to the radius of the largest sphere, constrained by the surrounding solid matrix, that can be inserted at the point of the migration pathway where the capillary pressure is measured. The wetting phase is the brine and the nonwetting phase is CO_2.

Equation 7.1 states that the pressure difference across the interface between the two immiscible fluids is proportional to the surface tension between the two phases and the wetting angle, but is inversely proportional to the effective radius of the pathway. The equation is only valid under capillary equilibrium which implies a no flow condition. Disturbance to the capillary equilibrium will cause the fluids to flow.

In water-wet reservoirs, under hydrostatic conditions, the dominant forces controlling CO_2 migration would be the competing forces of buoyancy (CO_2) and

capillary entry pressure (water). Hydrostatic conditions prevail when the vertical thickness of the reservoir is considerably smaller than the lateral dimension of the reservoir, as suggested by the theory of *Vertical Flow Equilibrium* (VFE) discussed in the following section.

7.4.2 Vertical Flow Equilibrium

Analytical results for displacement processes in porous media are often obtained based on the assumption of VFE, (Yortsos, 1995). Gravity is the central variable in the simplifications and, based on its relative strength, the analytical results can be classified into two categories: (a) those obtained assuming viscous forces and formation heterogeneity dominate the distribution of phases; and (b) those obtained assuming gravity dominates the distribution of phases. Assuming that conditions are under VFE simplifies the analytical representation of events during and after CO_2 injection.

Yortsos (1995) proved the validity of VFE for a series of analytical models and introduced the dimensionless parameter, $R_l = (l/h)\sqrt{k_v/k_h}$, where l is the lateral length of the formation, h is the formation thickness, and k_v and k_h, are the mean vertical and horizontal formation permeabilities, respectively. The assumption of VFE is valid for large values of R_l, and Yortsos (1995) reported that numerical calculations supported VFE very well when $R_l \geq 10$, and when $l/h \gg 1$. However, Lake et al. (1981) reported good results with values of $R_l \geq 2$.

To establish if VFE conditions prevail in the Donovan Sands, an R_l number was obtained using values for formation lateral length and thickness that produced the most

conservative ratio of length to thickness. The most conservative value was selected because of the wide variation in the lateral length and thickness of the sandstone reservoirs. In order to produce the most conservative estimate for R_l, the smallest value for lateral length and the greatest value for thickness were selected, among all the sands in the Upper, Middle, and Lower Donovan. It was assumed that the maximum thickness for any of the sands into which CO_2 would be injected was 20 m (65.6 ft), as indicated by the stratigraphic section and well log characteristics shown in Figure 7.1.

In estimating the most conservative lateral length for the Donovan Sands, it was assumed that all CO_2 injection wells were located at the center of 40-acre plots, and that no two CO_2 injection wells would be in adjacent plots. This assumption is based on a rational arrangement of CO_2 injection wells, which avoids creating elevated injection pressure regions. The smallest value for formation lateral length was considered to be the average distance between two CO_2 injection wells, and was estimated to be 402 m (1320 ft). The estimate is extremely conservative, considering that the Sand Continuity Study Report (1964) indicates that the lateral length of sandstones in the Upper and Lower Donovan traverses at least two 40-acre plots. It is assumed, because of their common depositional history, that the same is true for Middle Donovan sandstones.

Assuming a value of 0.1 for the ratio of vertical to horizontal permeability in sandstones (Permadi et al., 2004; Wehr and Brasher, 1996), and $l/h = 20.1$, a conservative estimate of $R_l = 6.35$ was obtained for the Donovan Sands. The value of R_l, as well as the formation's length to height ratio, are both sufficiently high to justify the assumption of VFE in the Donovan Sands.

7.5 Carbon Dioxide Vertical Migration Dynamics

Free-phase CO_2 will always be less dense than formation brine (Bachu, 2003), hence migration of CO_2 under VFE conditions will be promoted by buoyancy within the vertical profile of the sandstone reservoirs in the Donovan Sands. The magnitude of the buoyant force is controlled by the difference in densities between brine and CO_2. An increase in density difference will cause an increase in buoyancy, for a given CO_2 column height and vice versa. Upward CO_2 migration will be opposed by capillary pressure, which must be overcome for CO_2 to pass from one pore, through a pore-throat, to an adjacent pore. The magnitude of the opposing capillary pressure is controlled by the brine–CO_2 interfacial tension, the size of the smallest throat in the largest continuous pore, and the wettability of the rock grains.

Figure 7.3 shows a schematic of the rock grains in a formation, and a globule of CO_2, immersed in the brine which fills the pores and pore-throats formed by the grains. As shown in Figure 7.3, there are four distinct stages in the relationship between the competing forces of buoyancy and capillary pressure, during passage of the CO_2 globule from a pore, through a pore-throat, to an adjacent pore.

During stage A, shown in Figure 7.3, the CO_2 globule is at rest in the pore, and has a radius approximately equal to the radius of the pore. At this stage the capillary pressure in the pore is given by the expression, $p_p = 2\gamma/r_p$, where γ is the interfacial tension between brine and CO_2, and r_p is the radius of the pore. Buoyancy at this stage is not sufficient to distort the globule and force it through the pore-throat, thus the globule is in equilibrium with the surrounding brine.

During stage B, in Figure 7.3, the CO_2 globule is distorted and its upper end has reached midway into the pore-throat. At this stage, the capillary pressure at the upper end of the globule is given by the expression, $p_t = 2\gamma/r_t$, where, r_t, is the radius at the tip of the globule inside the pore-throat, and since $r_t < r_p$, the capillary pressure in the pore-throat is greater than the capillary pressure in the pore. The balance of capillary forces, which is in opposition to buoyancy, can be expressed by $2\gamma/r_t > 2\gamma/r_p$.

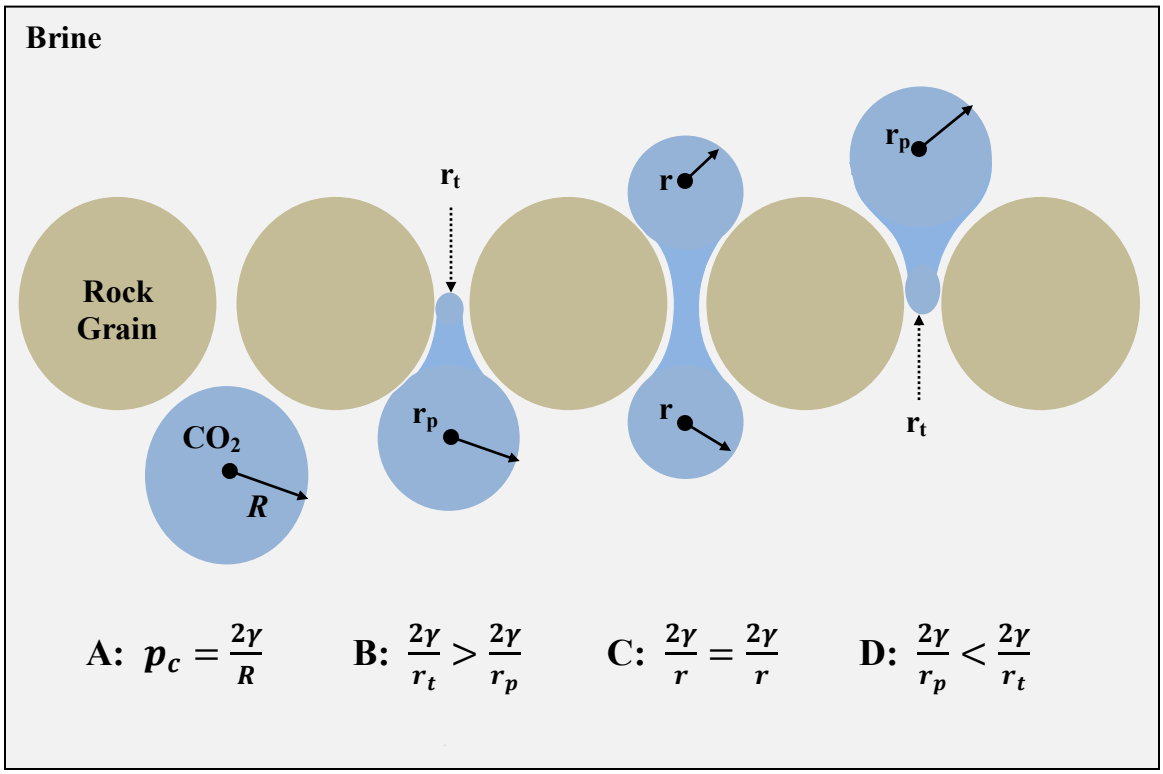

Figure 7.3. Diagram of a CO_2 globule migrating through rock grains, in a brine filled formation. Four distinct stages occur in the relationship between the competing forces of buoyancy and capillary pressure as the globule moves upward through the pore-throat into the next pore. During stage A, the globule is at equilibrium in the pore. During stage B, the globule has deformed upon entering the pore-throat. During stage C, the globule has entered half way through the pore-throat. During stage D, the globule is passing through the pore-throat into an adjacent pore (after Berg, 1975).

During stage C, as shown in Figure 7.3, the CO_2 globule is midway through the pore-throat, with two spheres of equal radii protruding through the upper and lower ends of the pore-throat. At this stage, the capillary pressures in the spheres at either end of the pore-throat are equal.

During stage D, in Figure 7.3, the CO_2 globule is more than midway through the pore-throat and the balance of forces reverses in comparison to stage B. At this stage the capillary pressure at the upper end of the globule is less than at the lower end, which is still midway in the pore-throat, and the resultant gradient of capillary pressure is in the same direction as buoyancy. The change of direction in the capillary pressure gradient forces the remainder of the globule to move upward from the pore-throat into the adjacent pore.

The analysis of the four stages shown in Figure 7.3 indicates that migration of CO_2 will occur when the buoyant force acting on a globule is large enough to overcome the capillary pressure gradient within the globule, which is created by the difference between the higher pressure in the pore-throat and the lower pressure in the pore. Since buoyancy acting on the distorted globule is caused by the hydrostatic pressure difference between the upper and lower ends of the globule, the net capillary pressure gradient can be expressed in terms of the vertical height of the distorted globule. The problem was analyzed by Berg (1975), who investigated the role of capillary pressure in stratigraphic traps and petroleum accumulation. Berg (1975), derived an equation for the minimum height a liquid or gas column must attain, in order for vertical migration driven by buoyancy to occur in the presence of an immiscible fluid.

Berg's (1975) equation is:

$$h_c = \frac{2\gamma}{g}\left[\frac{1}{r_t} - \frac{1}{r_p}\right]\left[\frac{1}{\rho_b - \rho_{CO_2}}\right] \tag{7.1}$$

where, r_t is the radius of the pore-throat, r_p is the radius of the pore, g is the acceleration due to gravity, and ρ_b and ρ_{CO_2} are the formation brine and CO_2 densities, respectively, under reservoir conditions. In this case where the buoyant fluid is CO_2, and the surrounding fluid is brine, γ is the surface tension of brine against CO_2.

Pore and pore-throat radii can be estimated by the following relationships, assuming rhombohedral packing of uniform-size spherical grains (Graton and Fraser, 1935, cited by Berg, 1975):

(a) pore,

$$r_p = 0.414(0.5\ D) \tag{7.2}$$

(b) pore-throat,

$$r_t = 0.154(0.5\ D) \tag{7.3}$$

where D is the grain diameter. The radii from Equations 7.2 and 7.3 determine the maximum capillary pressure difference that will exist in a continuous gas phase which is composed of *stringers* (sequence of connected globules) filling the pores. In the absence of grain or pore size measurements, the effective grain size can be estimated using the following correlation (Berg, 1975):

$$D_e = (1.89k\varphi^{-5.1})^{1/2} \tag{7.4}$$

where D_e is the effective grain size (cm), k is the permeability (mdarcy) and φ is the porosity (percent). Equation 7.4 was derived assuming well sorted packing of grains and porosity of 30%. Berg (1975) indicates that the relationship could be used for tighter as well as looser packings but does not provide a limiting range.

Based on Equation 7.1, the capacity of a rock formation to act as a seal is determined by the capillary entry pressure at the pore-throats. It is assumed that at the contact horizons between the sandstone reservoirs of the Upper, Middle, and Lower Donovan and the overlying shale, the only phases present in the pores and pore-throats are brine and CO_2. The same fluids are assumed to be present in the pores and pore-throats at the contact horizon between the Donovan shale and the overlying Ferry Lake Anhydrite.

7.5.1 Donovan Formation Parameter Estimates for Well Leakage Calculations

In order to estimate the critical CO_2 column height using Equation 7.1, values for the interfacial tension of the phases present, density of each phase, pore sizes, and pore-throat sizes must be determined.

An interfacial tension estimate of 0.026 N/m for CO_2–brine was obtained from Chalbaud et al. (2009), at a reservoir temperature of 100 °C (212 °F) temperature, and pressure of 30 MPa (4351.1 psi).

Density estimates for the brine were obtained from output produced by the TOUGH2-ECO2N simulation software, for the CO_2 injection scenarios discussed in Chapter 6. At hydrostatic conditions, in regions of 100% brine saturation, the brine

density, based on 10% NaCl by weight, was reported to be 1043.7 kg/m^3 (65.2 lb/ft^3). Density estimates for CO_2 were taken from Table 3.1 (Lemmon et al., 2002).

Pore and pore-throat sizes are a function of rock grain size and packing. Since grain size varies within the rock matrix, pore and pore-throat sizes will also vary. To minimize the error due to averaging, ranges of pore and pore-throat sizes for sandstone, shale, and anhydrite were determined, from which corresponding ranges of critical height estimates were obtained.

Estimates of pore and pore-throat radii for the sandstone reservoirs, obtained using Equations 7.2, 7.3, and 7.4, are summarized in Table 7.1.

Table 7.1 Input parameters used in Equations 7.2, 7.3, and 7.4 to estimate pore and pore-throat radii in the sandstone reservoirs.

Formation	φ^a percent	k^a mdarcy	D_e effective grain diameter, µm	r_p pore radius, µm	r_t pore-throat radius, µm
Upper Donovan	13.1	4.48	41.4	8.6	3.2
Middle Donovan	13.1	13.0[b]	70.2	14.5	5.4
Lower Donovan	13.1	4.48	41.4	8.6	3.2

[a] Average estimates from Fowler (1998).
[b] The Middle Donovan is more continuous than the Upper and Lower Donovan, so its permeability is assumed to be higher.

The estimates for pore and pore-throat radii shown in Table 7.1 match very closely those for coarse silts, obtained by Nelson (2009) based on analyses of sandstone and shale core samples, from a wide range of hydrocarbon-producing sedimentary formations. Therefore it can be assumed that Equation 7.4 is valid when applied to the Donovan reservoirs having porosity of 13.1%, which is less than half the 30% porosity upon which the derivation of the equation was based. The measurement methods used by Nelson (2009) to obtain pore-throat sizes included small-angle neutron scattering, mercury injection, scanning electron microscopy, and optical microscopy.

Estimates of pore and pore-throat radii for shale were obtained from Nelson (2009), since Equation 7.4 was not considered suitable for rock having very low porosity. Nelson (2009) reported pore-throat sizes ranging from an average of 0.02 μm for Cretaceous shale to 0.1 μm for Pennsylvanian shale. Pore sizes for shales were not reported. However using the sandstone sizes as reference, a factor of 2.7 was obtained for the size ratio of pore to pore-throat. However, a conservative value of 2 was selected for use in Equation 7.1. Applied to the shale, this conservative factor produces pore sizes in the range from 0.04 to 0.2 μm.

Anhydrites have low porosity and very low permeability, and are considered excellent seals. Bennion and Bachu (2007) reported that the Muskeg Anhydrite formation in northwestern Alberta, Canada, has porosity of only 0.5%. Its permeability was assumed to be less than 0.0001 mdarcy, since it was below the minimum detection limit of the analytical equipment. At these very low values, permeability–porosity relationships fail to yield reliable grain sizes, thus it was assumed that the anhydrite pore size is equal

to the shale pore-throat size. Although this assumption is arbitrary, it is considered a reasonable upper bound for the anhydrite pore size.

7.5.2 Calculation of Critical CO_2 Column Height in the Sandstone Reservoirs of the Upper, Middle, and Lower Donovan

Upward migration of CO_2 will begin in the sandstone reservoirs of the Upper, Middle, and Lower Donovan. If the critical CO_2 column height, necessary to overcome the capillary entry pressure at the pore-throats of the sandstone grains, is less than the vertical thickness of the sandstone reservoir, then CO_2 migration will stop before reaching the contact horizon between the sandstone and overlying shale.

Figure 7.4 is a schematic of CO_2 migration in a sandstone reservoir, based on the principles discussed in Section 7.5 and illustrated in Figure 7.3. The relationship of pore and pore-throat radii to rock grain diameter is based on Equations 7.2, and 7.3. Pore and pore-throat sizes were determined from the sandstone grain size. To estimate the critical CO_2 column height, Equation 7.1 was used with the appropriate parameter estimates from Tables 3.1 and 7.1, and from Section 7.5.1.

Figure 7.5 shows the range of critical CO_2 column heights formed using Equation 7.1 for pore-throat radii in the range $3.2 \leq r_t \leq 5.4$ μm, with the estimates for the Upper, Middle, and Lower Donovan, given in Table 7.1.

The critical heights, shown in Figure 7.5, are the most conservative regarding the density difference between brine and CO_2, since the CO_2 density is different at each of the three Donovan sections. However, the difference in critical heights among the three

sections, when changing the value of the CO_2 density, while holding all other parameters fixed, is less than 1%.

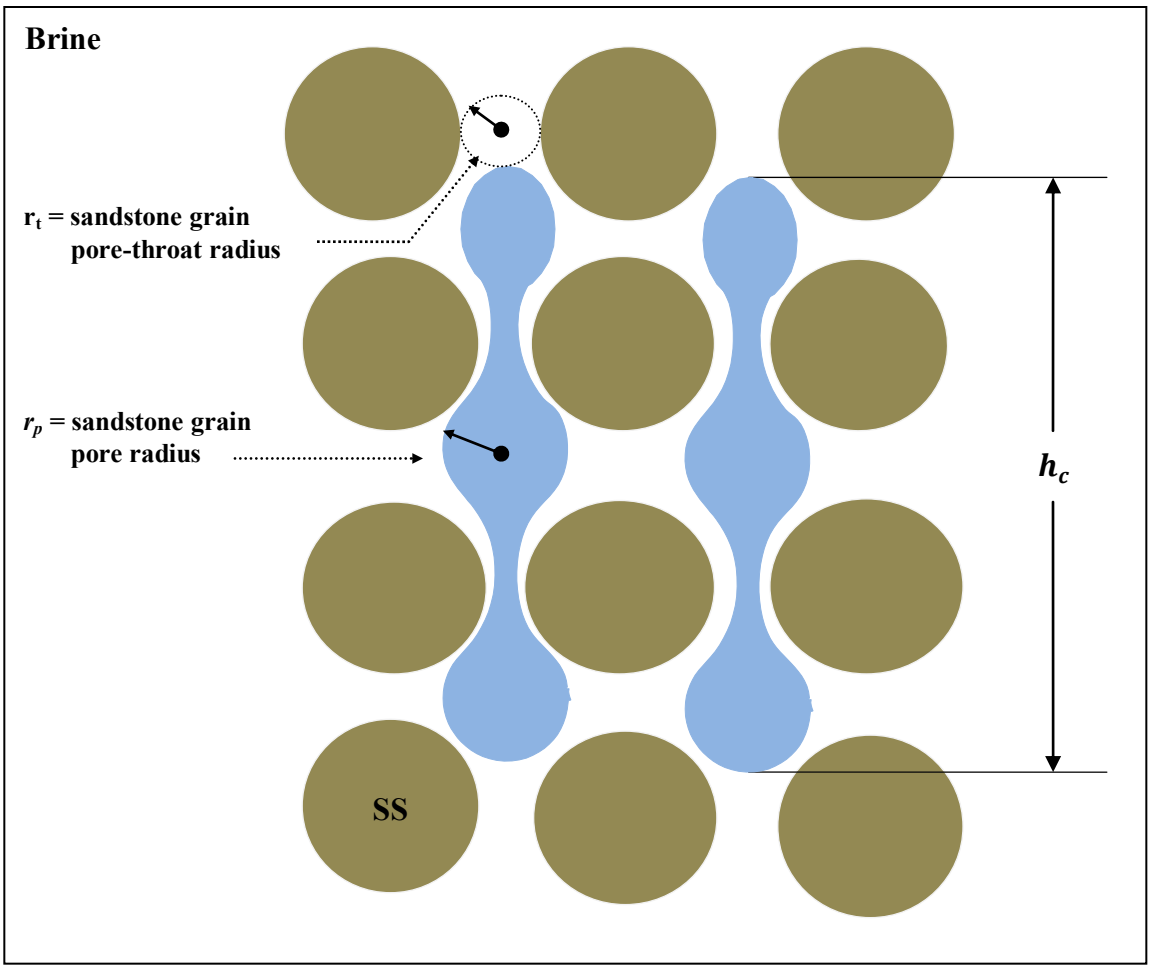

Figure 7.4. Diagram of CO_2 migration in the pores of a sandstone (SS) rock matrix. The CO_2 columns have achieved the critical height and are migrating through the water-wet sandstone grains (after Berg, 1975).

The results shown in Figure 7.5 indicate that the range of critical CO_2 column heights inside the sandstone reservoirs is from 1.1 m (3.6 ft), to 3.1 m (10.2 ft). If the thickness of a reservoir exceeds this range, and is filled with CO_2, CO_2 will begin to migrate vertically. In these cases the CO_2 will rise to the top of the reservoir and begin to

spread laterally on the underside of the shale or continue to migrate upward into the overlying shale. Esposito et al. (2008) reported that the sandstone reservoirs in the Upper and Lower Donovan ranged in thickness from 2.4 m (8 ft) to 12.2 m (40 ft).

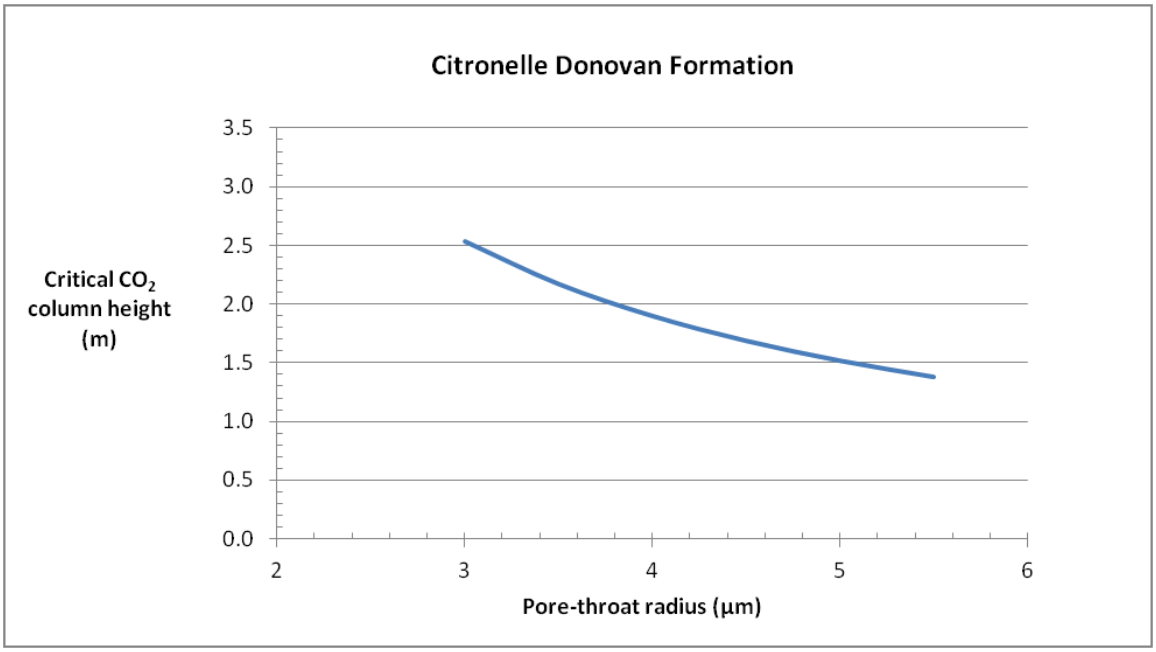

Figure 7.5. Estimates of critical CO_2 column height using Equation 7.1, for the sandstone reservoirs of the Upper, Middle, and Lower Donovan. Pore-throat radii were obtained using Equations 7.2, 7.3, and 7.4, and were in the range $3.2 \leq r_t \leq 5.4$ µm. A value of 622.6 kg/m^3 (38.9 lb/ft^3) was used for CO_2 density, producing the most conservative estimates of critical heights for the three Donovan sections.

7.5.3 Calculation of Critical CO_2 Column Height at the Sandstone–Shale Contact Horizon

Migration from a sandstone reservoir into the overlying shale will occur when the CO_2 column has sufficient buoyancy to overcome the capillary pressure in the pore-throat formed by the shale grains. Figure 7.6 is a schematic diagram of CO_2 migration from a sandstone reservoir into overlying shale, and is a modification of the principles discussed

in Section 7.5 and illustrated in Figures 7.3 and 7.4. The shale grains are smaller in size than the sandstone grains, thus the pore throat size at the sandstone–shale contact horizon is determined by the shale.

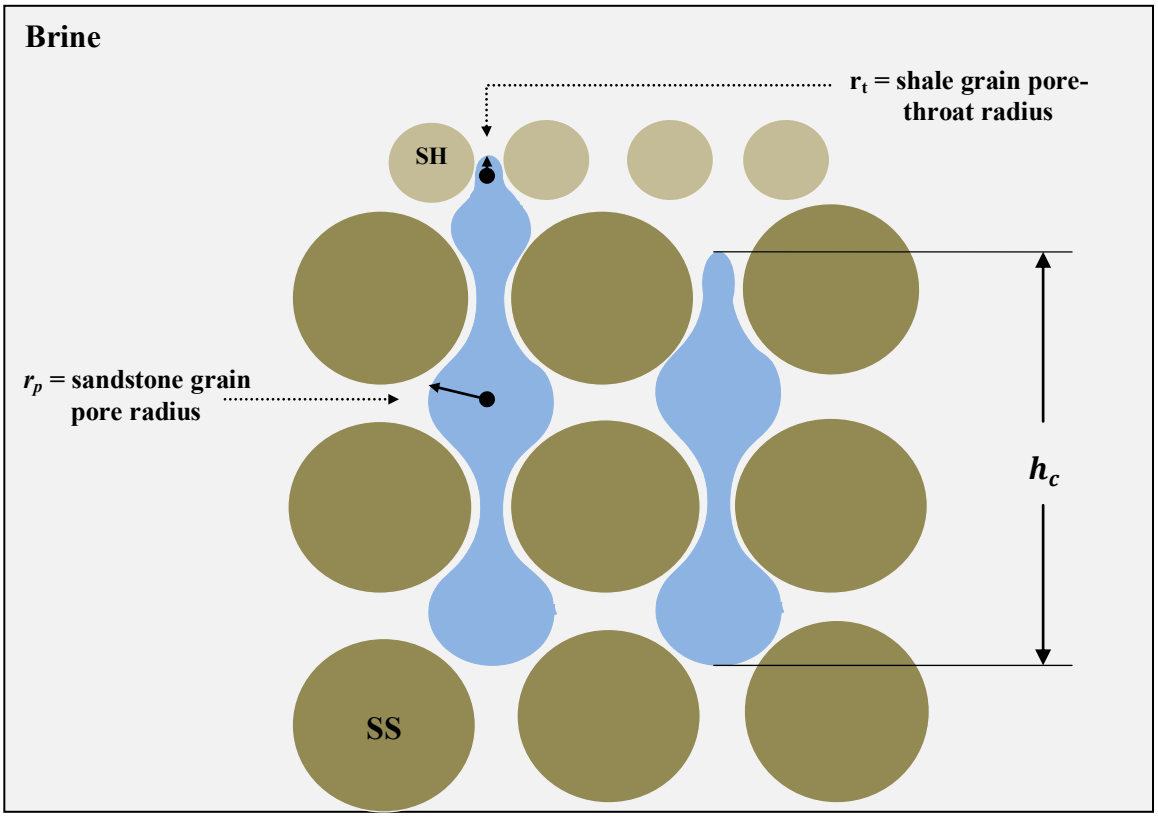

Figure 7.6. Diagram of CO_2 migration from a sandstone (SS) reservoir into overlying shale (SH). The CO_2 column on the right has achieved the critical height and is migrating through the water-wet sandstone grains The CO_2 column on the left is trapped by the increase in capillary pressure associated with the decrease in shale grain size (after Berg, 1975).

Equation 7.1 was modified so that the pore-throat radius refers to shale, and the pore radius to sandstone. Parameter estimates for the sandstone and shale were chosen from Tables 3.1 and 7.1, and Section 7.5.1. These estimates were used in Equation 7.1 to determine a range of critical CO_2 column heights corresponding to the range of pore-throat radii for shale, introduced in Section 7.5.1. The results, choosing the most

conservative value for CO_2 density among the three Donovan sections, are shown in Figure 7.7.

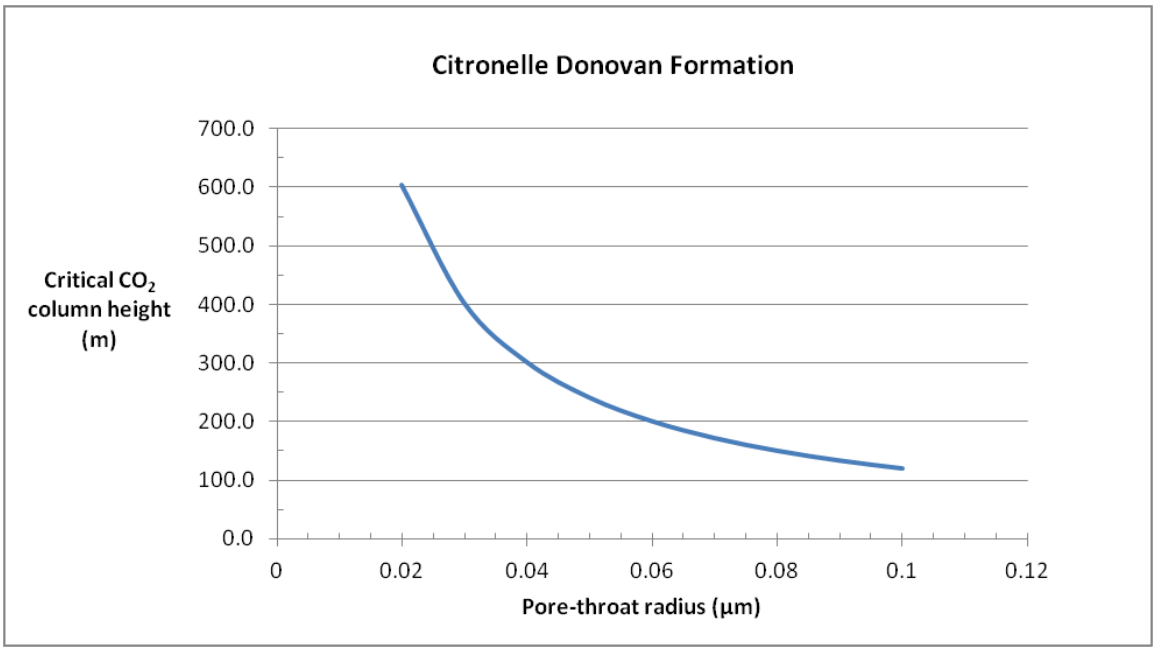

Figure 7.7. Estimates of critical CO_2 column height using Equation 7.1, at sandstone–shale contact horizons in the Donovan Formation. Estimates of pore-throat radii were in the range $0.02 \leq r_t \leq 0.1$ µm. A value of 622.6 kg/m^3 (38.9 lb/ft^3) was used for CO_2 density, producing the most conservative estimates of the critical height for the three Donovan sections.

The results shown in Figure 7.7 indicate that the range of critical CO_2 column heights at the sandstone–shale contact horizons is from 119 m (390 ft) to 603 m (1978 ft). Therefore, in order for CO_2 to migrate from sandstone into the overlying shale, the CO_2 column height must be greater than 119 m (390 ft), to overcome the capillary pressure in the shale pore throats.

Individually, none of the sandstone reservoirs has sufficient thickness for a column of this height to form. The Upper Donovan has a thickness of approximately 108 m (354 ft). The difference between the minimum critical CO_2 column height and the Upper Donovan thickness is 11 m (36 ft), which is approximately 10% of the formation thickness. This difference is sufficiently low to suggest that the Upper Donovan may have a thickness exceeding 119 m (390 ft) at certain locations. Furthermore, in reservoirs which share vertical communication, it is possible that a continuous pathway originating in the Middle or Lower Donovan may be sufficiently long for a vertical column of CO_2 to form that exceeds 119 m (390 ft). Eaves (1976) noted that the Upper, Middle, and Lower Donovan sections appear to be interconnected downdip, having registered the same pressure drop in the formations during primary production.

The Sand Continuity Study (1964) reported that, due to erosion, some of the sands were connected vertically and that within sandstone reservoirs, sand permeability had a profile that was greater near the base of the sand, decreasing upward. It is therefore possible that high permeability at the base of the sand could allow CO_2 to migrate along the base of the sand, as result of the high pressures present during the CO_2 injection period. If this occurs, it is possible that CO_2 may migrate vertically at a point where two or more stacked sands are connected, forming a pathway exceeding the critical height of 119 m (390 ft).

The critical CO_2 column height increased modestly with decreasing shale pore-throat size in the range $0.06 \leq r_t \leq 0.1$ μm, but increases dramatically for pore-throat radii below 0.06 μm. The sensitivity of Equation 7.1 to changes in the pore size of the

sandstone was negligible because the reciprocal value of the pore-throat radius is at least two orders of magnitude greater than that of the pore radius.

7.5.4 Calculation of Critical CO_2 Column Height at the Shale–Anhydrite Contact Horizon

Migration from the Donovan formation shale into the overlying Ferry Lake Anhydrite will occur when the CO_2 column has sufficient buoyancy to overcome the capillary pressure in the pore-throats formed by the anhydrite grains. Figure 7.8 is a schematic diagram of CO_2 migration from Donovan formation shale into the overlying anhydrite, and is a modification of the sandstone–shale scenario shown in Figure 7.6. Pores at the shale–anhydrite horizon are those formed by the shale grains.

It was assumed in Section 7.5.1 that the pore size of anhydrite is equal to the pore-throat size in shale. Since the pore-throat radius of the anhydrite is based on an arbitrary choice, a single estimate of the critical CO_2 column height at the shale–anhydrite contact horizon was produced. Unlike the cases in Sections 7.5.2 and 7.5.3, where a range of pore-throat radii was considered, determining a range of pore-throat radii for the anhydrite would involve considerable uncertainty.

Using appropriate values from Section 7.5.1, and 0.04 μm for the pore radius of shale, and 0.01 for the pore-throat radius of the anhydrite, the critical CO_2 column height at the shale–anhydrite contact horizon, was estimated to be 908 m (2979 ft). This value far exceeds the total thickness of 206 m (676 ft) for the Donovan formation, showing that the Ferry Lake Anhydrite has very high sealing capacity and will contain any CO_2 leakage from the sandstone reservoirs.

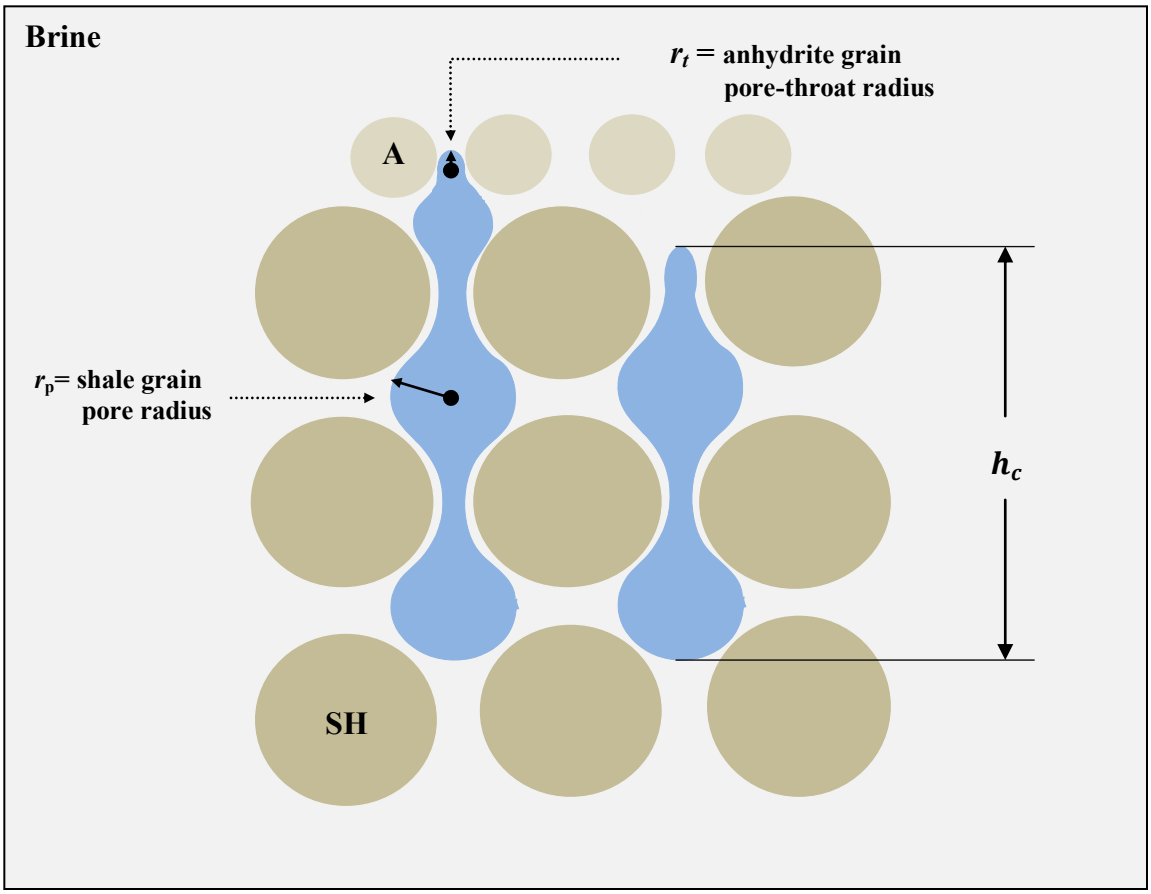

Figure 7.8. Diagram of CO_2 migration from shale (SH) into the overlying Ferry Lake Anhydrite (A). The CO_2 column on the right has achieved the critical height and is migrating through the water-wet shale grains. The CO_2 column on the left is trapped by the increase in capillary pressure associated with the decrease in anhydrite grain size (after Berg, 1975).

7.6 Vertical Leakage from Wells in the Citronelle Oil Field

Wells in the Citronelle Oil Field penetrate both the Upper and Lower hydrocarbon-bearing Donovan sandstones. Although the wells are not perforated at the depth of the Middle Donovan they do pass through that section. If migrating CO_2 encounters a well whose integrity at the depth of the three sections has been compromised, vertical leakage of CO_2 will occur. For the analysis of vertical leakage

from wells, any defect or compromise in the integrity of a well that may lead to CO_2 leakage is described as an *anomaly*.

Leakage from wells has a higher probability of reaching the ground surface than leakage through insufficient sealing capacity. The probability increases with older abandoned wells, or wells that have been improperly sealed. However, the consequences and management of this risk of CO_2 leakage from wells are not considered in the present work. The analysis is focused on identifying the leakage potential from wells whose integrity has been, or is likely to be compromised.

Figure 7.9 is a schematic diagram of a vertical cross section of a well. Assuming the well has been abandoned, it will be sealed with cement plugs inside the casing at appropriate depths. Cement fill is placed on the outside of the casing to stabilize the well and formation rock. Nordbotten et al. (2005), identified six critical locations along the vertical length of a well where anomalies could occur: (a) between cement and outside of casing; (b) between cement and inside of casing; (c) through cement; (d) through casing; (e) in cement fractures; (f) between cement and rock.

The list of critical locations where anomalies are most likely to occur in a well, allowing CO_2 to leak, consider only structural problems such as fractures or corrosion in the well casing, and fractures or fissures in the cement fill, inside and outside the casing. Operational well components such as valves, pumps, and packers which are part of active wells are not considered in the present work.

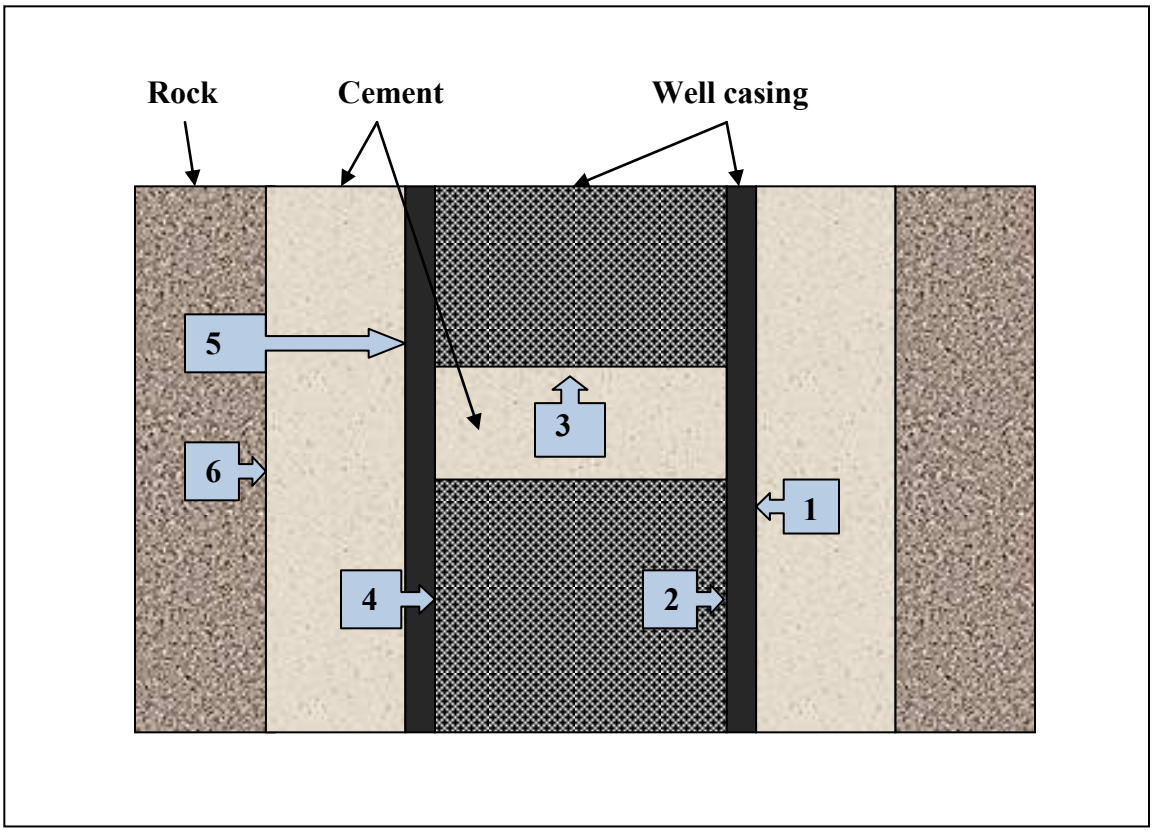

Figure 7.9. Diagram of the vertical cross section of a well, showing the critical locations where CO_2 leakage could occur: (1) between cement and outside of casing; (2) between cement and inside of casing; (3) through cement; (4) through casing; (5) in cement fractures; (6) between cement and rock (after Nordbotten et al., 2005).

Only structural integrity issues are considered. For example, Fowler et al. (1998) reported that more than 130 casing leaks had occurred at the Citronelle Oil Field by 1998, caused mainly by external corrosion in saline-water-bearing sands. Based on projections from a best fit line constructed by Fowler et al. (1998), 20 casing leaks per year are predicted for 2012 due to salt water corrosion.

7.7 A Rudimentary Estimate of Well Leakage Probability

Results of TOUGHREACT simulations in Chapter 6 indicate that a well injecting CO_2 for 40 years, at the rate of 36.3 t (40 short tons) of CO_2 per day, will produce a CO_2

plume that reaches 700 meters (2297 ft) from the point of injection after 10,000 years. If the injection well is located at the center of a 40-acre plot it will be at the center of a square having sides of length 402.3 m (1320 ft). Assuming that no two injection wells are in immediately adjacent plots, the CO_2 plume created by a single injection well, will encounter at most 8 other wells in its 700 m (2296.6 ft) radial travel.

In Section 7.5.4 it was concluded that leakage of CO_2 from the Donovan formation into the overlying Ferry Lake Anhydrite would be constrained by the high capillary pressure in the pore-throats of the anhydrite. Therefore, CO_2 will most likely leak upward through a well anomaly located in the Donovan formation. A comprehensive well integrity survey of North Sea oil rigs reported that an average of 18% of production and injection wells had some type of integrity problem (Vignes et al., 2010). Although this rate applied to offshore facilities, it is used as reference measure for well integrity anomalies at Citronelle.

The probability of a well anomaly occurring in the thickness interval of the Donovan formation can be estimated by the ratio of the total thickness of the Donovan formation, to the total well depth, measured from the ground surface. It is assumed that the well penetrates from the surface to the base of the Lower Donovan reservoirs. Table 2.1 shows that the thickness of the Donovan formation is 206 m (676 ft) and Figure 7.1 shows the depth to the base of the Lower Donovan reservoirs at 3444 m (11300 ft). Using these estimates, the probability that a well anomaly will occur in the section of the well aligned with the thickness of the Donovan formation, is estimated to be 0.06 per well.

To estimate the probability of CO_2 leakage occurring due to well anomalies, a conditional probability was formulated as follows: given the probability that a single anomaly is present in a well, what is the probability that an anomaly will appear at the same depth as the Donovan formation? The value of this conditional probability is given by the product of the ratio of formation thickness to total well depth (0.0598), and the probability of an anomaly per well (0.18). The probability was estimated at 0.0108, or 1.08%.

7.8 Citronelle Oil Field Wells with Leakage Potential

The estimate obtained in Section 7.7 is valid for no more than one anomaly per well, and it serves only as a rudimentary measure because it is based on an average estimate which incorporates all types of well integrity issues, types of wells, and levels of well anomalies, into a single metric. Well assemblies and associated equipment are comprised of numerous parts. Anomalies can manifest themselves in various forms of material or equipment defects or failures, and in compromises of the structural integrity of pipe, casing, wellbores, and other parts of the well assembly. Identifying or predicting the type, number, and location of anomalies in a well requires the collection, analysis, and assessment of data relating to the operational life of the components and materials comprising the well, which cannot be accurately expressed in a single measure. However, updated, detailed and reliable data on the condition of abandoned wells is difficult to obtain.

The Citronelle Field has been in operation for over 50 years and more than 400 wells have been drilled and put into operation during this period. The type, age,

condition, and operational status of the wells varies considerably. Currently there are 162 producing, 94 temporarily abandoned, and 180 permanently abandoned wells (AOGB database, accessed June 2013). It is reasonable to assume that the 162 producing wells are closely monitored with respect to their condition and maintenance requirements, and that they have a low likelihood of integrity issues.

The wells that are temporarily and permanently abandoned are of greater concern, since they are more likely to have sustained the types of anomalies listed in Section 7.6. Wells are temporarily abandoned during long periods of shut-down, workovers, or field development. Wells are permanently abandoned at the end of economic operations, when well repairs are cost prohibitive, or when raising the bottom-hole location to a shallower depth. The process of temporarily abandoning a well is different from that by which one is permanently abandoned, because of the different time periods under consideration. Figure 7.10 shows a schematic of vertical cross sections for temporarily and permanently abandoned wells, and the difference in number and location of cement plugs utilized to stop the flow of fluids up through the casing. Temporarily abandoned wells also utilize a corrosion cap at the surface end of the casing.

Well integrity issues for temporarily and permanently abandoned wells in the Citronelle Oil Field also depend on the type of *dual completion* process utilized in each well to produce oil from both the Upper and Lower Donovan reservoirs. In dual well completion, a single wellbore incorporates tubing and tools that enable production from two different zones. Two tubing strings are used to segregate and control the flow of fluids from the two zones in a single wellbore. The original arrangement consisted of a 17.8 cm (7 in) diameter casing, with two 5.1 cm (2 in) diameter tubing sets (Eaves,

1976). However, due to nontechnical issues, many wells produced from only one zone until 1960, when the Oil and Gas Board of the State of Alabama permitted wells to be dually completed using one string of tubing. In dual completions with a single tubing string, the annulus between the tubing and casing provides a passage for the other zone from the same wellbore.

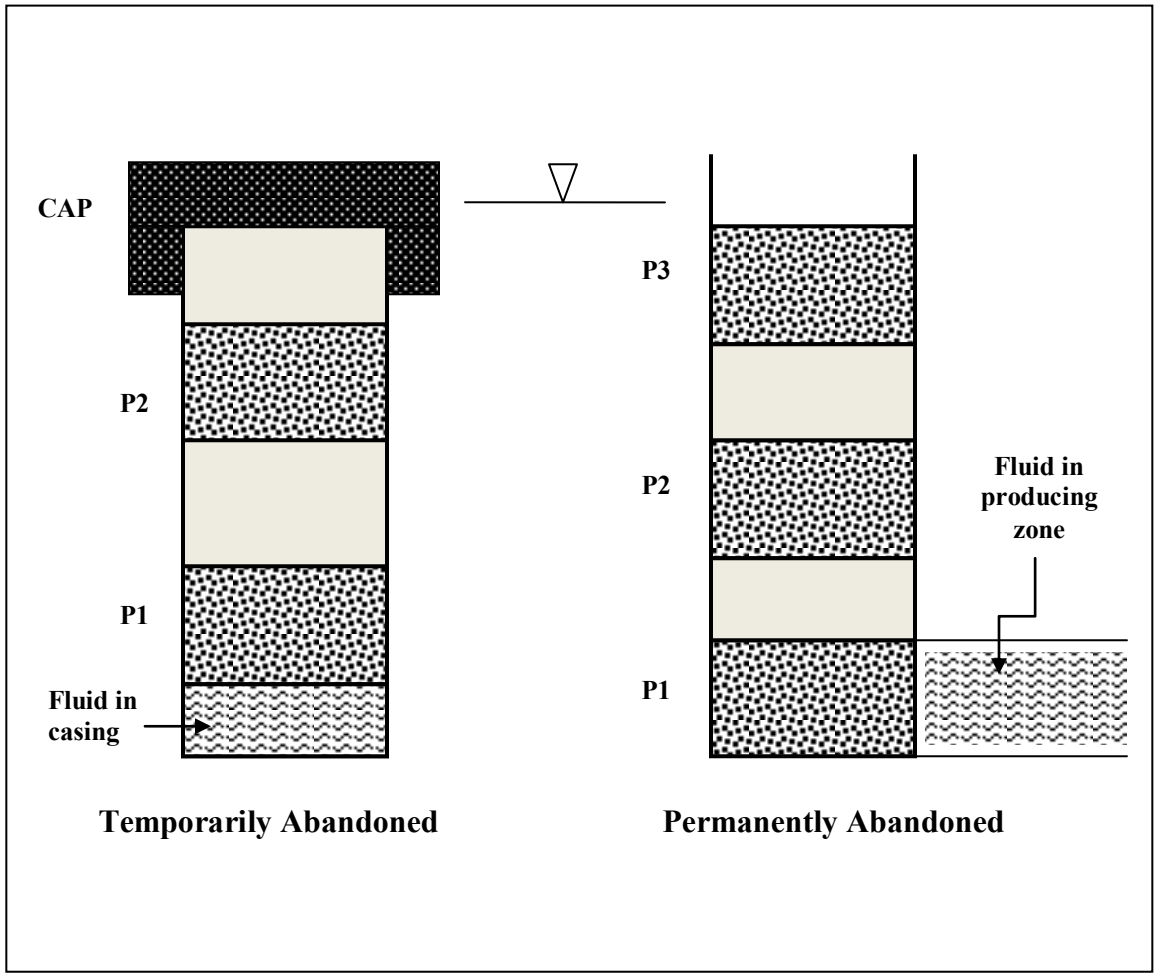

Figure 7.10. Diagram of temporarily and permanently abandoned wells. P_i indicates cement plug. Temporarily abandoned wells have a corrosion cap at the surface.

The wide variation in type, age, condition, and status of the wells in the Citronelle Oil Field, implies that well leakage probability estimates will range in value. Since leakage depends on proper functioning of the components of a well, utilizing reliability methods is a suitable approach to obtaining estimates for the probability of well leakage. In the section that follows, fault tree methods are applied to temporarily and permanently abandoned single tubing wells. It is assumed that dual completion wells would have at maximum double the number of integrity issues associated with single tubing wells, since the tubes utilize a single casing in either case.

7.9 A Reliability Fault Tree for Estimating Well Leakage Probability

Fault Tree is a common method used when an estimate of the probability of a system's failure is desired. It is based on identifying the combinations (pathways) of events within the system that lead to system failure. Logic symbols are used to interconnect the appropriate pathways among the contributory events and numerical probabilities of occurrence are assigned to each event. Beginning at the lowest level of contributory events in the pathways, the probabilities of the events are propagated upward to estimate the probability of the system's failure. The process is repeated for all pathways that result in system failure. Each set of events that leads to system failure forms a *cut-set*, and the cut-set with the lowest number of events required to cause system failure is defined as the *minimal cut-set*.

Construction of the fault tree begins with definition of the *top-event*, which is an abnormal, undesirable state of the system. In the present study the system is comprised of all the components in a well and the undesirable top-event is leakage. Top-events are

represented symbolically by rectangular boxes. The fault tree resolves the top-event into lower level events, developing the system's causality until the lowest resolution events are encountered. The lowest resolution events define the limits of the analysis, and the development of the fault tree is terminated. The events in the fault tree for the Citronelle oil wells are linked using the logic gate symbols shown in Figure 7.11.

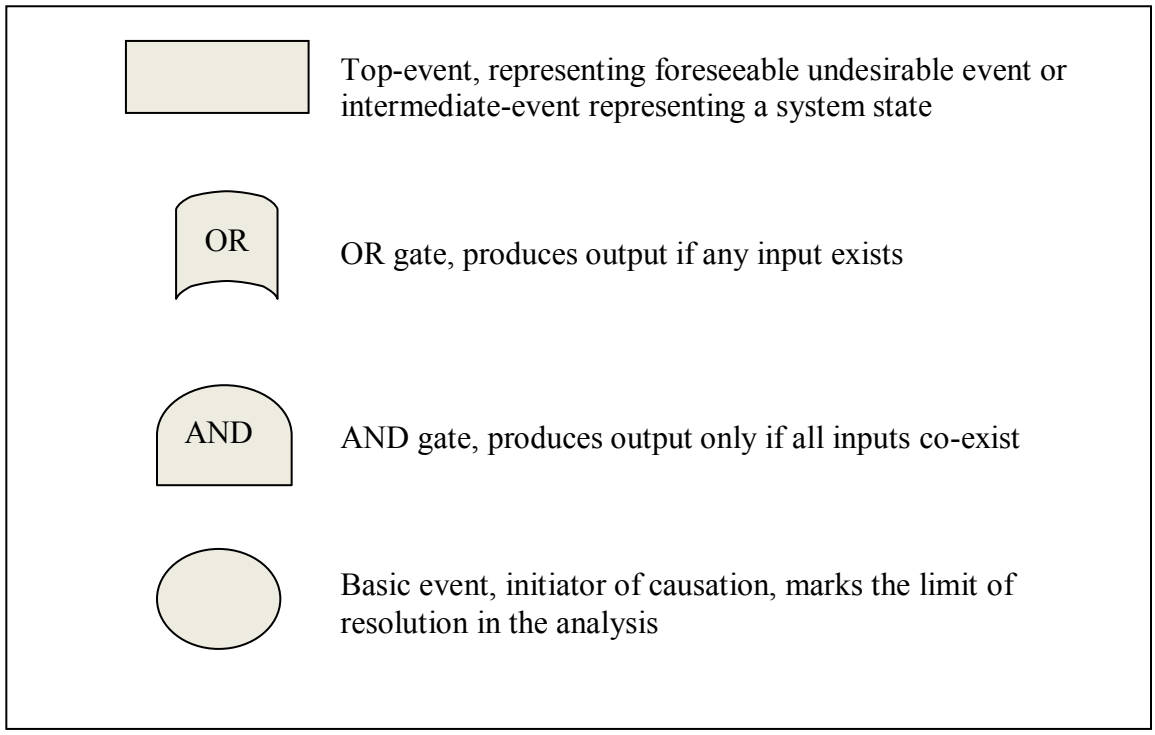

Figure 7.11. Logic symbols used in Fault Tree Analysis.

In the present investigation, the events considered in the fault tree were the six anomalies listed in Section 7.6, that can cause leakage from the wells in the Citronelle Oil Field. The tree starts with the top-event and links combinations of events through a sequence of OR and AND gates, by considering deductively the pathways that can cause leakage.

The development of the fault tree was based on the following assumptions:

a) the system is non-repairable, because the wells under consideration have been abandoned
b) potential leakage pathways are taken only to one level of pipe containment (i.e. the casing), and further leakage pathways from the nested piping and tubing, due to the additional complexity, have a negligible effect on the overall probability of the top event
c) potential leakage pathways are continuous over the thickness of the Donovan formation
d) combinatorial sequences in the order of occurrence of the six events do not alter the final probability of leakage through the well, since the probabilities obey the commutative property
e) constant component failure rate, over the lifetime of the component.

Figure 7.12, shows the fault tree for temporarily and permanently abandoned wells in the Citronelle Oil Field, based on the six anomalies discussed in Section 7.6. There are four minimal cut sets, each comprised of a single event that leads to the top-event. To estimate the probability of leakage from the well, each event must be assigned a probability. If a single measure of probability cannot be obtained, or is not sufficient to represent the event, then upper and lower bounds are estimated from which a logarithmic average is determined.

Probabilities arriving at an OR gate are additive, and those arriving at an AND gate are multiplicative. Defining as $P_0(t)$ the probability that the top-event occurs, and

$p_i(t)$ as the probability that a basic event *i* occurs, the following expressions can be used to calculate probabilities, arriving at an OR or AND gate, for *n* independent basic events:

(a) for a single AND gate,

$$P_0(t) = \prod_i^n p_i\,(t) \tag{7.5}$$

(b) for a single OR gate,

$$P_0(t) = 1 - \prod_i^n [1 - p_i\,(t)] \tag{7.6}$$

The assumption of constant failure rate is typical when considering structural components. The reliability $R(t)$ of a component having a constant failure rate is expressed by the following equation (Kottegoda and Rosso, 1997):

$$R(t) = e^{-\lambda t} \tag{7.7}$$

where, λ is the failure rate, calculated by 1/(Mean Time To Failure), and t is time. Using Equation 7.7 the probability of the top-event in a fault tree can also be obtained by $P_0(t) = 1 - R(t)$. Figure 7.11 serves as a template for well leakage estimation, and can be modified to incorporate additional events and well component arrangements to describe more complex scenarios. Manufacturer's design, operational specifications, component and material reliability data, field data, and maintenance records are some of the sources that can be utilized to obtain the information needed to estimate critical event probabilities.

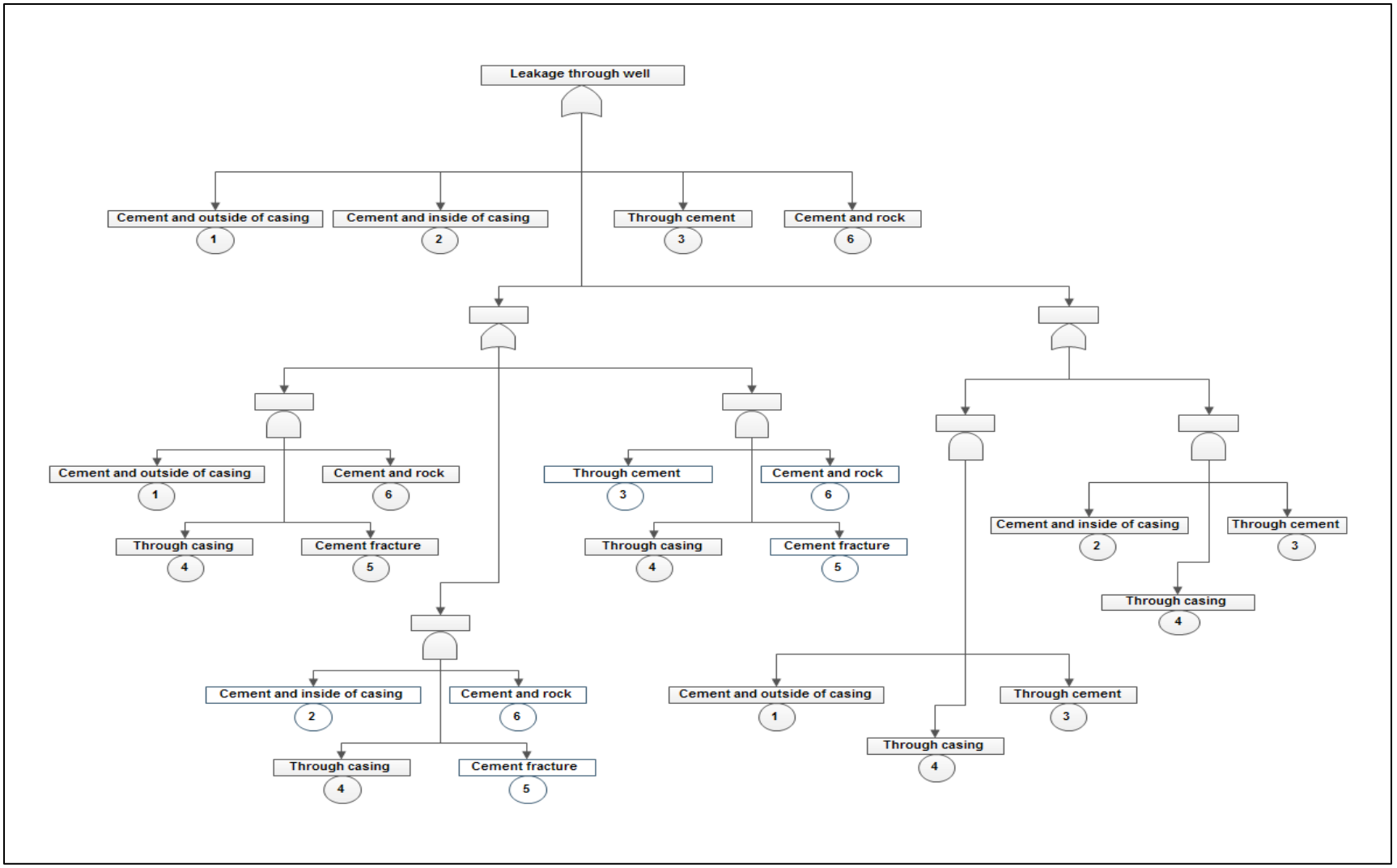

Figure 7.12. Fault tree of critical events for the temporarily and permanently abandoned wells at the Citronelle Oil Field.

CHAPTER 8

SUMMARY AND CONCLUSIONS

8.1 Objective

The objective of the present work was to investigate the oil recovery potential of a CO_2-EOR project in the Upper and Lower Donovan oil reservoirs of the Citronelle Oil Field, and the feasibility of CO_2 injection into the Middle Donovan during interruptions in CO_2-EOR operations. In the course of the investigation its scope was expanded to include scenarios that, although not part of the original objective, could become important at a later time in decision making by the stakeholders. A summary of the results of the work described in Chapters 4, 5, 6, and 7 is presented in the sections that follow.

8.2 Static CO_2 Storage Capacity Estimates for the Donovan Sand

Estimates of the static CO_2 capacity of reservoir sands in the Upper, Middle, and Lower Donovan are summarized in Table 8.1, for the five static capacity categories discussed in Section 3.3: (1) Upper Bound; (2) Depleted Oil Reservoir; (3) Enhanced Oil Recovery; (4) Saline-Water Formations; (5) Mineralization. The estimates range considerably for the depleted oil and saline reservoirs. The variation arises from the differences in assumptions and parameter selection in each formulation. Furthermore, the

wide disparity in capacity efficiency factors greatly influenced the results. Only one estimate was obtained in the EOR category.

Table 8.1. Summary of CO_2 static capacity estimates[a].

Formation	Category	Formulation	CO_2 Capacity	
			10^6 t	10^6 short tons
Upper and Lower Donovan	Depleted oil reservoir	Kovscek (2002)	44.2	48.7
Upper and Lower Donovan	Depleted oil reservoir	Shaw and Bachu (2002)	2.8	3.1
Upper and Lower Donovan	Depleted oil reservoir	US DOE CSP (2006)	19.1	21.1
Upper and Lower Donovan	Depleted oil reservoir	Esposito et al. (2008)	115–460	127–507
Upper and Lower Donovan	EOR	Shaw and Bachu (2002)	19.4 at BT[b] 23.0 at end of EOR	21.4 at BT 25.4 at end of EOR
Middle Donovan	Saline water reservoir	Pruess et al. (2001)	6.9	7.6
Middle Donovan	Saline water reservoir	US DOE CSP (2006)	0.16–0.64	0.18–0.71
Middle Donovan	Saline water reservoir	Esposito et al. (2008)	24	26.5
Middle Donovan	Mineralization	Present Work	0.524	0.577

[a]Estimated ultimate oil recovery at the end of EOR is 256,275,900 bbl.
[b]BT or Break-Through, indicates the time at which injected CO_2 appears in production wells during CO_2-EOR.

Static estimates are useful because they can be obtained using few inputs and without in-depth investigation. They can provide quick insight into the feasibility of

using a formation as a CO_2 sink, and suggest whether or not further investigation is warranted. Static estimates are especially useful in cases in which many candidate formations are under investigation. Using capacity estimates could save considerable effort by identifying formations that do not support the capacity goals of the project.

8.3 Simulation of CO_2 Enhanced Oil Recovery in the Upper and Lower Donovan Sand

The feasibility of a 10-year CO_2-EOR project was investigated using the MASTER 3.0 reservoir simulator. The incremental oil recovery for ten WAG scenarios is shown in Table 8.2.

Table 8.2. Incremental oil recovery during 10-year CO_2-EOR, using the MASTER 3.0 reservoir simulator, for ten WAG scenarios.

WAG Injection Scenario (total time is 10 years)	EOR incremental oil recovery (STB)
3 months CO_2 – 3 months water	127,675
6 months CO_2 – 6 months water	126,263
12 months CO_2 – 12 months water	122,537
2 months CO_2 – 6 months water	106,706
4 months CO_2 – 6 months water	121,144
6 months CO_2 – 6 months water	126,263
12 months CO_2 – 6 months water	128,735
24 months CO_2 – 6 months water	127,002
CO_2-only	116,476
Water-only	0

The results shown in Table 8.2 indicate that the optimal WAG scenario is 12 months CO_2 and 6 months water. The oil recovery represents that from only a small fraction of the Citronelle Oil Field, since the simulations considered only two reservoir sands (14-1 and 16-2), and the well cluster consisted of one CO_2 injector, four water injectors, and eleven oil producing wells. A field-wide application of CO_2-EOR could yield significant incremental oil recovery.

The simulations were surprisingly insensitive to changes in the MMP and oil and water flow allocation to Sands 14-1 and 16-2, which increases the confidence in the results produced.

8.4 Simulation of CO_2 Sequestration in the Middle Donovan Sand

A study was done of the feasibility of CO_2 sequestration in the saline-water sandstones of the Middle Donovan. Although the initial objective was to investigate the feasibility for interim CO_2 injection during interruptions in CO_2-EOR operations in the Upper and Lower Donovan, the scope was broadened to an investigation of the feasibility of large-scale CO_2 sequestration. The results suggest that the Middle Donovan is a potential large capacity CO_2 sink, and therefore, and that it can also be used as an interim sink for the duration of a CO_2-EOR project.

Simulations of CO_2 injection into the Middle Donovan using the TOUGH2-ECO2N (Pruess, 2005) and TOUGHREACT (Xu et al., 2004) simulators, indicate that CO_2 could be injected at the rate of 36.3 t/day (40 short tons/day) for 40 years, yielding a total of 530,000 t (584,224 short tons) injected. Considering that the wells are on 40-acre plots, every well is on a square plot 402 x 402 m^2 (1,742,400 ft^2). Results for 40 years of

injection show that the leading edge of the CO_2 front, at a distance of approximately 600 m (1969 ft) from the injection well, is at 25% CO_2 saturation,. The 95% saturation contour is at 30 m (98 ft) from the injection well. Using a carefully designed injection scheme, to prevent pressurization of reservoirs in adjacent plots, 300 wells in the Citronelle Field could inject a total of 159 x 10^6 t (175 x 10^6 short tons), which is approximately 40 years of CO_2 emissions from a 500 MW (electric) coal-fired plant, operating at 35% efficiency. One possible option, to avoid over-pressurization is to use horizontal injection, taking advantage of the stratification due to the grain increase from bottom to the top of the sandstone reservoirs. This method of injection promotes capillary trapping, since horizontal migration of CO_2 would be minimized, due to the orientation of the pressure field.

8.5 Carbon Dioxide Leakage Potential from the Donovan Sand

A study was made of the potential for leakage from the Upper, Middle, and Lower Donovan reservoirs. Two leakage pathways were considered: (a) leakage from the sandstone reservoirs into the overlying shale and leakage from the shale into the overlying Ferry Lake Anhydrite; and (b) leakage due to structural integrity issues in the wells of the Citronelle Oil Field.

The greatest challenge, in obtaining estimates of the potential for leakage from the sandstone reservoirs, was estimating the grain size in the formations of interest. Data on the grain size of sandstone reservoir rock was based on data from a wide variety of sandstone formations. Data on shales was limited and grain sizes for the anhydrite had to be inferred. Considering the most conservative estimates for grain size, the results

indicate that it is possible for CO_2 to migrate vertically from the sandstone reservoirs into the overlying shale, if the height of the CO_2 column exceeds 119 m (390 ft), the height at which the pressure at the top of the column exceeds the capillary pressure at the pore-throats in the shale. However, the results also indicate that it would take a CO_2 column having a height exceeding 908 m (2979 ft) to overcome the capillary pressure at the pore-throats in the anhydrite and enter the Ferry Lake Anhydrite. Therefore it is concluded that the Ferry Lake Anhydrite can serve as a long-term seal against vertical migration of CO_2.

The greatest challenge in estimating leakage from the Citronelle Oil Field wells remains the availability of data on the reliability of the components of the wells. Although some data could be gathered from manufacturers and suppliers, a complete and thorough analysis of all the components of all the wells in the Citronelle Oil Field would be challenging, given the age of the field and the disparity in ages and condition of the wells.

A rudimentary estimate of 0.0108 was obtained for the probability that a single well has sustained a single incident or acquired a defect causing of structural compromise sufficient to permit leakage. More detailed estimates are possible, but require the collection and analysis of reliability data for the numerous components that comprise the well structure. In the absence of tangible reliability data, a Fault Tree chart was constructed to serve as a prototype, when such data become available for the well components in the Citronelle Oil Field.

REFERENCES

Ammer, J. R.; Brummert, A. C. *Miscible Applied Simulation Techniques for Energy Recovery Version 2.0, User's Guide*. U.S. Department of Energy, DOE/BC–91/2/SP, February 1991.

Ammer, J. R.; Brummert, A. C.; Sams, W. N. *Miscible Applied Simulation Techniques for Energy Recovery Version 2.0, Technical Manual*. U.S. Department of Energy, DOE/BC–91/2/SP, February 1991.

Advanced Resources International. *Basin Oriented Strategies for CO_2 Enhanced Oil Recovery: ONSHORE GULF COAST*. Technical Report for the United States Department of Energy, Office of Fossil Energy. February, 2006.

Alabama State Oil and Gas Board–Geological Survey of Alabama. http://www.gsa.state.al.us/ogb/db_field.aspx (accessed May 21, 2013).

Aronow, S. Review of Geology of the Mississippi-Alabama Coastal Area and Nearshore Zone. *American Association of Petroleum Geologists*, **1974,** *58*, 157–158.

Bachu, S. Screening and Ranking of Sedimentary Basins for Sequestration of CO_2 in Geologic Media in Response to Climate Change. *Environmental Geology,* **2003,** *44,* 277–289.

Bachu, S.; Gunter, W. D.; Perkins, E. H. Aquifer Disposal of CO_2: Hydrodynamic and Mineral Trapping. *Energy Conversion and Management,* **1994,** *35* (4), 269–279.

Bennion, B. D.; Bachu, S. *Permeability and Relative Permeability Measurements at Reservoir Conditions for CO_2–Water Systems in Ultra Low Permeability Confining Caprocks.* SPE Paper 106995.SPE Europe/EAGE Annual Conference and Exhibition. London, UK, June 11–14, 2007.

Berg, R. R. Capillary Pressure in Stratigraphic Traps. *American Association of Petroleum Geologists Bulletin,* **1975,** *59* (6), 939–956.

REFERENCES

Bloomfield, J. P.; Goody, D. C.; Bright, M. I.; Williams, P. J. Pore-Throat Size Distributions in Permo-Triassic Sandstones from the United Kingdom and Some Implications for Contaminant Hydrogeology. *Hydrogeology Journal,* **2001,** *9,* 219–230.

Carlson, E. S. Chemical and Biological Engineering, The University of Alabama, Tuscaloosa, AL. Personal communication, 2012.

Chalbaud, C.; Robin, M.; Lombard J. M.; Martin F.; Egermann, P.; Bertin, H. Interfacial Tension Measurements and Wettability Evaluation for Geological CO_2 Storage. Advances in Water Resources, **2009,** *32,* 98–109.

Clark, P. E. Chemical and Biological Engineering, The University of Alabama, Tuscaloosa, AL. Personal communication, 2011.

Cook, P. J.; Rigg, A. J.; Bradshaw, J. Putting it Back where it Came from: Is Geological Disposal of Carbon Dioxide an Option for Australia? *Australian Petroleum Production and Exploration Association*, **2000,** *1*, 1–13.

Corey, A. T. The Interrelation Between Gas and Oil Relative Permeabilities. *Producers Monthly,* **1954,** *19,* 38–41.

Det Norske Veritas, *SWIFT Review of CO_2 Sequestration, 2003.* http://webarchive.nationalarchives.gov.uk/+/http://www.berr.gov.uk/files/file21926.pdf (accessed November 18, 2011).

Doughty, C.; Pruess, K.; Benson, S. M.; Hovorka, S. D.; Knox, P. R.; Green, C. T. Capacity Investigation of Brine-Bearing Sands of the Frio Formation for Geologic Sequestration of CO_2. *Proceedings of the First National Conference on Carbon Sequestration*, Washington, DC. May 14–17, 2001.

Eaves, E. Citronelle Oil Field, Mobile County, Alabama. *American Association of Petroleum Geologists*, **1976,** *24*, 259–275

Esposito, R. A.; Pashin, J. C.; Walsh, P. M. Citronelle Dome: A Giant Opportunity for Multi-Zone Carbon Storage and Enhanced Oil Recovery in the Mississippi Interior Salt Basin of Alabama. *Environmental Geosciences,* **2008,** *15*, 53–62.

Esposito, R. A.; Pashin, J. C.; Hills, D. J.; Walsh, P. M. Geologic Assessment and Injection Design for a Pilot CO_2-Enhanced Oil Recovery and Sequestration Demonstration in a Heterogeneous Oil Reservoir: Citronelle Field, Alabama. *Environmental Earth Sciences,* **2010,** *60*, 431–444.

REFERENCES

Fowler, M. I.; Safley, L. E.; Young, M. A.; Stechmann, R. H.; Blair, E. S.; Crumb, R. E. *Reservoir Management Strategy for Citronelle Field, Mobile County, Alabama*; Technical Report for the United States Department of Energy National Petroleum Technology Office: BDM NIPER/BDM-0353 (DE98000490), BDM Petroleum Technologies, Bartlesville, OK, July 1998.

Gerdemann, S. J.; O'Connor, W. K.; Dahlin, D. C.; Pener, L. R; Rush, H. Ex Situ Aqueous Mineral Carbonation. *Environmental Science and Technology*, **2007,** *41* (7), 2587–2593.

Ghomian, Y.; Pope, G. A.; Sepehrnoori, K. *Economical Co-Optimization of CO_2 Sequestration and Enhanced Oil Recovery*. Sixth Annual Conference on Carbon Capture and Sequestration, Pittsburgh, PA, May 7–10, 2007.

Gilchrist, R. E. *Miscibility Study (Repeat 50% P. V. Slug) in Cores. Citronelle Unit, Mobile County, Alabama*. Technical Report for the Unit Manager, Citronelle Unit. Ralph E. Gilchrist, Inc., Houston, TX, November 3, 1981.

Graton, L. C.; Fraser, H. J. Systematic Packing of Spheres, with Particular Relation to Porosity and Permeability. *Journal of Geology,* **1935,** *43* (8), 785–848.

Gunter, W. D.; Perkins, E. H.; McCann, T. J. Aquifer Disposal of CO_2-Rich Gases: Reaction Design for Added Capacity. *Energy Conversion and Management,* **1993,** *34* (9–11), 941-948.

Hadlow, R. E. *Update of Industry Experience with CO_2 Injection*. Sixty-seventh SPE Annual Technical Conference and Exhibition, Society of Petroleum Engineers, Washington, D.C., October 4–7, 1992.

Herzog, H. *Carbon Sequestration via Mineral Carbonation: Overview and Assessment.* Technical Report for the Carbon Sequestration Initiative: MIT Laboratory for Energy and the Environment, Cambridge, MA, March 14, 2002.

Hesse, M. A.; Tchelepi, H. A.; Orr, F. M. *Scaling Analysis of the Migration of CO_2 in Saline Aquifers*. Society of Petroleum Engineers Annual Technical Conference and Exhibition, San Antonio, TX, September 24–26, 2006.

REFERENCES

Hills, D. J.; Kopaska-Merkel, D.; Pashin, J. C. *Depositional and Diagenetic Factors Influencing CO_2-Enhanced Oil Recovery in Estuarine Sandstone Facies of the Donovan Sand (Lower Cretaceous), Citronelle Oil Field, Southwest Alabama.* American Association of Petroleum Geologists Annual Convention and Exhibition, New Orleans, LA, April 11–14, 2010.

Hitchon, B.; Gunter, W. D.; Gentzis, T.; Bailey, R. T. Sedimentary Basins and Greenhouse Gases: A Serendipitous Association. *Energy Conversion and Management,* **1999,** *40,* 825–843.

Holtz, M. H.; Núñez-López, V.; Breton, C. L. Moving Permian Basin Technology to the Gulf Coast: the Geologic Distribution of CO_2-EOR Potential in Gulf Coast Reservoirs. *West Texas Geological Society Fall Symposium*, Publication no. 05–115, October 26–28, 2005.

Hovorka, S. D. *Proposed Methodology for Construction of a 2006 National Geological Carbon Sequestration Capacity Assessment*. Technical Report for the U.S. Department of Energy Regional Carbon Sequestration Partnership Program; Capacity and Fairways Subgroup of the Geologic Working Group of the DOE Carbon Sequestration Regional Partnerships, October 1, 2006

Intergovernmental Panel on Climate Change (IPCC*). Carbon Dioxide Capture and Storage: Special Report of the IPCC, Working Group III;* Cambridge University Press: Cambridge, UK, and New York, USA, 2005, 195–276.

Isphording, W. C.; Lamb, G. M. Age and Origin of the Citronelle Formation in Alabama. *Geological Society of America Bulletin*, **1971,** *82* (3), 775–779

Jarrell, P. M.; Fox, C.; Stein, M.; Webb, S. *Practical Aspects of CO_2 Flooding*; SPE Monograph Series; Society of Petroleum Engineers: Richardson, TX, 2002; Vol 22.

Johnson, J. W.; Nitao, J. J.; Knauss, K. G. *Reactive Transport Modeling of CO_2 Storage in Saline Aquifers to Elucidate Fundamental Processes, Trapping Mechanisms, and Sequestration Partitioning*. Geological Society of London Special Publication on Carbon Sequestration Technologies. Lawrence, Livermore National Laboratory, UCRL–JRNL–205627. July 29, 2004.

REFERENCES

Kottegoda, N. T.; Rosso, R. Risk and Reliability Analysis. *Statistics, Probability, and Reliability for Civil and Environmental Engineers.* McGraw-Hill: New York, NY, 1997; p 613.

Kovscek, A. R. Screening Criteria for CO_2 Storage in Oil Reservoirs. *Petroleum Science and Technology,* **2002,** *20*, (7–8), 841–866.

Lackner, K. S.; Wendt, C. H.; Butt, D. P.; Sharp, D. H.; Joyce, E. L. Carbon Dioxide Disposal in Carbonate Minerals. *Energy,* **1995,** *20* (11), 1153–1170.

Lake, L. W.; Hirasaki, G. J. Taylor's Dispersion in Stratified Porous Media. *Society of Petroleum Engineers Journal,* **1981,** *21,* 459–468.

Lemmon, E. W.; Huber, M. L.; McLinden, M. O. *NIST Reference Fluid Thermodynamic and Transport Properties—REFPROP Version 7.0 Users' Guide*. Physical and Chemical Properties Division, National Institute of Standards and Technology Boulder, CO, August 2002.

Mancini, E. A.; Mink, R. M.; Bearden, B. L.; Wilkerson, R. P. Norphlet Formation (Upper Jurassic) of Southwest and Offshore Alabama: Environment of Deposition and Petroleum Geology. *American Association of Petroleum Geologists*, **1985,** *69*, 881–898.

Matter, J. M.; Broecker, W. S.; Stute, M.; Gislason, S. R.; Oelkers, E. H.; Stefánsson, A.; Wolff-Boenisch, D.; Gunnlaugsson, E.; Axelsson, G.; Björnsson, G. Permanent Carbon Dioxide Storage into Basalt: The CarbFix Pilot Project, Iceland. *Energy Procedia*, **2009,** *1,* 3641–3646.

Nelson, C. R.; Evans, J. M.; Sorensen, J. A.; Steadman, E. N.; Harju, J. A. Factors Affecting the Potential for CO_2 Leakage from Geologic Sinks. Technical Report for Plains CO_2 Reduction (PCOR) Partnership; Energy and Environmental Research Center, at the University of North Dakota: Bismark, ND, October 2005.

Nelson, P. H. Pore-Throat Sizes in Sandstones, Tight Sandstones, and Shales. *American Association of Petroleum Geologists,* **2009,** *93* (3), 329–340.

Nordbotten, J. M.; Celia, M. A.; Bachu, S.; Dahle, H. K. Semianalytical Solution for CO_2 Leakage through an Abandoned Well. *Environmental Science and Technology,* **2005,** *39* (2), 602–611.

REFERENCES

Pape, H.; Clauser, C.; Iffland, J. Permeability Prediction Based on Fractal Pore-Space Geometry. *Geophysics*, **1999,** *64* (5), 1447–1460.

Parson, E. A.; Keith, D. W. Climate Change: Fossil Fuels without CO_2 Emissions. *Science*, **1998,** *282,* 1053–1054.

Pashin, J. C. Geological Survey of Alabama, Tuscaloosa, AL. Personal communication, 2009, 2010; and 2012.

Penner, L.; O'Connor, W. K.; Dahlin, D. C.; Gerdermann, S.; Rush, G. E. Mineral Carbonation: Energy Costs of Pretreatment Options and Insights Gained from Flow Loop Reaction Studies. *Proceedings of the Second Annual Conference in Carbon Sequestration*, Alexandria, VA, May 5–9, 2003.

Permadi, A.K.; Yuwono, I. P.; Simanjuntak, A. J. S. Effect of Vertical Heterogeneity on Waterflood Performance in Stratified Reservoirs: A Case Study in Bangko Field, Indonesia. SPE Paper 87016. Asia Pacific Conference on Integrated Modelling for Asset Management, Kuala Lumpur, Malaysia, March 29-30, 2004.

Petroleum Technology Research Center, Weyburn-Midale CO_2 Project. Home Page. ptrc.ca/projects/weyburn-midale (accessed November 11, 2011).

Pruess, K. *ECO2N: A TOUGH2 Fluid Property Module for Mixtures of Water, NaCl, and CO_2 User's Guide*. LBNL–57952, Lawrence Berkeley National Laboratory, Berkeley, CA, August 2005.

Pruess, K.; Oldenburg, C.; Moridis, G. *TOUGH2 User's Guide, Version 2.0*. LBNL–43134, Lawrence Berkeley National Laboratory, Berkeley, CA, November, 1999.

Pruess, K.; Xu, T.; Apps, J.; Garcia, J. Numerical Modeling of Aquifer Disposal of CO_2. SPE/EPA/DOE Exploration and Production Environmental Conference, San Antonio, TX, February 26–28, 2001.

Raymond, D. E. The Lower Cretaceous Ferry Lake Anhydrite in Alabama, Including Supplemental Information on the Overlying Mooringsport Formation and the Petroleum Potential of the Lower Cretaceous. *Alabama Geological Survey Circular*, no. 183, 1995, p 66.

Scheidegger, A. E. Statistical Hydrodynamics in Porous Media. *Applied Physics Journal,* **1954,** *25*, 994-1001; *The Physics of Flow Through Porous Media;* University of Toronto Press: Toronto, ON, Canada, 1960; p 313.

REFERENCES

Schlumberger Oilfield Glossary. http://www.glossary.oilfield.slb.com/en/Terms.aspx (accessed December 2, 2011).

Schroeder W.J.; Martin K.; Lorensen W. E. *The Visualization Toolkit: An Object-Oriented Approach to 3D Graphics, Third Edition*. Kitware, Inc. (formerly Prentice-Hall), **2003**, p 496.

Scott, J. B. T.; Barker, R. D. Characterization of Sandstone by Electrical Spectroscopy for Stratigraphical and Hydrogeological Investigations. *Quarterly Journal of Engineering Geology and Hydrogeology,* **2005,** *38,* 143–154.

Shaw, J.; Bachu, S. Screening, Evaluation, and Ranking of Oil Reservoirs Suitable for CO_2-Flood EOR and Carbon Dioxide Sequestration. *Journal of Canadian Petroleum Technology*, **2002,** *41* (9), 51–61.

Song, J.; Zhang, D. Comprehensive Review of Caprock-Sealing Mechanisms for Geologic Carbon Sequestration. *Environmental Science and Technology,* **2013,** *47,* 9–22.

Statoil, Sleipner Vest Home Page. http://www.statoil.com/en/TechnologyInnovation/ProtectingTheEnvironment/CarboncaptureAndStorage/Pages/CarbonDioxideInjectionSleipnerVest.aspx (accessed November 12, 2011).

Theodorou, K.; Walsh, P. M. University of Alabama at Birmingham, Birmingham, AL. Unpublished Work, 2007.

Unit Manager's Report. *Reservoir Analyses of Oil Migration: Citronelle Oil Field, Mobile County, Alabama*. Technical Report for the Unit Manager, Citronelle Unit, July 29, 1999.

Van Genuchten, M. Th. A Closed–Form Equation for Predicting the Hydraulic Conductivity of Unsaturated Soils. *Soil Science Society of America Journal,* **1980,** *44,* 892–898.

Verma, A.; Pruess, K. Thermohydrological Conditions and Silica Redistribution Near High-Level Nuclear Wastes Emplaced in Saturated Geological Formations. *Journal of Geophysical Research*, **1988,** *93*, 1159–1173.

Vignes, B.; Aadnoy, B. S. Well-Integrity Issues Offshore Norway. *Society of Petroleum Engineers Productions and Operations*, **2010,** *25* (2), 145–150.

REFERENCES

Wehr, F. L.; Brasher, L. D. Impact of Sequence-Based Correlation Style on Reservoir Model Behaviour, Lower Brent Group, North Comorant Field, UK North Sea. In *Stratigraphy: Innovations and Applications;* Howell, J. A., Aitken, J. F.; Geological Society Special Publication no. 104; The Geological Society: Bath, UK, 1996; 115–128.

Wilson, M. D.; Warne, J. R. *Sand Continuity Study: Citronelle Field, Mobile County, Alabama*. Technical Report for the Unit Manager, Citronelle Unit, November 25, 1964.

Xu, T.; Sonnenthal, E.; Spycher, N.; Pruess, K. *TOUGHREACT User's Guide: A Simulation Program for Nonisothermal Multiphase Reactive Geochemical Transport in Variably Saturated Geologic Media*. LBNL–55460, Lawrence Berkeley National Laboratory, Berkeley, CA, September, 2004.

Yortsos, Y. C. A Theoretical Analysis of Vertical Flow Equilibrium. *Transport in Porous Media,* **1995,** *18,* 107–129.

Zeng, Z.; Grigg, R. B.; Chang, S. H. *Miscible Applied Simulation Techniques for Energy Recovery Version 3.0 User's Guide. Improving CO_2 Efficiency for Recovering Oil in Heterogeneous Reservoirs*. DOE Contract No. DE–FG26–01BC15364, U.S. Department of Energy, July 26, 2005.